

1 Analysis Note:  
2 Measurement of  $D^0$ -meson production in Au+Au collisions  
3 at  $\sqrt{s_{\text{NN}}} = 200 \text{ GeV}$

4 Xiaolong Chen, Xin Dong, Mustafa Mustafa, Guannan Xie, Yifei Zhang, Long Zhou

5 October 24, 2018

6 **Abstract**

7 Heavy quarks nuclear modification factor ( $R_{AA}$ ) has been proposed as an important mea-  
8 surement to study the flavor dependence of partons energy loss in the medium, and eventually  
9 to help in extracting the medium transport, drag and diffusion coefficients.

10 We report measurements of  $D^0$ -meson production at mid-rapidity ( $|y| < 1$ ) in Au + Au  
11 collisions at  $\sqrt{s_{\text{NN}}} = 200 \text{ GeV}$  utilizing the Heavy Flavor Tracker, high resolution silicon detec-  
12 tor at the STAR experiment.  $D^0$ -mesons are reconstructed via their hadronic decay channel  
13  $D^0 \rightarrow K^- + \pi^+$  and its charge conjugate via topological reconstruction of  $D^0$  decay ver-  
14 tices. After corrected for the detector acceptance, tracking and geometric selection efficiency,  
15 invariant yields of  $D^0$ -mesons are reported in various centrality bins covering a transverse  
16 momentum region of  $0 - 8 \text{ GeV}/c$ . Nuclear modification factors ( $R_{CP}$ ) are obtained and com-  
17 pared to various phenomenological model calculations. Physics implications on charm hadron  
18 production and charm quark dynamics in the Quark-Gluon Plasma are discussed.

# 19 Contents

|    |                                                                                         |    |
|----|-----------------------------------------------------------------------------------------|----|
| 20 | <b>1 Introduction</b>                                                                   | 4  |
| 21 | <b>2 Datasets and Event Selection</b>                                                   | 5  |
| 22 | 2.1 Centrality Definition . . . . .                                                     | 5  |
| 23 | <b>3 <math>D^0</math> Reconstruction</b>                                                | 11 |
| 24 | 3.1 Daughter Selection . . . . .                                                        | 11 |
| 25 | 3.2 Topological Cut Optimization . . . . .                                              | 12 |
| 26 | 3.3 Raw Yield extraction . . . . .                                                      | 18 |
| 27 | 3.4 Mixed Event Background . . . . .                                                    | 20 |
| 28 | 3.5 Correlated background ‘bump’ for $D^0$ meson . . . . .                              | 21 |
| 29 | <b>4 Efficiency Correction</b>                                                          | 24 |
| 30 | 4.1 Single Track Efficiency . . . . .                                                   | 24 |
| 31 | 4.2 TPC Tracking Efficiency . . . . .                                                   | 24 |
| 32 | 4.3 TOF Matching Efficiency . . . . .                                                   | 25 |
| 33 | 4.4 PID Cut Efficiency . . . . .                                                        | 27 |
| 34 | 4.4.1 $n\sigma_{K/\pi}$ Cut Efficiency . . . . .                                        | 29 |
| 35 | 4.4.2 $1/\beta$ Cut Efficiency . . . . .                                                | 29 |
| 36 | 4.5 Data-driven fast Monte Carlo setup for HFT and Topological Cut Efficiency . . . . . | 29 |
| 37 | 4.5.1 Assumptions . . . . .                                                             | 32 |
| 38 | 4.5.2 Ingredients . . . . .                                                             | 32 |
| 39 | 4.5.3 Recipe . . . . .                                                                  | 33 |
| 40 | 4.5.4 $D^0$ Efficiency and Topological Distribution . . . . .                           | 33 |
| 41 | 4.6 Validation with Full GEANT+Hijing Simulation . . . . .                              | 37 |
| 42 | 4.7 Hijing Samples Performance . . . . .                                                | 37 |
| 43 | 4.8 Validation Procedures . . . . .                                                     | 39 |
| 44 | 4.8.1 Validation Efficiency . . . . .                                                   | 39 |
| 45 | 4.8.2 Validation Topological Distributions . . . . .                                    | 43 |
| 46 | 4.8.3 Validation with Ks Spectra Measurement . . . . .                                  | 44 |
| 47 | 4.9 Secondary Track Contribution . . . . .                                              | 47 |
| 48 | 4.10 Vertex Resolution Contribution . . . . .                                           | 51 |
| 49 | 4.11 Double Counting Correction . . . . .                                               | 56 |
| 50 | 4.12 Input $p_T$ shape . . . . .                                                        | 60 |
| 51 | 4.13 $p_T$ smearing effect . . . . .                                                    | 61 |
| 52 | 4.14 Lifetime uncertainties effect . . . . .                                            | 62 |
| 53 | <b>5 Systematic Uncertainties</b>                                                       | 65 |
| 54 | <b>6 Results and Discussion</b>                                                         | 71 |
| 55 | 6.1 $p_T$ Spectra and Integrated Yields . . . . .                                       | 71 |
| 56 | 6.2 Collectivity . . . . .                                                              | 71 |
| 57 | 6.2.1 $m_T$ Spectra . . . . .                                                           | 71 |
| 58 | 6.2.2 Blast-wave fit . . . . .                                                          | 75 |
| 59 | 6.3 Nuclear Modification Factor - $R_{CP}$ and $R_{AA}$ . . . . .                       | 76 |
| 60 | 6.4 $\bar{D}^0$ and $D^0$ spectra and double ratio . . . . .                            | 79 |
| 61 | 6.5 Comparison to Models . . . . .                                                      | 83 |
| 62 | 6.6 Total ccbar cross section . . . . .                                                 | 86 |
| 63 | <b>7 Re-analysis of Run10/11 data ...</b>                                               | 86 |
| 64 | 7.1 Long and Yifei’s re-analysis ... . . . . .                                          | 86 |
| 65 | 7.1.1 Added by Long Zhou . . . . .                                                      | 90 |
| 66 | 7.2 Xiaolong’s re-analysis . . . . .                                                    | 93 |
| 67 | 7.2.1 Datasets and Cuts . . . . .                                                       | 93 |
| 68 | 7.2.2 $D^0$ reconstruction . . . . .                                                    | 94 |
| 69 | 7.2.3 Efficiency and acceptance correction . . . . .                                    | 94 |
| 70 | 7.2.4 Results . . . . .                                                                 | 98 |

|    |                                                    |            |
|----|----------------------------------------------------|------------|
| 71 | <b>8 Run14 TPC analysis</b>                        | <b>102</b> |
| 72 | 8.1 Datasets and Cuts . . . . .                    | 102        |
| 73 | 8.2 $D^0$ reconstruction . . . . .                 | 104        |
| 74 | 8.3 Efficiency and acceptance correction . . . . . | 104        |
| 75 | 8.4 Results . . . . .                              | 110        |



Figure 1: Jet flavor tomography level crossing pattern of nuclear modification factors at middle rapidity of  $\pi$ , D, B, e calculations for central Au + Au 200 GeV collisions.



Figure 2: (upper)  $D^0$ ,  $\pi$ ,  $h^\pm$   $R_{AA}$  from different measurements. (bottom)  $v_2$  of  $D$  and  $h^\pm$  from ALICE.

## 1 Introduction

Heavy quarks nuclear modification factor ( $R_{AA}$ ) has been proposed as an important measurement to study the flavor dependence of partons energy loss in the medium, and eventually to help in extracting the medium transport, drag and diffusion coefficients. There are lots of theoretical calculations for the energy losses for different flavor particles. Fig. 1 shows the jet flavor tomography level crossing pattern of nuclear modification factors at middle rapidity of  $\pi$ , D, B, e from CUJT calculations for central Au + Au 200 GeV collisions. As clearly see the mass hierarchy of the different flavor energy loss.

The hadronic channels allow to fully reconstruct the charmed hadrons and do not suffer from the complications in the semi-leptonic decays, however the measurement can be challenging due to large combinatorial backgrounds and lower branching ratios. One approach is to use the decay topology to reduce this background by distinguishing between tracks that come from the collision itself (primary vertex) and those from a secondary decay vertex. This requires the detectors must be able to resolve differences on the order of tens of microns. Heavy Flavor Tracker (HFT) is essence the right detector for this mission.

Fig. 2 shows the  $R_{AA}$  of  $D^0$ ,  $\pi$ ,  $h^\pm$  from various measurements. A significant suppression is clearly seen at the high  $p_T$  range for both light hadrons and charmed hadrons both in RHIC energy and LHC energy. The enhancement observed in the intermediate  $p_T$  range from STAR can be described by the models including coalescence of charm and light quarks, even though the uncertainties are still large in the low transverse momentum range. It will be critical to precise measure the low  $p_T$  structure.

## 97 2 Datasets and Event Selection

98 The dataset used in this analysis is P16id production of 2014 Au+Au 200 GeV data. This is the  
 99 first year of physics running the new STAR HFT Detector. The analysis uses picoDst which is  
 100 produced from MuDst.

101 The Minimum-Bias (MinBias) trigger is defined as a coincidence between the two VPDs, and  
 102 an online collision vertex cut. Moreover, a pile-up protection at the trigger level was applied  
 103 for the data taking. In this analysis, the MinBias trigger, denoted as "vpdmb-5-p-nobsmd" and  
 104 "vpdmb-5-p-nobsmd-hlt", is used. The triggers used in this analysis are listed in Table 1.

Table 1: Triggers ID used in this analysis from run14

| Trigger ID | description          |
|------------|----------------------|
| 450050     | vpdmb-5-p-nobsmd-hlt |
| 450060     | vpdmb-5-p-nobsmd-hlt |
| 450005     | vpdmb-5-p-nobsmd     |
| 450015     | vpdmb-5-p-nobsmd     |
| 450025     | vpdmb-5-p-nobsmd     |

105 Events used in this analysis are required to have a valid collision vertex  $V_z$  (primary vertex)  
 106 within 6 cm of the TPC center along  $z$  direction (the beam direction) to ensure a uniform TPC  
 107 acceptance and make sure the most tracks are within the PiXeL (PXL) detector coverage. The  
 108 PXL detector is about 20 cm along the  $z$  direction, and the radius of the inner layer is about 2.8cm  
 109 and outer layer is about 8 cm. Furthermore, the distance between the  $V_z$  constructed by TPC and  
 110 the vertex constructed by VPD ( $V_z^{VPD}$ , fast detector) is within 3 cm to reject the bad events. A  
 111 radial length less than 2 cm for the vertex is required to reject the events from the beam hitting the  
 112 beam pipe. After event selection,  $\sim 875$  million MinBias events are used for this analysis. Table 2  
 113 lists the event selection criterion.

Table 2: Event selection in Au+Au collisions at 200 GeV for  $D^0$ .

| Event Selection Criteria                            |
|-----------------------------------------------------|
| $!( V_x  == 0 \ \&\&  V_y  == 0 \ \&\&  V_z  == 0)$ |
| $ V_z  < 6$ cm                                      |
| $ V_r  < 2$ cm                                      |
| $ V_z - V_z^{VPD}  < 3$ cm                          |

### 114 2.1 Centrality Definition

115 The centrality for Run14 200GeV Au+Au collisions MinBias sample is based on gRefMult. The  
 116 gRefMult is defined as the number of global tracks with  $|\eta| < 0.5$ , no less than 10 TPC hits,  
 117 and Distance of Closest Approach (DCA) to primary vertex less than 3 cm with some correction  
 118 according to  $V_z$  and luminosity. The centrality definition according to the corrected gRefMult is  
 119 listed in Table 3. This is decided by comparing the measured gRefMult distribution with the  
 120 Glauber model simulation.

121 The basic procedure for centrality definition have three steps. First, need the quality assurance  
 122 (QA) for the data set and remove those outlier runs. The second step would be correct the  $V_z$  and  
 123 luminosity dependence for the reference multiplicity (gRefmult). The last step would be compare  
 124 our data with Glauber MC simulation and determine the centrality classification.

125 For the QA, several variables are used for the outlier selection, such as Refmult (primary track  
 126 multiplicity), gRefmult (global track multiplicity), TofRefmult (tof track multiplicity) and etc. In  
 127 the Fig. 3 shows the  $\langle g\text{Refmult} \rangle$  as a function of run index for the QA, and there are several

outliers are identified. Those dashed lines are the  $4 \times \text{RMS}$  range, beyond those range, the runs are identified as bad run. And several iterations are did until all the runs are within these  $4 \times \text{RMS}$  range.

In the Fig. 4 shows the  $\langle \text{HFT } p_T \rangle$ , which is the mean  $p_T$  of HFT tracks, as a function of run index for the QA, and we can clearly see there is a deep before the run index  $\sim 520$  which corresponding to the run number 15107008. And also we saw the same structure in the Fig. 5, which shows the average of HFT matching Ratio in the  $p_T$  range between 0.7 to 0.8  $\text{GeV}/c$  and Fig. 6 shows this HFT matching ratio in the high  $p_T$  range. So, basically those runs before day 107 were taken out for this analysis, since it will complicate our efficiency calculation.

This deep was identified later on with a lot of effort, it was due to the firmware issue. And more details can be found in the STAR documents below.

[https://drupal.star.bnl.gov/STAR/system/files/STAR\\_PXL\\_Firmware\\_Issue\\_Solved\\_Final\\_Report\\_Oct3\\_v2.pdf](https://drupal.star.bnl.gov/STAR/system/files/STAR_PXL_Firmware_Issue_Solved_Final_Report_Oct3_v2.pdf)

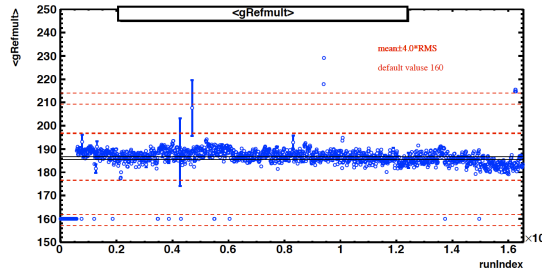


Figure 3: The mean value of gRefmult ( $\langle \text{gRefmult} \rangle$ ) as a function of run index from QA.

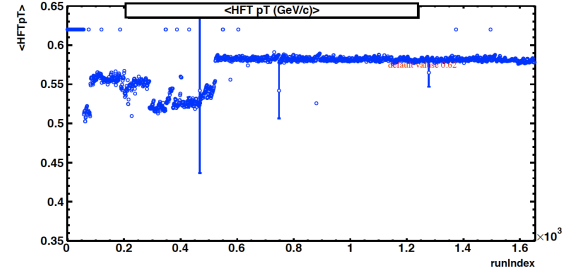


Figure 4: The mean value of  $p_T$  for HFT matched track ( $\langle \text{HFT } p_T \rangle$ ) as a function of index.

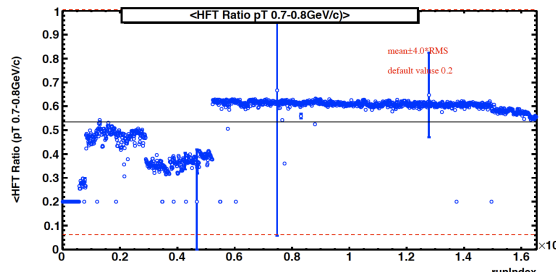


Figure 5: The HFT matching ratio at the transverse momentum range  $0.7 < p_T < 0.8 \text{ GeV}/c$  as a function of run index .

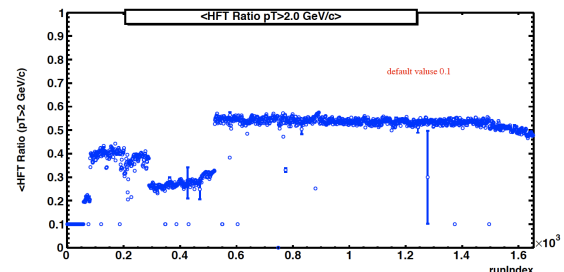


Figure 6: The mean value of HFT matching ratio at the transverse momenaum range  $p_T \sim 2.0 \text{ GeV}/c$  as a function of run index .

Fig. 7 and Fig. 8 show the normalized gRefmult distribution for several different  $V_z$  range from -6 cm to 6 cm. The shape are quite different for VpdMB5 trigger in Fig. 7 while the Fig. 8 shows the same plots for VpdMB30 trigger ( $V_z$  within range from -30 cm to 30 cm). This difference was explained by that the online Vpd vertex cut have a negative offset and the Vpd resolution has centrality dependence. As for the most central collisions, the resolution will be better than the most peripheral collisions. That is the reason we saw more events in the negative  $V_z$  range and more central events for VpdMB5 trigger compared to VpdMB30 trigger.

As the gRefmult have the luminosity dependence (related to the TPC tracking efficiency have luminosity dependence), we need to take out this effect by doing ZdcX (Zdc coincidence rate) correction. Fig. 9 shows the mean value of gRefmult ( $\langle \text{gRefmult} \rangle$ ) distribution as a function of ZdcX. There was a clear slope for this distribution as shown by the fitting parameters. Here the fitting function is Eq. 1,

$$f_{ZdcX} = p0 + p1 * ZdcX \quad (1)$$

The goal of this correction is try to flatten this ZdcX dependence to take out of the luminosity effect. So here the correction factor was shown by Eq. 2.

$$f_{ZdcX} = \frac{1}{1 + p1/p0 * ZdcX} \quad (2)$$

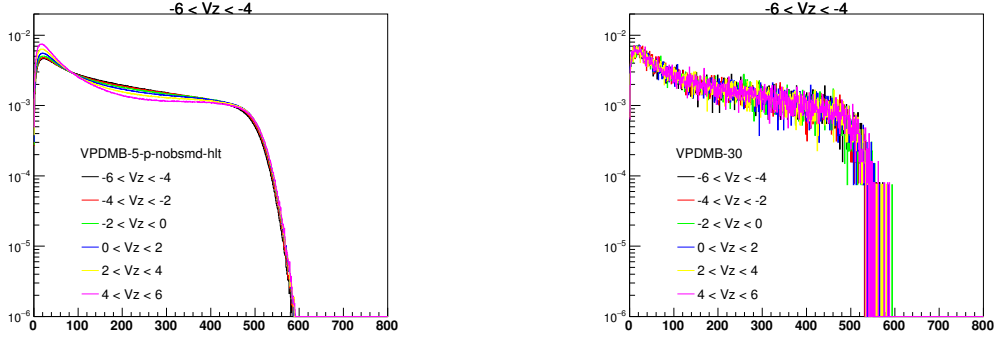


Figure 7: Normalized gRefmult distribution for VpdMB5 trigger along different  $V_z$  range  
Figure 8: Normalized gRefmult distribution for VpdMB30 trigger along different  $V_z$  range

157 After the ZdcX correction, this  $\langle g\text{Refmult} \rangle$  is flat as shown by Fig. 10.

158 For the  $V_z$  dependence correction, we extract the high end point (h) from the fitting of gRefmult  
159 tail by the function of Eq. 3.

$$160 f_x = A * TMath::Erf(-\sigma * (x - h)) + A \quad (3)$$

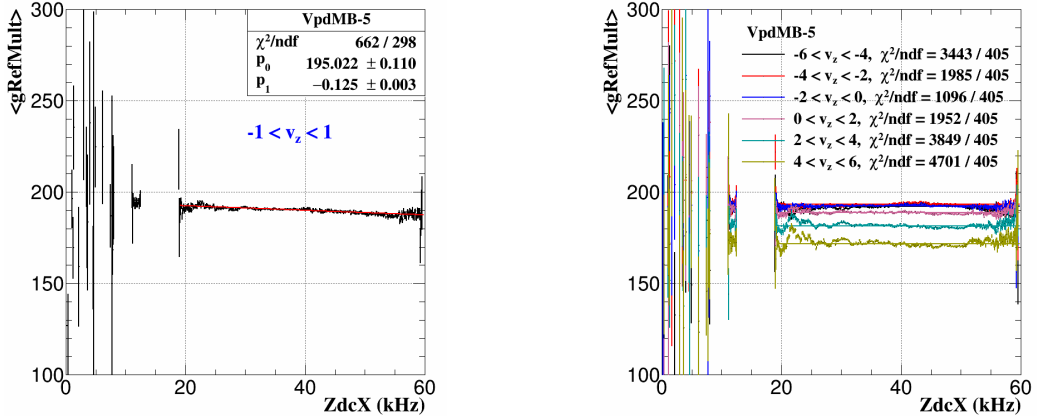


Figure 9:  $\langle g\text{Refmult} \rangle$  as function of ZdcX before correction.  
Figure 10:  $\langle g\text{Refmult} \rangle$  as function of ZdcX after correction.

161 Fig. 11 shows an example of the fitting of gRefmult tail in the  $V_z$  range from 1 cm to 2 cm.  
162 The fitting parameters were shown on the plot.

163 With all the high end point value extracted along  $V_z$  direction, this  $V_z$  dependence was shown  
164 on Fig. 12. The similar method as ZdcX correction, we need to flatten this  $V_z$  dependence, then  
165 the data point was fitted by 5th order polynomial function Eq. 4, and then the correction factor  
166 was shown by Eq. 5 After the  $V_z$  correction, this high end point is flat as shown by Fig. 13.

$$167 f_{V_z} = p0 + p1 * x + p2 * x^2 + p3 * x^3 + p4 * x^4 + p5 * x^5 \quad (4)$$

$$168 f_{V_z} = \frac{p0}{p0 + p1 * x + p2 * x^2 + p3 * x^3 + p4 * x^4 + p5 * x^5} \quad (5)$$

169 As shown from Fig. 7 and Fig. 8, the clear  $V_z$  dependence need to avoid for VpdMB5 trigger.  
170 So, the centrality definition for VpdMB5 trigger was normalized to VpdMB30. After the ZdcX  
171 correction and  $V_z$  correction, we directly take it as an additional correction factor for VpdMB5.  
172 These correction factor was show in Fig. 14. After this additional correction, the distributions  
173 from VpdMB5 and VpdMB30 are same.

174 The Vpd MinBias trigger has a trigger efficiency that are lower for peripheral events. Fig. 15  
175 shows the gRefmult after  $V_z$  and ZdcX correction from data comparison with Glauber MC simula-  
176 tion. In the high end part the agreement was well, but in the low end part, due to this trigger

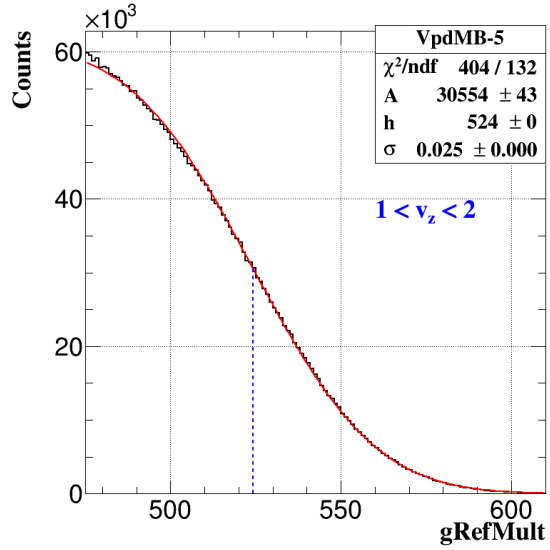


Figure 11: Fitting gRefmult tail distribution in the range of  $1 < V_z < 2$  cm by Eq. 3.

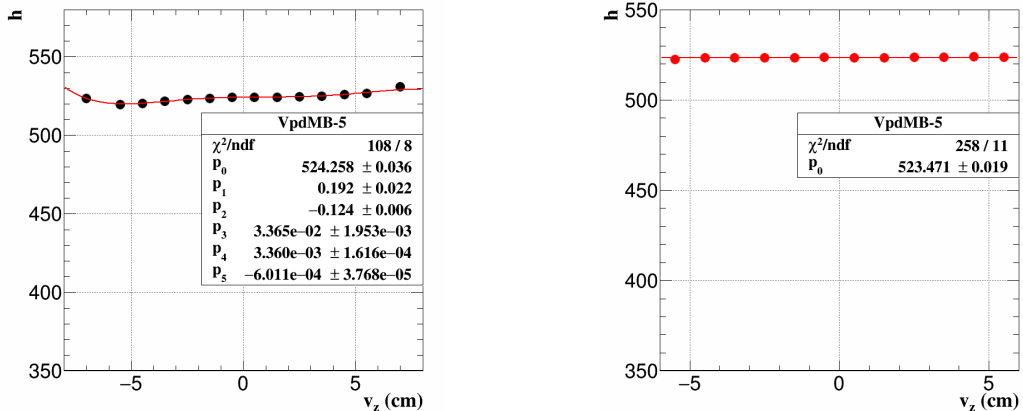


Figure 12: High end point as function of  $V_z$  before Figure 13: High end point as function of  $V_z$  after correction.

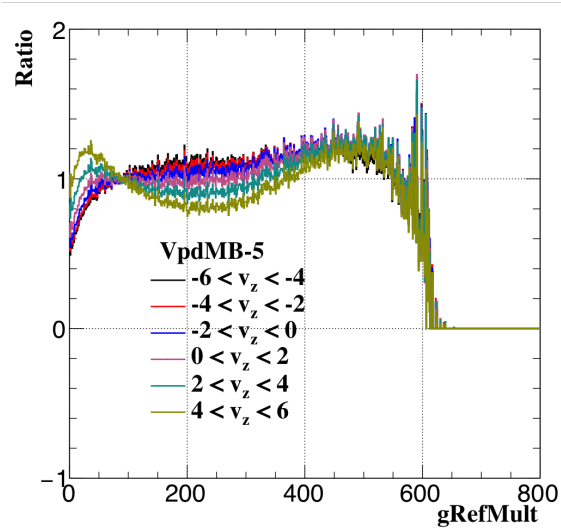


Figure 14: The double ratio of normalized gRefmult distribution from VpdMB5 over VpdMB30, this additional correction factor was try to normalized VpdMB5 to VpdMB30 trigger.

177 inefficiency, there is clearly discrepancy between data and simulation. To do the measurement  
 178 without centrality bias, a weight proportional to inverse trigger efficiency is applied. The weight  
 179 as a function of corrected gRefMult is shown in Fig. 16.

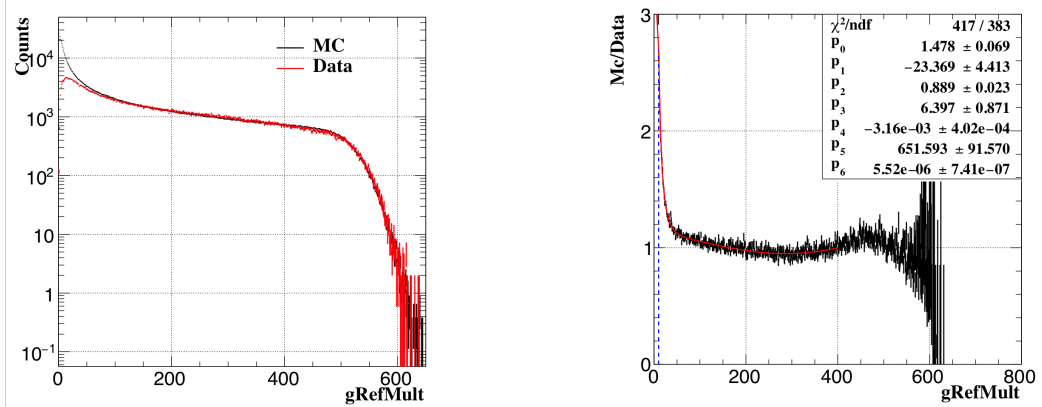


Figure 15: The comparison of corrected gRefMult between Data and Glauber MC. The red line is data MinBias trigger efficiency correction. The red line and the black line is from Glauber MC.

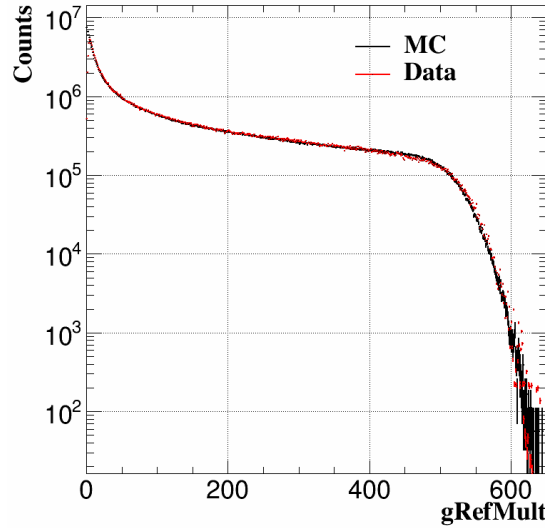


Figure 17: The comparison of corrected gRefMult (after all corrections and reweight) between Data and Glauber MC. The red line is data and the black line is from Glauber MC.

180 After all these corrections including  $V_z$ , ZdcX, Vpd trigger inefficiency, and Vpd resolution  
 181 for different centralities as discussed before. Final step, the data was compared to Glauber MC  
 182 simulation as shown in Fig. 17. And then the determined centrality classification can be found at  
 183 Table 3.

| centrality | gRefMult | $\langle N_{coll} \rangle$ | $\langle N_{part} \rangle$ |
|------------|----------|----------------------------|----------------------------|
| 75-80%     | 10-15    | 10.48                      | 11.82                      |
| 70-75%     | 15-21    | 16.11                      | 16.68                      |
| 65-70%     | 21-30    | 24.59                      | 23.25                      |
| 60-65%     | 30-41    | 36.13                      | 31.15                      |
| 55-60%     | 41-56    | 52.77                      | 41.27                      |
| 50-55%     | 56-73    | 75.36                      | 53.46                      |
| 45-50%     | 73-94    | 105.25                     | 67.93                      |
| 40-45%     | 94-119   | 143.54                     | 84.71                      |
| 35-40%     | 119-148  | 191.83                     | 103.99                     |
| 30-35%     | 148-182  | 253.13                     | 126.52                     |
| 25-30%     | 182-221  | 328.99                     | 152.31                     |
| 20-25%     | 221-266  | 422.49                     | 181.93                     |
| 15-20%     | 266-317  | 537.52                     | 215.98                     |
| 10-15%     | 317-376  | 677.99                     | 254.90                     |
| 5-10 %     | 376-443  | 852.75                     | 299.95                     |
| 0-5 %      | >443     | 1066.50                    | 348.74                     |

Table 3: Centrality definition based on gRefMult

### 184 3 $D^0$ Reconstruction

185  $D^0$  and  $\bar{D}^0$  are reconstructed through the typically hadronic channel  $K^\mp\pi^\pm$  using the topological  
 186 method. In the following we will describe the daughter selection, the geometry cuts and how they  
 187 are obtained through the TMVA tuning. We will show the  $D^0$  signals for different  $p_T$  bins. We will  
 188 also discuss some related topics: the mixed event to reconstruct the combinatorial background,  
 189 and the correlated background source shown as a ‘bump’ at invariant mass lower than the  $D^0$ .

#### 190 3.1 Daughter Selection

191  $D^0$  have a lifetime of  $c\tau \sim 123\mu\text{m}$ . Thus the global tracks for daughter tracks are used in this  
 192 analysis. The transverse momentum are required to  $\geq 0.3 \text{ GeV}/c$  to ensure that the track can pass  
 193 through the TPC and have less HFT miss matching, the number of hit points (nHits) along the  
 194 track is  $\geq 20$  (of a maximum of 45) to ensure good momentum resolution.

195 The pion and kaon tracks are identified by combining Time Projection Chamber (TPC) and  
 196 Time Of Flight detector (TOF). The TPC provides particle identification utilizing the energy loss  
 197 information  $dE/dx$ , different particle species with the same momentum may have different  $dE/dx$ .  
 198 In additional, different particle species with the same momentum have different velocities, thus the  
 199 TOF can be used to identify different particle species in the  $dE/dx$  crossover regions by precise  
 200 velocity information ( $1/\beta = ct/l$ ). The normalized  $dE/dx$ ,  $n\sigma_x$  ( $x = \pi, K, p, e$  etc.), defined in  
 201 Eq. 6, instead of  $dE/dx$  is used in this analysis. Where  $\langle dE/dx \rangle_{\text{measured}}$  and  $\langle dE/dx \rangle_x$  represent  
 202 measured and theoretical  $dE/dx$ , and  $R$  is the STAR TPC  $dE/dx$  resolution (typically  $\sim 8\%$ ). The  
 203  $n\sigma_x$  should be close to a standard Gaussian distribution for each corresponding particle species  
 204 (mean = 0,  $\sigma = 1$ ).

$$205 n\sigma_x = \frac{1}{R} \log \frac{\langle dE/dx \rangle_{\text{measured}}}{\langle dE/dx \rangle_x} \quad (6)$$

206 Fig. 18 shows the TPC energy loss  $dE/dx$  information versus momentum achieved from Run14  
 207 Au+Au 200GeV, there are several clear bands for different particle species such as  $\pi$ ,  $K$ ,  $p$  and  $e$ .

208 Fig. 19 shows the TOF 1/Beta information versus momentum achieved from Run14 Au+Au  
 209 200GeV, also there are several clear bands for different particle species such as  $\pi$ ,  $K$ ,  $p$ .

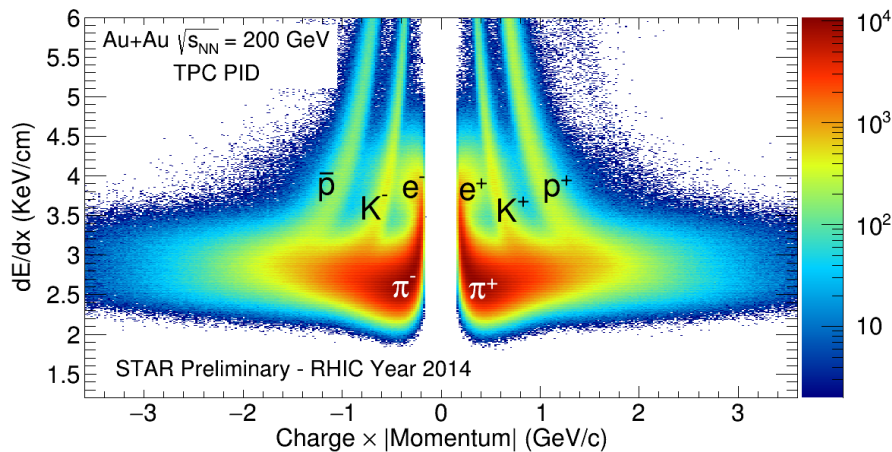


Figure 18: TPC  $dE/dx$  versus charge  $\times$  momentum achieved from Run14 Au+Au 200GeV.

210 In summary, next list all the related track selections for  $D^0$  daughters including track quality  
 211 cut and particle identification cut.

- 212 • global tracks
- 213 •  $p_T > 0.3 \text{ GeV}/c$  (next plots are based on 0.3 GeV cut, but the final result central value was  
 214 from 0.6 GeV cut, same as  $D^0$  v2 analysis)
- 215 •  $|\eta| < 1$

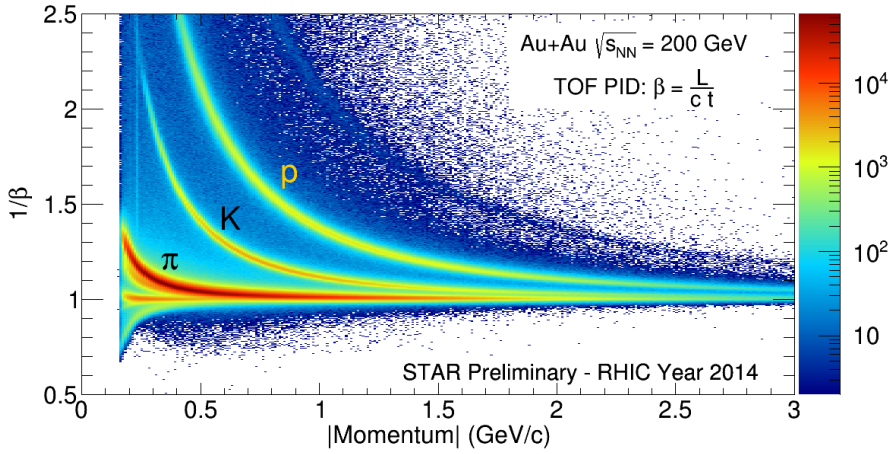


Figure 19: TOF 1/Beta versus momentum achieved from Run14 Au+Au 200GeV.

- 216     •  $nHitsFit \geq 20$ , in TPC
- 217     • at least one hit in every layer of PXL and IST
- 218     pion PID:
  - 219       •  $|n\sigma_\pi| < 3.0$ , based on TPC dE/dx
  - 220       • If TOF is available (hybrid PID):  $|\frac{1}{\beta} - \frac{1}{\beta_{exp}}| < 0.03$
- 221     kaon PID:
  - 222       •  $|n\sigma_K| < 2.0$ , based on TPC dE/dx
  - 223       • If TOF is available (hybrid PID):  $|\frac{1}{\beta} - \frac{1}{\beta_{exp}}| < 0.03$

### 224     3.2 Topological Cut Optimization

225     The secondary vertex is reconstructed with selected kaon and pion global tracks. In this analysis,  
 226     the middle point on the Distance of the Closest Approach (DCA) between two daughter tracks is  
 227     considered as the secondary decay vertex of the candidate  $D^0$ . As shown in Fig. 20, 5 geometrical  
 228     variables are chosen to select  $D^0$  and reject combinatorial background, which is dominated by a  
 229     pair of tracks directly from the primary vertex: decay length (the distance between the decay  
 230     vertex and Primary Vertex PV), DCA between the 2 daughters, DCA between the reconstructed  
 231      $D^0$  flying path and PV, DCA between the  $\pi$  track and PV, and DCA between the  $K$  track and PV.  
 232     The cuts on these variables are optimized by the Toolkit for Multivariate Data Analysis (TMVA)  
 233     package. They change according to the  $D^0$  candidate  $p_T$  and centrality in order to have the best  
 234     significance in all the covered  $p_T$  and centrality range. Additionally there is a  $\cos(\theta) > 0.95$  cut  
 235     to make sure the decay vertex with respect to the primary vertex is roughly close to the same  
 236     direction as the momentum.

237     The TMVA need signal and background sample input for training. The signal sample is obtained  
 238     from the real data fast-simulation which will discuss later and the background sample is from real  
 239     data like sign pairs in the  $D^0$  mass window and unlike sign pairs in side bands range.

240     Fig. 21 shows an example of the distributions of the 5 geometry variables for signal (blue) and  
 241     background (red) plotted by the TMVA, for  $p_T$  between 1 and 2 GeV/c and centrality for 0-10%.

242     When used for TMVA training, since we know the  $D^0$  pt spectra, so the signal yield is calculated  
 243     and scaled to what is expected for the whole data set. And for the background sample, we can  
 244     obtain it from the real data, and then scale to the level of data set you needed.

245     The ‘cuts’ option of TMVA is used to tune  $D^0$  cuts. This option randomly sample different cut  
 246     sets in the variable space, calculate signal and background efficiency for each cut set. Then one  
 247     cut set with lowest background efficiency at certain signal efficiency. We can then pick the cut set  
 248     with the best significance according to the signal and background yield corresponding to the whole



Figure 20: The topology of a  $D^0$  decaying to a kaon and a pion.

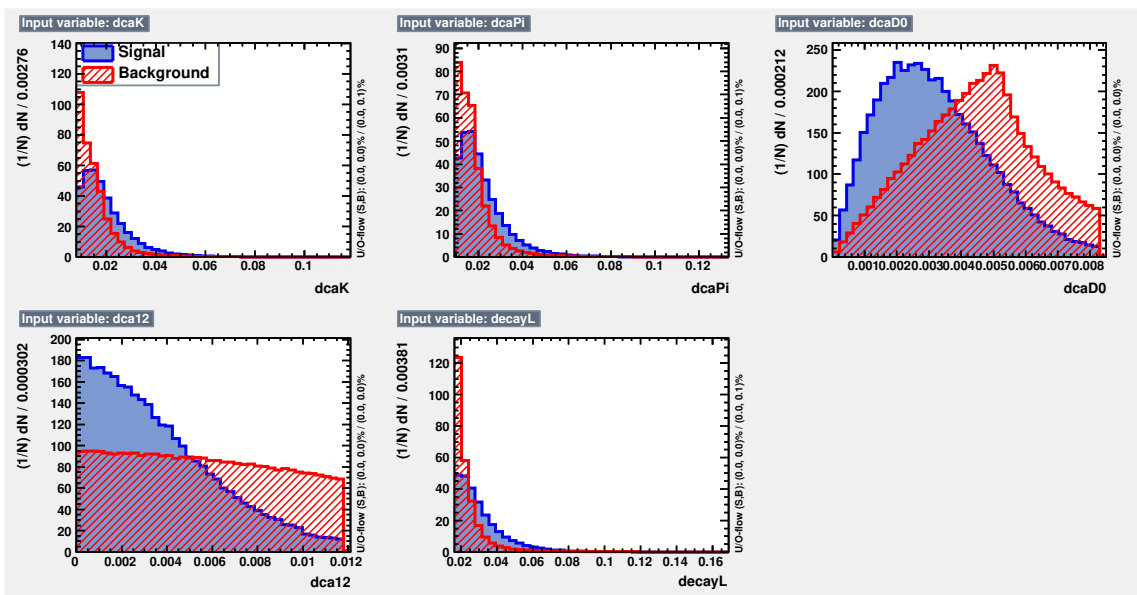


Figure 21: Distributions of the 5 geometry variables for signal (blue) and background (red) from 0-10% and 1-2 GeV/c.

249 data set. Fig. 23 shows the lowest background efficiency, significance and so on vs. signal efficiency  
 250 for  $p_T$  between 1 and 2 GeV/c for the centrality 0-10%. We can see that as cuts get tighter, signal  
 251 and background efficiency both decrease, but background efficiency decreases much faster.

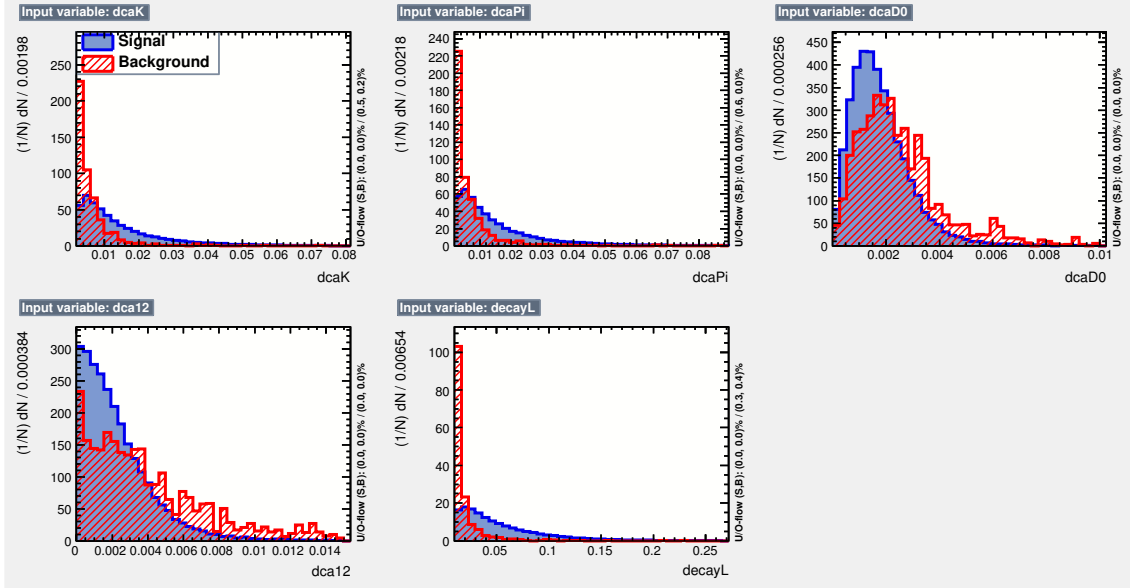


Figure 22: Distributions of the 5 geometry variables for signal (blue) and background (red) from 60-80% and 5-8 GeV/c.

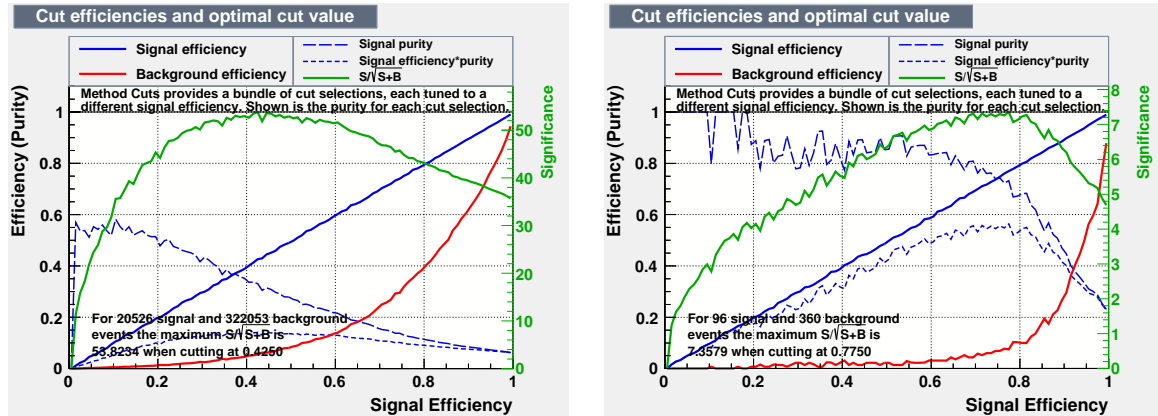


Figure 23: Signal efficiency, lowest background efficiency, significance and so on vs. signal efficiency from 0-10% and 1-2 GeV/c.

Figure 24: Signal efficiency, lowest background efficiency, significance and so on vs. signal efficiency from 60-80% and 5-8 GeV/c.

252 Fig. 22 and Fig. 24 shows the similar plots for the 5-8 GeV/c in the centrality 60-80%.  
 253

254 The result of the geometry cuts tuned for best significance are shown in Table 4. These are the  
 255 standard cuts used in the  $D^0$  reconstruction to calculate the spectra central value.

256 For  $D^0$  estimation, another 2 sets of geometry cuts are tuned with TMVA, with 50% and 150%  
 257 signal efficiency relative to the standard cuts. They do not give the overall best  $D^0$  significance,  
 258 but for the certain signal efficiency, they are still the cuts with the lowest background efficiency  
 259 and best  $D^0$  significance. With 50% and 150% signal efficiency relative to the standard cuts, their  
 260 significance is still about 80% of the standard cuts with the overall best significance. These 2 cuts  
 sets are listed in Table 5 and 6.

261 For more details can be found in the  $D^0 v_2$  technicl note, basically we use the same cuts for  
 262 spectra analysis and  $v_2$  analysis.

263 <https://drupal.star.bnl.gov/STAR/starnotes/private/psn0651>

Table 4: Standard geometrical cuts for different  $D^0 p_T$ .

| $D^0 p_T$ (GeV/c)                      | 0-0.5 | 0.5-1 | 1-2  | 2-3  | 3-5  | 5-10 |
|----------------------------------------|-------|-------|------|------|------|------|
| Centrality 60-80%                      |       |       |      |      |      |      |
| significance                           | 6.7   | 13.3  | 25.4 | 28.4 | 23.4 | 12.0 |
| decay length ( $\mu m$ ) >             | 175   | 175   | 187  | 178  | 184  | 187  |
| DCA between 2 daughters ( $\mu m$ ) <  | 77    | 77    | 94   | 78   | 81   | 120  |
| DCA between $D^0$ and PV ( $\mu m$ ) < | 76    | 76    | 53   | 54   | 54   | 42   |
| DCA between $\pi$ and PV ( $\mu m$ ) > | 98    | 98    | 83   | 73   | 56   | 50   |
| DCA between $K$ and PV ( $\mu m$ ) >   | 106   | 106   | 69   | 68   | 50   | 50   |
| Centrality 40-60%                      |       |       |      |      |      |      |
| significance                           | 8.1   | 20.0  | 53.4 | 57.8 | 49.7 | 19.0 |
| decay length ( $\mu m$ ) >             | 171   | 196   | 210  | 187  | 190  | 214  |
| DCA between 2 daughters ( $\mu m$ ) <  | 80    | 83    | 92   | 81   | 94   | 106  |
| DCA between $D^0$ and PV ( $\mu m$ ) < | 72    | 57    | 58   | 49   | 49   | 47   |
| DCA between $\pi$ and PV ( $\mu m$ ) > | 145   | 128   | 72   | 79   | 60   | 51   |
| DCA between $K$ and PV ( $\mu m$ ) >   | 140   | 100   | 75   | 72   | 60   | 50   |
| Centrality 20-40%                      |       |       |      |      |      |      |
| significance                           | 10.9  | 24.0  | 77.4 | 84.8 | 72.7 | 27.3 |
| decay length ( $\mu m$ ) >             | 178   | 206   | 221  | 209  | 219  | 240  |
| DCA between 2 daughters ( $\mu m$ ) <  | 78    | 73    | 80   | 93   | 96   | 103  |
| DCA between $D^0$ and PV ( $\mu m$ ) < | 66    | 55    | 53   | 46   | 41   | 50   |
| DCA between $\pi$ and PV ( $\mu m$ ) > | 131   | 113   | 99   | 106  | 65   | 52   |
| DCA between $K$ and PV ( $\mu m$ ) >   | 151   | 102   | 104  | 99   | 63   | 50   |
| Centrality 10-20%                      |       |       |      |      |      |      |
| significance                           | 7.5   | 17.2  | 56.2 | 69.5 | 58.0 | 20.6 |
| decay length ( $\mu m$ ) >             | 172   | 215   | 252  | 232  | 236  | 237  |
| DCA between 2 daughters ( $\mu m$ ) <  | 76    | 78    | 92   | 72   | 86   | 85   |
| DCA between $D^0$ and PV ( $\mu m$ ) < | 63    | 47    | 45   | 46   | 42   | 44   |
| DCA between $\pi$ and PV ( $\mu m$ ) > | 141   | 100   | 74   | 77   | 66   | 52   |
| DCA between $K$ and PV ( $\mu m$ ) >   | 145   | 113   | 94   | 89   | 69   | 50   |
| Centrality 0-10%                       |       |       |      |      |      |      |
| decay length ( $\mu m$ ) >             | 100   | 199   | 227  | 232  | 236  | 255  |
| DCA between 2 daughters ( $\mu m$ ) <  | 71    | 64    | 70   | 63   | 82   | 80   |
| DCA between $D^0$ and PV ( $\mu m$ ) < | 62    | 55    | 40   | 40   | 40   | 44   |
| DCA between $\pi$ and PV ( $\mu m$ ) > | 131   | 105   | 93   | 97   | 67   | 55   |
| DCA between $K$ and PV ( $\mu m$ ) >   | 138   | 109   | 82   | 94   | 76   | 54   |

Table 5: Tight geometrical cuts for different  $D^0 p_T$ .

| $D^0 p_T$ (GeV/c)                      | 0-0.5 | 0.5-1 | 1-2 | 2-3 | 3-5 | 5-10 |
|----------------------------------------|-------|-------|-----|-----|-----|------|
| Centrality 60-80%                      |       |       |     |     |     |      |
| decay length ( $\mu m$ ) >             | 203   | 203   | 206 | 228 | 161 | 216  |
| DCA between 2 daughters ( $\mu m$ ) <  | 76    | 76    | 78  | 95  | 76  | 93   |
| DCA between $D^0$ and PV ( $\mu m$ ) < | 58    | 58    | 51  | 36  | 36  | 31   |
| DCA between $\pi$ and PV ( $\mu m$ ) > | 130   | 130   | 130 | 95  | 97  | 86   |
| DCA between $K$ and PV ( $\mu m$ ) >   | 126   | 126   | 116 | 97  | 76  | 50   |
| Centrality 40-60%                      |       |       |     |     |     |      |
| decay length ( $\mu m$ ) >             | 222   | 229   | 269 | 236 | 232 | 182  |
| DCA between 2 daughters ( $\mu m$ ) <  | 88    | 59    | 81  | 83  | 73  | 108  |
| DCA between $D^0$ and PV ( $\mu m$ ) < | 56    | 45    | 50  | 37  | 29  | 26   |
| DCA between $\pi$ and PV ( $\mu m$ ) > | 143   | 100   | 72  | 145 | 113 | 95   |
| DCA between $K$ and PV ( $\mu m$ ) >   | 176   | 100   | 123 | 92  | 68  | 56   |
| Centrality 20-40%                      |       |       |     |     |     |      |
| decay length ( $\mu m$ ) >             | 240   | 242   | 268 | 319 | 176 | 338  |
| DCA between 2 daughters ( $\mu m$ ) <  | 61    | 43    | 70  | 89  | 66  | 70   |
| DCA between $D^0$ and PV ( $\mu m$ ) < | 62    | 60    | 37  | 38  | 30  | 26   |
| DCA between $\pi$ and PV ( $\mu m$ ) > | 150   | 113   | 63  | 149 | 107 | 105  |
| DCA between $K$ and PV ( $\mu m$ ) >   | 158   | 123   | 133 | 125 | 103 | 53   |
| Centrality 10-20%                      |       |       |     |     |     |      |
| decay length ( $\mu m$ ) >             | 219   | 240   | 213 | 231 | 261 | 399  |
| DCA between 2 daughters ( $\mu m$ ) <  | 77    | 49    | 42  | 56  | 53  | 119  |
| DCA between $D^0$ and PV ( $\mu m$ ) < | 56    | 49    | 39  | 36  | 33  | 28   |
| DCA between $\pi$ and PV ( $\mu m$ ) > | 172   | 100   | 144 | 133 | 130 | 92   |
| DCA between $K$ and PV ( $\mu m$ ) >   | 172   | 165   | 119 | 125 | 91  | 57   |
| Centrality 0-10%                       |       |       |     |     |     |      |
| decay length ( $\mu m$ ) >             | 100   | 230   | 268 | 292 | 249 | 225  |
| DCA between 2 daughters ( $\mu m$ ) <  | 77    | 44    | 47  | 73  | 60  | 61   |
| DCA between $D^0$ and PV ( $\mu m$ ) < | 55    | 53    | 37  | 27  | 26  | 25   |
| DCA between $\pi$ and PV ( $\mu m$ ) > | 139   | 148   | 93  | 133 | 80  | 88   |
| DCA between $K$ and PV ( $\mu m$ ) >   | 170   | 109   | 117 | 109 | 111 | 59   |

Table 6: Loose geometrical cuts for different  $D^0 p_T$ .

| $D^0 p_T$ (GeV/c)                      | 0-0.5 | 0.5-1 | 1-2 | 2-3 | 3-5 | 5-10 |
|----------------------------------------|-------|-------|-----|-----|-----|------|
| Centrality 60-80%                      |       |       |     |     |     |      |
| decay length ( $\mu m$ ) >             | 154   | 154   | 163 | 147 | 126 | 140  |
| DCA between 2 daughters ( $\mu m$ ) <  | 97    | 97    | 123 | 92  | 93  | 92   |
| DCA between $D^0$ and PV ( $\mu m$ ) < | 83    | 83    | 90  | 77  | 59  | 55   |
| DCA between $\pi$ and PV ( $\mu m$ ) > | 98    | 98    | 80  | 58  | 50  | 50   |
| DCA between $K$ and PV ( $\mu m$ ) >   | 90    | 90    | 73  | 57  | 50  | 50   |
| Centrality 40-60%                      |       |       |     |     |     |      |
| decay length ( $\mu m$ ) >             | 158   | 153   | 172 | 150 | 126 | 164  |
| DCA between 2 daughters ( $\mu m$ ) <  | 95    | 84    | 100 | 108 | 130 | 113  |
| DCA between $D^0$ and PV ( $\mu m$ ) < | 69    | 83    | 87  | 77  | 85  | 72   |
| DCA between $\pi$ and PV ( $\mu m$ ) > | 124   | 114   | 72  | 50  | 50  | 50   |
| DCA between $K$ and PV ( $\mu m$ ) >   | 115   | 114   | 67  | 50  | 50  | 50   |
| Centrality 20-40%                      |       |       |     |     |     |      |
| decay length ( $\mu m$ ) >             | 100   | 177   | 177 | 194 | 131 | 150  |
| DCA between 2 daughters ( $\mu m$ ) <  | 81    | 90    | 78  | 94  | 137 | 121  |
| DCA between $D^0$ and PV ( $\mu m$ ) < | 75    | 73    | 56  | 53  | 100 | 90   |
| DCA between $\pi$ and PV ( $\mu m$ ) > | 111   | 113   | 89  | 62  | 50  | 50   |
| DCA between $K$ and PV ( $\mu m$ ) >   | 134   | 112   | 74  | 63  | 50  | 50   |
| Centrality 10-20%                      |       |       |     |     |     |      |
| decay length ( $\mu m$ ) >             | 157   | 197   | 222 | 180 | 155 | 189  |
| DCA between 2 daughters ( $\mu m$ ) <  | 82    | 86    | 99  | 102 | 121 | 105  |
| DCA between $D^0$ and PV ( $\mu m$ ) < | 71    | 63    | 55  | 52  | 65  | 55   |
| DCA between $\pi$ and PV ( $\mu m$ ) > | 108   | 100   | 74  | 69  | 50  | 50   |
| DCA between $K$ and PV ( $\mu m$ ) >   | 135   | 120   | 70  | 60  | 50  | 50   |
| Centrality 0-10%                       |       |       |     |     |     |      |
| decay length ( $\mu m$ ) >             | 148   | 179   | 215 | 198 | 167 | 206  |
| DCA between 2 daughters ( $\mu m$ ) <  | 98    | 87    | 88  | 78  | 100 | 101  |
| DCA between $D^0$ and PV ( $\mu m$ ) < | 78    | 63    | 54  | 45  | 62  | 47   |
| DCA between $\pi$ and PV ( $\mu m$ ) > | 116   | 105   | 93  | 72  | 50  | 50   |
| DCA between $K$ and PV ( $\mu m$ ) >   | 111   | 109   | 80  | 67  | 50  | 50   |

264 Fig. 25 and Fig. 27 shows the invariant mass distribution for foreground and two descriptions  
 265 of combinatorial background in three different pT range and for three different centrality species.

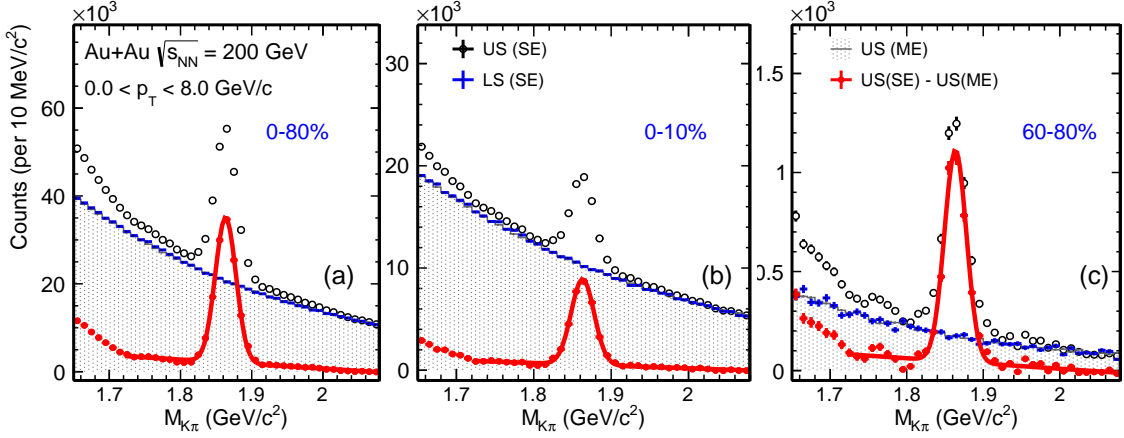


Figure 25: Invariant mass distribution for foreground and two descriptions of combinatorial background in  $0 < p_T < 8 \text{ GeV}/c$  for three different centrality species.

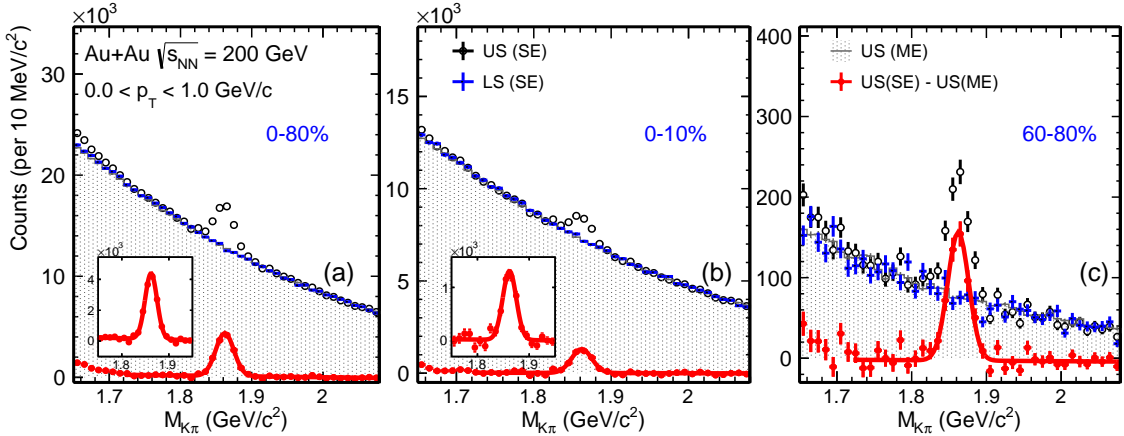


Figure 26: Invariant mass distribution for foreground and two descriptions of combinatorial background in  $0 < p_T < 1 \text{ GeV}/c$  for three different centrality species.

### 266 3.3 Raw Yield extraction

267 For the raw yield extraction, several methods are tried. The central value was from the fitting  
 268 method. After the normalized mixed Event background subtraction, we use a gaussian + pol1  
 269 function to extract the raw signal yield. The statistics error was propagate from the fitting.

270 For the fitting method, the line shape of the pol1 function was determined using a pre-fitted  
 271 function which exclude the  $D^0$  mass range. And then propagate to the gaussian+pol1 function as  
 272 the initial and free parameters.

273 We also tried the binning counting method, after the normalized mixed events background  
 274 subtraction. The residual background and signal distribution was fitted with an gaussian function  
 275 to determine the signal width, then the counts within  $3\sigma$  was counted. And the residual background  
 276 was estimated with the sideband method or from the fitted background. The statistics errors was  
 277 propagated accordingly and comparable with the previous fitting method.

278 Fig. 28 shows the  $D^0$  raw counts comparison with these two methods, binning counting method  
 279 and fitting method. As can see, the two results are consistent with each other.

280 We also tried the same-event like-sign background method, but as clearly the background  
 281 fluctuation was large compared to the mix-event method. These raw yield difference from these  
 282 methods will be contributed the final systematic source which will be discussed in the later section.

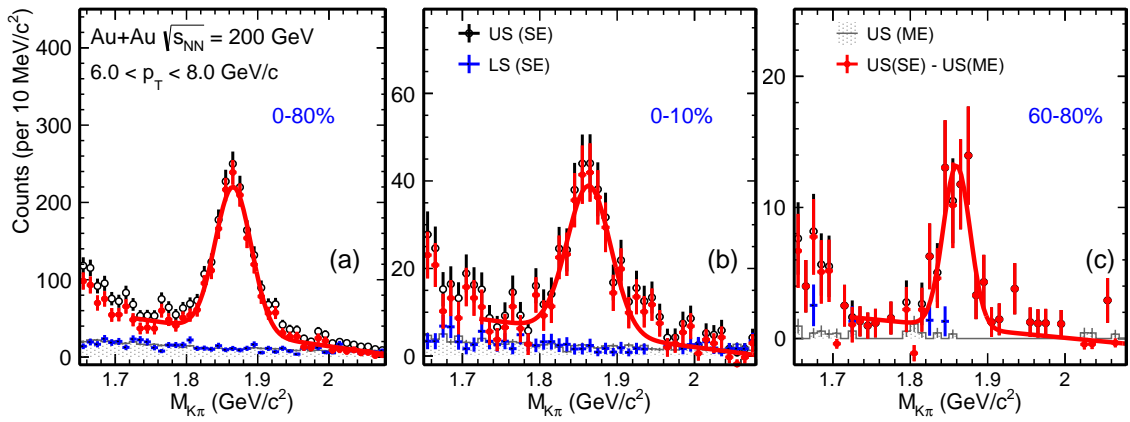


Figure 27: Invariant mass distribution for foreground and two descriptions of combinatorial background in  $0 < p_T < 1 \text{ GeV}/c$  for three different centrality species.

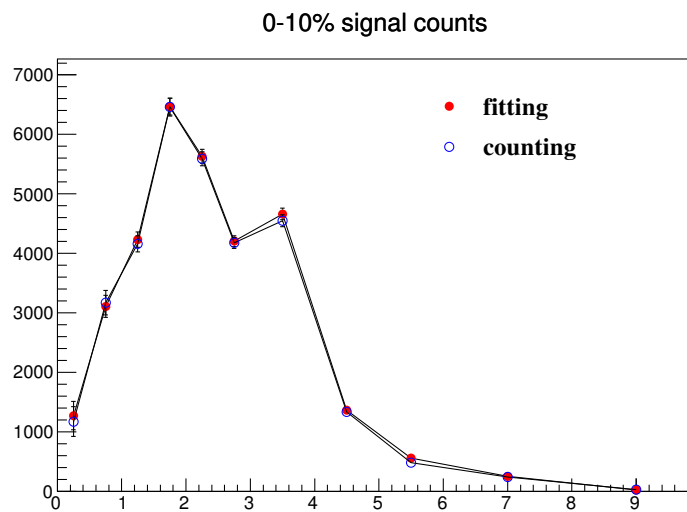


Figure 28:  $D^0$  raw counts comparison for the two different methods in the centrality species 0-10%.

For all the signals plots, they can be found in the link below.  
<http://www.star.bnl.gov/protected/heavy/xgn1992/paper/D0spectra/signal/yieldExtraction/>

### 3.4 Mixed Event Background

To construct the mixed event background it is important to combine events with some degree of similarity, such as events are classified according to the position of the primary vertex (PV) along the beam-line, the centrality class and the orientation of the event plane. Ten bins of equal width were used for both the event plane ( $\Psi \in [-\pi, \pi]$ ) and the position of the primary vertex( $V_z \in [-6, 6]$ ), as well as nine centrality classes between 0-80%, for a total of 900 event ‘categories’. For the 9 centralities, it was divided from the StRefmultCor class, from 70-80%, 60-70%, ..., 20-30%, 10-20%, 5-10% and 0-5%.

Table 7 summarizes the important information saved for the event mixing:

Table 7: Summary of information saved for the event mixing

| StMixerTrack      | StMixerEvent                                                                                          |
|-------------------|-------------------------------------------------------------------------------------------------------|
| Origin            | PV Origin                                                                                             |
| Momentum          | Magnetic Field                                                                                        |
| Q-Vector          | Event Plane                                                                                           |
| Track information | Array of mixer tracks<br>Array of indices to identified pions<br>Array of indices to identified kaons |

Fig. 29 and Fig. 30 show the invariant mass distribution for the foreground and two different uncorrelated backgrounds: same event like-sign and mixed event unlike-sign in two  $p_T$  bins include 1-2 GeV/c and 4-5 GeV/c. The mixed event backgrounds have been scaled to the foreground using the integration range  $m_{K\pi} \in [1.6, 2.1]$  GeV/c<sup>2</sup>.

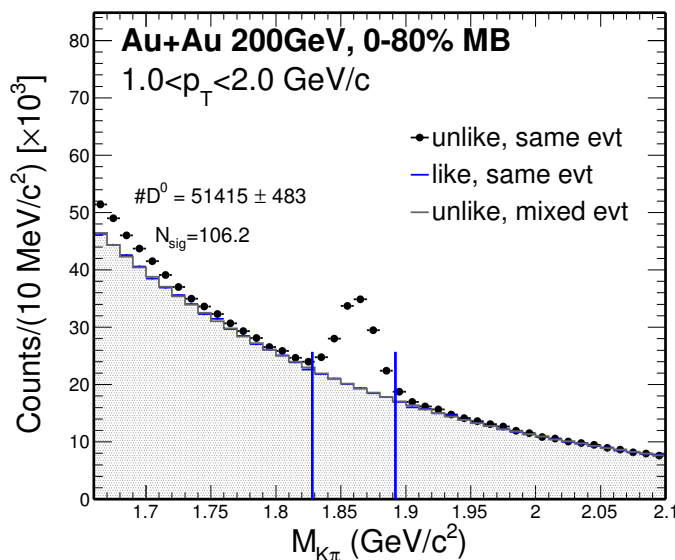


Figure 29: Invariant mass distribution for foreground and two descriptions of combinatorial background in  $1 < p_T < 2$  GeV/c.

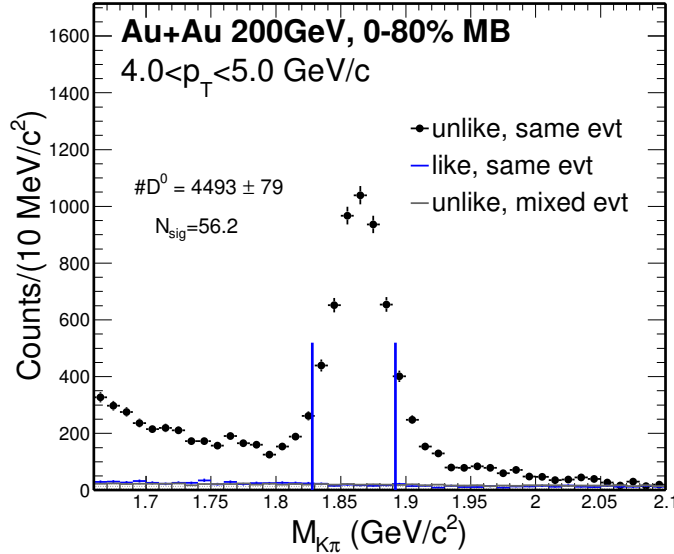


Figure 30: Invariant mass distribution for foreground and two descriptions of combinatorial background in  $4 < p_T < 5 \text{ GeV}/c$ .

298 There is good agreement between the two descriptions of the combinatorial background and  
 299 they appear to provide an adequate description in the vicinity of the  $D^0$  signal and the mixed  
 300 event backgrounds have improved statistical precision.

301 It is interesting to observe the presence of an ‘excess’ in the foreground, relative to all of the  
 302 background curves, below roughly  $1.75 \text{ GeV}/c^2$ . This so called bump was investigated using the  
 303 Data Driven Fast Simulator, and will be covered briefly in the following section.

### 304 3.5 Correlated background ‘bump’ for $D^0$ meson

305 The contributions to the invariant mass spectrum from the following  $D^0$  and  $D^\pm$  decays were  
 306 included in a qualitative study of the correlated background:

- 307 •  $D^0 \rightarrow K^-\pi^+$  (B.R. 0.039)
- 308 •  $D^0 \rightarrow K^-\pi^+\pi^0$  (B.R. 0.011)
- 309 •  $D^0 \rightarrow K^-\rho^+ \rightarrow K^-\pi^+\pi^0$  (B.R. 0.108)
- 310 •  $D^0 \rightarrow K^{*-}\pi^+ \rightarrow K^-\pi^+\pi^0$  (B.R. 0.007)
- 311 •  $D^+ \rightarrow K^-\pi^+\pi^+$  (B.R.  $0.073 \times 0.415$ )

312 The charm fragmentation ratio used is the following from ZEUS Collaboration (arXiv:hep-  
 313 ex/0508019 - Table 4):

- 314 •  $f(c \rightarrow D^+) = 0.217$
- 315 •  $f(c \rightarrow D^0) = 0.523$
- 316 •  $f(c \rightarrow D_s^+) = 0.095$
- 317 •  $f(c \rightarrow \Lambda_c^+) = 0.144$
- 318 •  $f(c \rightarrow D^{*+}) = 0.200$

319 Fig. 31 and Fig. 32 show the invariant mass spectrum obtained from the cocktail after scaling by  
 320 the branching ratio for different decays as well as the fragmentation ratio for the different charmed  
 321 meson species.

322 The spectrum is shown before and after the  $D^0 \rightarrow K\pi$  topological cuts have been applied. It  
 323 is clear that the contributions from correlated background can, at least in part, account for the  
 324 enhancement observed below roughly  $1.7 \text{ GeV}/c^2$ .

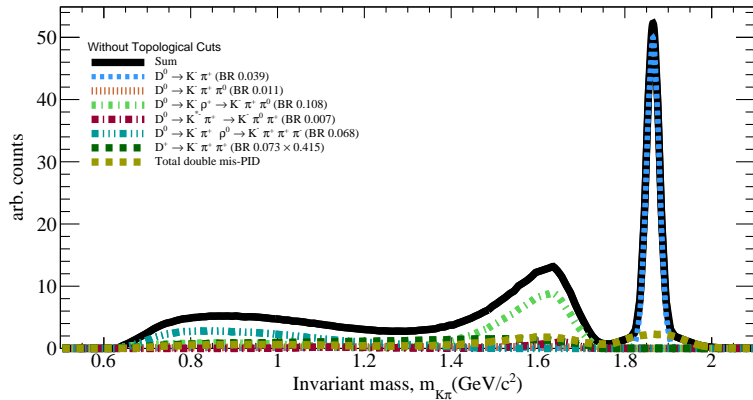


Figure 31: Simulated contribution to the invariant mass spectrum from cocktail without topological cut

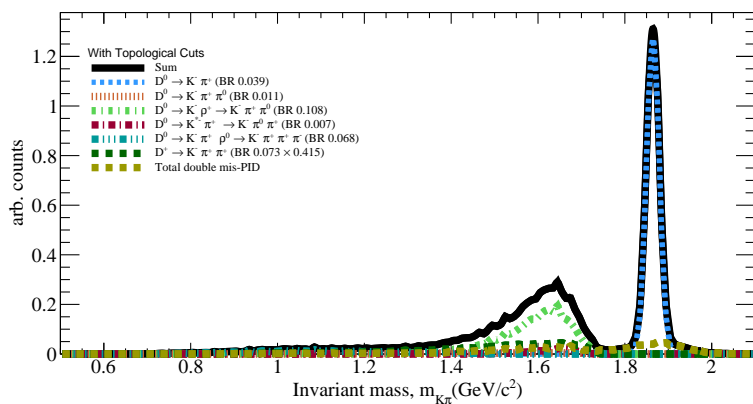


Figure 32: Simulated contribution to the invariant mass spectrum from cocktail with topological cut

325     The cocktail simulation was then scaled by fitting the amplitude of the  $D^0$  peak obtained from  
 326 fast simulator to the signal observed in data, and the cocktail was then added to the mixed event  
 327 background. Fig. 33 and Fig. 34 shows a comparison between the invariant mass distribution  
 328 obtained from data and the spectrum obtained by combining the mixed event background and the  
 329 results from the data-driven Fast-Simulator.

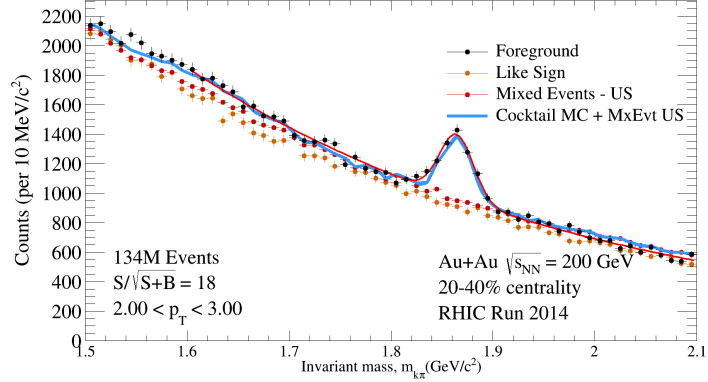


Figure 33: Comparison of  $K\pi$  invariant mass distribution for unlike-sign (US) foreground, like-sign combinatorial background, unlike-sign (US) mixed events combinatorial background, and unlike-sign (US) mixed events combinatorial background + toy montecarlo cocktail for correlated background, for  $2 < p_T < 3$  GeV/ $c$ .

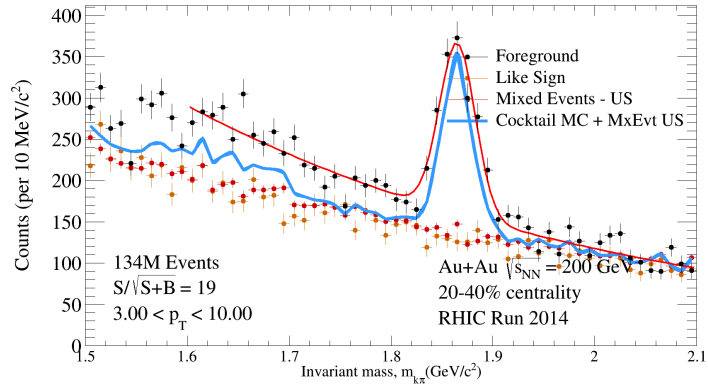


Figure 34: Similar Comparison of  $K\pi$  invariant mass distribution as Fig. 33, for  $3 < p_T < 10$  GeV/ $c$ .

330     The inclusion of correlated background sources can qualitatively describe the foreground ob-  
 331 served, reproducing the location of the bump structure albeit underestimating the degree of en-  
 332 hancement itself. Furthermore, there is likely a finite contribution to the observed bump originating  
 333 from jet correlations which should be included to improve on the description of the background.

334     It should also be noted that the studies presented here were done with an early version of  
 335 the fast simulator which only included the  $p_T$  and centrality dependence of sampled distributions,  
 336 revisiting the studies with more differential distributions should improve on these results.

337     Nonetheless, the results provide confidence in a qualitative understanding on the sources of the  
 338 correlated background and, what is more, suggest that the contribution from these source in the  
 339  $D^0$  signal range is dominated by double mis-PID, and is nearly negligible as shown in the following  
 340 sub-section.

## 341 4 Efficiency Correction

342 To obtain the real invariant mass spectrum of  $D^0$  within STAR acceptance ( $|\eta_\pi| \leq 1, |\eta_K| \leq$   
 343  $1, |Y_{K\pi}| \leq 1$ ), the raw spectrum should correct for the efficiency. The  $K\pi$  pair efficiency within  
 344 STAR acceptance is evaluated by folding the TPC related efficiency to the HFT related efficiency  
 345 as shown on Eq. 7. For the TPC related tracking efficiency shows on the first term, we use STAR  
 346 standard Full GEANT simulation. For the HFT related efficiency include the second and third  
 347 terms which reflect to HFT acceptance and topological cuts, we developed the ‘Data-Driven Fast  
 348 simulation’ which will discuss later.

$$349 \quad \text{Efficiency} \times \text{Acceptance} = \text{TPC Tracking Eff} \otimes \text{HFT Tracking Eff} \otimes \text{Topollogy Cuts} \quad (7)$$

350 This formula can be written in another way when we consider the particles identification (PID)  
 351 Eq. 8. Here the PID part are able to factorized as Eq. 9, Eq. 10.

$$352 \quad \frac{\text{HFT}}{\text{MC}} = \frac{\text{TPC}_{\text{withPID}}}{\text{MC}} \otimes \frac{\text{HFT}_{\text{withPID}}}{\text{TPC}_{\text{withPID}}} \otimes \text{PID} \quad (8)$$

$$353 \quad \varepsilon(\text{HFT} \& \text{PID}_{\text{TPC}} \& \text{PID}_{\text{TOF}}) = \varepsilon(\text{HFT} | \text{PID}_{\text{TPC}} \& \text{PID}_{\text{TOF}}) \times \varepsilon_{\text{PID}}(\text{TPC} \& \text{TOF}) \quad (9)$$

$$354 \quad \varepsilon_{\text{PID}}(\text{TPC} \& \text{TOF}) = (1 - \varepsilon_{\text{TofMatch}} + \varepsilon_{\text{TofMatch}} \times \varepsilon_{\text{TofPID}}) \times \varepsilon_{\text{TPC}} \quad (10)$$

### 355 4.1 Single Track Efficiency

356 The single track efficiency losses have two contributions, the detector inefficiency and particle  
 357 identification cuts. The detector efficiency includes the TPC tracking efficiency ( $\varepsilon_{\text{TPC}}$ ) and the  
 358 TOF matching efficiency ( $\varepsilon_{\text{TOF}}$ ). The particle identification cut efficiency ( $\varepsilon_{\text{PID}}$ ) includes the  
 359 efficiencies of TOF velocity ( $1/\beta$ ) and the  $dE/dx$  selection cuts. So the single track efficiency can  
 360 be derived by the Eq. 11

$$361 \quad \varepsilon = \varepsilon_{\text{TPC}} \otimes \varepsilon_{\text{TOF}} \otimes \varepsilon_{\text{PID}} \quad (11)$$

### 362 4.2 TPC Tracking Efficiency

363 The TPC tracking efficiency ( $\varepsilon_{\text{TPC}}$ ) is evaluated via the standard STAR embedding technique.  
 364 TPC efficiency including two parts, TPC response and acceptance efficiency. The Monte Carlo  
 365 (MC) tracks are embedded into the raw data to have a realistic detector occupancy environment.  
 366 The raw data is randomly sampled over the entire Au+Au minimum-bias data set, while the  
 367 number of embedded MC tracks is constrained to 5% of the measured multiplicity of the real  
 368 events to avoid a sizable impact on the realistic TPC tracking efficiency. The MC tracks, with flat  
 369  $p_T$ ,  $\eta$ , and  $\phi$ , are generated and passed through the full GEANT simulation of the STAR detector  
 370 geometry, and then mixed with the real data. The mixed signals are processed using the same  
 371 procedures as real data. The quality assurance is made to ensure the MC simulation reproduces  
 372 the real data before studying the TPC tracking efficiency (Embedding QA). The TPC tracking  
 373 efficiency is derived by taking the ratio of the number of reconstructed MC tracks ( $N_{\text{rec}}$ ), satisfying  
 374 the track quality cuts used in the data analysis, over the number of embedded MC tracks ( $N_{\text{emb}}$ ),  
 375 as shown in Eq. 12

$$376 \quad \varepsilon_{\text{TPC}} = \frac{N_{\text{rec}} (\text{nHitsFit} \geq 20 \& \text{dca} \leq 1 \& |\eta| \leq 1 \& \text{nCommonHits} > 10)}{N_{\text{emb}} (|\eta| \leq 1)} \quad (12)$$

377 The TPC tracking efficiency in Run14 Au+Au collisions at 200 GeV is shown below. Fig 35  
 378 shows the TPC tracking efficiency for pion plus from four different classifications, from up to down,  
 379 the centrality is from the most peripheral to most central collision. As we see, in the most central  
 380 top 0-5% collisions, due to the large occupancy the TPC tracking efficiency is much lower than the  
 381 central one. Fig. 36 shows the same plot for kaon minus. The Kaon can be decay inside TPC,  
 382 that’s the reason the TPC tracking efficiency is lower than pion.



Figure 35: TPC tracking efficiency in Run14 Au+Au collisions at 200 GeV for Pion.

Figure 36: TPC tracking efficiency in Run14 Au+Au collisions at 200 GeV for Kaon.

### 383 4.3 TOF Matching Efficiency

384 For the  $D^0$  analysis, we use the hybrid PID for TOF. Which means when TOF is available we use  
 385 TOF and TPC, when it's not available we just use TPC. The TOF matching efficiency ( $\varepsilon_{TOF}$ ),  
 386 including the TOF response and the acceptance difference between the TPC and TOF, is evaluated  
 387 by the real data. It can be calculated by comparing the number of qualified tracks matched with  
 388 the TOF (with  $\beta > 0$ ,  $N_{matched}$ ) over the number of qualified tracks ( $N_{TPC}$ ).

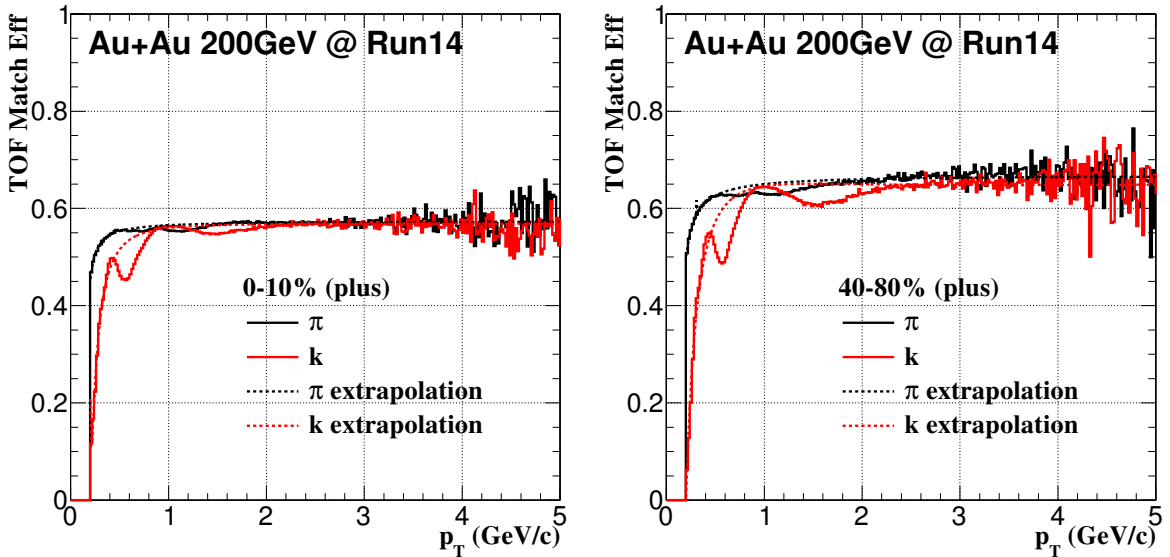


Figure 37: TOF match efficiency in Run14 Au+Au collisions at 200 GeV for positive charge particle in 0-10%.

Figure 38: TOF match efficiency in Run14 Au+Au collisions at 200 GeV for positive charge particle in 40-80%.

389 Fig. 37 shows the TOF match efficiency in Run14 Au+Au collisions at 200 GeV for positive  
 390 charge particles such as  $\pi^+, K^+$  in the centrality 0-10%. Fig. 38 shows the same plots for positive  
 391 charge particles in the centrality from 40-80%.

392 For more plots in different centrality and different charged, they can be find in the link:

393      <https://drupal.star.bnl.gov/STAR/blog/xgn1992/tof-match-efficiency-vs-centrality>

394      For the pion TOF match efficiency, the trend is much smooth compare to kaon. As we see,  
 395      there are some deep for the TOF match efficiency at some certain  $p_T$  range from kaon, such as  
 396      kaon in the  $p_T$  around  $0.6 \text{ GeV}/c$ . This effect was studied using Hijing simulation, it's found that  
 397      this is due to the hadron contaminations.

398      Fig. 39 right hand plot shows the  $n\sigma_K$  distributions from Hijing in the  $p_T$  range from  $0.5 -$   
 399       $0.7 \text{ GeV}/c$ . The solid lines are for particles from TPC , and the dashed lines are for particles also  
 400      include TOF match information. The total yield was scaled to have the same number of pions for  
 401      this comparison, since the TOF matching have  $\sim 30\text{-}40\%$  efficiency lost. In a simple case, if we  
 402      select kaons with the cut  $|n\sigma_K| < 1$ , after the requiring of TOF match, the width of this  $n\sigma_K/\pi$   
 403      distribution changed, and the contaminations from pions are reduced. As what we see the dashed  
 404      black line have less contributions to the kaons peak within  $|n\sigma_K| < 1$  compare to the solid black  
 405      line. We also checked this effect in the other  $p_T$  range such as  $0.2 - 0.5 \text{ GeV}/c$ ,  $0.7 - 1.0 \text{ GeV}/c$ ,  $1.0$   
 406      -  $1.4 \text{ GeV}/c$ ,  $1.4 - 2.0 \text{ GeV}/c$  and  $2.0 - 3.0 \text{ GeV}/c$  as shown in Fig. 40 and Fig. 41. This effect is  
 407      neglectable in the low  $p_T$  range  $0.2 - 0.5 \text{ GeV}/c$  since the TPC can well separate pions and kaon.  
 408      In the high  $p_T$  range, the dE/dx are overlap with each other for kaon and pion, it's not able to  
 409      distinguish them only use TPC.

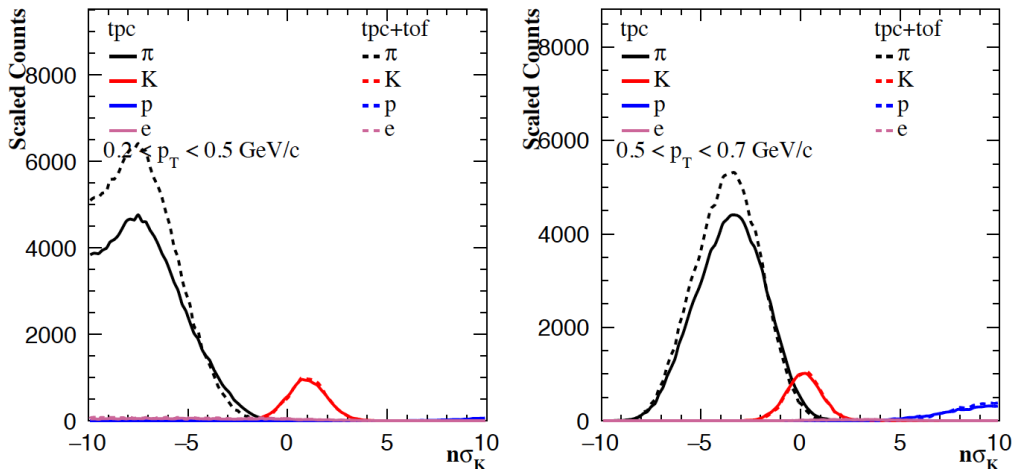


Figure 39:  $n\sigma_K$  distributions for  $0.2 < p_T < 0.5 \text{ GeV}/c$  and  $0.5 < p_T < 0.7 \text{ GeV}/c$ . The solid lines are from TPC and dashed lines are from TPC + TOF.

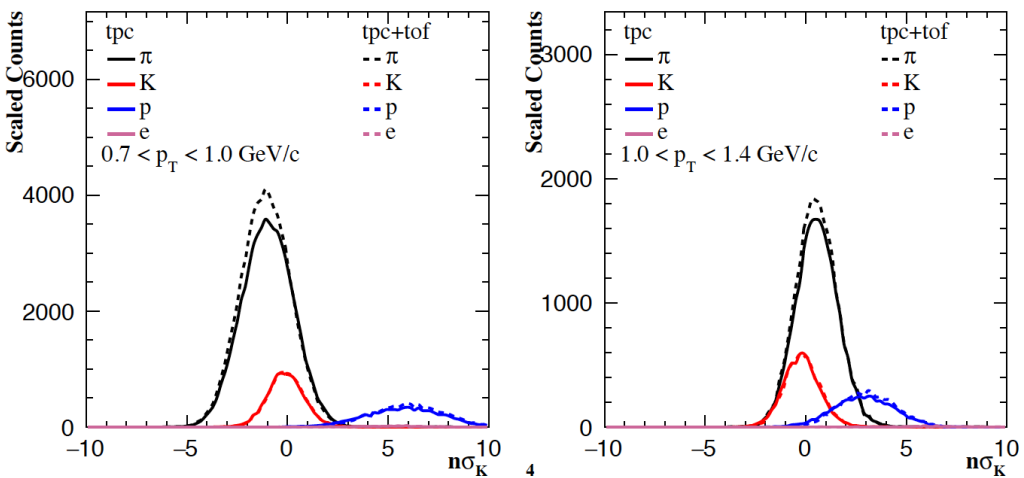


Figure 40:  $n\sigma_K$  distributions for  $0.7 < p_T < 1.0 \text{ GeV}/c$  and  $1.0 < p_T < 1.4 \text{ GeV}/c$ . The solid lines are from TPC and dashed lines are from TPC + TOF.

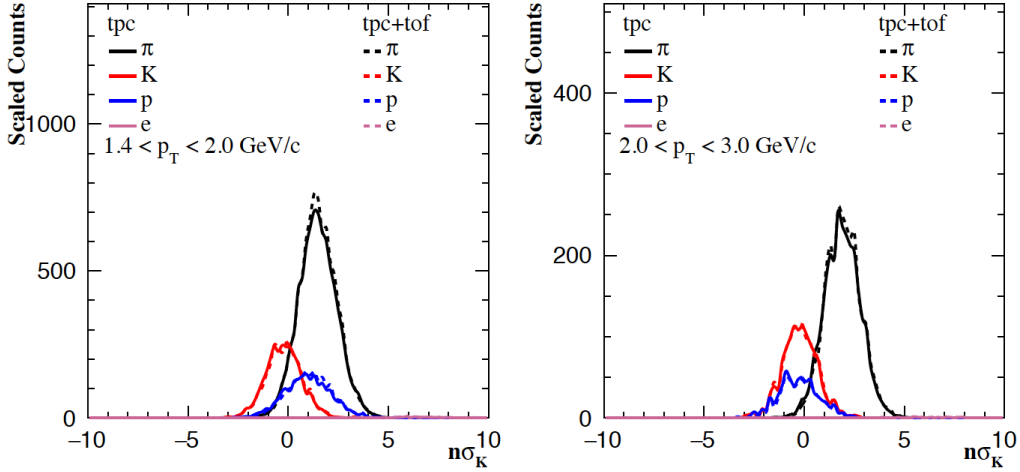


Figure 41:  $n\sigma_K$  distributions for  $1.4 < p_T < 2.0 \text{ GeV}/c$  and  $2.0 < p_T < 3.0 \text{ GeV}/c$ . The solid lines are from TPC and dashed lines are from TPC + TOF.

Fig. 42 summary the TOF match efficiency from this Hijing study for  $\pi^\pm, K^\pm$  and p. They show the similar behavior as we observed in the real data and it's indeed due to the hadron contaminations.

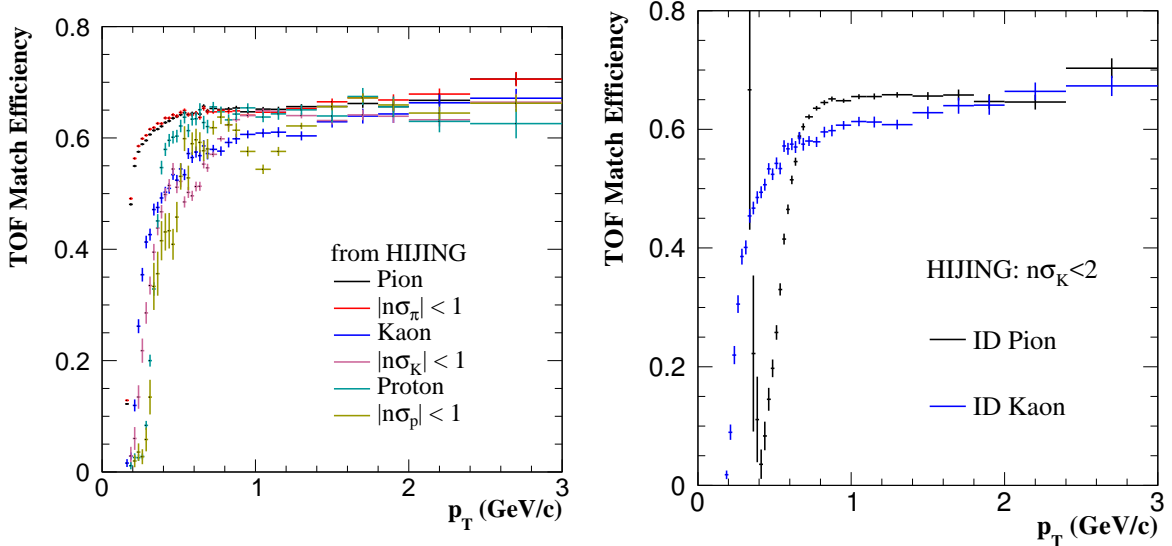


Figure 42: Tof match efficiency from the HIJING study.

#### 413 4.4 PID Cut Efficiency

The particle identification cut efficiency ( $\varepsilon_{PID}$ ) includes two components: the TOF velocity ( $1/\beta$ ) cut efficiency and  $dE/dx$  cut ( $n\sigma_{K/\pi}$ ) efficiency. Pure pions and kaons sample are used to evaluate the TOF velocity cut efficiency and TPC  $n\sigma_{K/\pi}$  cut efficiency. Fig. 43 shows the  $\pi\pi$  pairs invariant mass distributions. The black line is the unlikesign foreground, and the red line is background using likesign method. With this  $K_s^0$  candidates, we can statistical extract the pure pion sample for the PID efficiency study. Fig. 44 shows the  $KK$  pairs invariant mass distributions. Still with the unlikesign and likesign method, the  $\Phi$  meson candidates are reconstructed, and we can statistical extract the pure kaon sample for the PID efficiency study.

Some details from previous study can be found below.

[https://drupal.star.bnl.gov/STAR/system/files/Pid\\_eff\\_new.pdf](https://drupal.star.bnl.gov/STAR/system/files/Pid_eff_new.pdf)

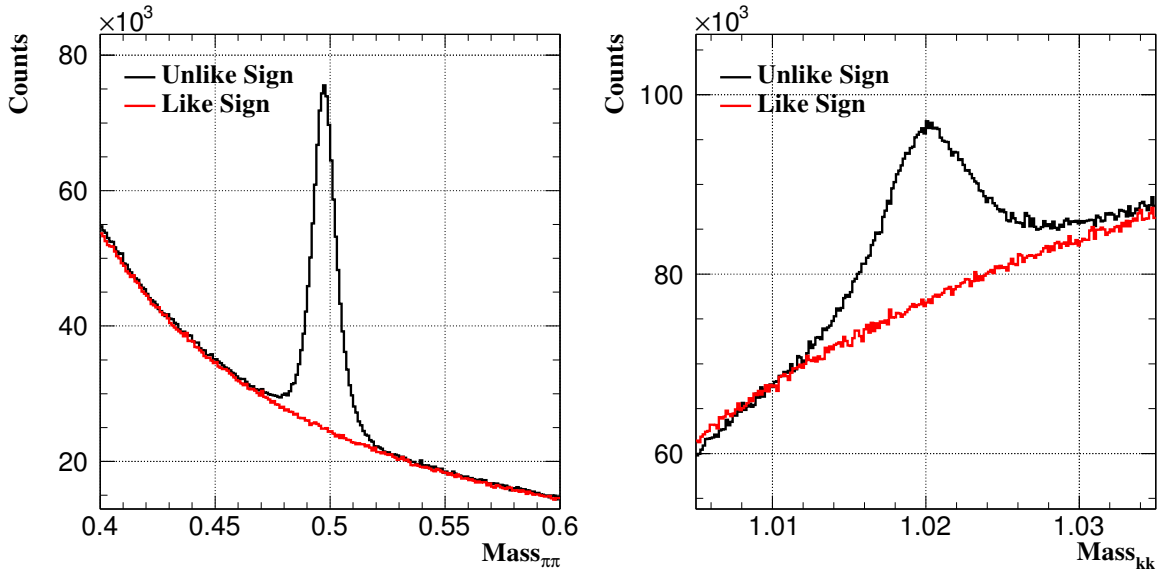


Figure 43: The  $\pi\pi$  pairs invariant mass distributions. The black line is the unlikesign foreground, and the red line is background using like-sign method.

Figure 44: The  $KK$  pairs invariant mass distributions. The black line is the unlikesign foreground, and the red line is background using like-sign method.

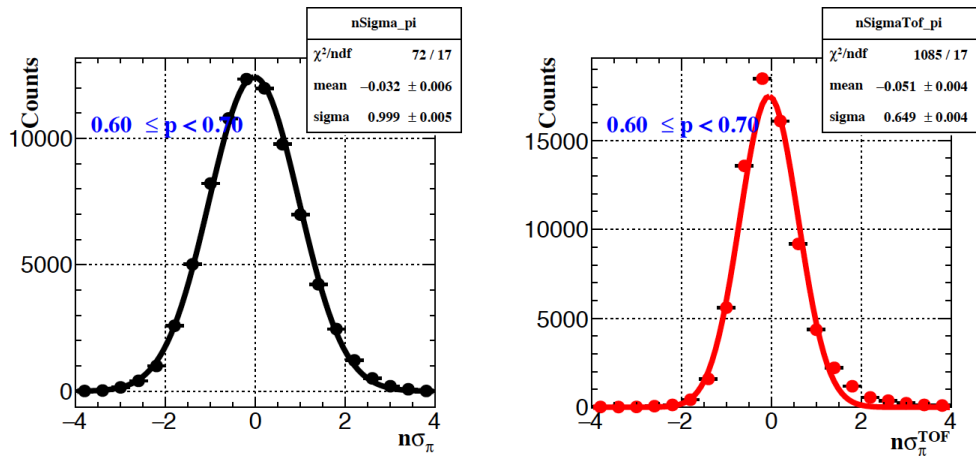


Figure 45:  $n\sigma_\pi$  and  $n\sigma_\pi^{TOF}$  distributions for  $p_T$  around 0.6-0.7 GeV/ $c$ .

424 **4.4.1  $n\sigma_{K/\pi}$  Cut Efficiency**

425 The  $n\sigma_{K/\pi}$  cut efficiency is derived from the Gaussian fit using those pure samples. The  $n\sigma_{K/\pi}$   
 426 distributions are fitted with Gaussian function, the mean value and sigma value are plotted as  
 427 Fig. 46 and Fig. 47. With these mean and sigma distributions, assuming they follow the Gaussian  
 428 function, for example, Fig. 54 depicts the  $n\sigma_\pi$  cut efficiency in Run14 Au + Au collisions at 200  
 429 GeV for pions. For kaons, we use the same method extracting this  $n\sigma_K$  cut efficiency. Above 4  
 430 GeV, we use the fitting result to extrapolate the efficiency since we do not expect a big difference  
 431 vs pt.

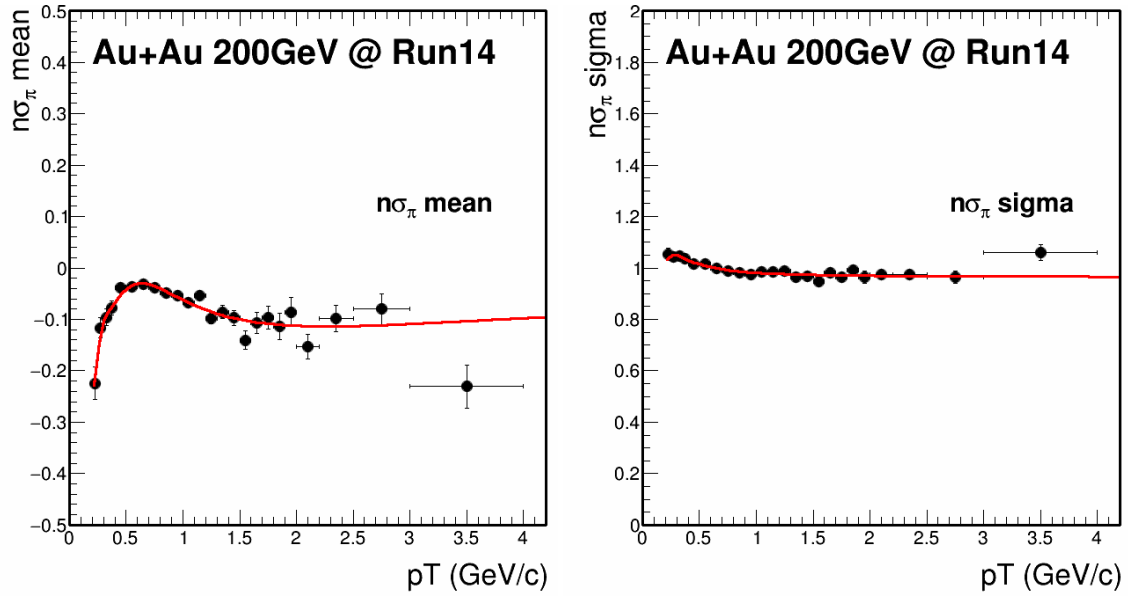


Figure 46: The mean value of  $n\sigma_\pi$  distributions vs momentum. The red line is fitted function with polynomial function.

Figure 47: The sigma value of  $n\sigma_\pi$  distributions vs momentum. The red line is fitted function with polynomial function.

432 **4.4.2  $1/\beta$  Cut Efficiency**

433 The  $1/\beta$  cut efficiency is derived from the  $1/\beta$  distributions, two methods are used, one is the  
 434 bin counting method and another is using Gaussian fitting and calculate the efficiency from the  
 435 fitting parameters. The default value is from bin counting and the difference between these two  
 436 methods are quoted as systematic uncertainties as shown on Fig. 56 and Fig. 57 as fitting method.  
 437 The fluctuations for kaons samples were due to the hadron contaminations at some  $p_T$  range. To  
 438 avoid this, we use the function to fit the data and using fitting result. Fig. 52 and Fig. 53 show an  
 439 example of the  $n\sigma_K^{TOF}$ . Here even though we use  $\phi$  to select the Kaon samples, but limited with  
 440 the S/B ratio in the  $\phi$  mass region, we still suffer this tiny effect. We also try using directly using  
 441  $n\sigma_K$  with a much narrow range say less than 0.1, but as they are physical contaminations limited  
 442 with the TPC capacity, it's shows similar structure. Above 4 GeV we use the line fitting result to  
 443 extrapolate the efficiency similar as nSigma.

444 **4.5 Data-driven fast Monte Carlo setup for HFT and Topological Cut  
 445 Efficiency**

446 As discussed in the beginning of this section, the HFT related efficiency shown on Eq. 7 including  
 447 two items: HFT acceptance and topological cuts. Since the HFT embedding is not ready yet at  
 448 that time, we developed the ‘Data-Driven Fast simulation’ for the HFT related efficiency correction.  
 449 And this method was validated with full GEANT simulation and will be discuss later.

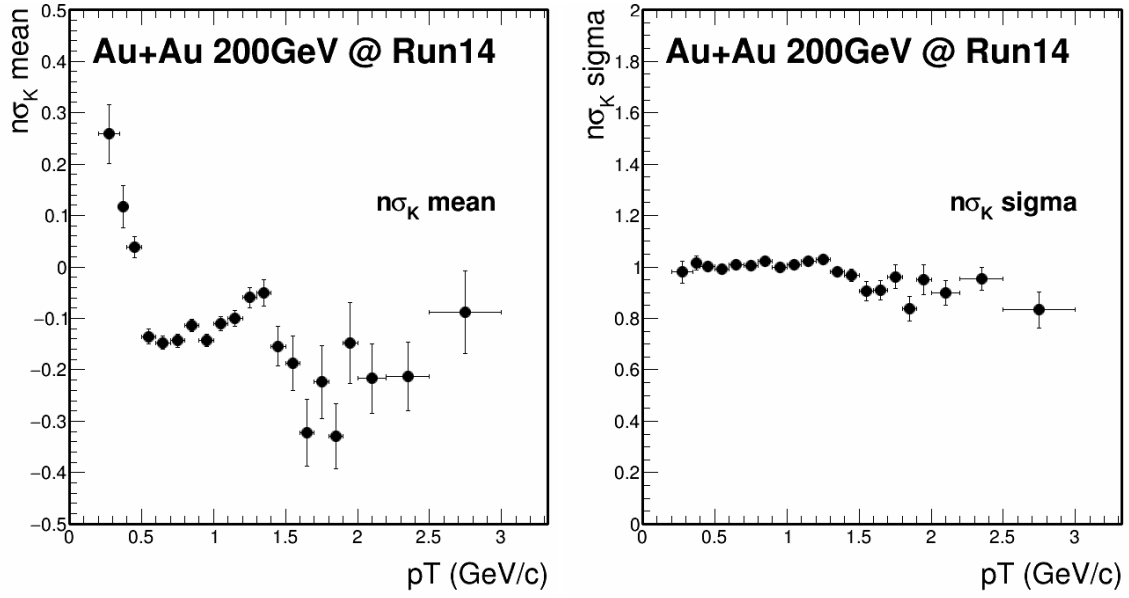


Figure 48: The mean value of  $n\sigma_K$  distributions vs momentum. The red line is fitted function with polynomial function.

Figure 49: The sigma value of  $n\sigma_K$  distributions vs momentum. The red line is fitted function with polynomial function.

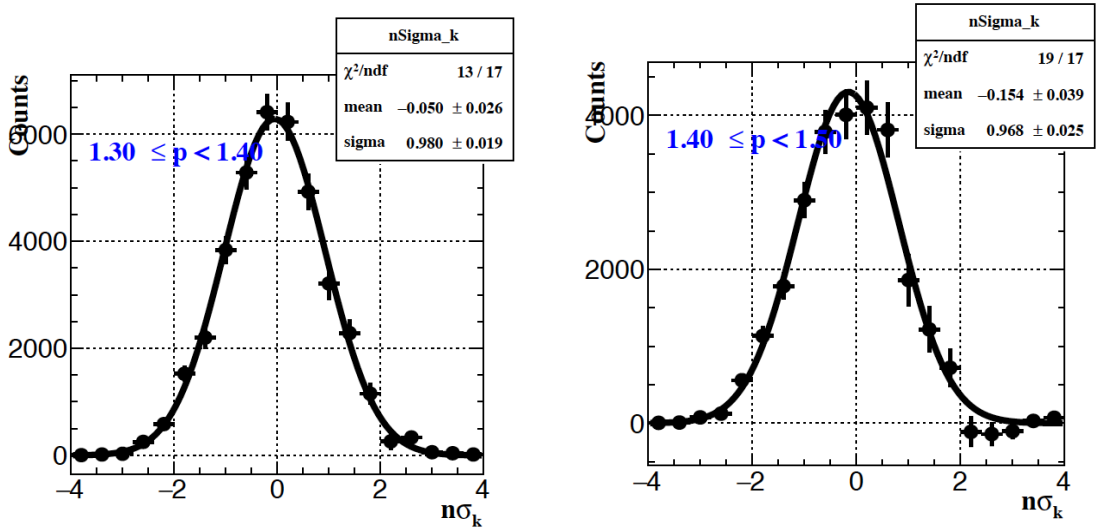


Figure 50: The  $n\sigma_K$  distributions for kaon for pt around 1.35GeV.

Figure 51: The  $n\sigma_K$  distributions for kaon for pt around 1.45GeV.

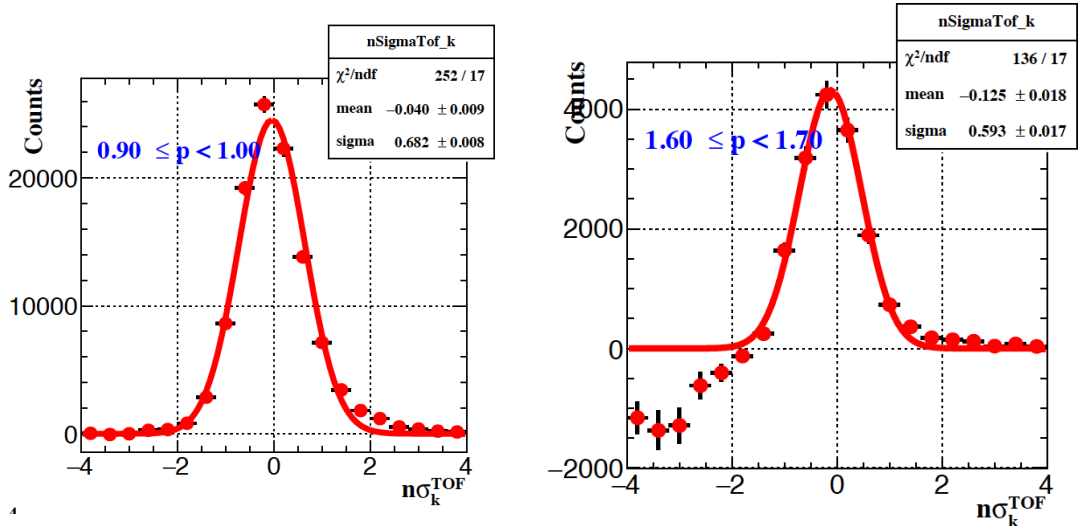


Figure 52: The  $1/\beta$  distributions for kaon for  $p_T$  around 0.9GeV.

Figure 53: The  $1/\beta$  distributions for kaon for  $p_T$  around 1.6GeV.

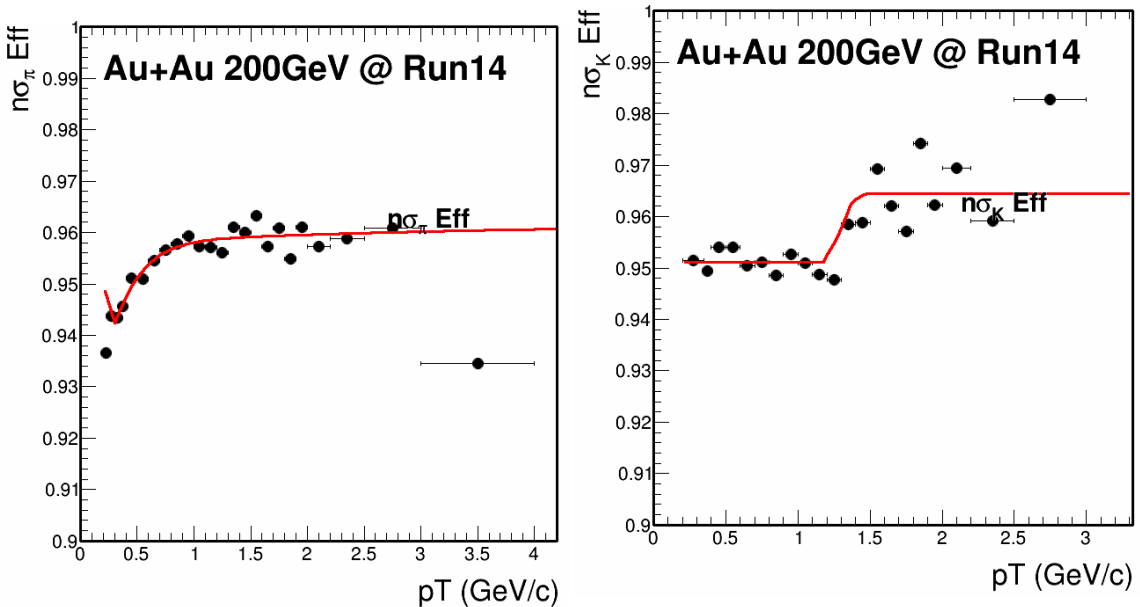


Figure 54:  $n\sigma_\pi$  cut efficiency along with momentum. Red line is the fitted polynomial function.

Figure 55: The sigma value of  $n\sigma_K$  distributions vs momentum. The red line is fitted function with step linear function.

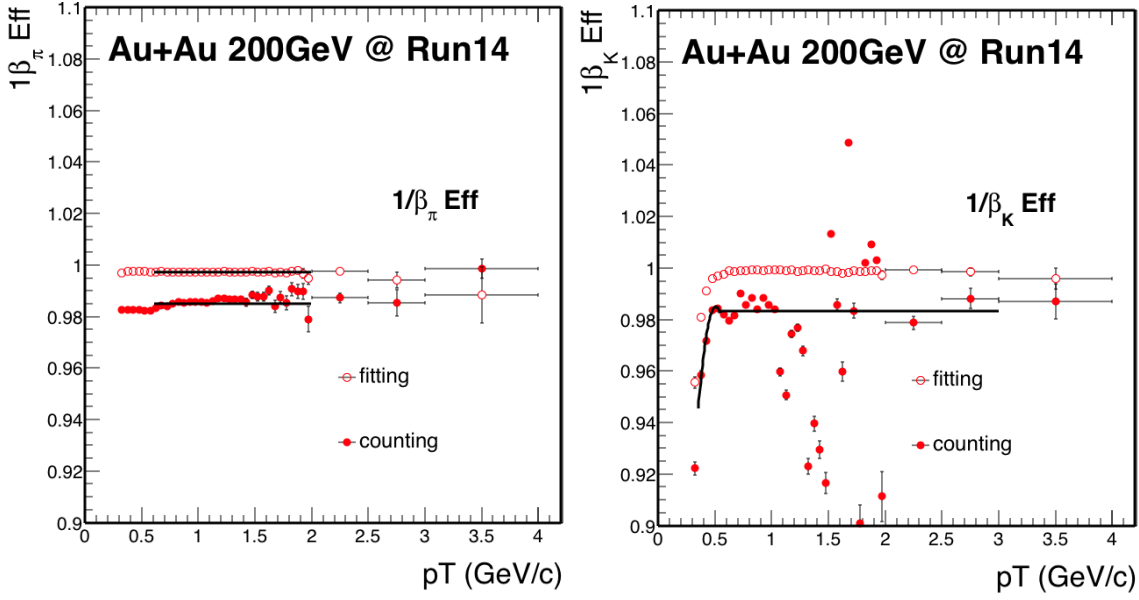


Figure 56:  $1/\beta$  cut efficiency along with momentum for pion. Red line is the fitted function.

Figure 57:  $1/\beta$  cut efficiency along with momentum for kaon. Red line is the fitted function.

#### 450 4.5.1 Assumptions

451 Before we discuss the details procedure of the method, it's better to make it clear, this data-driven  
 452 simulation is based on several assumptions. And the validating will be tested step by step in the  
 453 later section.

- 454 • Factorization of tracking efficiency:

$$455 \frac{HFT}{MC} = \frac{HFT}{TPC} \times \frac{TPC}{MC} \quad (13)$$

- 456 • Spatial resolution of HFT is encoded in two variables:  $DCA_{XY}$  and  $DCA_Z$  (two dimensions  
 457 correlated).
- 458 • Vertex resolution, which is possibly folded in the DCA resolution of single tracks and corre-  
 459 lated for kaons and pions, is a negligible, at least for semi-central to central events.
- 460 • The contribution of feed-down particles from secondary decays to DCA distributions is neg-  
 461 ligible.
- 462 • Mis-matched daughter tracks are removed by topological cuts.

#### 463 4.5.2 Ingredients

464 There are several input ingredients for this fast-simulation package which is extracted from data.

- 465 • Extract  $V_z$  distributions from data (centrality dependent).
- 466 • Extract ratio of HFT matched tracks to TPC tracks from data (This ratio includes all  
 467 mismatched tracks) (particle species, centrality,  $p_T$ ,  $\eta$ ,  $\phi$ ,  $V_z$  dependence).
- 468 • Extract  $DCA_{XY}$  -  $DCA_Z$  distributions from data. Assuming that data DCA distributions is  
 469 dominated by primary particles (particle species, centrality,  $p_T$ ,  $\eta$ ,  $V_z$  dependence).
- 470 • Extract TPC efficiency and momentum resolution from embedding (particles, centrality and  
 471  $p_T$  dependence).

472 Fig. 58 shows an example of the input HFT match ratio in the certain  $\eta$ ,  $V_z$ ,  $\phi$  and centrality  
 473 range. The HFT match ratio increase in the low  $p_T$  range due to the high mismatch occupancy  
 474 and keep flat in the high  $p_T$  range. This ratio have a strong dependence on these differential such

475 as  $\eta$  and  $V_Z$  since this is effected by HFT acceptance. Fig. 59 shows an example of the  $D_{\text{caxy}}$   
476 vs  $D_{\text{caz}}$  distribution in the certain  $p_T$ ,  $\eta$ ,  $V_Z$  and centrality range. The axis binning is dynamic  
477 binning (non-uniform) since the most central (around 0) part is the dominate part. Limited by the  
478 computing memory, the most central part use fine binning and others use the unrefined binning as  
479 shown on the plots.

480 In total, there are  $11 (\phi) \times 10 (\eta) \times 6 (V_z) \times 9 (\text{centrality}) \times 2 (\text{particles})$  1D histograms (36  
481  $p_T$  binning) for HFT match efficiency. There are  $5 (\eta) \times 4 (V_z) \times 9 (\text{centrality}) \times 2 (\text{particles})$   
482 histograms  $\times 19 (p_T)$  2D histograms ( $144 \times 144$   $D_{\text{ca}}$  binning) for  $D_{\text{ca}}$  resolution smearing.

483 Effectively, these 1D and 2D histograms encode HFT efficiency, acceptance and spatial resolu-  
484 tion performance in Run14 data.

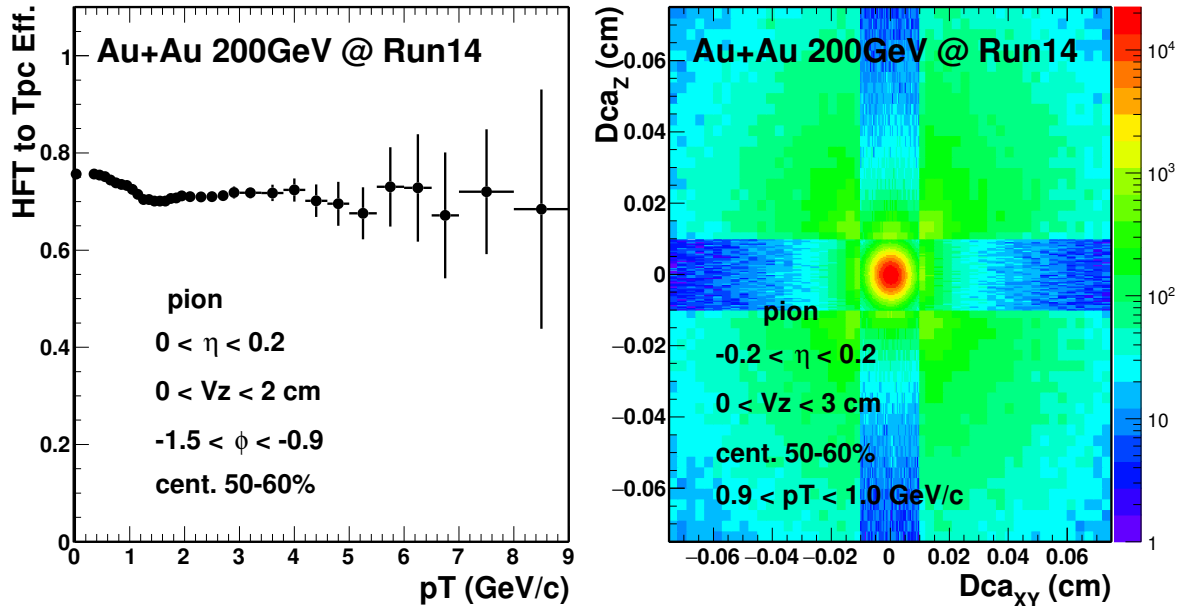


Figure 58: HFT to TPC track match ratio for pion at certain  $\eta, V_Z, \phi, \text{centrality}$  range.

Figure 59:  $D_{\text{caxy}}$  vs.  $D_{\text{caz}}$  for pion at certain  $\eta, V_Z, \text{centrality}$  range.

#### 485 4.5.3 Recipe

486 After all the input ingredients ready for the fast-simulation, a simple toy MC simulation (PYTHIA/EvtGen)  
487 is applied for the efficiency study. The basic recipe is following:

- 488 • Sample  $V_Z$  distribution according to data distribution.
- 489 • Generate  $D^0$  flat in  $p_T$  and rapidity and decay it.
- 490 • Smear momentum according the embedding.
- 491 • Smear  $DCA_{XY}$  and  $DCA_Z$  of Kaons and Pions independently according to distributions from  
492 data.
- 493 • Apply HFT matching efficiency from HFT ratio.
- 494 • Apply TPC reconstruction efficiency.
- 495 • Reconstruct  $D^0$

#### 496 4.5.4 $D^0$ Efficiency and Topological Distribution

497 As discussed in the recipe, we obtain the efficiency step by step as shown from Fig. 60 to Fig. 62.  
498 First we have the TPC efficiency shown in Fig. 60 which is after the  $p_T$ ,  $\eta$  acceptance cut and  
499 TPC tracking efficiency from embedding. Then another contribution is from the pid part shown in  
500 Fig. 61. Also the HFT matching efficiency together with the topological cut efficiency was shown

in Fig. 62. As seen in the low  $p_T$  part, the topological cut efficiency is really small due to the tight cut as the combinatorial background is huge. And the final efficiency combined with all the sources are shown in Fig. 63.

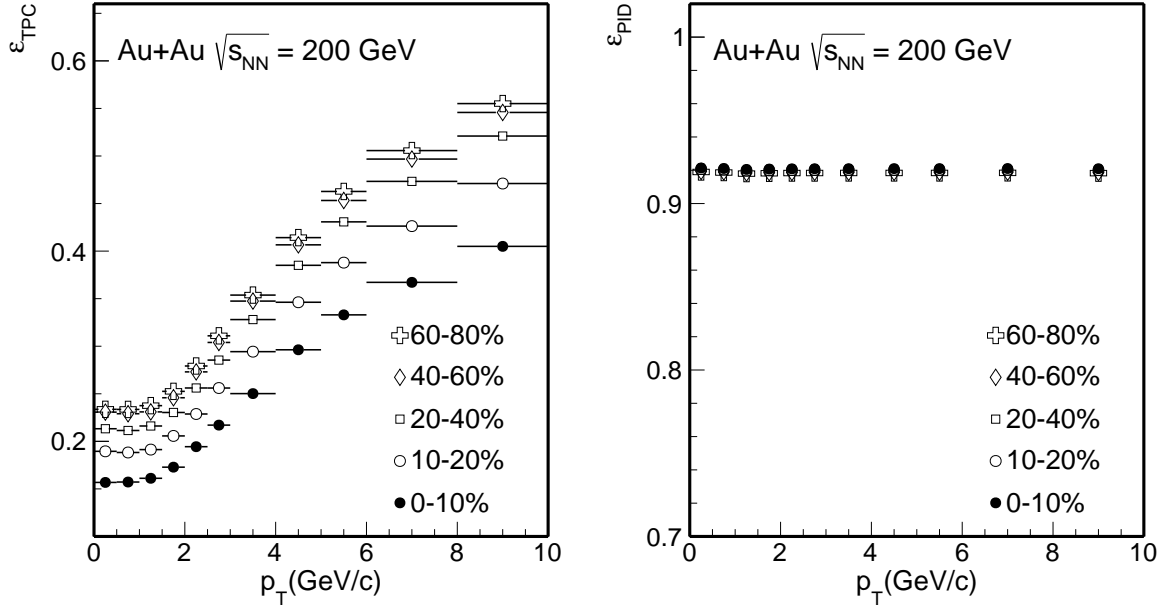


Figure 60:  $D^0$  efficiency step by step from TPC in Figure 61:  $D^0$  efficiency including PID in several different centralities.

We study all the efficiencies with small centrality bin width, in total we have 9 centrality bins from our StRefmultCorr class. Since the  $D^0$  production is scaled by the number of binary collisions ( $N_{bin}$ ), the  $D^0$  is favor produced in more central collisions. So the final efficiencies for the wider centrality bins 0-10%, 10-40%, 40-80% and 0-80% are calculated using  $N_{bin}$  as weights, for example, the efficiency in 0-80% is calculated as the following Eq. 14. Fig 63 shows the  $D^0$  efficiency for 4 wide centralities after TPC, HFT match and Topological efficiency included.

$$\text{Efficiency}_{0-80\%} = \sum_{i=1}^9 (\text{Efficiency}_i \times N_{bin}^i) / \langle N_{bin} \rangle \quad (14)$$

The Data-Driven Fast-Simulation also provide the topological information, can be used for the comparison with real data. For the real data part, within the  $D^0$  mass window we can statistical subtract the background and extract the pure  $D^0$  topological distributions. The invariant mass plots shown as Fig. 64.  $D^0$  is in the  $2 < p_T < 3$  GeV/c, 0-10% centrality. Black is unlikesign foreground, blue is likesign background and red is mixed event background. The blue vertical lines are the mass window used for the topological comparison. For each topological variable, that corresponding topological cut was removed when reconstruct the  $D^0$  candidate, so that we can compare that variable in a wide range.

From Fig. 65 to Fig. 70, these are the topological variables ( $\cos(\theta)$ , decayLength, dcaDaughters, D0DcaToVtx, PionDca and KaonDca) used for the  $D^0$  reconstruction. The distributions from the real data part are using same-event like-sign method to statistical subtract the background. The Data-Driven Fast-Simulation part was the package we relayed on for our efficiency study as shown before.

Comparison these topological variables between real data and Fast-Simulation, the agreement is reasonable good, which means our Data-Driven Fast-Simulation method can well reproduce the topological variables in real data. In another word, the efficiency estimation from Data-Driven Fast-Simulation is reliable. Note here, there are some small discrepancy such as single track Dca distributions in the low end, that's because in the data analysis part, we already require some minimum cut in order to save the computing resource. There is another method we are going to discuss in the following section, also can be used to validating our Fast-Simulation method.

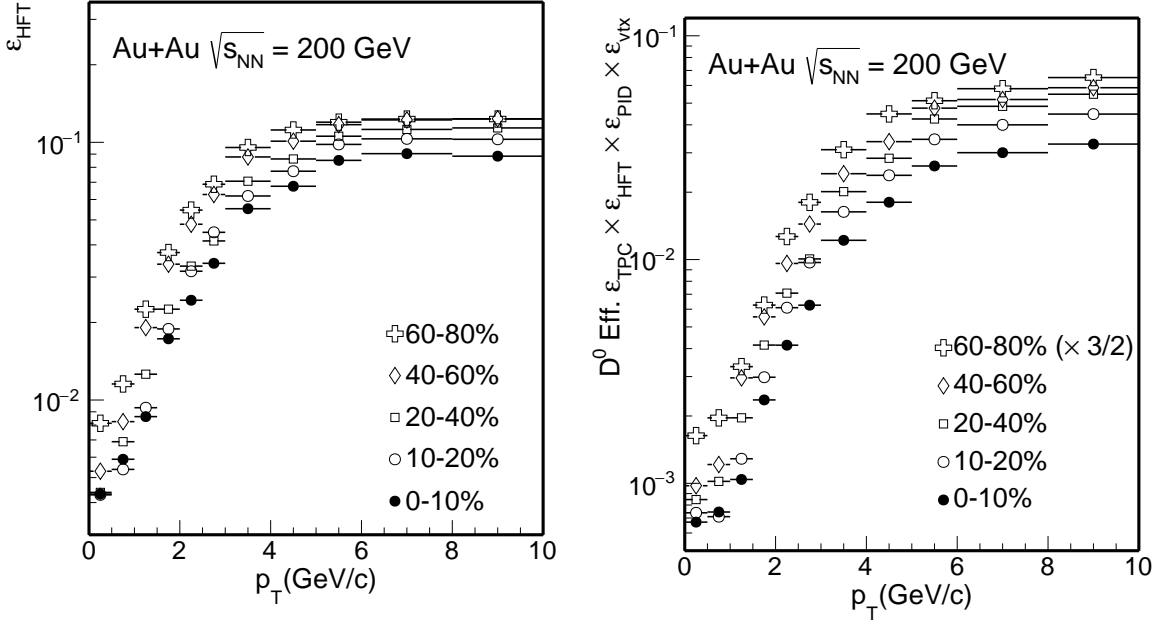


Figure 62:  $D^0$  efficiency step by step from HFT acceptance tracking and topological cuts in different centralities.

Figure 63:  $D^0$  efficiency including PID in several centralities.

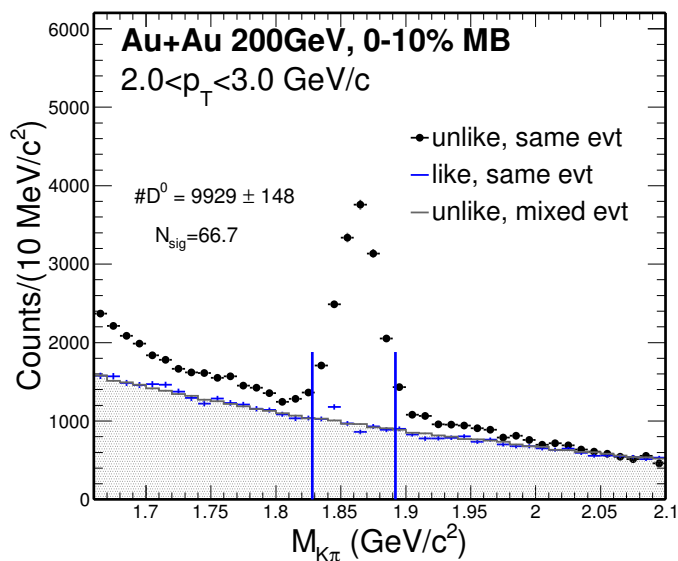


Figure 64:  $D^0$  invariant mass distributions in the  $2 < p_T < 3$   $\text{GeV}/c$ , 0-10% centrality. Black is unlikesign foreground, blue is likesign background and red is mixed event background. The blue vertical lines are the mass window used for the topological comparison.

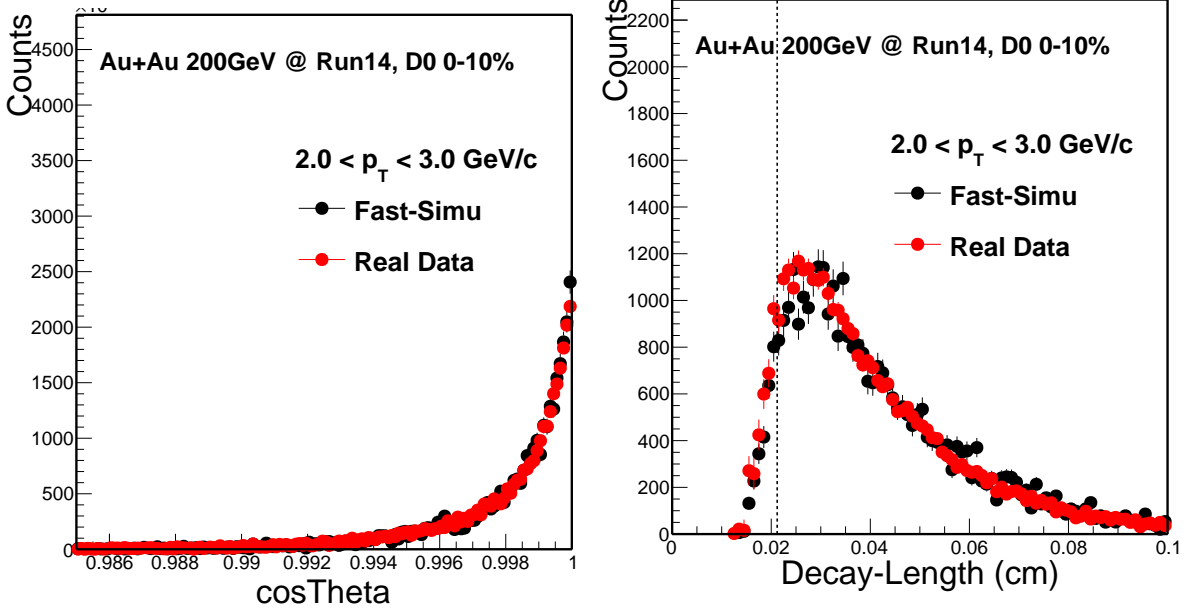


Figure 65:  $D^0$  cosTheta distribution in most central 0-10% between Fast-Simulation and Real Data.

Figure 66:  $D^0$  decay length distribution in most central 0-10% between Fast-Simulation and Real Data.

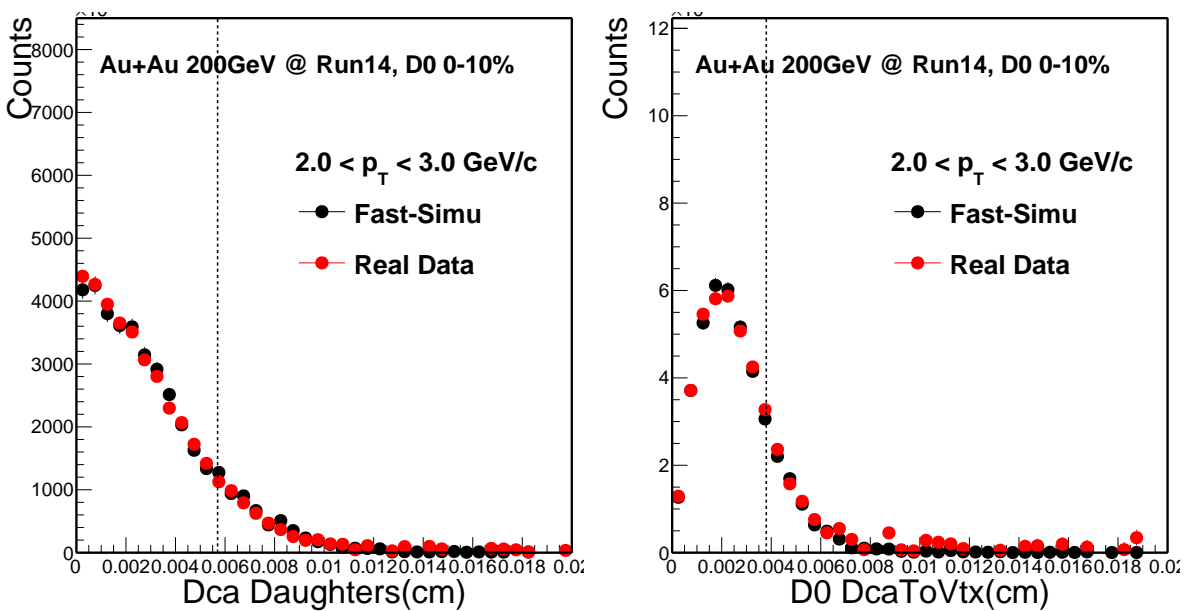


Figure 67:  $D^0$   $dca_{Daughters}$  distribution in most central 0-10% between Fast-Simulation and Real Data.

Figure 68:  $D^0$   $dca$  to Vertex distribution in most central 0-10% between Fast-Simulation and Real Data.

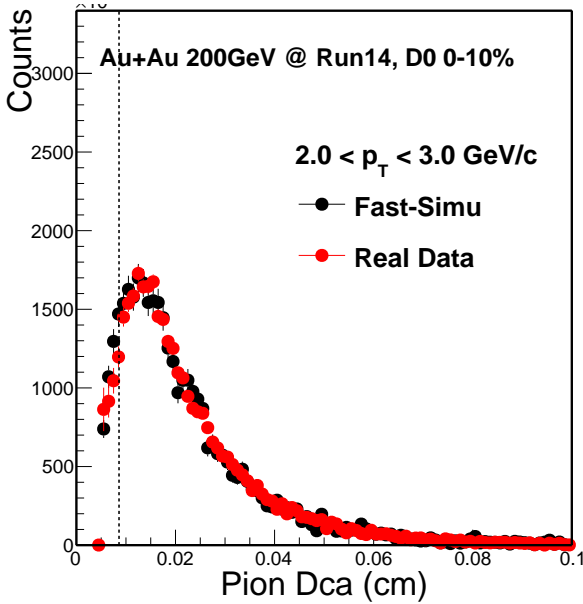


Figure 69:  $D^0$  pionDca distribution in most central 0-10% between Fast-Simulation and Real Data.

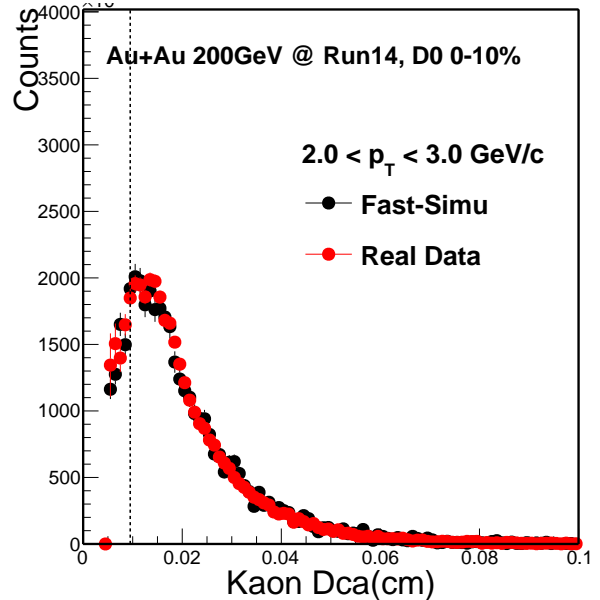


Figure 70:  $D^0$  kaonDca distribution in most central 0-10% between Fast-Simulation and Real Data.

#### 531 4.6 Validation with Full GEANT+Hijing Simulation

532 Before discuss the details of this Hijing validation, it's better to conclude those assumptions we  
 533 made before. The first assumption is the factorization shown in Eq. 13. Relaying on the Hijing  
 534 simulation, we have two samples. One is only include TPC tracking, another one include both  
 535 HFT and TPC in tracking. From the first sample, we can extract the TPC factorized tracking  
 536 efficiency, and the second sample can be used to extract the overall total efficiency and HFT over  
 537 TPC factorized efficiency separately. Fig. 71 shows the comparison between the overall efficiency  
 538 and the multiplied factorization efficiency. The red one is from overall efficiency from the second  
 539 sample, and the blue one is multiplied efficiency from two components. The bottom panel shows  
 540 the double ratio of these two efficiency, and they are perfectly factorized as the ratio is flat as unity.

541 The second assumption is for the spatial resolution, it is encoded in those  $Dca_{XY}$  and  $Dca_z$   
 542 variables, and they are correlated in the two dimensions. Fig. 72 shows the comparison between  
 543 the input Dca from real data and output Dca from Fast-Simulation in three dimensions. The first  
 544 row is Dca in XY plane, the second row is in Z plane and the last row is in the 3-D dimension.  
 545 From the left to right is the comparison from low  $p_T$  to high  $p_T$ . As shown the red line is from data  
 546 and black line is from fast simulation, the agreement is pretty good. For the others assumption,  
 547 they will be discussed separately in the following section.

#### 548 4.7 Hijing Samples Performance

549 The Hijing sample was run through the Full Hijing + GEANT simulation with realistic pileup hits  
 550 (UPC+MB) in PXL and sensor masking tables.

551 Pileup hits seen in the PXL detector include hits caused by UPC electrons as well as pileup  
 552 hadronic minimum bias collision tracks. Details about this part of simulation can be found here  
[553 https://drupal.star.bnl.gov/STAR/system/files/pileup\\_2014-1-3.pdf](https://drupal.star.bnl.gov/STAR/system/files/pileup_2014-1-3.pdf)

554 The UPC electrons were estimated using the STARlight generator and embedded into GSTAR  
 555 with 1MeV threshold cut (1.9 MeV cut to reach first layer of PXL due to magnetic field) and the  
 556 minimum bias pileup collisions were simulated using Hijing generator. We took the collision rate  
 557 at 50kHz and the PXL integration time 0.2ms for estimating the total pileup events. The total  
 558 number of hit density for for pileup hits is about  $46 \text{ cm}^{-2}$ . MB signal event hit density is  $\sim 8$   
 559  $\text{cm}^{-2}$ . The sum of these two is comparable to the hit density seen in real AuAu mb triggered data  
 560 (about  $\sim 50 \text{ cm}^{-2}$ ).

561 They can provide reasonable performance for the HFT matching ratio and Dca resolution. In

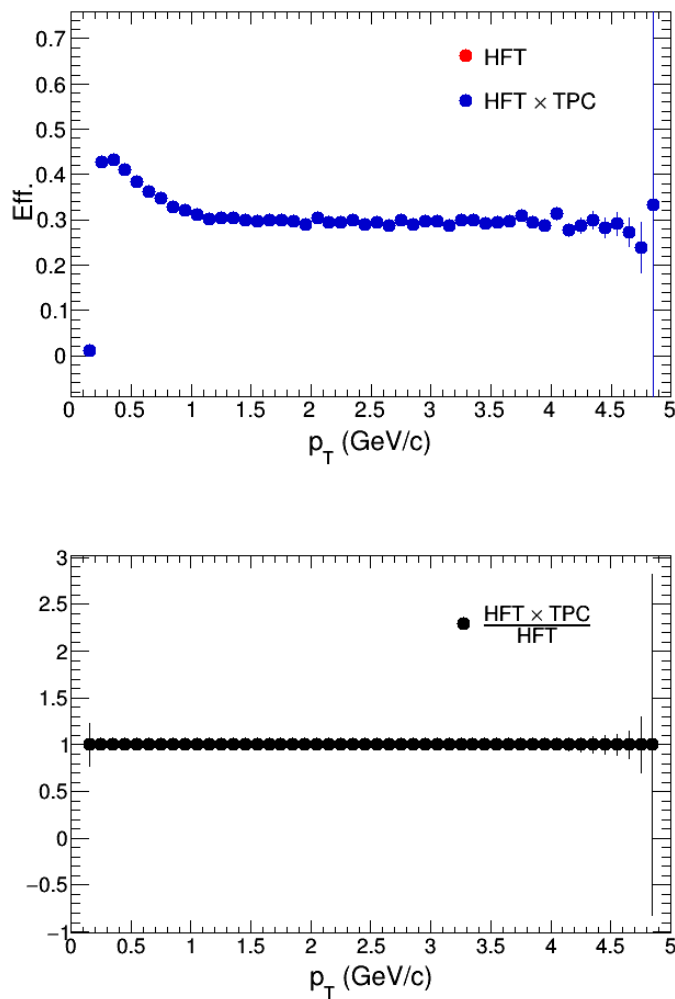


Figure 71: (top) HFT Efficiency Factorization comparison. (bottom) Double Ratio of these factorization.

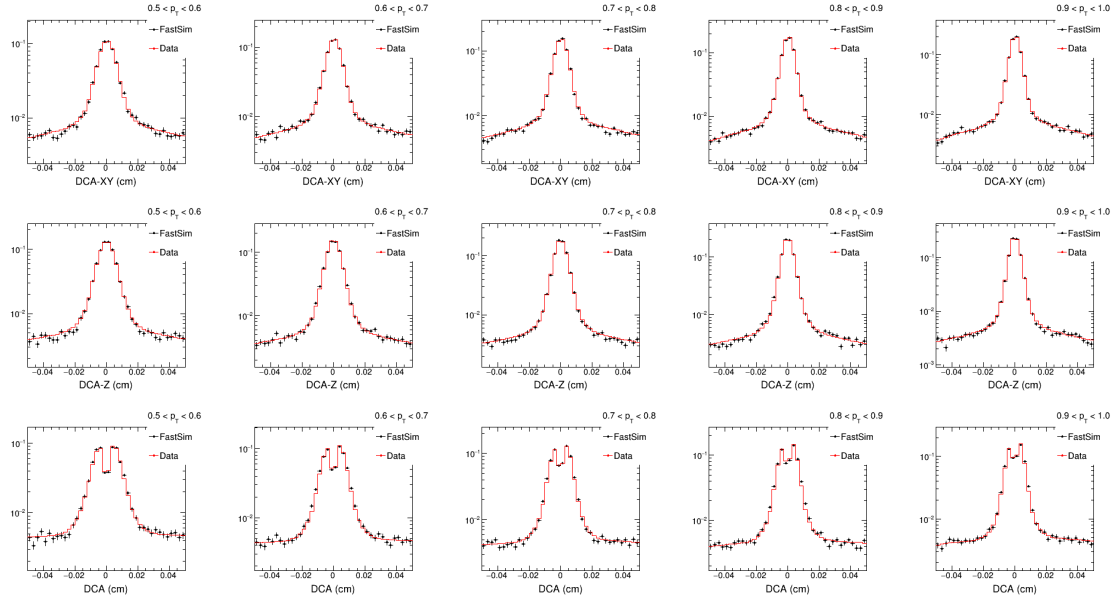


Figure 72: Comparison of Dca between data (red) and Fast-Simulation (black). From top to bottom, the comparison is for Dcaxy, Dcaz and Dca. From left to right the transverse momentum is from low  $p_T$  to high  $p_T$ .

total we have  $\sim 45K$  0-10% centrality Hijing events, and for each event is embedded with 20  $D^0$ 's. So in total, we have  $\sim 900K$   $D^0$  for this Hijing sample. The embedded  $D^0$  has small effect on the tracking since the multiplicity is much higher compared to  $20 \times 2$   $D^0$ , decayed daughters.

As shown in Fig. 73 is the HFT matching ratio comparison between data (red) and Hijing samples (black) in Au+Au 200 GeV/c from 0-10% centrality, the bottom panel is the double ratio of these two HFT matching ratio. The value is around unity, which means the Hijing simulation can well reproduce these matching performance.

Fig. 74 shows the pions Dcaxy comparison between data (red) and Hijing samples (black) in Au+Au 200 GeV/c from 0-10% centrality at  $1.0 < p_T < 1.2$  GeV/c, the bottom panel is the double ratio of these two Dca distributions. The value is also around unity, which means the Hijing simulation well describes the real data.

## 4.8 Validation Procedures

The idea is simple for this Hijing validation, we have the enriched  $D^0$  Hijing sample. (Here To estimate the vertex resolution effect, we embedded a PYTHIA  $c\bar{c}$  event into a Hijing Au+Au event. The PYTHIA  $c\bar{c}$  events are pre-selected to have at least one  $D^0 \rightarrow K^-\pi^+$  decay or its charge conjugate to enhance the statistics.) After run through the detector and full GEANT simulation, the  $D^0$  efficiency and topological variables distributions can be extracted. Another procedure is extract the necessary ingredients from Hijing sample for the Fast-Simulation input (Fast-Simulation with Hijing input), such as the TPC Tracking efficiency, the HFT matching ratio and the 2D Dcaxy-Dcaz distributions similar as we used in real data analysis and discussed in the previous section. Then run through the Fast Simulation, as discussed before, the  $D^0$  efficiency and topological variables are also available in this way and can be compared to the first Hijing + GEANT procedure. The workflow is shown in Fig. 75.

### 4.8.1 Validation Efficiency

The first step is to check the kinematic form different MC decayer such as PYTHIA, Hijing, evtGen and PhaseSpace class from ROOT. Need to make sure the decayer used for Fast-Simulation has the same kinematic as the Hijing. After the basic acceptance cut, such as  $D^0 |y| < 1$ , daughter  $p_T > 0.2$  GeV/c and  $|\eta| < 1$  cut.  $D^0$  is the simple phase space decay, all these decayer give the same acceptance efficiency as shown in Fig. 76 left panel, the right panel shows the double ratio to

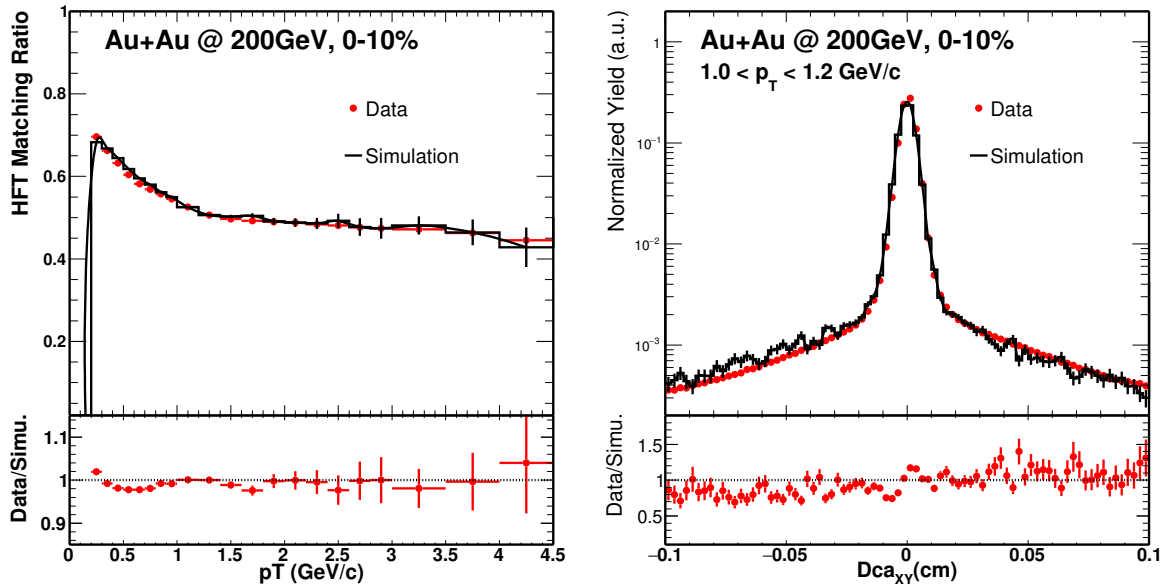


Figure 73: HFT Ratio comparison between data and simulation in Au+Au 200 GeV/c, 0-10%.

Figure 74:  $\pi^\pm$  Dca<sub>XY</sub> comparison between data and Hijing simulation in Au+Au 200 GeV/c, 0-10%.

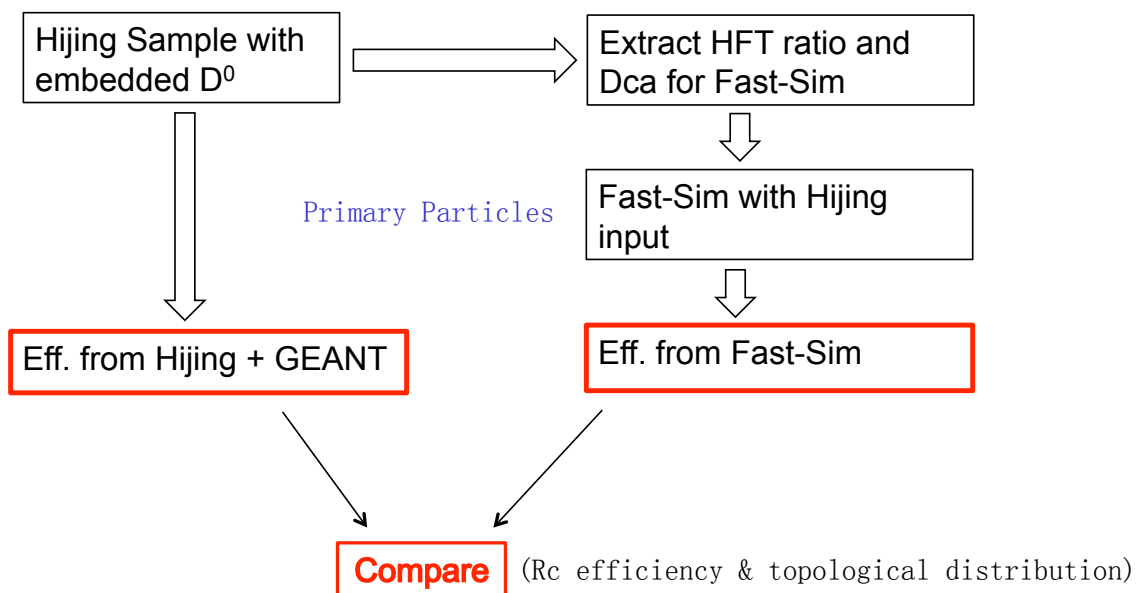


Figure 75: Hijing validation procedure and workflow

591 PYTHIA. As all the decayer follow the same trend they have the same decay kinematic, so, for our  
 592 Fast-Simulation decayer we choose PYTHIA for this validation and also for our real data analysis.

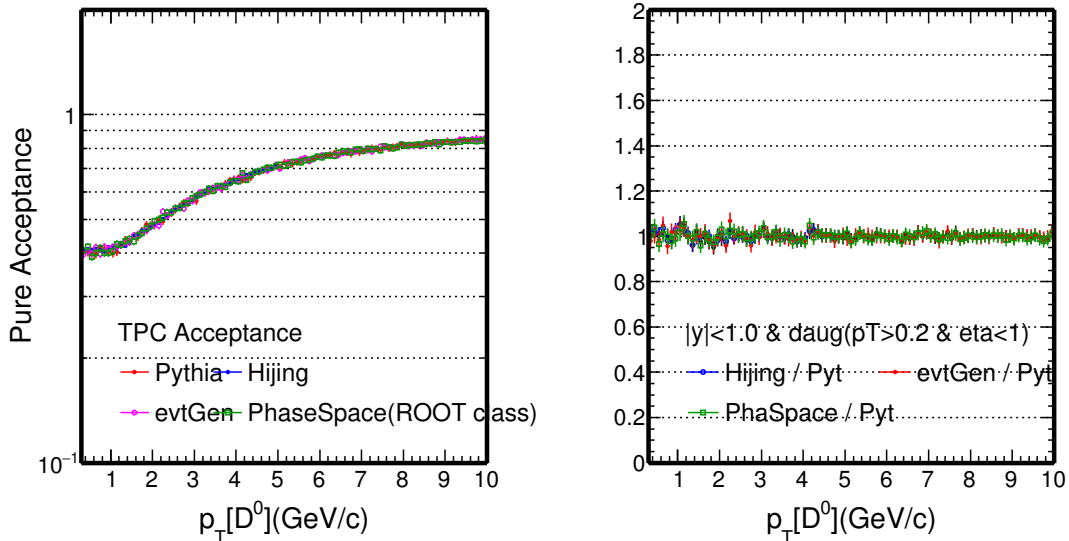


Figure 76:  $D^0$  pure acceptance from different MC decayer, such as PYTHIA, Hijing, evtGen and PhaseSpace class. (right) Double ratio of the acceptance to PYTHIA.

593 The second step is to check the kinematic with the reconstructed TPC tracking information.  
 594 Compare to the first step, this one fold in the momentum resolution and the TPC acceptance effect.  
 595 Fig. 77 left panel shows this efficiency  $\times$  Acceptance comparison between Hijing + GEANT (red)  
 596 and Fast-Simulation with Hijing input (black), the right panel shows the double ratio to Hijing.  
 597 As the red line is the fit function and the fit results around  $\sim 1$  shows very good agreement, which  
 598 means this step is also doing right work.

599 The next step is to trying to fold in the HFT matching efficiency and this is to consider the  
 600 HFT acceptance effect. Fig. 78 left panel shows this efficiency  $\times$  Acceptance comparison after  
 601 TPC and HFT matching between Hijing + GEANT (red) and Fast-Simulation (black), the right  
 602 panel shows the double ratio to Hijing. As the red line is the fit function and the fit results around  
 603  $\sim 1$  shows good agreement, which means this HFT matching step is also correctly implemented  
 604 in the package. For the small discrepancy at the high  $p_T$  range, this is purely due to the limited  
 605 statistics. Since the Hijing sample is time consumption, we do not have enough statistics for the  
 606 HFT match ratio input. But this problem is not exist for our real data analysis since we have  
 607  $\sim 900M$  events which is totally enough and we checked the HFT match ratio, they can extend to a  
 608 reasonable high  $p_T$  range in real data. We did another small check, use one quart of these Hijing  
 609 statistics for this validation, and the discrepancy shown here is bigger than the current results,  
 610 which is another approve of the limited Hijing statistics.

611 The last step is folding in the topological cuts and then compare between the Hijing and Fast-  
 612 Simulation. Fig. 79 left panel shows this efficiency  $\times$  Acceptance comparison after TPC, HFT  
 613 matching and topological cuts between Hijing + GEANT (red) and Fast-Simulation (black), the  
 614 right panel shows the double ratio to Hijing. Still the red line is the fit function and the fit results  
 615 around  $\sim 0.93$  shows good agreement, which means this topological variables are well described in  
 616 the package. For the left panel, there are some twist for this efficiency  $\times$  acceptance at  $p_T \sim 1$   
 617 GeV/c and 2 GeV/c, this is due to the topological cuts are different in separate  $p_T$  ranges. As the  
 618 red points show the efficiency from Hijing + GEANT, the statistics error is larger compared to the  
 619 Fast-Simulation which shows by black. This is also the reason we use data-driven Fast-Simulation  
 620 for our efficiency study, it can be easily enlarge the statistics by a factor of 100 or even 1000 compare  
 621 to the traditional Full GEANT simulation especially for this kind of low efficiency studies. Fig. 79  
 622 shows the same plots of the comparison as Fig. 79 with different binning, we merged some binning  
 623 for statistics concern. After merged the binning, the agreement is even better from the fitting  
 624 shown on the right panel, the fitting results is  $\sim 0.96$ .

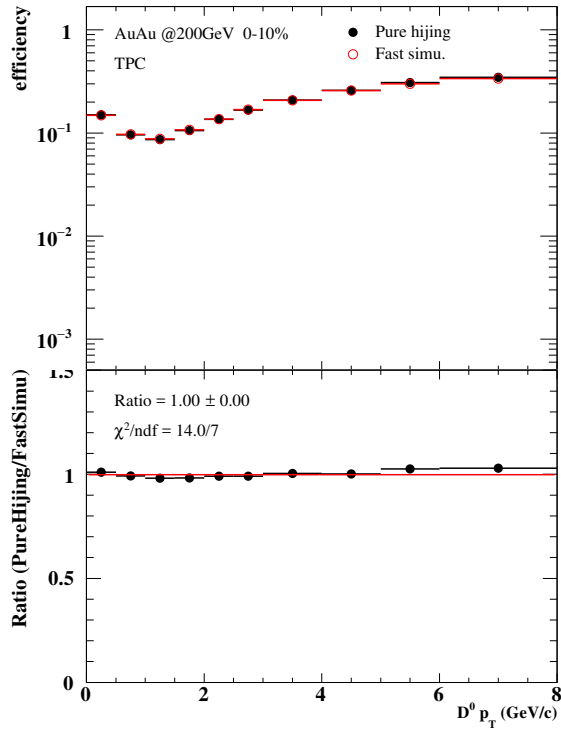


Figure 77: The comparison of  $D^0$  TPC acceptance  $\times$  efficiency between Hijing + GEANT (red) and Fast-Simulation with Hijing input (black). (right) Double ratio of these acceptance to Hijing.

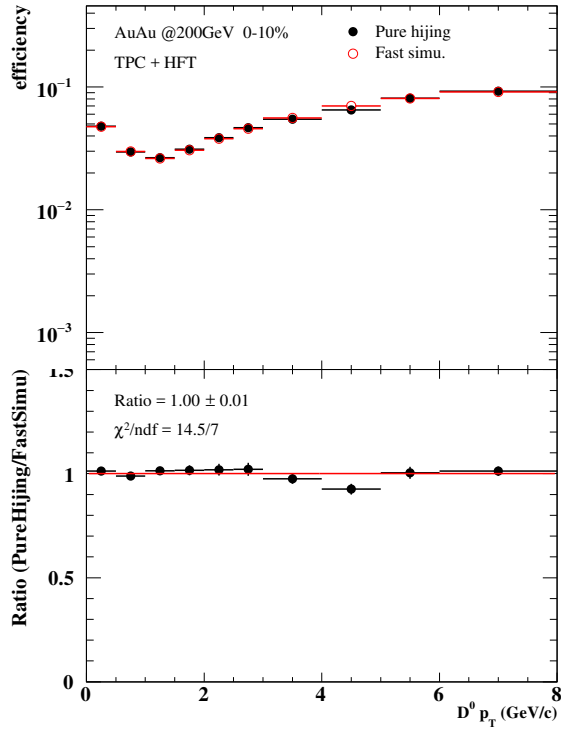


Figure 78: The comparison of  $D^0$  TPC + HFT match acceptance  $\times$  efficiency between Hijing + GEANT (red) and Fast-Simulation with Hijing input (black). (right) Double ratio of these acceptance to Hijing.

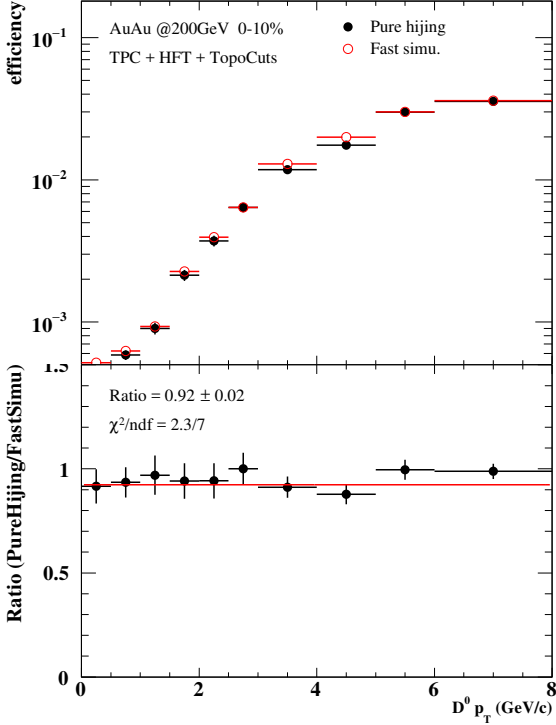


Figure 79: The comparison of  $D^0$  TPC + HFT match + Topological acceptance  $\times$  efficiency between Hijing + GEANT (red) and Fast-Simulation with Hijing input with wide binning (black). (right) Double ratio of these acceptance to Hijing.

From Hijing + GEANT simulation, we know exactly whether the HFT matched track is real match or mismatch, so we can determine the HFT real matched efficiency  $\times$  acceptance for  $D^0$  reconstruction from Hijing sample. If we compare with the previous Hijing HFT matched efficiency (not necessary to be real matched), it also indicate that most of the Mis-matched daughter tracks are removed by topological cuts as we said in the assumptions. Fig. 80 shows the different components contributions directly from Hijing, the black one is HFT matched, red one requires all the daughter tracks are real matched and the blue one shows at least one of the daughter tracks are mis-matched. Bottom panel shows the relative fraction of the real match and mis-mismatch contribution. As see, most of the mis-matched tracks are removed, but still there are  $\sim 5\%$  contribution for the most central events from this study while we except this contribution will be even smaller ( $< 2\%$ ) in the peripheral collisions as shown in the link below.

<https://drupal.star.bnl.gov/STAR/blog/xgn1992/d0-hijing-check-mismatch-tracks>

Above all the discussions in this section 4.8.1, we are confident that the Fast-Simulation method can well reproduce the acceptance and efficiency for this HFT related analysis. The precision as shown on Fig. 79 and Fig. 81 are good enough for our efficiency study. For the missed-match check, there are  $\sim 5\%$  contributions in the signals for the most central.

Note, that 5% (in most central) mismatch doesn't contribute to the results. That's juts for our understanding. As far as the tracks are matched to hft and pass our topological cuts, that's what we needed for our efficiency correction. Not necessary to be real matched tracks.

And there is another approvement that will describe in the following section.

As mentioned before, some of the input variables have eta dependence such as the HFT Mathing ratio, so similar studies was also presented along eta dependence. The link to the study can be found below.

<https://drupal.star.bnl.gov/STAR/blog/xgn1992/data-driven-fastsimu-eta-dependence-check>

#### 4.8.2 Validation Topological Distributions

As discussed before, we can extract the topological variables from both Hijing + GEANT and Fast-Simulation relay on those Hijing input. Similar as we did in Sec. 4.5.4, we can compare the topological distributions from these two procedures. This will be another evidence that our Fast-

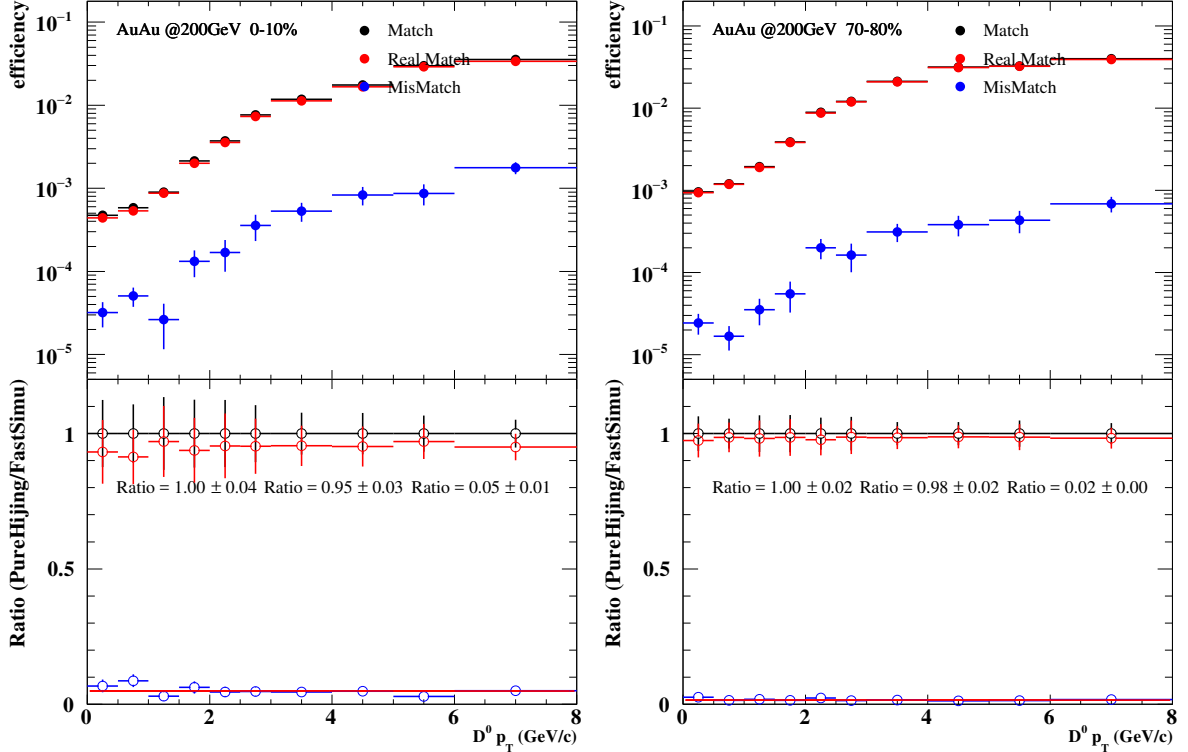


Figure 80: The comparison of  $D^0$  TPC + HFT match + Topological acceptance  $\times$  efficiency for Hijing + GEANT and Fast-simu with Hijing as input. The Hijing samples was updated with a large statistics compare to the previous ones. (bottom) Double ratio of the comparison. (Left) 0-10%, adnd (right) 70-80%.

653    Simulation can well reproduce the topological variables which is crucial for these kind of secondary  
654    vertex reconstruction analysis.

655    From Fig. 82 to Fig. 86, these are the topological variables used for the  $D^0$  reconstruction.  
656    The topological distributions can be extracted both directly from Hijng + GEANT and from Fast-  
657    Simulation relay on Hijing input. The Fast-Simulation part was the same package as we used for  
658    the efficiency study before.

659    As seen, the comparison of topological variables from Hijing have a very good agreement,  
660    which means again our Fast-Simulation method can well reproduce the topological variables in  
661    Hijing sample just as in the real data case. In another word, the efficiency estimation from this  
662    Hijing-Data-Driven Fast-Simulation is reliable. This is the other confident as we discussed in the  
663    last part of previous section 4.8.1.

664    There are two more assumptions which were not answered yet. Here we are trying to discuss a  
665    little bit in the following part.

#### 666    4.8.3 Validation with Ks Spectra Measurement

667    To verify the data-driven fast-simulation procedures, we calculated the efficiency corrected spectra  
668    for  $K_s$  in 10-20% centralities using the data-driven methods.

669    The event and track quality cuts are using the same as  $D^0$  analysis. For the topological  
670    cuts, they are chosen as similar as the  $D^0$  cuts.  $dca1 > 0.01 \&& dca2 > 0.01 \&& dca12 < 0.006 \&&$   
671     $dca2vtx < 0.015 \&& \cos(\theta) > 0 \&& decayL_{XY} < 1.5$ .

672    After corrected with the efficiency from data-driven simulation, the result shows very good  
673    agreement with the published result as in Fig. 87. This is the corrected spectra for  $K_s^0$  for 10-20%  
674    centrality. Open symbols are the published results while the solid one is from this study. The  
675    lower panel shows the double ratio comparison between run 14 and the published one, it shows  
676    good agreement.

677    The details study can be found from the below links  
678    [http://www.star.bnl.gov/protected/heavy/dongx/presentation/HFPWG\\_Ks\\_PID\\_09172015.html](http://www.star.bnl.gov/protected/heavy/dongx/presentation/HFPWG_Ks_PID_09172015.html).

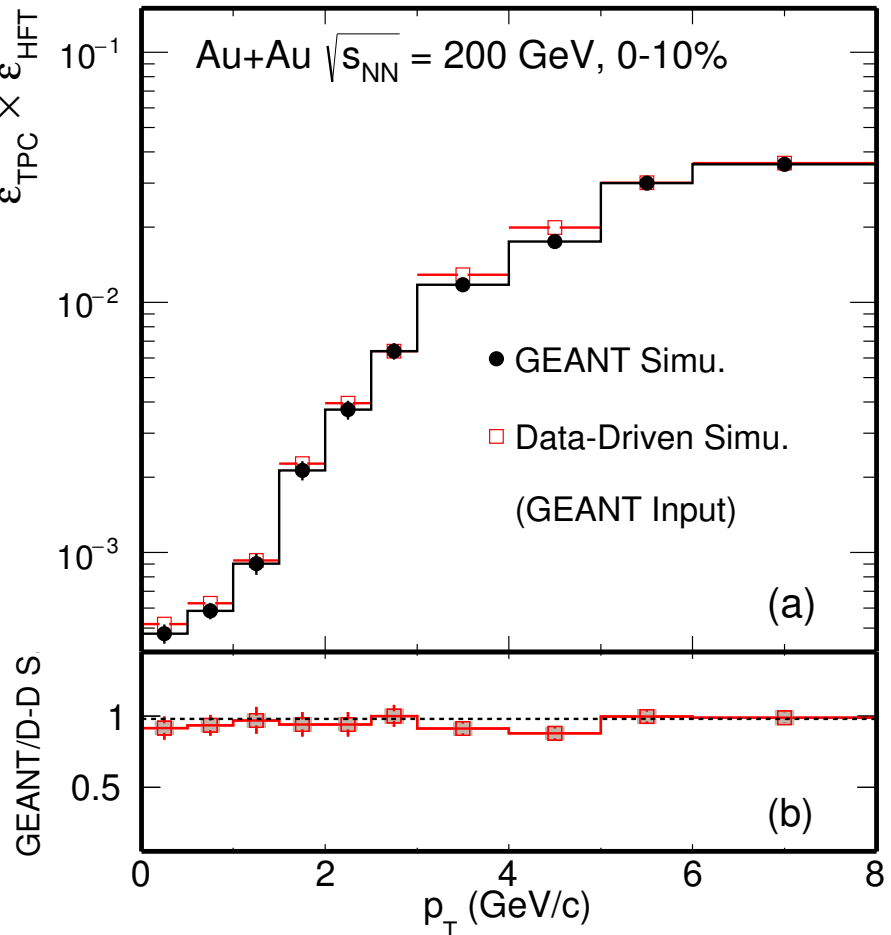


Figure 81: The comparison of  $D^0$  TPC + HFT match + Topological acceptance  $\times$  efficiency for Hijing + GEANT and Fast-simul with Hijing as input. The Hijing samples was updated with a large statistics compare to the previous ones. (bottom) Double ratio of the comparison.

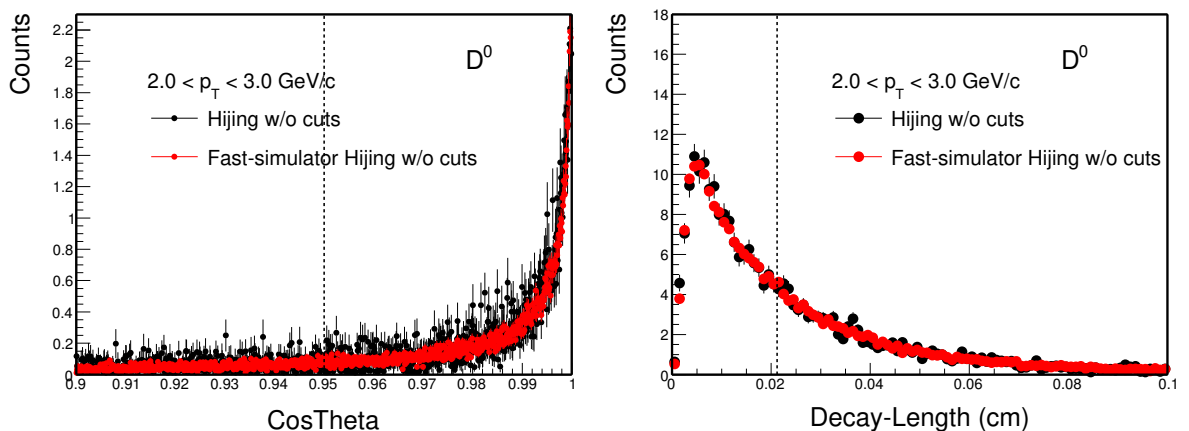


Figure 82:  $D^0$  cosTheta distribution in most central 0-10% between Hijing and Fast-Simulation. Figure 83:  $D^0$  decay length distribution in most central 0-10% between Hijing and Fast-Simulation.

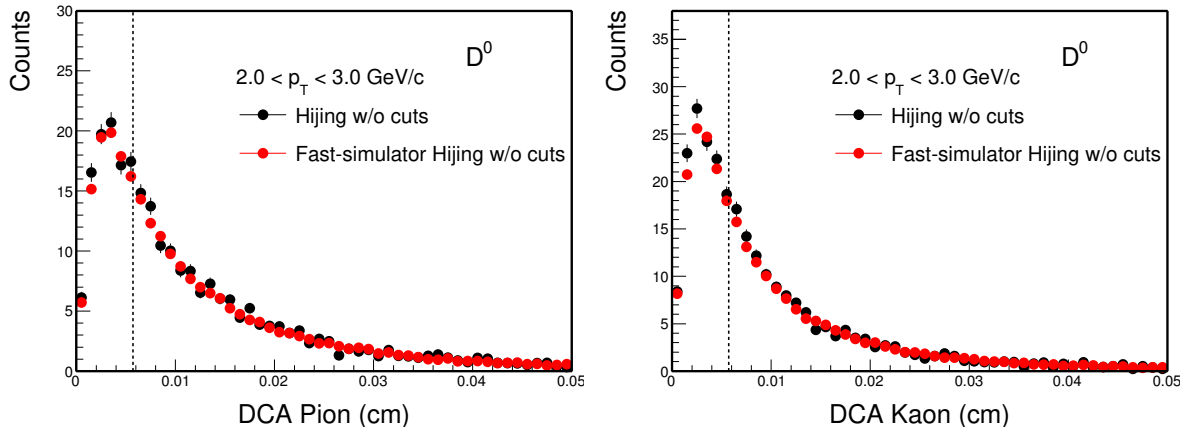


Figure 84:  $D^0$  pions Dca distribution in most central 0-10% between Hijing and Fast-Simulation.

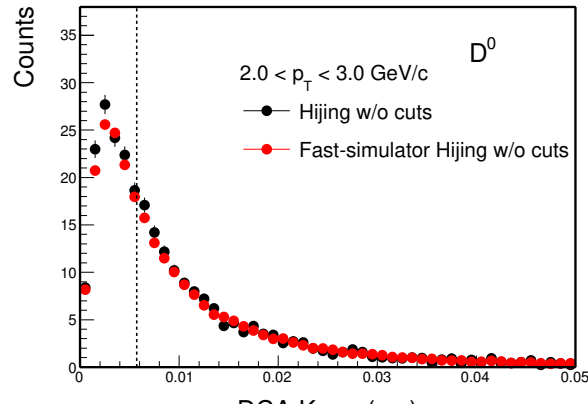


Figure 85:  $D^0$  kaons Dca distribution in most central 0-10% between Hijing and Fast-Simulation.

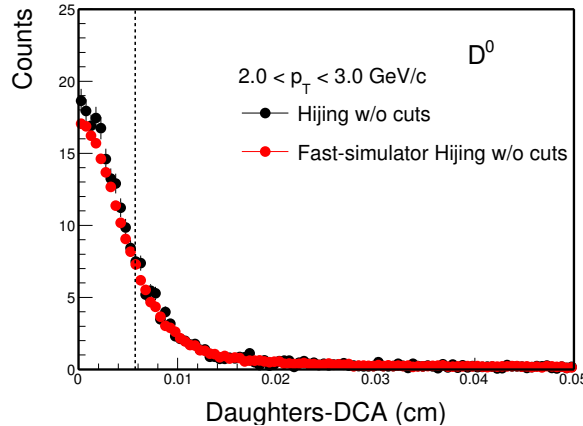


Figure 86:  $D^0$  dcaDaughters distribution in most central 0-10% between Hijing and Fast-Simulation.

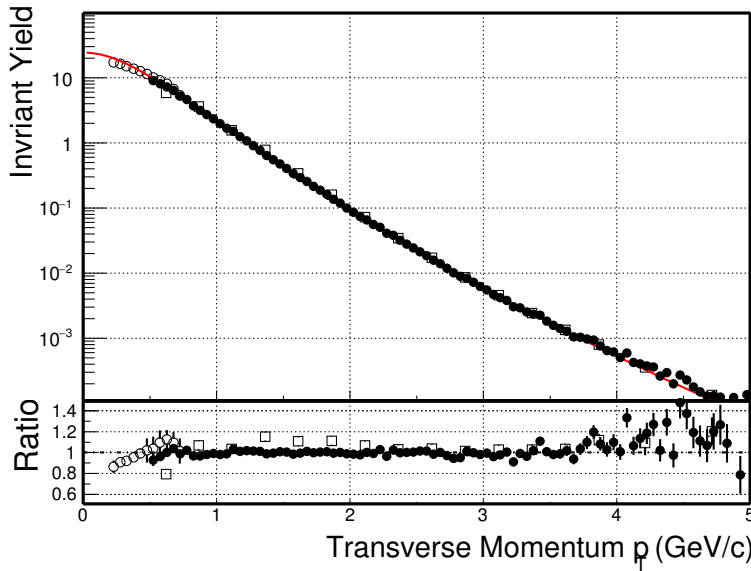


Figure 87: Corrected spectra for  $K_s^0$  for 10-20% centrality. Open symbols are the published results while the solid one is run14 result. The lower panel shows the double ratio comparison between run 14 and the published one.

```

679 pdf
680 https://drupal.star.bnl.gov/STAR/system/files/userfiles/131/HFPWG_KsSpectra_09102015.
681 pdf

```

## 682 4.9 Secondary Track Contribution

683 The Fast-Simulation is validated with primary track in the procedure Fig. 75. All the tracks  
 684 for HFT matching ratio and Dca inputted to Fast-Simulation is primary track. Based on the  
 685 Hijing sample we can study the secondary track contribution since in the real data part we can't  
 686 distinguish primary track and secondary track. In Hijing simulation, we use the start vertex of  
 687 that track to determine whether it's primary track or secondary track.

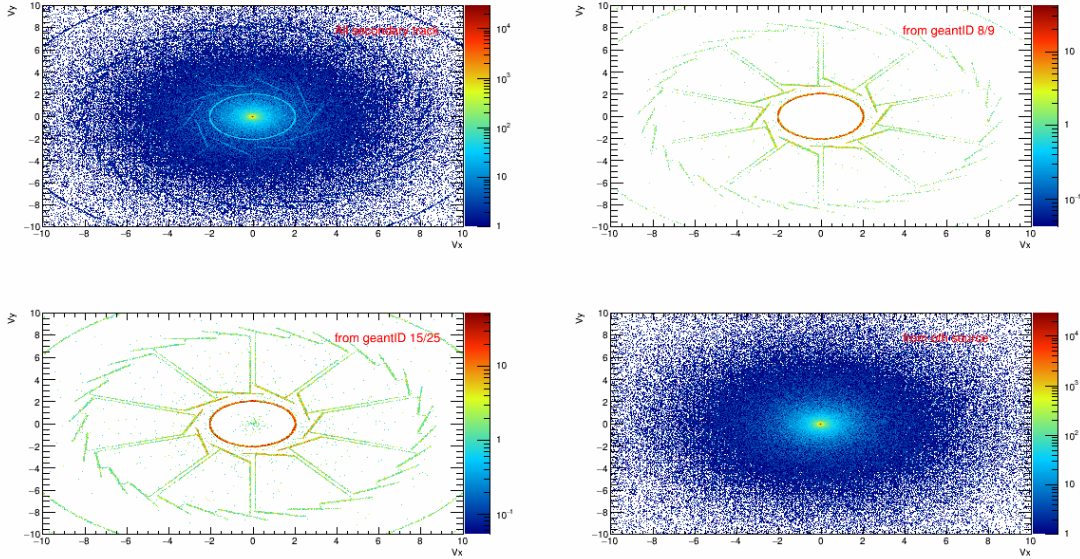


Figure 88: The vertex distribution for Pions from secondary decay. Top left is the overall secondary pion tracks, top right is pion decayed from GeantID=8/9 (which is  $\pi^\pm$ ), bottom left is pion decayed from GeantID=15/25 (which is anti-proton and anti-neutron), bottom right is decayed from other source such as the lambda (anti)sigma and  $\Xi_0$

688 Fig. 88 shows the pions vertex distributions from the secondary decay. The first one is the  
 689 overall secondary pion vertex distributions and we can clearly see some HFT structure. Top right  
 690 panel is pions decayed from GeantID==8/9 (which is  $\pi^\pm$ ), this part is the knocked out particles  
 691 with HFT. The bottom left is pion decayed from GeantID==15/25 (which is anti-proton and  
 692 anti-neutron), this is the normal annihilation particles. The last one bottom right shows the pions  
 693 decayed from other source such as the lambda (anti)sigma and  $\Xi_0$ .

694 For the secondary tracks, they have different contributions to the HFT matching ratio. The  
 695 fraction of the secondary tracks contributions can be found in the Fig. 90, as seen in the  $p_T$  range  
 696 around 2-3 GeV/c there is a visible contributions from the annihilation with the materials, which  
 697 will final contribute to the HFT matching ratio.

698 The secondary track have kind of different performance compare to the primary track such as  
 699 the HFT match ratio shown on Fig. 92. The solid circle is the inclusive one for HFT matching  
 700 ratio, the empty circle is for the primary pions and the solid square is for the secondary pions. All  
 701 these HFT match ratios are after applying exactly the same cut as real data analysis. The low  
 702 match ratio for secondary track is reasonable since they are decayed far away from the vertex and  
 703 most of them do not have three HFT hits. The more contribution from the secondary track, the  
 704 more difference we observed between inclusive one and primary one. The bottom panel shows the  
 705 HFT matching double ratio of inclusive one over primary one. For the pions, since the secondary  
 706 pion have some contributions, we do saw the different between primary one and inclusive one at  
 707 some certain  $p_T$  range for this HFT match ratio. For the kaons, the relative secondary contribution  
 708 is small, that's why there is no big difference between primary and inclusive ones as see on Fig. 93.

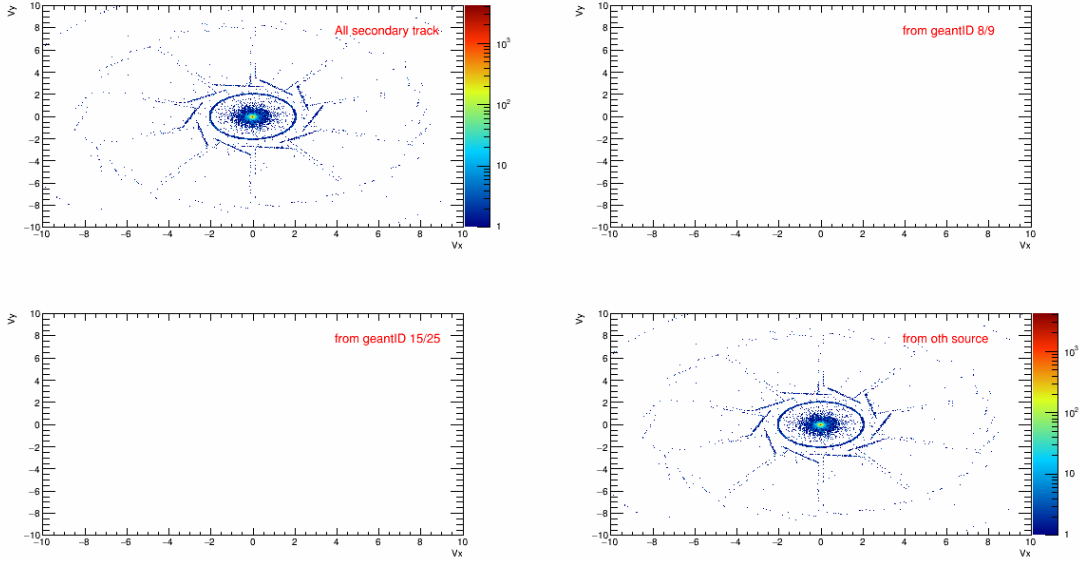


Figure 89: The vertex distribution for Kaons from secondary decay. Top left is the overall secondary kaon tracks, top right is kaon decayed from GeantID=8/9 (which is  $\pi^\pm$ ), bottom left is kaon decayed from GeantID=15/25 (which is anti-proton and anti-neutron), bottom right is decayed from other source

This secondary track contribution for our efficiency correction need to be taken care, especially for Pions. There are a few percent contributions from our Hijing simulation study. In our real data efficiency correction, we took this double ratio from Hijing as an additional correction factor for the HFT matching ratio, since the data part can only obtain the inclusive one. After this additional correction, we still be able to obtain the precision like Fig. 79.

For the secondary track Dca contributions, we tested with the inclusive track Dca or primary track Dca. In principle, with the inclusive tracks, they should have slightly broader distributions. But in our test, it seems that these contributions to the final  $D^0$  efficiency is really small. This maybe due to the limited Hijing statistics or the slightly Dca difference does not contribute much. But in our real data case, we do not take this secondary Dca contributions as additional correction factor yet.

We also checked the secondary track contributions between our study and previous published result from study. The secondary contribution shows reasonable agreement and the studies can be found below.

[https://drupal.star.bnl.gov/STAR/system/files/20171122\\_GXie.pdf](https://drupal.star.bnl.gov/STAR/system/files/20171122_GXie.pdf)

An additional check was done during the PWG review, since the secondary pion do have some contribution from the anti-proton and anti-neutron (GeantID 15/25). What we did is simple, we check the primary pion and proton spectra, then compared to the publish results. The Hijing sample can reproduce the pion spectra quite well, but not for the proton spectra. So we took the proton spectra from Hijing to the published one, and take the ratio as an weight factor. Then check the HFT matching ratio effect, the result shows tiny difference < 2%. This one was take as the systematic uncertainties.

The details study can be found in the drupal-page.

[https://drupal.star.bnl.gov/STAR/system/files/20180327\\_DMeson\\_GXie.pdf](https://drupal.star.bnl.gov/STAR/system/files/20180327_DMeson_GXie.pdf)

As can be seen in the Fig. 90, The transverse momenta of these pions are mostly around  $2\text{--}3\text{ GeV}/c$  and the fraction of total inclusive pions is  $\sim 10\text{--}12\%$  at  $p_T = 2\text{--}3\text{ GeV}/c$  based on this simulation and contribute  $\sim 5\text{--}8\%$  to the HFT matching ratio. This was obtained using the GEANT with GHEISHA hadronic package. During the GPC review, we found that With a difference hadronic package, FLUKA, the secondary pion fraction in  $2\text{--}3\text{ GeV}/c$  region is significantly reduced to be negligible. The difference between the primary pions and the inclusive pions in the HFT matching ratio has been considered as one additional correction factor to take into account these secondary pions in our data-driven simulation method when calculating the efficiency cor-

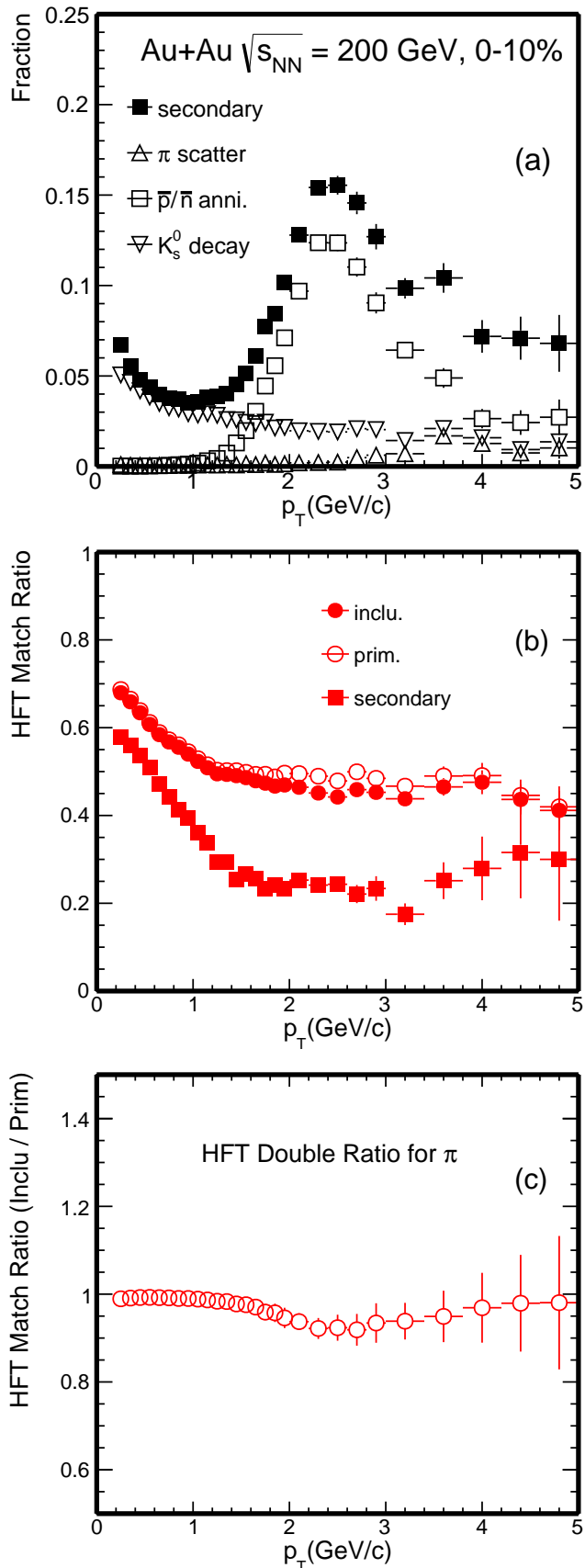


Figure 90: The fraction of the different sources for the pion spectra, including the primary particles which is out of the range, the secondary sources include form parent GeantId = 8/9, GeantId = 15/25 and others source. The black makers are for TPC tracks while the red makers are fro HFT matched tracks.

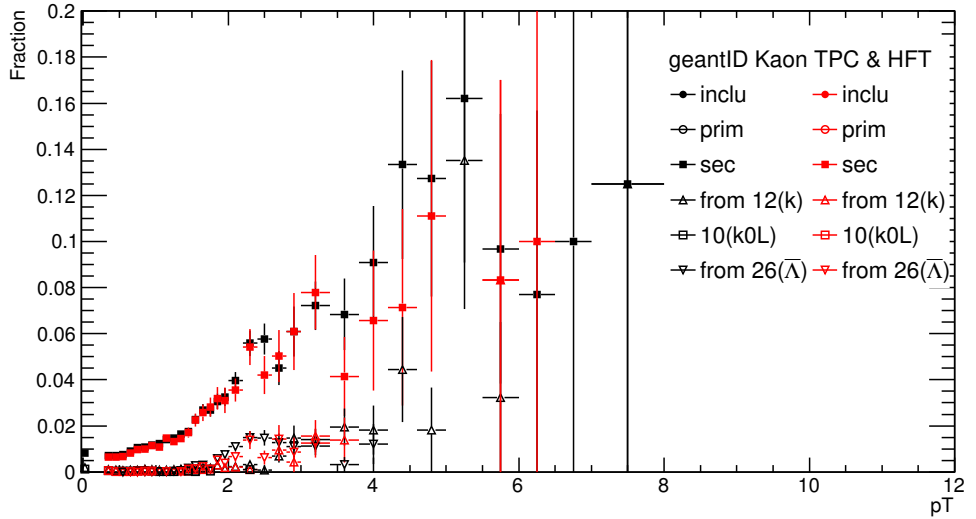


Figure 91: The fraction of the different sources for the kaon spectra, including the primary particles which is out of the range, the secondary sources include form parent GeantId =12, 10 and 26 and others source. The black makers are for TPC tracks while the red makers are fro HFT matched tracks.

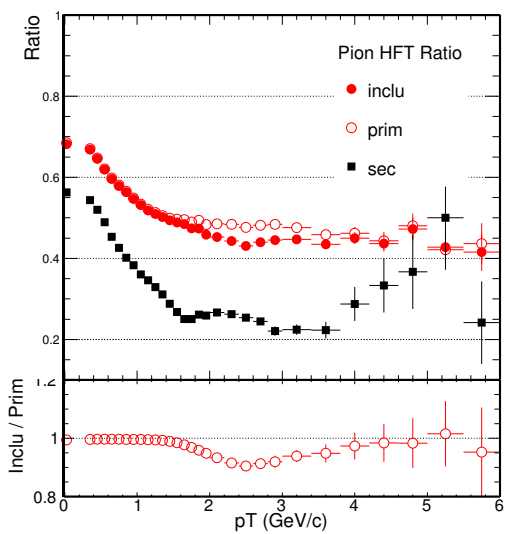


Figure 92: HFT Matching Ratio for Pions, compare between primary track and secondary tracks relay on Hijing. (bottom) The double ratios of inclusive one to primary tracks.

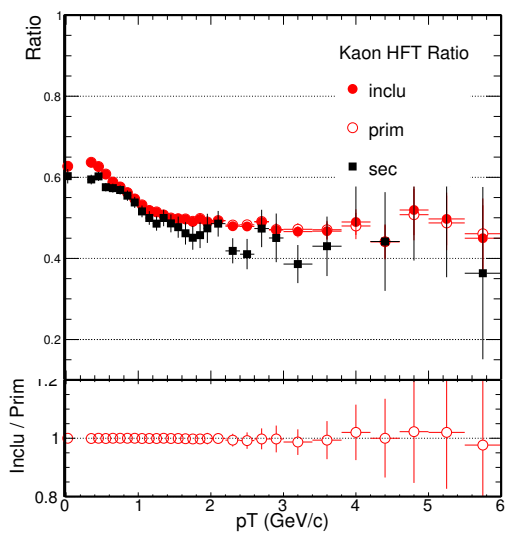


Figure 93: HFT Matching Ratio for Kaons, compare between primary track and secondary tracks relay on Hijing. (bottom) The double ratios of inclusive one to primary tracks.

rection, while the maximum difference with respect to the result obtained using the GHEISHA hadronic package is included as the systematic uncertainty for this source.

Some details study can be found in the drupal-page.

[https://drupal.star.bnl.gov/STAR/system/files/20180926\\_UIC\\_GXie.pdf](https://drupal.star.bnl.gov/STAR/system/files/20180926_UIC_GXie.pdf)

## 4.10 Vertex Resolution Contribution

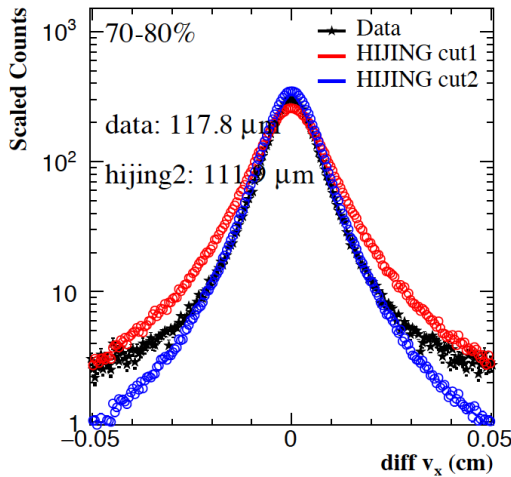


Figure 94: Comparison of the FWHM of the subEvent vertex resolutions for 70-80%. black is real data and blue is from Hijing.

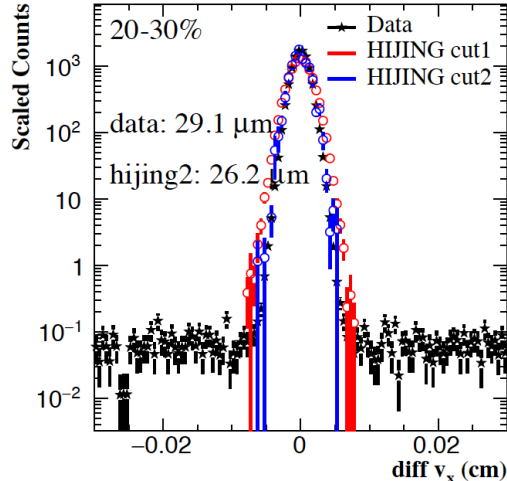


Figure 95: FWHM of the subEvent vertex resolutions for 20-30%. black is real data and blue is from Hijing.

As discussed before, the vertex resolution in peripheral events still have some contributions. If those peripheral events vertices are out of hundreds or dozens of  $\mu\text{m}$  vertex resolution, they are not likely to contribute to the D mesons foreground (maybe not even the background). The 2D Dca<sub>XY</sub> Dca<sub>Z</sub> distributions are the only input to the Fast-Simulation for this effect. They contain both the vertices and tracks contribution.

Fig. 94 and Fig. 95 show the vertex difference in the X direction using the sub-event method for centrality 70-80% and 20-30%. They are the difference of the refitted vertex from the two sub-events. Fig. 96 shows the Full Width of the Half Maximum (FWHM) to capture the vertex resolution in the X direction using this sub-event method. In the sub-event method, the event was divide to two randomly subevent, and then reconstruct two vertexes. The difference of the two vertexes can be somehow demonstrate the vertex resolutions. As can see the Hijing sample can reasonable describe our real data.

To solve this problem, we need to unfold the vertex resolution from 2D Dca distributions, and this is not straightforward since the vertex resolution contribution could be in the same order of the Dca resolution and this is not reliable (subtracting two numbers that are close to each other have very large uncertainties). There is another way we can rely on to obtain this correction factor, which is the Minimum Bias Hjing simulation sample. From Hijing sample we know the true efficiency for any centrality species, and from the Fast-Simulation we can obtain the efficiency including those vertex effect. The difference was took as the additional correction factor for real data analysis. To estimate the vertex resolution effect, we embedded a PYTHIA  $c\bar{c}$  event into a Hijing Au+Au event, and ran through the STAR GEANT simulation followed by the same offline reconstruction as in the real data production. The PYTHIA  $c\bar{c}$  events are pre-selected to have at least one  $D^0 \rightarrow K^-\pi^+$  decay or its charge conjugate to enhance the statistics. The MB Hijing sample we used here is from the same setup as we discussed before, and the only difference compared to the 0-10% Hjing sample is the impact parameters ( $b$ ). But for our centrality selection, we still use grefumlt for both data and simulation.

For the QA of the simulation samples, including HFT matching ratio and Dca resolutions for different centralities, all the details can be found in the next links:

[http://portal.nersc.gov/project/star/xlchen/D0\\_Hijing/QA/all/](http://portal.nersc.gov/project/star/xlchen/D0_Hijing/QA/all/)

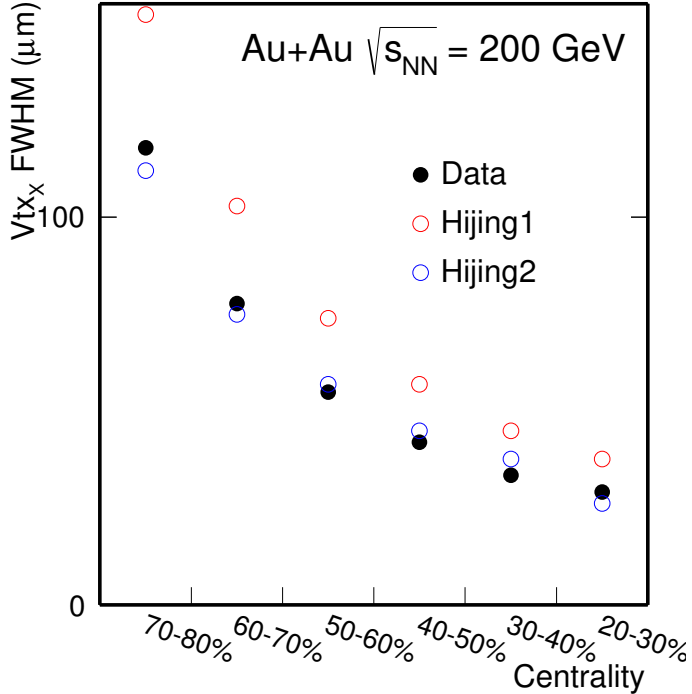


Figure 96: FWHM for Vertex resolution using sub-event method versus centralities in Au + Au collisions.

In general, our Hijing sample can reasonable reproduce the track performance such as the HFT matching ratio and Dca distributions for different centralities. Which means we can relay on this MB Hijing sample to evaluate this vertex resolution contribution.

The first contribution we checked is for the 70-80% centrality species. Follow the same procedures as we discussed for 0-10%, we did the validation step by step. First is the acceptance check as shown on Fig. 97, the results from Hijing and Fast-Simulation matched very well for this most peripheral events, which is the same as our expection. The second step is check the kinematic with the reconstructed TPC tracking information. These was involved with the TPC tracking efficiency lost and the momentum resolution. The result in Fig. 98 shows good agreement.

The next step for this peripheral centrality will be fold in the HFT matching efficiency and the results shown in Fig. 99. As see, the two curves are close with each other and the double ratio was close to unity. The last step will be the topological contributions which also including the vertex contributions. Fig. 100 shows this efficiency  $\times$  Acceptance comparison between Hijing and Fast-Simulation after the TPC, HFT matching and topological cuts for the 70-80% centralities. As see, due to the involved vertex resolution contribution for this peripheral events, the agreement between Hijing and Fast-Simulation was not good anymore. If we try to fit the double ratio shown in the lower panel, the difference can be as large as a factor of  $\sim 1/0.59$  (with Hiing Cut2).

For the vertex contributions, we use these double ratios as our additional correction factor for the final results. As discussed before, the most central events will suffer less this vertex contribution, but only the most peripheral and mid-peripheral events need to consider this effect. The following plots show these correction factor for different centrality species from the most peripheral to most central events.

Fig. 100 and the following figures show the comparison between Hijing and Fast-Simulation from different centralities, in each bottom panel, the fitted results show the expected trend. For the most peripheral events the correction factor is as large as  $\sim 1/0.59$  for centrality 70-80%,  $\sim 1/0.83$  for centrality 60-70%,  $\sim 1/0.90$  for 50-60%,  $\sim 1/0.94$  for 40-50% and  $\sim 1/0.96$  for 30-40% and  $\sim 1/0.97$  for 20-30%. For the most central, 10 – 20% and 0 – 10% centralities, the correction effect is already small, the double ratio is close to 1.

For the most central collisions, the correction factor was small, but in our analysis we still consider this effect to be consistent for all the centralities. This was validated and confirmed by our Hijing samples.

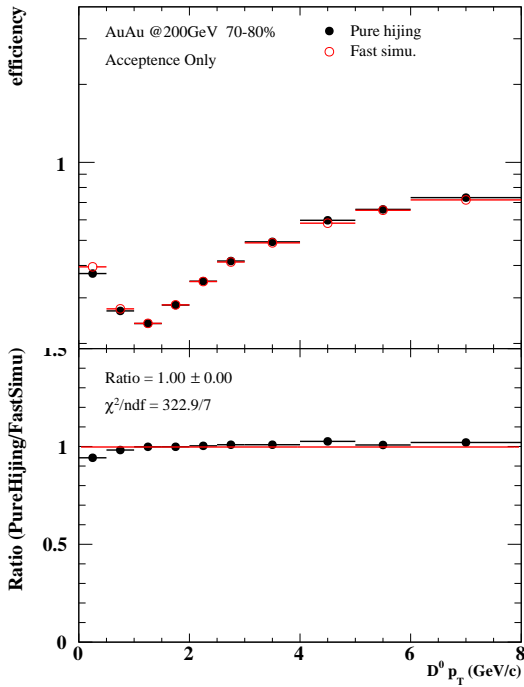


Figure 97: The comparison of  $D^0$  acceptance between Hijing + GEANT (black) and Fast-Simulation with Hijing input (red). (bottom) Double ratio of these acceptance of Hijing to Fast-Simulation.

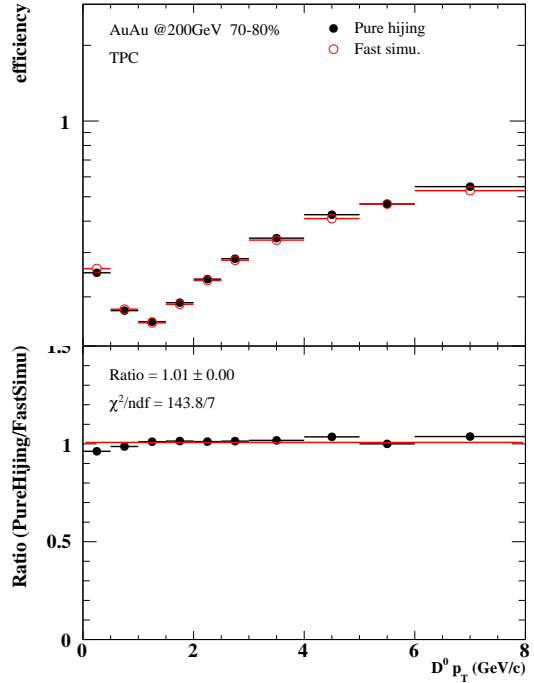


Figure 98: The comparison of  $D^0$  TPC acceptance  $\times$  efficiency between Hijing + GEANT (black) and Fast-Simulation with Hijing input (red). (bottom) Double ratio of these efficiency of Hijing to Fast-Simulation.

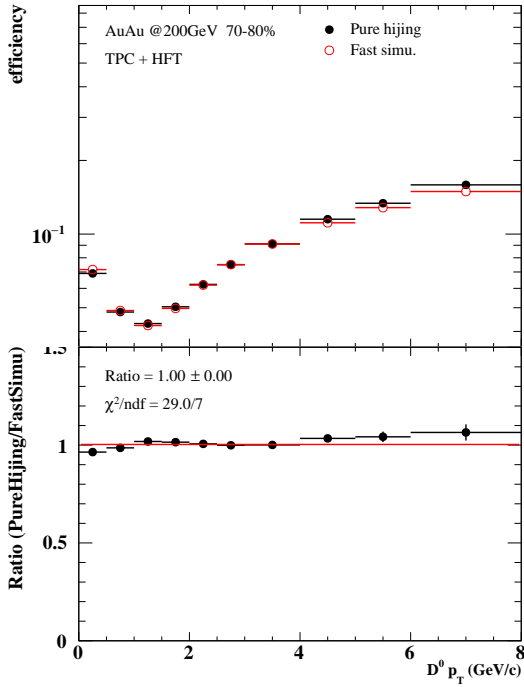


Figure 99: The comparison of  $D^0$  TPC + HFT match acceptance  $\times$  efficiency between Hijing + GEANT (black) and Fast-Simulation with Hijing input (red). (bottom) Double ratio of these acceptance of Hijing to Fast-Simulation.

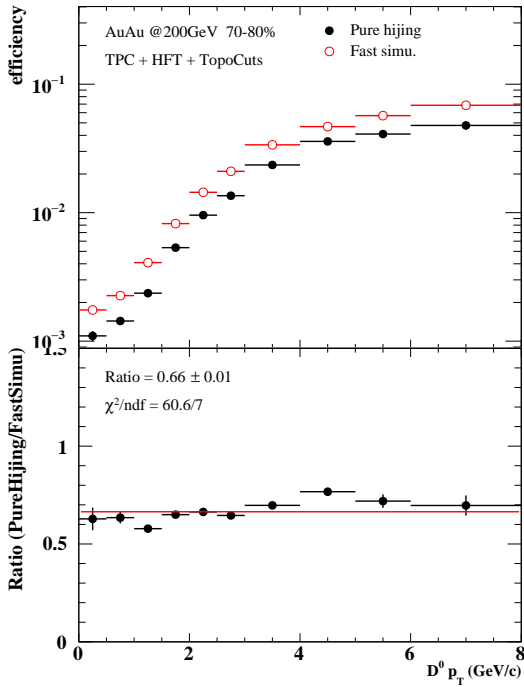


Figure 100: The comparison of  $D^0$  TPC + HFT match + Topological between Hijing (black) and Fast-Simulation (red). (bottom) Double ratio to Fast-Simulation.

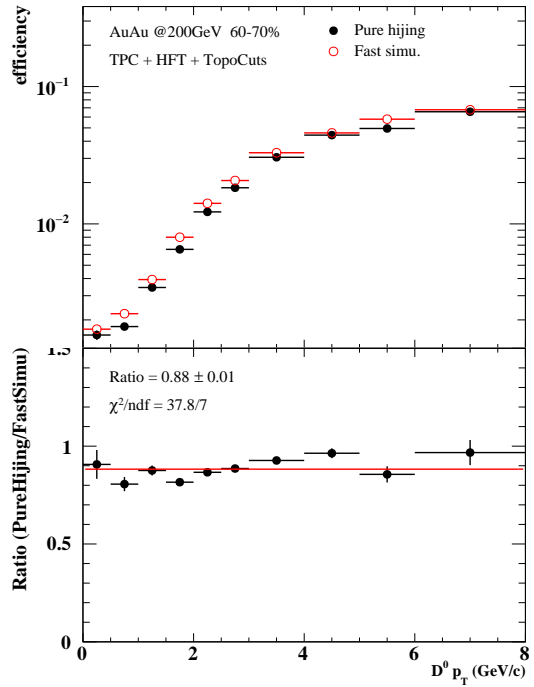


Figure 101: The comparison of  $D^0$  TPC + HFT match + Topological between Hijing (black) and Fast-Simulation (red). (bottom) Double ratio to Fast-Simulation.

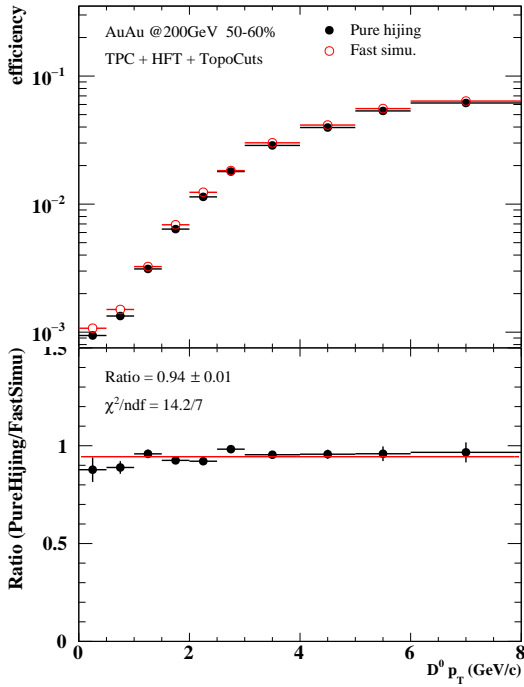


Figure 102: The comparison of  $D^0$  TPC + HFT match + Topological between Hijing (black) and Fast-Simulation (red). (bottom) Double ratio to Fast-Simulation.

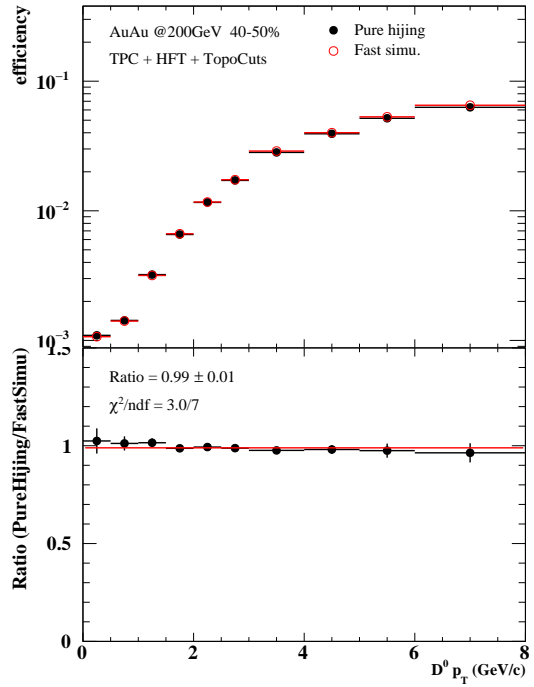


Figure 103: The comparison of  $D^0$  TPC + HFT match + Topological between Hijing (black) and Fast-Simulation (red). (bottom) Double ratio to Fast-Simulation.

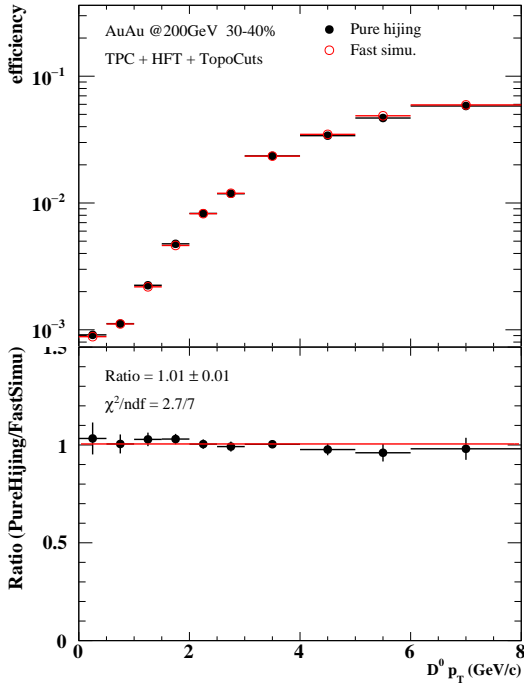


Figure 104: The comparison of  $D^0$  TPC + HFT match + Topological between Hijing (black) and Fast-Simulation (red). (bottom) Double ratio to Fast-Simulation.

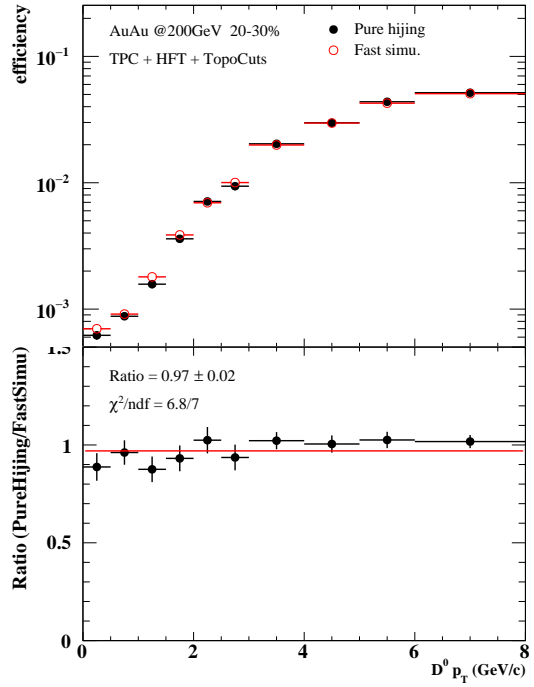


Figure 105: The comparison of  $D^0$  TPC + HFT match + Topological between Hijing (black) and Fast-Simulation (red). (bottom) Double ratio to Fast-Simulation.

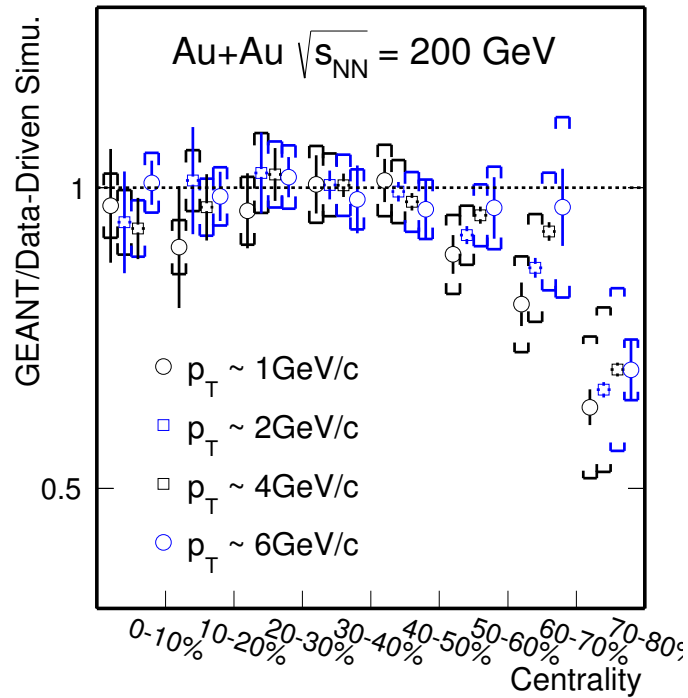


Figure 106: The correction factor between Hijing and Fast-Simulation for difference centralities in the  $p_T$  ranges.

For the systematic uncertainties from this vertex correction, we validate them by change the gRefmult cut. We choose two gRefmult cuts as the centrality definitation for Hijing sample, and trying to capture this systematic source. One cut is using the same as real data for centrality definitation (Hijing Cut1) and another one is trying to minimum the difference for the vertex resolution between data and Hijing(Hijing Cut2). As shown in Fig.96, cut1 from Hijing was the same gRefmult cut as real data, cut2 from hijing was the optimized gRefmult cut try to reproduce the vertex resolution in data. As can see, these two sets of gRefmult cuts can cover the real data resolution. As can see, the Hijing2 cut are more close to the real data. so The central value for this correction was obtained from the Hijing2 cut value of the correction. And we quota the difference of these two cuts as the systematic source. The statistics uncertainties from this correction was directly from the samples statistics with Hijingcut2, and then properate to the final systematic results.

## 4.11 Double Counting Correction

$D^0$  candidates are reconstructed with pairing  $K^-$  and  $\pi^+$  candidate tracks. When  $D^0$  daughter  $K^-$  is misidentified as a  $\pi^-$  while the other daughter  $\pi^+$  is misidentified as a  $K^+$ , the resulting pair  $K^+\pi^-$  will enter into the distribution for reconstructing  $\bar{D}^0$ . Although the mass assignments are wrong, the pair  $K^+\pi^-$  invariant mass will be still peak around the  $D^0$  region with typically a broader distribution compared to the real signal. When counting the final  $D^0$  candidates, these within the mass selection window will be counted twice. (See also study in previous STAR open charm hadron measurements - STAR notes below).

<https://drupal.star.bnl.gov/STAR/starnotes/private/psn0594>  
<https://drupal.star.bnl.gov/STAR/starnotes/private/psn0550>  
<https://drupal.star.bnl.gov/STAR/starnotes/private/psn0651>  
[http://www.star.bnl.gov/protected/heavy/dongx/presentation/HFPWG\\_PID\\_09032015.pdf](http://www.star.bnl.gov/protected/heavy/dongx/presentation/HFPWG_PID_09032015.pdf)

The double counting issue will certainly affect the obtained  $D^0$  raw yields. In the  $v_2$  analysis, since the doubly counted candidates are still coming from  $D^0$ , this issue should not affect the obtained central value of  $v_2$ . However, the statistical errors could be slightly off. For the spectra analysis, we need to consider this effect.

The double counting probability estimation need a precise determination of the PID variable distributions,  $n\sigma_X$  from  $dE/dx$  and  $1/\beta$  from TOF. For  $dE/dx$  calculation, we tried two methods  
1) Select pure pion and proton samples from weak decays ( $K^S, \Lambda$ )  
2) Look at the single particle distributions directly and perform multi-component fit in the region where the  $dE/dx$  bands can be separated out.

Figure 107 summarized the extracted  $n\sigma_X$  mean values vs.  $\beta\gamma$  for both methods discussed above. It looks good that in the overlapping region between different particles and different methods, the results look consistent. The dashed blue lines are parametrized function fits to the data points. These will be used to estimated the mis-identification probability.

The PID of  $D^0$  daughters also involves the TOF detector. We also estimated the TOF PID variable  $1/\beta$  distributions and TOF matching/PID efficiency. Figure 108 shows the fit results on the mean and width values for  $1/\beta - 1/\beta_{expected}$  distributions vs. particle momentum for different particles. Similar as  $dE/dx$ , results in the region beyond the TOF PID are not reliable. We use results which are safe in PID for later analysis, which are  $p < 1.5$  GeV/c for pions,  $p < 1$  GeV/c and kaons and  $p < 2$  GeV/c for protons. It is good to see the mean and width values are quite stable in a broad momentum region. At very low momentum, the multiple scattering effect will increase momentum resolution and  $1/\beta - 1/\beta_{expected}$  spread, and track energy loss will also shift the mean of  $1/\beta - 1/\beta_{expected}$  away from 0. But these will not affect the study here since tracks with  $p_T < 0.6$  GeV/c are not used for  $D^0$  reconstruction.

With all these at hand, we can evaluate the PID efficiency. The mis-identification probability for pion and kaon daughters can be also evaluated, as shown in Figure 109.

With the misidentification probability, we can reconstruct the invariant mass distributions from doubly mis-PID. The momentum resolution for pion and kaon tracks are chosen to fit to the  $D^0$  signal peak. Figure 110 and Figure 111 show these distributions compared to the signal distributions in different  $D^0 p_T$  regions. The red line with a narrow peak represent the input signals while black curve with broader width represent the double misPID distributions. The distributions are normalized to the input real  $D^0$  signals.

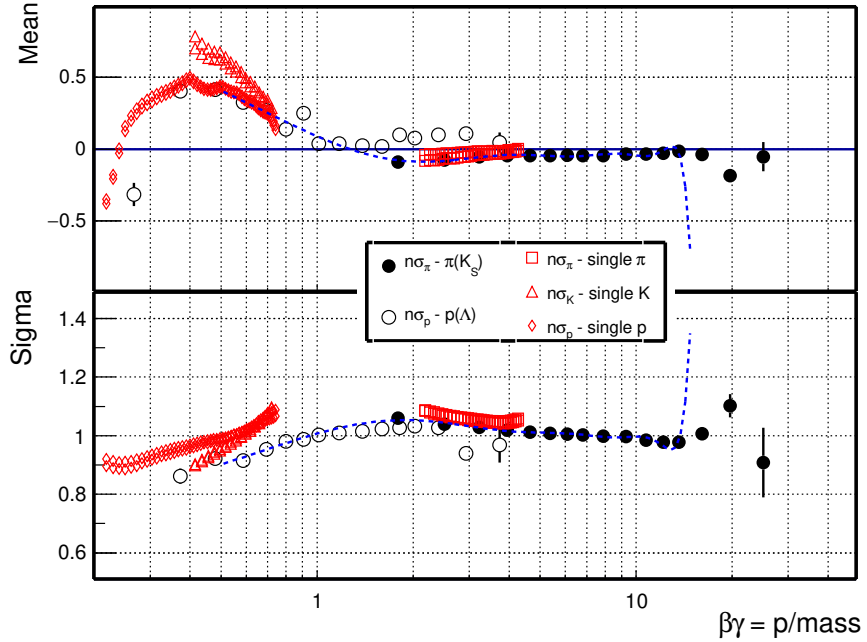


Figure 107: Top 0-10% central Au+Au collisions: extracted  $n\sigma_X$  mean values vs.  $\beta\gamma$  for both methods discussed in the text.

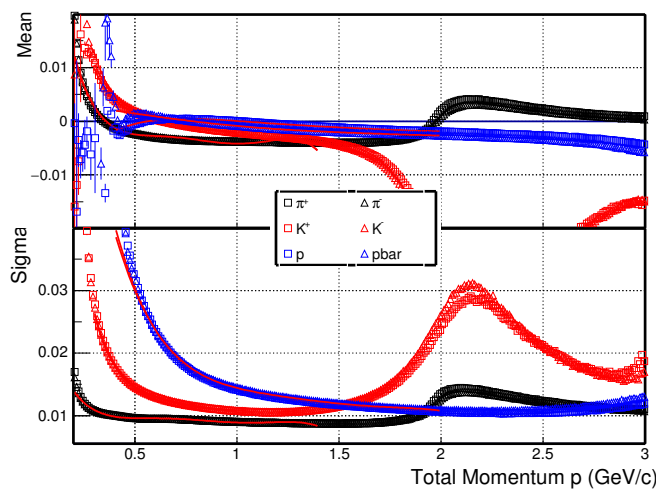


Figure 108: Top 0-10% central Au+Au collisions: extracted  $1/\beta - 1/\beta_{expected}$  mean and width values vs. particle momentum for pions, kaons and protons. Results for pions and kaons at  $p > 1.5$  GeV/c are beyond the TOF PID capability. The fit results are not reliable.

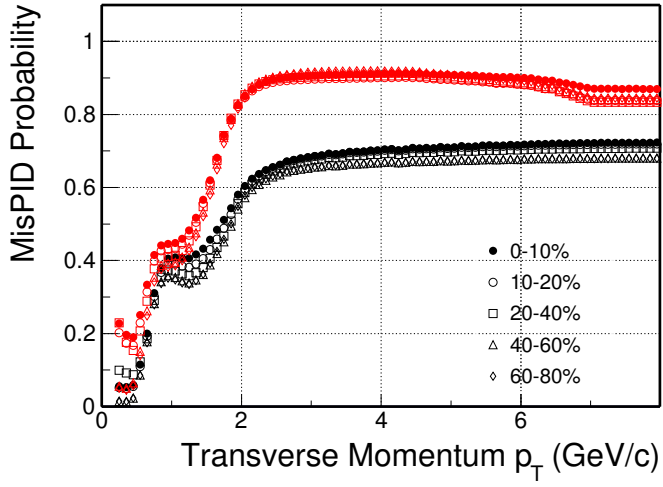


Figure 109: Particle misidentification probability for kaons (red) and pions (black) from different centrality bins in Au+Au collisions.

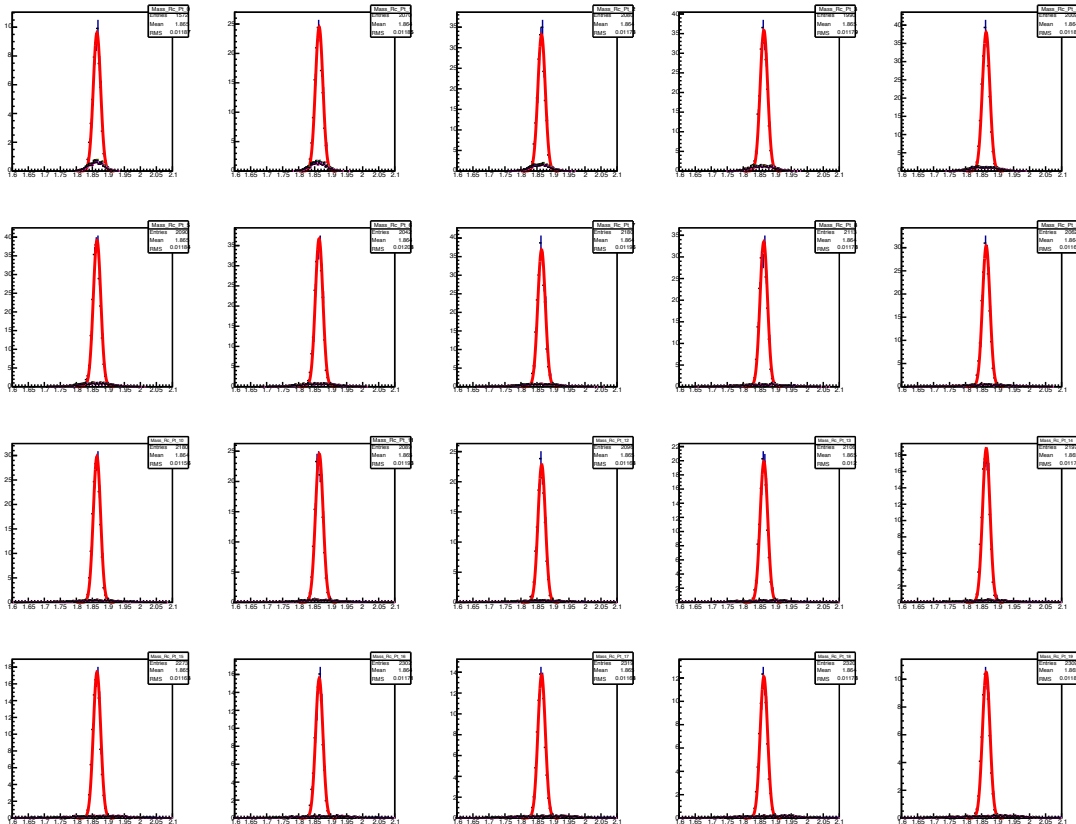


Figure 110: Reconstructed  $K\pi$  invariant mass distributions from clean PID and doubly misidentification. The relative magnitude is fixed according to the realistic mis-identification probability. From top left to bottom right shows the distributions in  $p_T$  bins 0-0.1 GeV/c, 0.1-0.2 GeV/c, ..., 1.9-2.0 GeV/c.

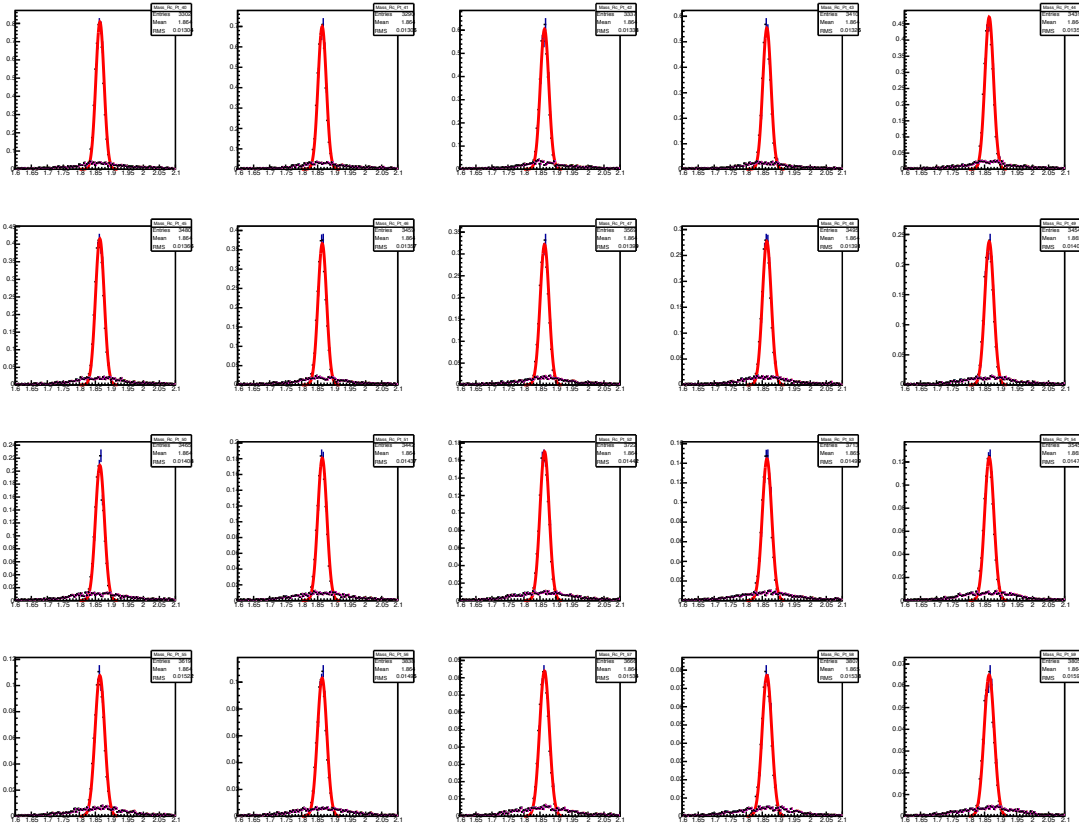


Figure 111: Reconstructed  $K\pi$  invariant mass distributions from clean PID and doubly mis-identification. The relative magnitude is fixed according to the realistic mis-identification probability. From top left to bottom right shows the distributions in  $p_T$  bins 4-4.1  $\text{GeV}/c$ , 4.1-4.2  $\text{GeV}/c$ , ..., 5.9-6.0  $\text{GeV}/c$ .

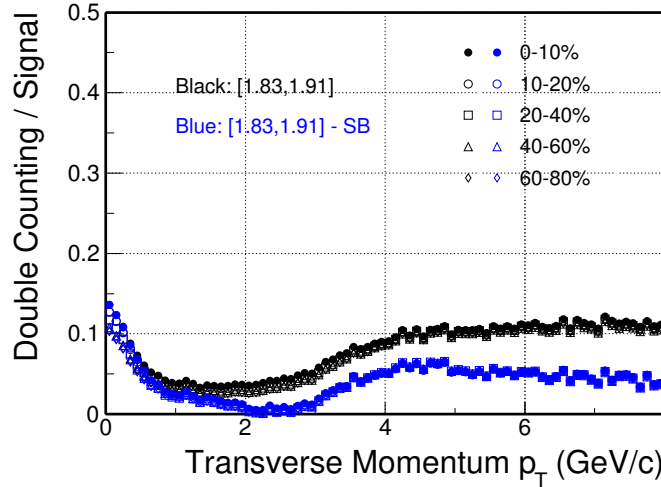


Figure 112: Estimated doubly-counted  $D^0$  fraction to the real signal with two calculation methods from different centrality bins in Au+Au 200 GeV collisions.

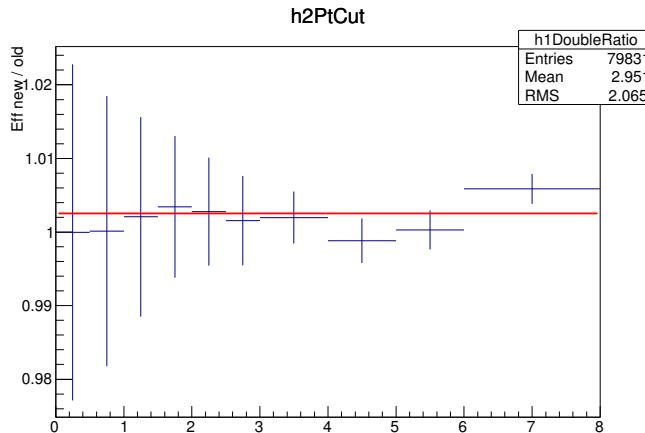


Figure 113: The efficiency difference with taking the old run10 and run14 spectra as weight

861     Figure 112 shows the final estimated double-counting contribution to the real signal with two  
 862     different calculation methods. The black symbols show the result from directly counting the entries  
 863     within  $2.5\sigma$  of the  $D^0$  mass window. In real data analysis, we used the side-band distributions to  
 864     normalize our fit or estimate our background. The blue data points show the result by subtracting  
 865     also the side-band distributions with the same mass window selection as in event plane method  $v_2$   
 866     calculation.

867     In general, the influence by double mis-PID is relative small. For the spectra analysis, we use  
 868     the blue data points in Fig. 112 as the central correction value and quote the range from 0 to the  
 869     black data points as systematic errors on double-counting correction.

#### 870     **4.12 Input $p_T$ shape**

871     For the efficiency correction, the toy MC simulation have the flat pt input distributions and then  
 872     weight by the pt shape from run10 published 0-10% spectra. As we know that the input publish  
 873     spectra do have some issues, we need to quality the contribution to our final result. So after we  
 874     have the run14 spectra, in principle, we can do iteration for several times to correct the efficiency  
 875     with the new shape. But after we checked one time as shown in Fig. 113, the difference is really  
 876     small, less than 0.2%. So we just ignore this effect.

### 877 4.13 $p_T$ smearing effect

878 The input  $p_T$  smearing function was extracted from the Hijing sample, instead of using from  
 879 Embedding since embedding does not include HFT in tracking. For the efficiency calculation, they  
 880 are obtained from the data-driven simulation. The input Monte Carlo (MC  $p_T$ ) momentum was  
 881 smeared to the reconstructed momentum (RC  $p_T$ ) in the simulation. So for the final efficiency  
 882 calculation, We checked two case to consider this momentum smearing effect. One case is using  
 883 input Monte Carlo (MC)  $p_T$  divide MC  $p_T$  and another case is using the reconstructed momentum  
 884 (RC  $p_T$ ) divide MC  $p_T$ . The comparison result shows from Fig. 114 to Fig. 117. The bottom panel  
 885 shows the double ratios between these two case, as seen the difference is really small which indicate  
 886 this is not a big effect we need to worry. Note here, in our real analysis, we are using RC/MC for  
 887 our efficiency correction.

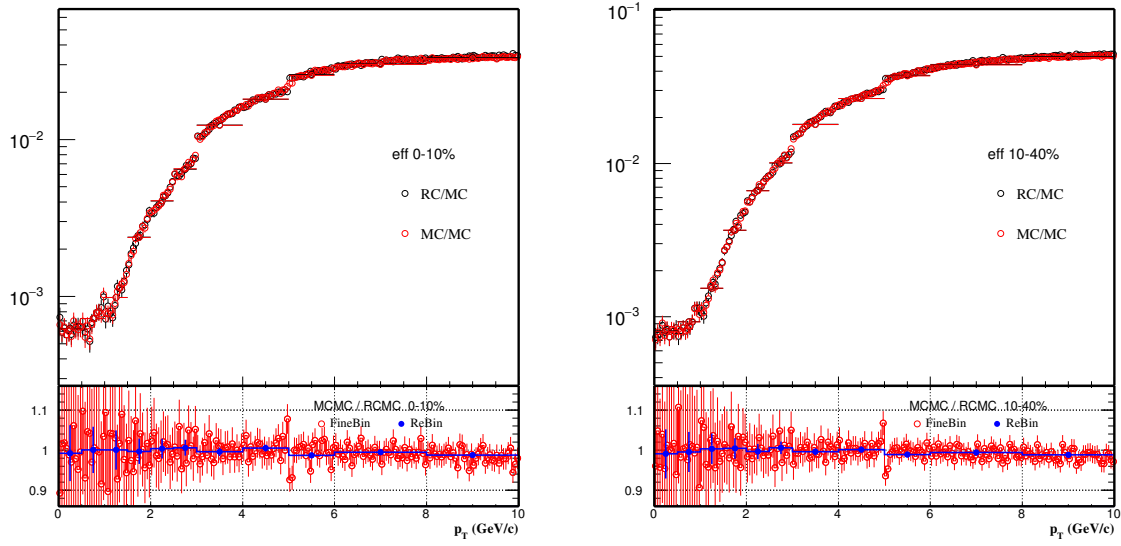


Figure 114:  $D^0$  efficiency comparison between RC/MC and MC/MC in 0-10%.  
 Figure 115:  $D^0$  efficiency comparison between RC/MC and MC/MC in 10-40%.

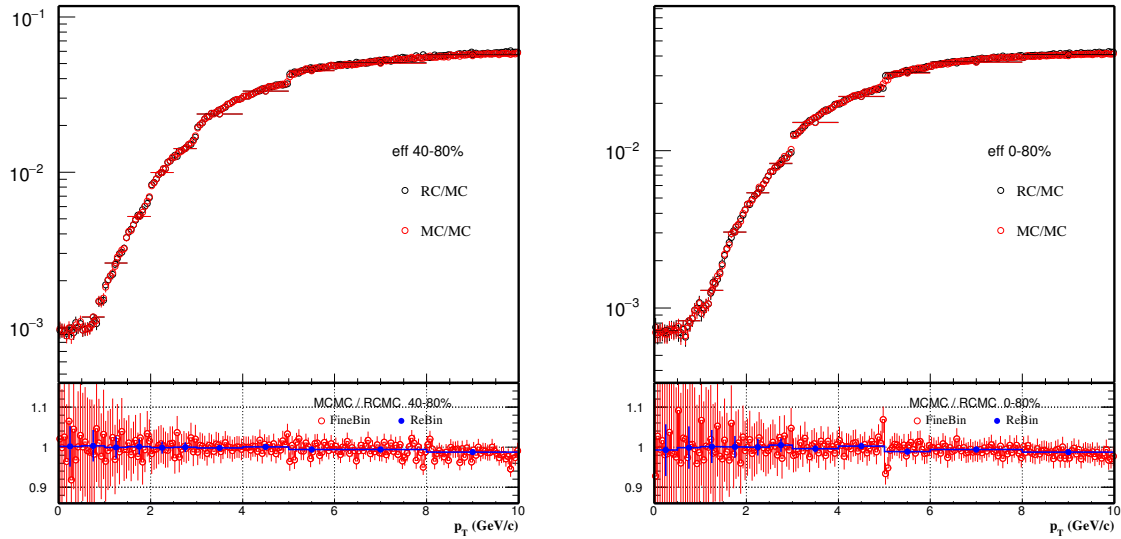


Figure 116:  $D^0$  efficiency comparison between RC/MC and MC/MC in 40-80%.  
 Figure 117:  $D^0$  efficiency comparison between RC/MC and MC/MC in 0-80%.

888 Fig. 118, we also compared the invariant mass distributions between real data and our data-

889 driven simulations in the most central 0-10% collisions at several  $p_T$  range. The signal from real  
 890 data part was after mixevent background subtraction. The result shows reasonable agreement,  
 891 even though we didn't cut the invmass rely on data-driven simulations.

892 Fig. 119 shows the comparison of the momentum smearing effect between Embedding and  
 893 Hijing. As the embedding doesn't have HFT in tracking, the momentum smearing was much worse  
 894 compare to Hijing. Fig. 120 just shows the similar plots as the Fig. 118 but with the smearing  
 895 from Embedding, as clearly see, the  $D^0$  mass from data-driven simulation can not reproduce the  
 896 real data.

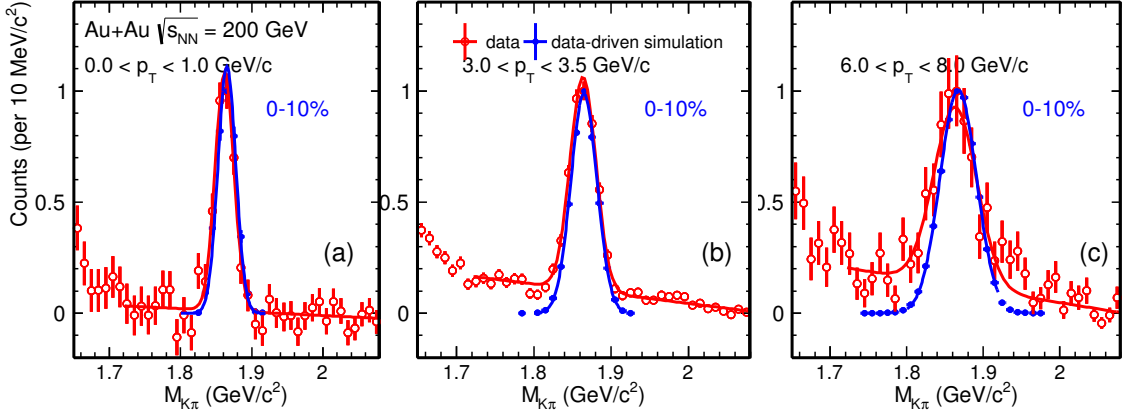


Figure 118: Comparison of invariant mass distributions between real data and data-driven simulation (with Hijing smearing input) for 0-10% in several  $p_T$  range.

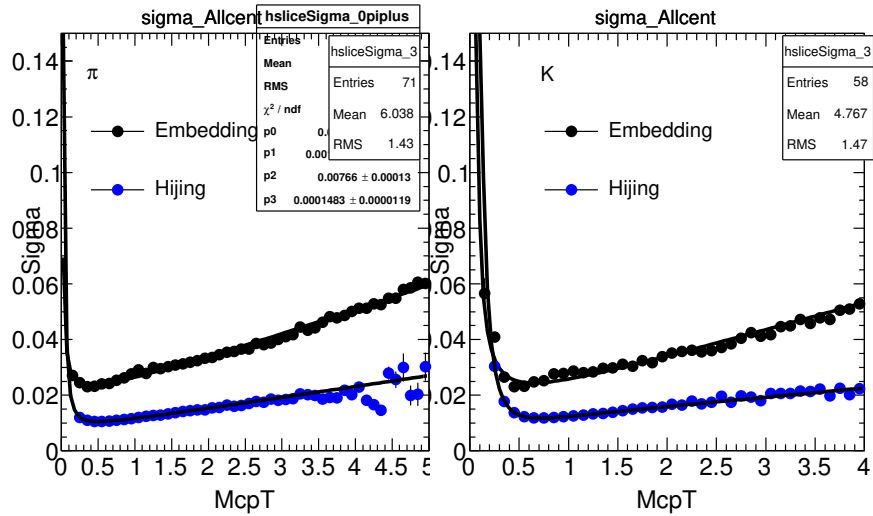


Figure 119: Comparison of momentum resolution between embedding (without HFT in tracking) and Hijing simulation (with HFT tracking).

#### 897 4.14 Lifetime uncertainties effect

898 The  $D^0$  lifetime have some uncertainties from the latest PDG, say 0.3% uncertainties. This could  
 899 potential effect our efficiency calculation especially for the low  $p_T$  part. In order to check this, we  
 900 run through the toyMC simulation with different  $D^0$  lifetime. We varied the decay length from  
 901 129.9  $\mu\text{m}$  to 123.3  $\mu\text{m}$ . After apply all the topological cuts, the final efficiency comparison from  
 902 these two scenarios are shown from Fig. 122 to Fig. 124. The bottom panel shows the double ratios  
 903 between these two case, as seen the difference in high  $p_T$  range is really small which make sense  
 904 and also in the very  $p_T$  the difference is 1-2%. Compare to our current uncertainties form other

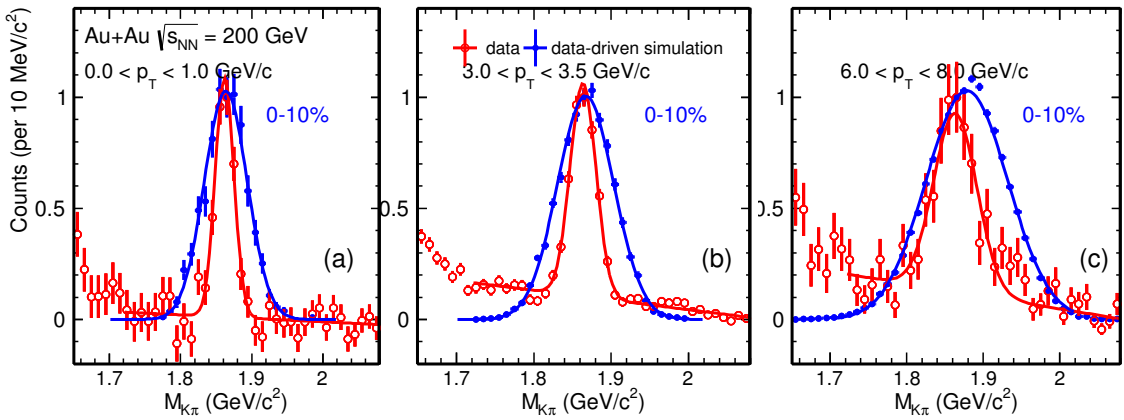


Figure 120: Comparison of invariant mass distributions between real data and data-driven simulation (with Embedding smearing input) for 0-10% in several  $p_T$  range.

sources, this is not a big effect we need to worry. Note here, in our real analysis, we are using the default value from PYTHIA setup.

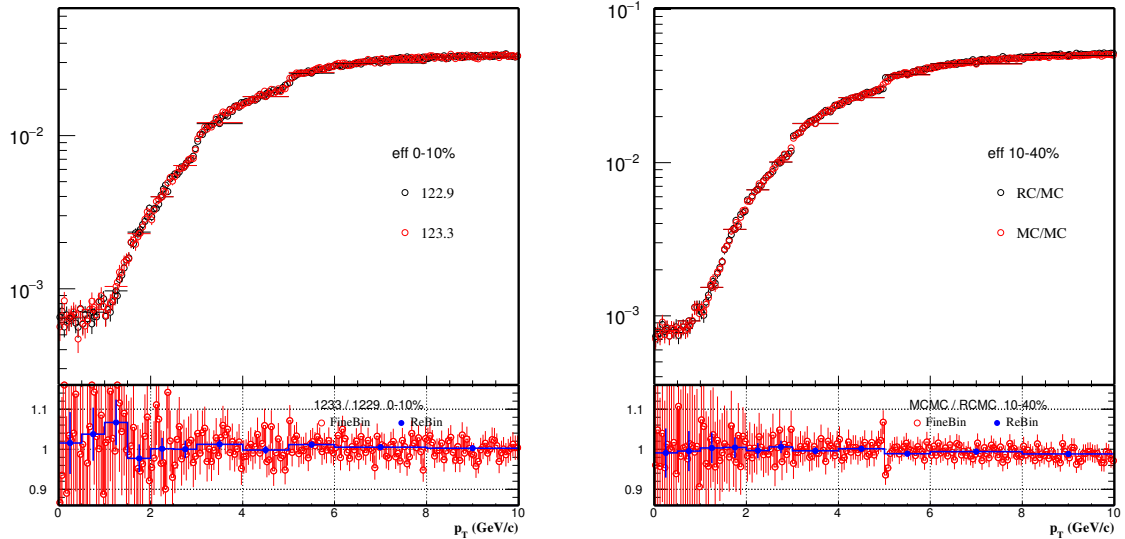


Figure 121:  $D^0$  efficiency comparison between cTau from 129.9 and 133.3 in 0-10%.

Figure 122:  $D^0$  efficiency comparison between cTau from 129.9 and 133.3 in 10-40%.

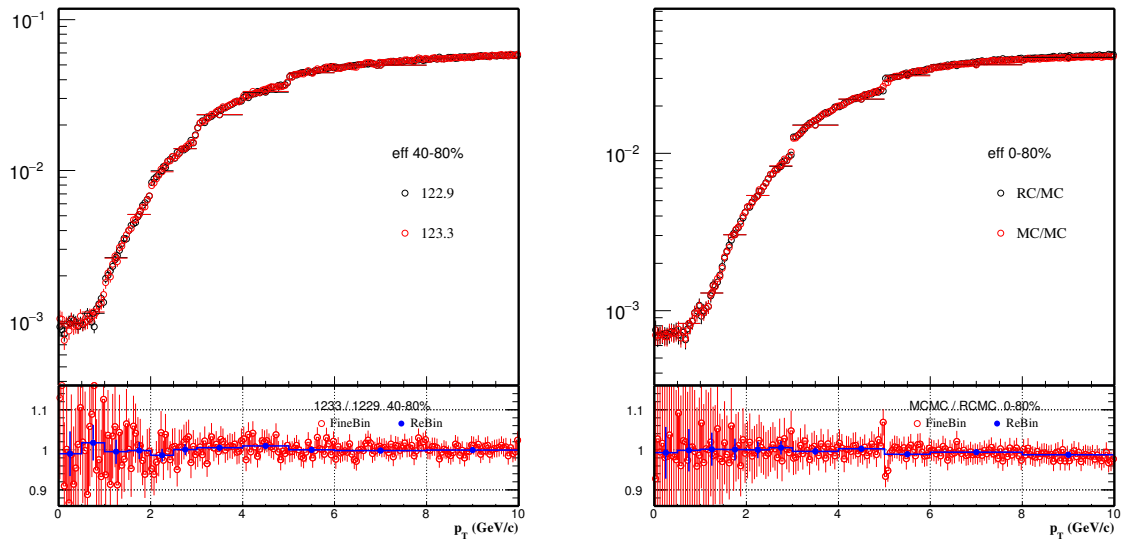


Figure 123:  $D^0$  efficiency comparison between cTau from 129.9 and 133.3 in 40-80%.

Figure 124:  $D^0$  efficiency comparison between cTau from 129.9 and 133.3 in 0-80%.

## 907 5 Systematic Uncertainties

908 The approach for the  $D^0$  spectrum systematic uncertainties are well studied. Several sources can  
 909 be contributed to the uncertainties. The first one is coming from the raw yield extraction. We  
 910 varied the signals extraction methods instead of use fitting method, we tried using binning counting  
 911 methods, tried vary the fitting range, and also tried using like-sign for background to estimate the  
 912 uncertainties for raw yield extraction. And using the maximum deviation to the default value as  
 913 the systematic uncertainty.

914 For the raw yield extraction, currently the central value was from the fitting method. After  
 915 the normalized mixed Event background subtraction, we use a gaus + pol1 function to extract the  
 916 raw signal yield. The statistics error was propagate from the fitting.

917 The binning counting method means after the normalized mixed events background subtraction.  
 918 The residual background and signal distribution was fitted with a gaus+pol1 function to  
 919 determinate the signal width, then the counts within  $3\sigma$  was counted. And the residual back-  
 920 ground was estimated with the sideband method. The statistics errors was propagated accordingly  
 921 and is comparable with the previous fitting method. The same-event likesign method was also  
 922 tried, but as clearly the background fluctuation was larger compared to the mixevent method.  
 923 These raw yield difference from these methods will be contributed to the final systematic source  
 924 which will be discussed in the later section.

925 The second source would be coming from the TPC embedding uncertainties, this one is well  
 926 studied by comparison the nHits and Dca distributions between data and embedding. Here the  
 927 real data iswithout HFT in tracking. This is a self-produced testing sample with the office library  
 928 and chain option. Fig. 127, Fig. 125, Fig. 128 and Fig. 126 show the nHits and Dca comparison  
 929 between real data and embedding for 0-80% centrality. Bottom panels show the double ratio, and  
 930 a fitted line as guidance. As seen, the embedding sample can reproduce the real data reasonable  
 931 well. Then the systematic uncertainties can be estimate by varying the cuts from nHits>20 to  
 932 nHits>25, and Dca<1.0 to Dca<1.5 as Equ. 15.

$$933 \begin{aligned} r_{nHits} &= (nHits > 25)/(nHits > 20)_{data}/(nHits > 25)/(nHits > 20)_{MC} \\ r_{Dca} &= (Dca < 1.0)/(Dca < 1.5)_{data}/(Dca < 1.0)/(Dca < 1.5)_{MC} \end{aligned} \quad (15)$$

934 Then after varying nHits and Dca, the comparison of data and embedding shown as Fig. 129 for  
 935 nHits (left) and Dca (right). Fig. 130 shows the comparison of the HFT Matching ratio due to the  
 936 change of Dca cuts for 0-80% centrality. As seen, due to the change of Dca cut, the contribution  
 937 for Embedding and HFT matching ratio can be canceled out at some pint but not fully canceled,  
 938 So in the final result we decide still include this contribution from Dca. The bottom panels show  
 939 these double ratio. For the  $R_{CP}$  calculations, at some point they are correlated for central and  
 940 peripheral collisions and somehow can be canceled out. So, for the  $R_{CP}$  systematic, we using  
 941  $r_{nHits} - cent/r_{nHits} - peripheral$  to calculate the uncertainties. The nHits, Dca (included) and  
 942 ToFPID (as discussed in the pid part) systematic are added up quadratical for single track. For the  
 943  $D^0$  calculations, the pion and kaon tracks are correlated with the momentum dependence, so we  
 944 run a simple toyMC simulation to convolute the momentum dependence to the  $D^0$  momentum.

945 The next source is by varying the topological cuts and daughter  $p_t$  cuts. The standard TMVA  
 946 cuts, the 50% efficiency and 150% efficiency cuts are calculated, and also the daughter  $p_T$  cuts are  
 947 checked for 300 MeV and 500 MeV beside of the default value 600 MeV. The difference between  
 948 the corrected yield are quoted as the systematic source. Also there is a source coming from the  
 949 double counting and vertex resolution contribution as we discussed in the previous sections.

950 For the data-driven simulation vertex correction part, the vertex correction was applied to all  
 951 the centralities species, even though in the most central and mid-central centralities say 0-20%  
 952 and 20-40% the correction factor is small. We also quote an additional  $\sim 5\%$  difference to capture  
 953 the difference between the pure Hijing and data-driven simulation validation (Fig. 81). The vertex  
 954 systematic uncertainties other middle-central centralities are roughly  $\sim 5\%$ . This additional source  
 955 is kind of conservative since we already using the 50% and 150% efficiency method to calculate the  
 956 systematic source. But it still worth to be conservative. Note here, this 5% systematic source was  
 957 applied to 0-80% where we think this is a general source. Note, the vertex correction factor was  
 958 applied for all the centralities from most central 0-10% to most peripheral 70-80%. The same for  
 959 this general 5% uncertainties source, it was applied to all the centrality species.

960 Note here, for the  $R_{CP}$  calculations since there are correlated uncertainties, so similar as TPC  
 961 part,for the daughter  $p_T$  scan and topological cuts scan uncertainties, we calculate the  $R_{CP}$  for

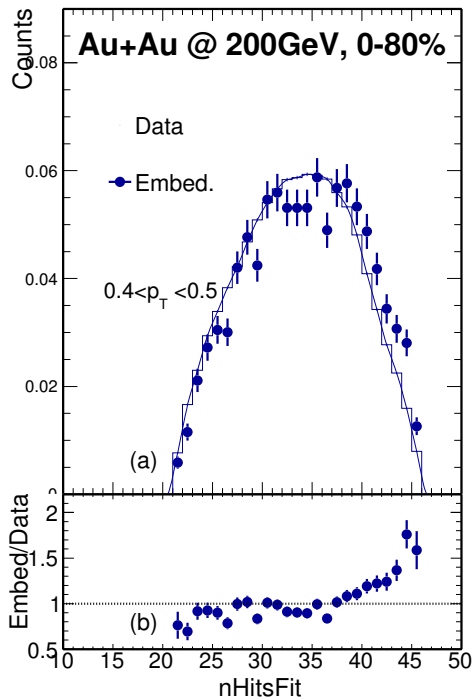


Figure 125: nHits comparison between real data and embedding for 0-80%.

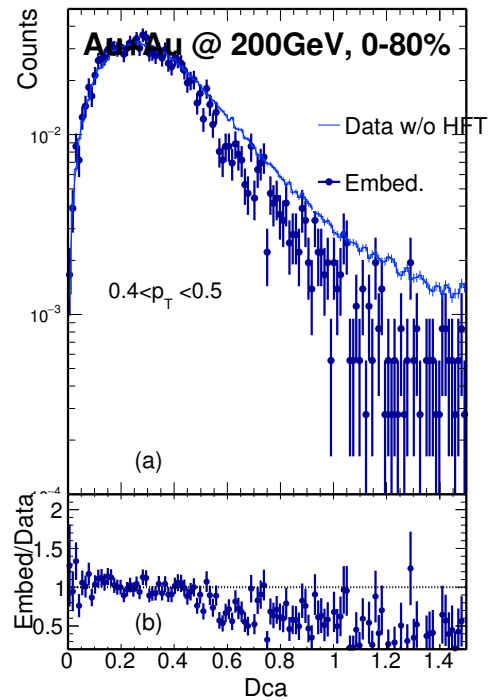


Figure 126: Dca comparison between real data and embedding for 0-80%.

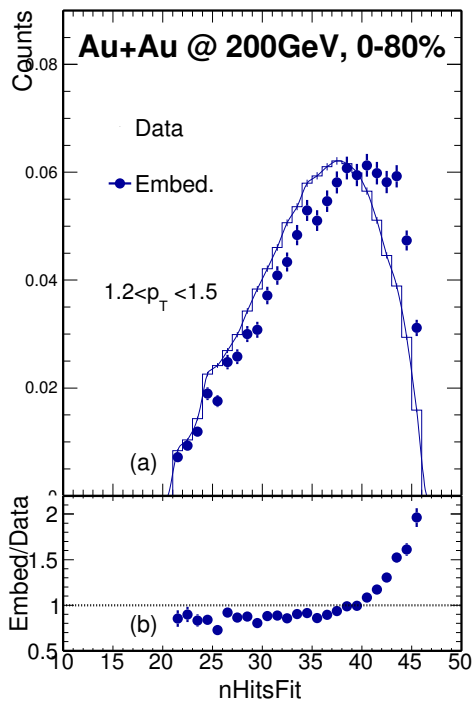


Figure 127: nHits comparison between real data and embedding for 0-80%.

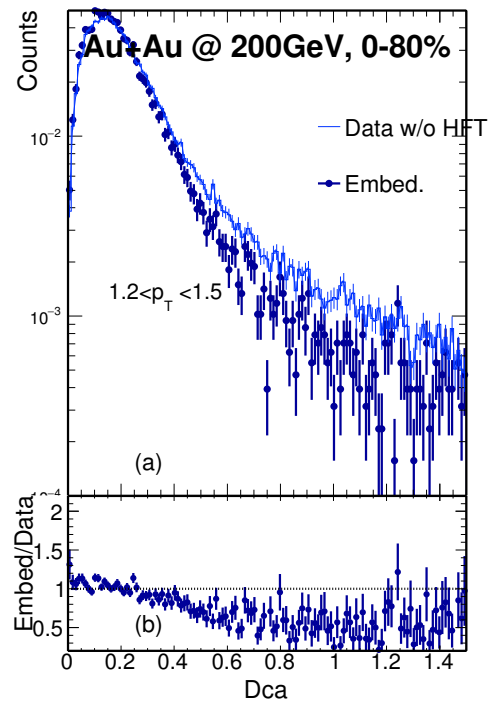


Figure 128: Dca comparison between real data and embedding for 0-80%.

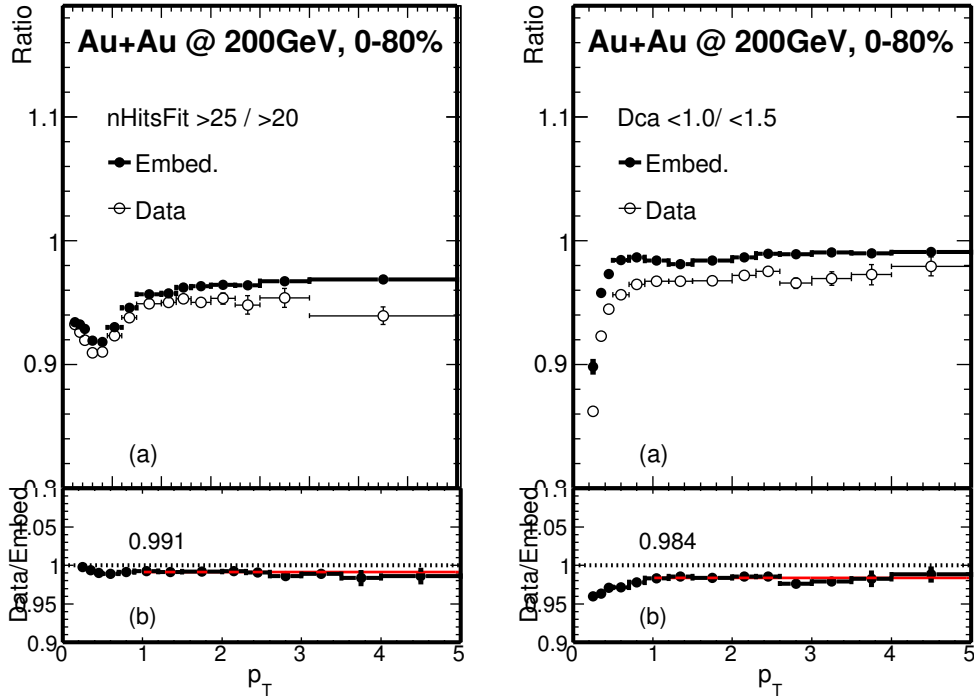


Figure 129: Varying nHit(left) and Dca(right) comparison between real data and embedding for 0-80%

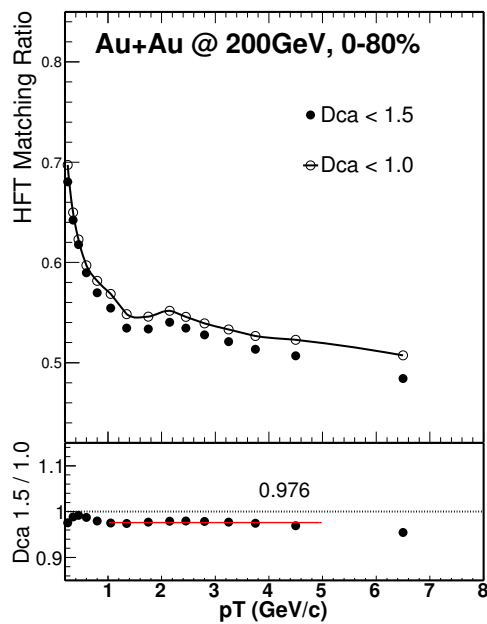


Figure 130: HFT Matching ratio comparison with the Dca cut varying from 1.5 to 1.0 for 0-80%

962 each individual setup or cuts, then quota the difference of  $R_{CP}$  for each cuts as systematic errors.  
 963 For the others, such as yield extraction and vertex resolutions, those uncertainties was quadratically  
 964 added up for  $R_{CP}$  and double counting and PID part are largely canceled out.

965 Note here, for the  $\bar{D}^0/D^0$  ratio calculations, since there are also correlated uncertainties, so  
 966 similar as the  $R_{CP}$  calculation, for the daughter  $p_T$  scan and topological cuts scan uncertainties,  
 967 we calculate the ratio for each individual setup or cuts, then quota the difference of  $\bar{D}^0/D^0$  ratio  
 968 for each cuts as systematic errors. For the yield extraction, those uncertainties were quadratically  
 969 added up for the  $\bar{D}^0/D^0$  ratio. For the double counting and PID part, they are largely canceled  
 970 out.

971 Fig. 131 to Fig. 136 shows the  $D^0$  spectrum different sources contribution in various centralities.  
 972 As we see, the systematic uncertainties is quite small in the most of the  $p_T$  range except some of  
 973 the  $p_T$  ranges due to the limited statistics and large contribution from yield extraction.

974 Fig. 137 to Fig. 140 shows the  $D^0$  Rcp with 60-80% as baseline systematic uncertainties from  
 975 different sources contribution in various centralities.

976 Note here, during the pwg review. We do find some addition uncertainties source from TPC  
 977 Embedding part. The main reason is that from real data, an inefficiency TPC sector was identified  
 978 from the Jpsi analysis, which will have the same effect for  $D^0$  analysis. But it was not properly  
 979 reflected in the Embedding.

980 [http://www.star.bnl.gov/protected/heavy/marr/paper/Run14\\_AuAu200\\_Jpsi/AnalysisNote/JpsiRaa\\_AN\\_v1.pdf](http://www.star.bnl.gov/protected/heavy/marr/paper/Run14_AuAu200_Jpsi/AnalysisNote/JpsiRaa_AN_v1.pdf)

982 From the Jpsi analysis note, Fig. 64 and Fig. 65. If we take an extreme case, say the efficiency  
 983 drop from 0.03 to 0.02. So the average contribution would be  $(1/24) * (1/3) \sim 1.4\%$ . With this  
 984 simple and quick estimation, we quote it as an additional systematic source.

985 note here, during the pwg review, there is an additional uncertainties (2%) from the secondary  
 986 particles was added. The details can be found in the section of secondary contribution 4.9.

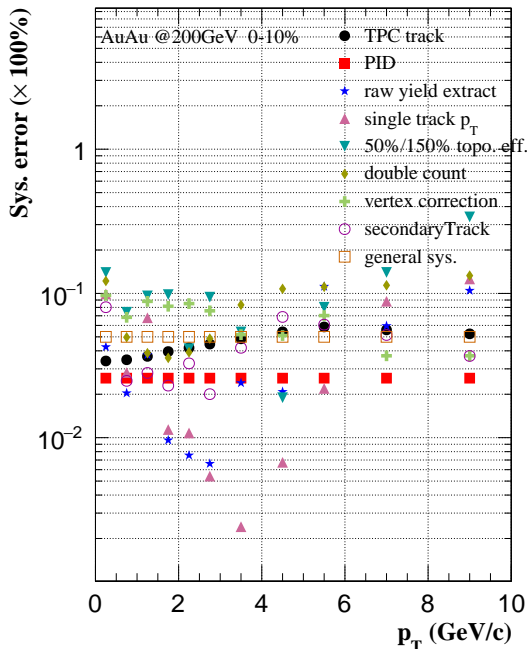


Figure 131: Systematic uncertainties from different sources for 0-10% spectra. Note here, the 5% vertex correction quoted here was not exactly the vertex correction but the overall 5% uncertainties for the data-driven simulation.

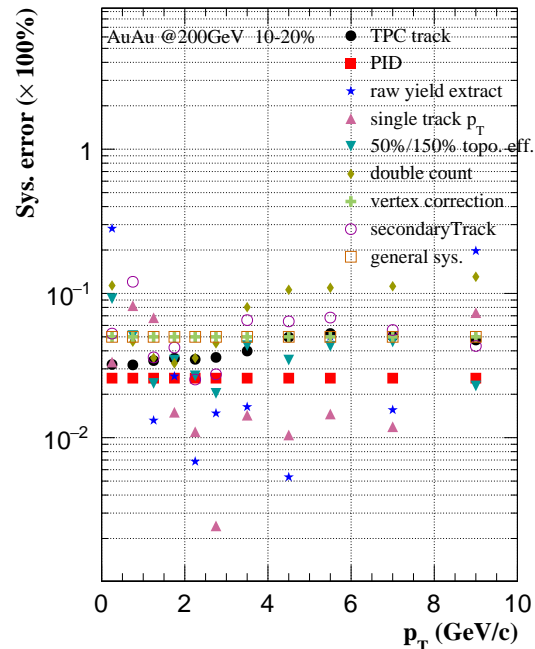


Figure 132: Systematic uncertainties from different sources for 10-20% spectra. Note here, the 5% vertex correction quoted here was not exactly the vertex correction but the overall 5% uncertainties for the data-driven simulation.

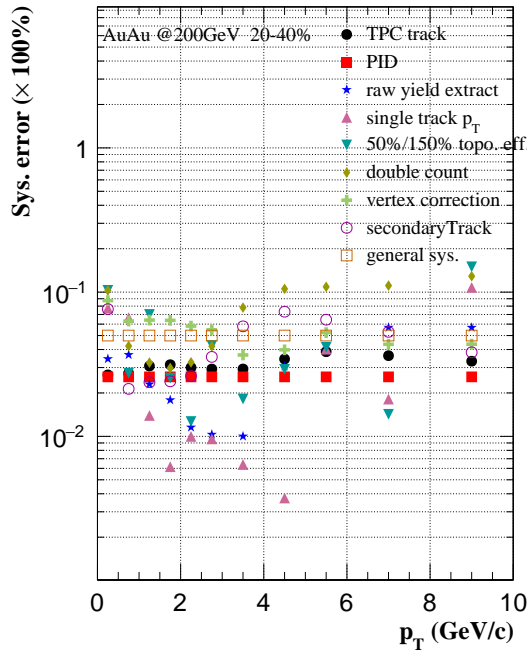


Figure 133: Systematic uncertainties from different sources for 20-40% spectra.

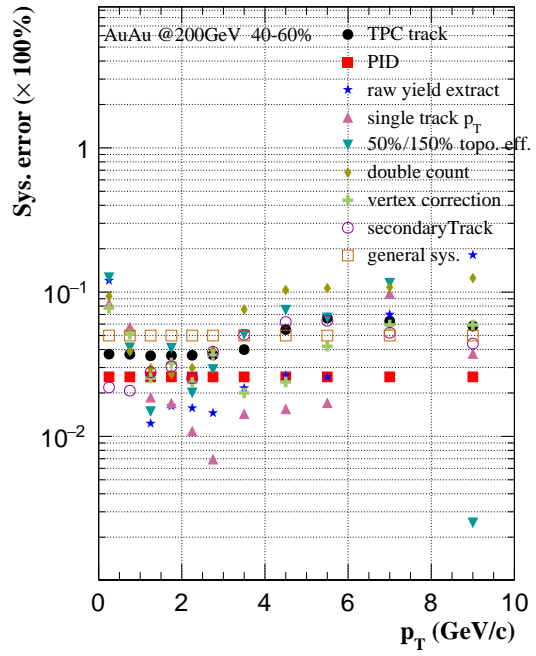


Figure 134: Systematic uncertainties from different sources for 40-60% spectra.

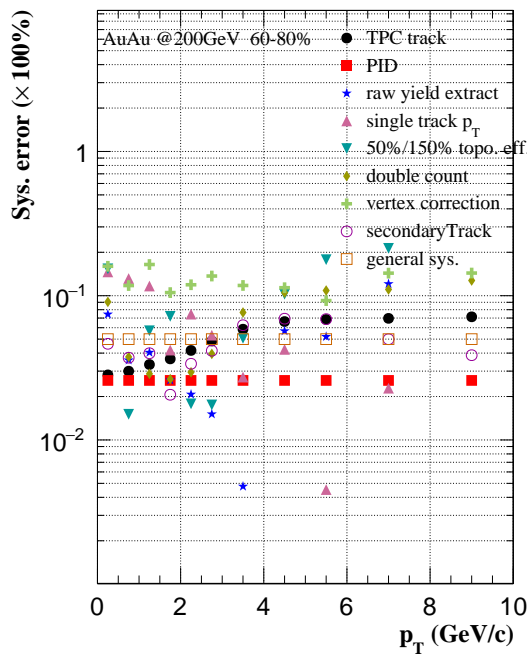


Figure 135: Systematic uncertainties from different sources for 60-80% spectra.

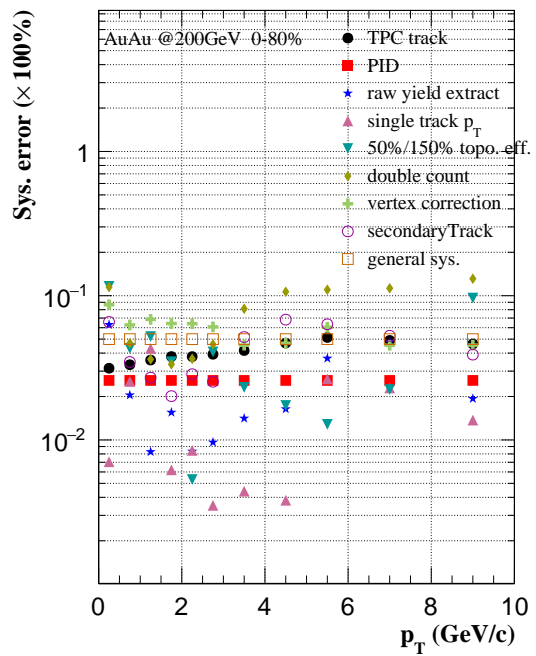


Figure 136: Systematic uncertainties from different sources for 0-80% spectra.

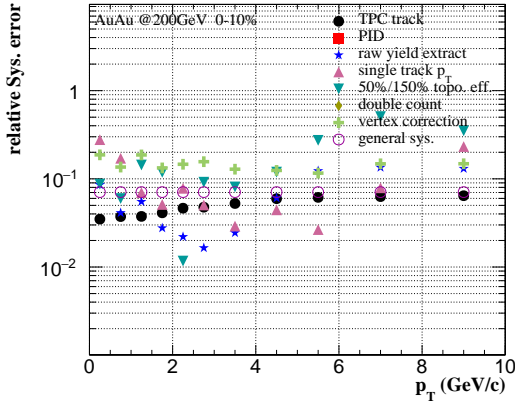


Figure 137: Systematic uncertainties from different sources for 0-10% Rcp as 60-80% as baseline.

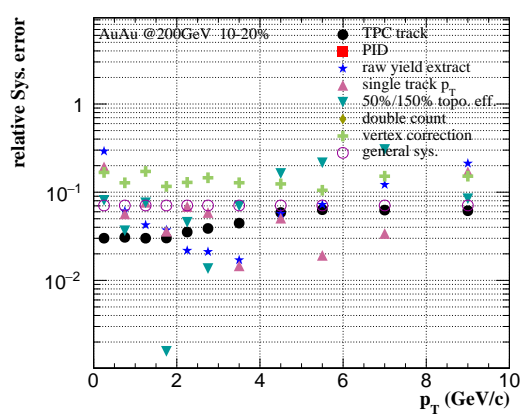


Figure 138: Systematic uncertainties from different sources for 10-20% spectra.

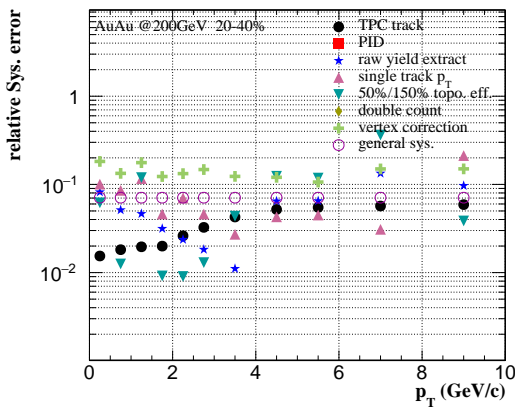


Figure 139: Systematic uncertainties from different sources for 20-40% Rcp as 60-80% as baseline.

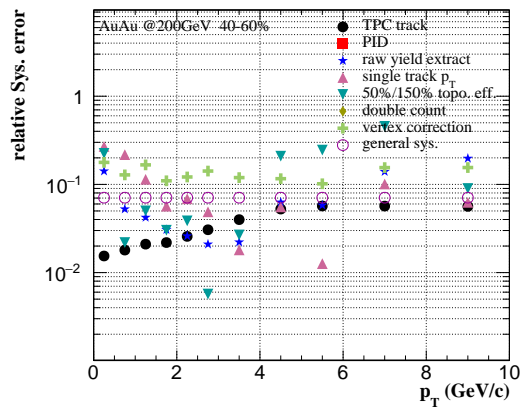


Figure 140: Systematic uncertainties from different sources for 40-60% Rcp as 60-80% as baseline.

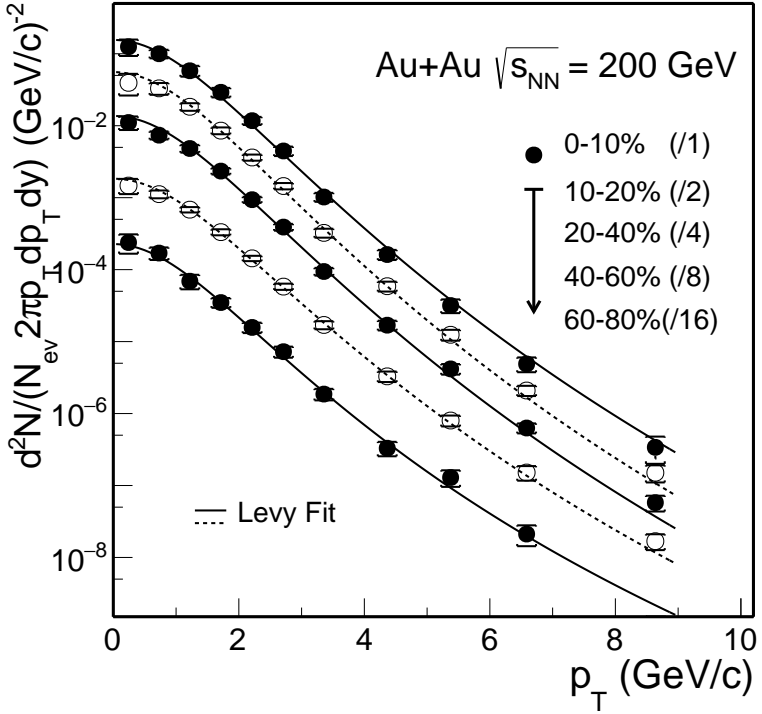


Figure 141:  $D^0$  invariant yield at mid-rapidity ( $|y| < 1$ ) vs. transverse momentum for different centrality classes in Au + Au collisions at  $\sqrt{s_{\text{NN}}} = 200$  GeV. Error bars (not visible for many data points) indicate statistical uncertainties and brackets depict systematical uncertainties. Global systematic uncertainties in  $B.R.$  and  $N_{\text{bin}}$  are not plotted. Solid and dashed lines depict Levy function fits.

## 6 Results and Discussion

### 6.1 $p_T$ Spectra and Integrated Yields

Figure 141 shows the efficiency corrected  $D^0$  invariant yield at mid-rapidity ( $|y| < 1$ ) vs. transverse momentum ( $p_T$ ) in 0–10%, 10–20%, 20–40%, 40–60%, 60–80% and 0–80% Au + Au collisions at  $\sqrt{s_{\text{NN}}} = 200$  GeV.  $D^0$  invariant spectra in some centrality bins are arbitrarily scaled with factors indicated on the plot for clarity. Dashed lines depict fits to these spectra with the following Levy function

$$\frac{d^2N}{2\pi p_T dp_T dy} = \frac{1}{2\pi} \frac{dN}{dy} \frac{(n-1)(n-2)}{nT(nT+m_0(n-2))} \left(1 + \frac{\sqrt{p_T^2 + m_0^2} - m_0}{nT}\right)^{-n} \quad (16)$$

where  $m_0$  is the  $D^0$  particle mass and  $\frac{dN}{dy}$ ,  $T$  and  $n$  are the free parameters. The Levy function fit shows nice descriptions to the  $D^0$  spectra in all centrality bins up to 8 GeV/c.

After got the efficiency corrected  $p_T$  spectra, the integrated  $D^0$  yield was also obtained as shown in the next equation.

$$d\sigma = \sum \frac{dN_i}{dy} \frac{1}{Events} \frac{1}{N_{\text{bin}}} * 42e^3 * 0.0388 \quad (17)$$

Fig.142 shows the integrated cross section per nucleon-nucleon collision in different centralities.

### 6.2 Collectivity

#### 6.2.1 $m_T$ Spectra

Transverse mass spectra have often used to study the collectivity of produced hadrons in heavy-ion collisions. Figure 143 shows the  $D^0$  invariant yield at mid-rapidity ( $|y| < 1$ ) vs. transverse kinetic energy ( $m_T - m_0$ ) for different centrality classes in Au + Au collisions at  $\sqrt{s_{\text{NN}}} = 200$  GeV, where

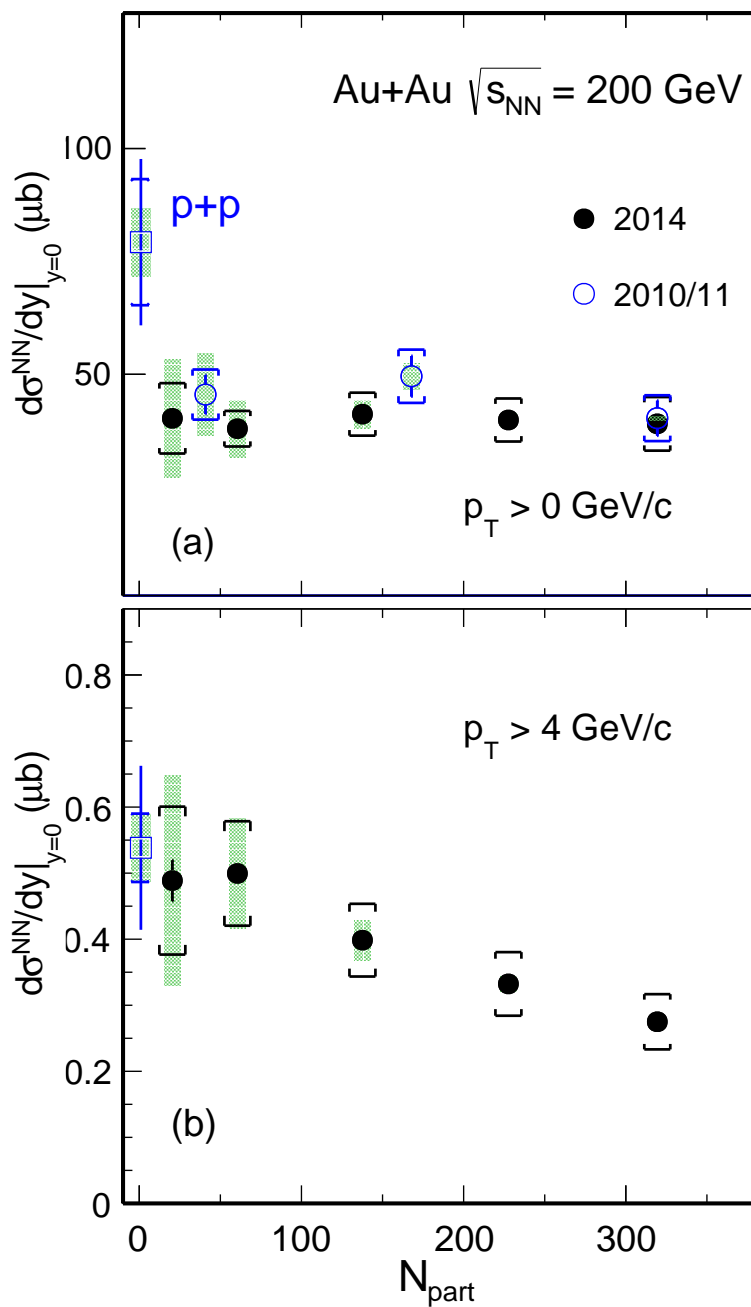


Figure 142:  $D^0$  integrated cross sections per nucleon-nucleon collision at mid-rapidity for  $p_T > 0$  and  $p_T > 4$  GeV/c regions as a function of centrality  $N_{\text{bin}}$ .

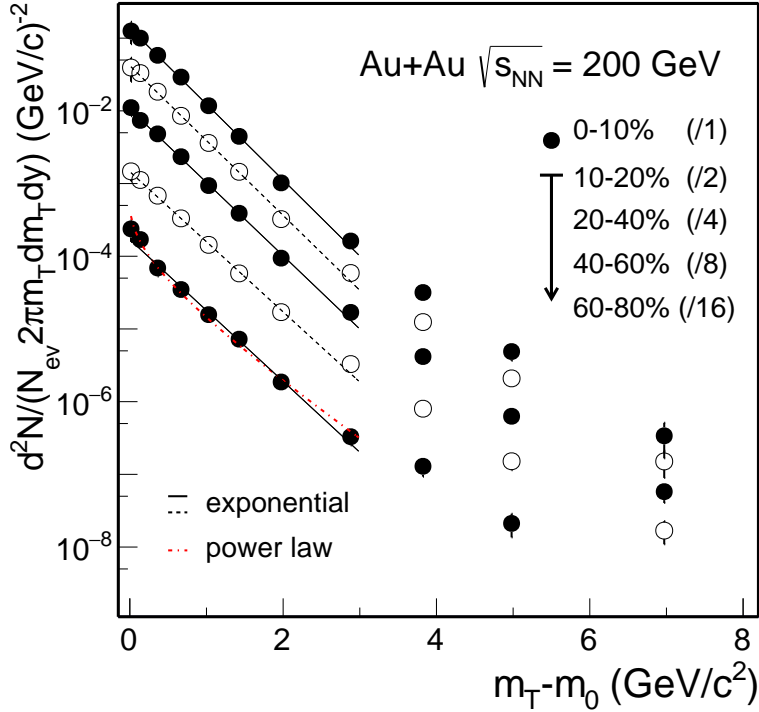


Figure 143:  $D^0$  invariant yield at mid-rapidity ( $|y| < 1$ ) vs. transverse kinetic energy ( $m_T - m_0$ ) for different centrality classes in Au + Au collisions at  $\sqrt{s_{NN}} = 200$  GeV. Error bars (not visible for many data points) indicate statistical uncertainties and brackets depict systematical uncertainties. Global systematic uncertainties in  $B.R.$  and  $N_{bin}$  are not plotted. Solid and dashed black lines depict exponential function fits and the dot-dash line depict a power-law function fit to the spectrum in 60–80% centrality bin.

1006  $m_T = \sqrt{p_T^2 + m_0^2}$  and  $m_0$  is the  $D^0$  meson mass. Solid and dashed black lines depict exponential  
1007 function fits to various centrality bins up to  $m_T = 3m_0$  and the fit function is shown below

$$\frac{d^2N}{2\pi m_T dm_T dy} = \frac{dN/dy}{2\pi T_{eff}(m_0 + T_{eff})} e^{-(m_T - m_0)/T_{eff}} \quad (18)$$

1009 A power-law function (shown below) is also used to fit the spectrum in 60–80% centrality bin.

$$\frac{d^2N}{2\pi p_T dp_T dy} = \frac{dN}{dy} \frac{4(n-1)(n-2)}{2\pi(n-3)^2 \langle p_T \rangle^2} \left(1 + \frac{2p_T}{\langle p_T \rangle(n-3)}\right)^{-n} \quad (19)$$

1011 where  $dN/dy$ ,  $\langle p_T \rangle$ , and  $n$  are three free parameters.

1012 The power-law function fit shows a good description ( $x^2/ndf = 4.973/5$  for power-law while  
1013 the exponential gives  $x^2/ndf = 4.717/6$  with the fit range from 0 – 3) to the 60–80% centrality  
1014 data indicating the  $D^0$  meson production in this peripheral bin is close to the perturbative QCD  
1015 feature. The  $D^0$  meson spectra in more central collisions can be well described by the exponential  
1016 function fit suggesting the  $D^0$  mesons have gained collectivity in the medium evolution in these  
1017 collisions.

1018 Figure 144 shows the  $m_T$  spectra slope parameter  $T_{eff}$  (obtained from the exponential fit  
1019 described above) vs. collision centrality. Statistical and point-to-point systematic uncertainties,  
1020 but no global systematic uncertainties, are added quadratically when performing the exponential fit.  
1021 Therefore uncertainties shown in this plot are the total uncertainties on this fit parameter. The  
1022 obtained  $T_{eff}$  parameter increases from peripheral to central collisions, suggesting more collectivity  
1023 that  $D^0$  mesons gain in more central collisions.

1024 The obtained slope parameter  $T_{eff}$  for  $D^0$  mesons is compared to other light and strange hadrons  
1025 measured at RHIC. Figure 147 summarizes the slope parameter  $T_{eff}$  for various identified hadrons  
1026 ( $\pi^\pm, K^\pm, p/\bar{p}, \phi, \Lambda, \Xi^-, \Omega, D^0$  and  $J/\psi$ ) in central Au + Au collisions at  $\sqrt{s_{NN}} = 200$  GeV. All fits are  
1027 performed up to  $m_T = 3m_0$ .

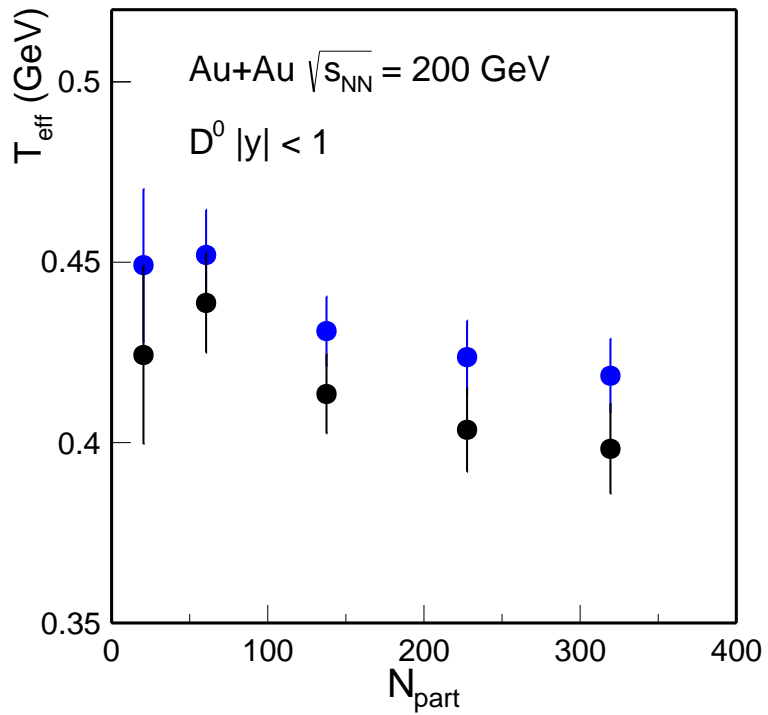


Figure 144:  $T_{eff}$  vs.  $N_{bin}$  for different centrality classes in Au + Au collisions at  $\sqrt{s_{NN}} = 200$  GeV.

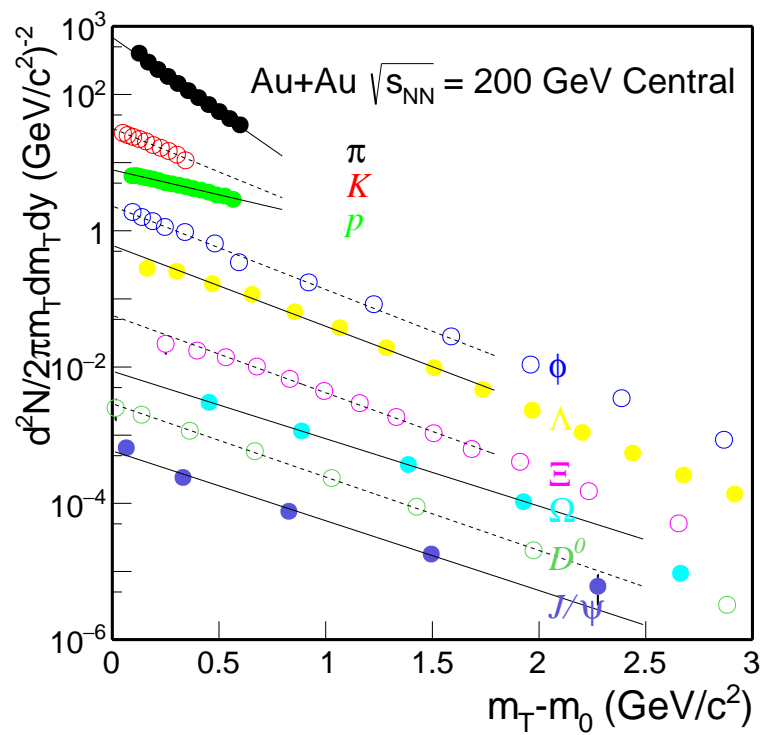


Figure 145:  $D^0$  invariant yield at mid-rapidity ( $|y| < 1$ ) vs.  $(m_T - m_0)$  for central collisions in Au + Au collisions at  $\sqrt{s_{NN}} = 200$  GeV.

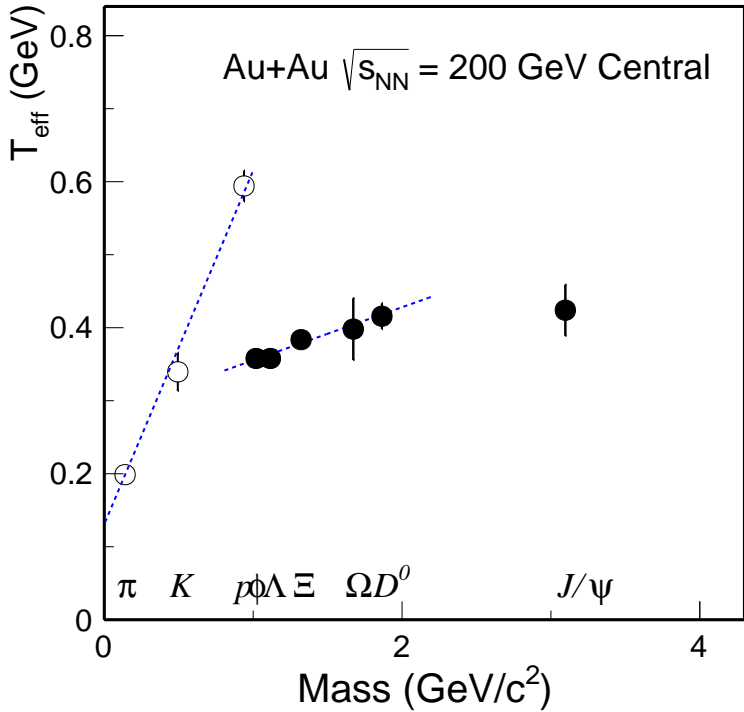


Figure 146:  $T_{\text{eff}}$  for different particles in central Au + Au collisions at  $\sqrt{s_{\text{NN}}} = 200 \text{ GeV}$ .

### 6.2.2 Blast-wave fit

Blast-wave model is extensively used to study the particle kinetic freeze-out properties.

Assuming a hard-sphere uniform density particle source with a kinetic freeze-out temperature  $T_{\text{kin}}$  and a transverse radial flow velocity  $\beta$ , the particle transverse momentum spectral shape is given by :

$$\frac{dN}{p_T dp_T} = \frac{dN}{m_T dm_T} \propto \int_0^R r dr m_T I_0\left(\frac{p_T \sinh \rho}{T_{\text{kin}}}\right) K_1\left(\frac{m_T \cosh \rho}{T_{\text{kin}}}\right) \quad (20)$$

where  $\rho = \tanh^{-1} \beta$ , and  $I_0$  and  $K_1$  are the modified Bessel functions. The flow velocity profile is taken as

$$\beta = \beta_S \left(\frac{r}{R}\right)^n \quad (21)$$

where  $\beta_S$  is the maximum velocity at the surface and  $r/R$  is the relative radial position in the thermal source. The choice of  $R$  only affects the overall spectrum magnitude while the spectrum shape constrains the three free parameters  $T_{\text{kin}}$ ,  $\langle \beta \rangle = 2/(2+n)\beta_S$  and  $n$ .

To account for the degree of non-equilibrium, Tsallis statistics has been introduced into the Blast-wave model with an additional parameter  $q - 1$ , and the Blast-Wave distribution can be modified as

$$\frac{dN}{m_T dm_T} \propto m_T \int_{-Y}^{+Y} \cosh(y) dy \int_{-\pi}^{+\pi} d\phi \int_0^R r dr \left(1 + \frac{q-1}{T_{\text{kin}}} (m_T \cosh(y) \cosh(\rho) - p_T \sinh(\rho) \cos(\phi))\right)^{-\frac{1}{q-1}} \quad (22)$$

In the limit of  $q \rightarrow 1$ , the TBW distribution returns to the regular Blast-Wave one. The new Tsallis Blast-Wave (TBW) model has been used to fit the RHIC light and strange hadron spectra and it shows nice description of these particle spectra up to 3 GeV/c.

The TBW fit is also implemented on  $D^0$  to account the degree of non-equilibrium in a system. Results show similar trend as BW, the most central data point locate at the larger  $\langle \beta \rangle$  value. While the  $(q-1)$  parameter in TBW, which characterizes the degree of non-equilibrium in a system, shows

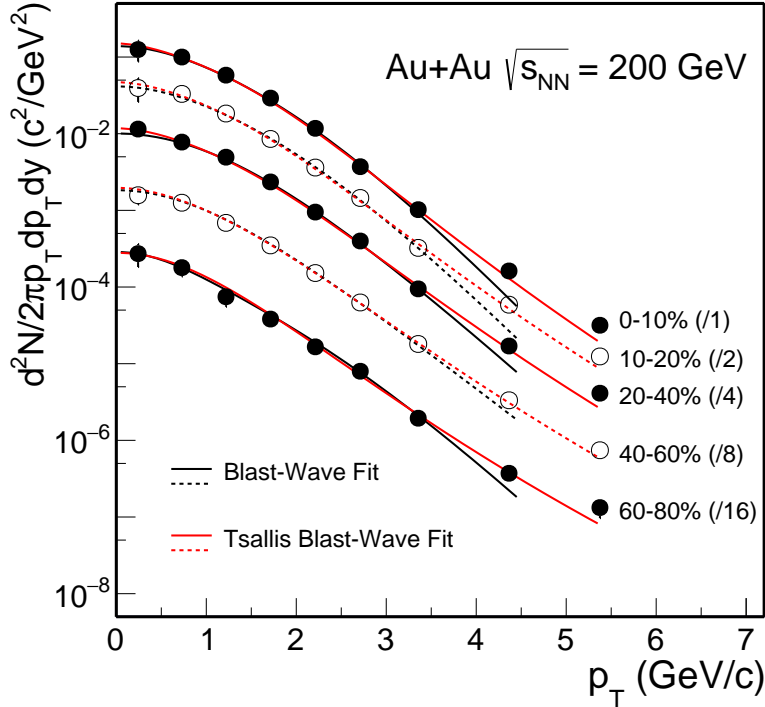


Figure 147:  $D^0$  invariant yield at mid-rapidity ( $|y| < 1$ ) vs. transverse momentum for different centrality classes in Au + Au collisions at  $\sqrt{s_{NN}} = 200$  GeV. Solid and dashed black lines depict Blast-Wave function fits.

a decrease trend with the increase centralities. The system is towards to thermalization with the centrality.

### 6.3 Nuclear Modification Factor - $R_{CP}$ and $R_{AA}$

To calculate the  $R_{AA}$ , we need the p+p baseline measurements. Here, the baseline measurement was from STAR Run09 p+p results. It was combined of  $D^0$  and  $D^*$  measurement with consider the  $p_T$  dependence of the  $D^*/D^0$  ratio. It's kind of different compare to the previous publish result, but we just keep the same as the new run10/11 PRL erratum to select the p+p baseline. Details please find in the erratum note. Here we just want to clarify how the baseline and systematic uncertainty was chosen and calculated.

The central value for p+p result was from the fitted Levy function. As can see, the levy function can describe the measured data quite well. In the whole  $p_T$  range, we quote the  $1\sigma$  band from the fitting as the systematic uncertainties source. Due to the constrains from the function shape, the  $1\sigma$  band is kind of smaller compare to the data uncertainties in the measured pt range, but the error band in the unmeasured range is huge. For the unmeasured  $p_T$  range, say  $p_T < 1\text{GeV}$  and  $> 6\text{ GeV}$ , together with the measured range, we have a consistent procedures to add an additional source from the different fitting functions. This is kind of systematic source from our limited knowledge of the spectra shapes. As can see we also have run12 preliminary results can be used as guidance spectra. In the low  $p_T$  and high  $p_T$  region ( $<1\text{GeV}$  and  $>6\text{GeV}$ ) together with the measured range ( $1\text{GeV} < p_T < 6\text{GeV}$ ), we quote the difference between levy and powlaw to consider as the additional systematic uncertainty source. The plots shown in Fig. 149 and Fig. 150 are the p+p base lines. Note here The TBW fit parameters were obtained from fitting with strangeness particle spectra in peripheral 60-80% and  $D^0+D^*$  in p+p together. And the TBW fit is just for a check and not included in the final results.

Fig. 151 and Fig. 152 are the p+p spectra divided to the levy functions. Red points were from run9 publish result while the Black ones are from run12. The band present the  $1\sigma$  fitting uncertainty for Fig. 151 while Fig. 151 also including the additional systematic source from other functions as described above.

[https://www.star.bnl.gov/protected/heavy/xgn1992/paper/D0spectra/comments/180426\\_](https://www.star.bnl.gov/protected/heavy/xgn1992/paper/D0spectra/comments/180426_)

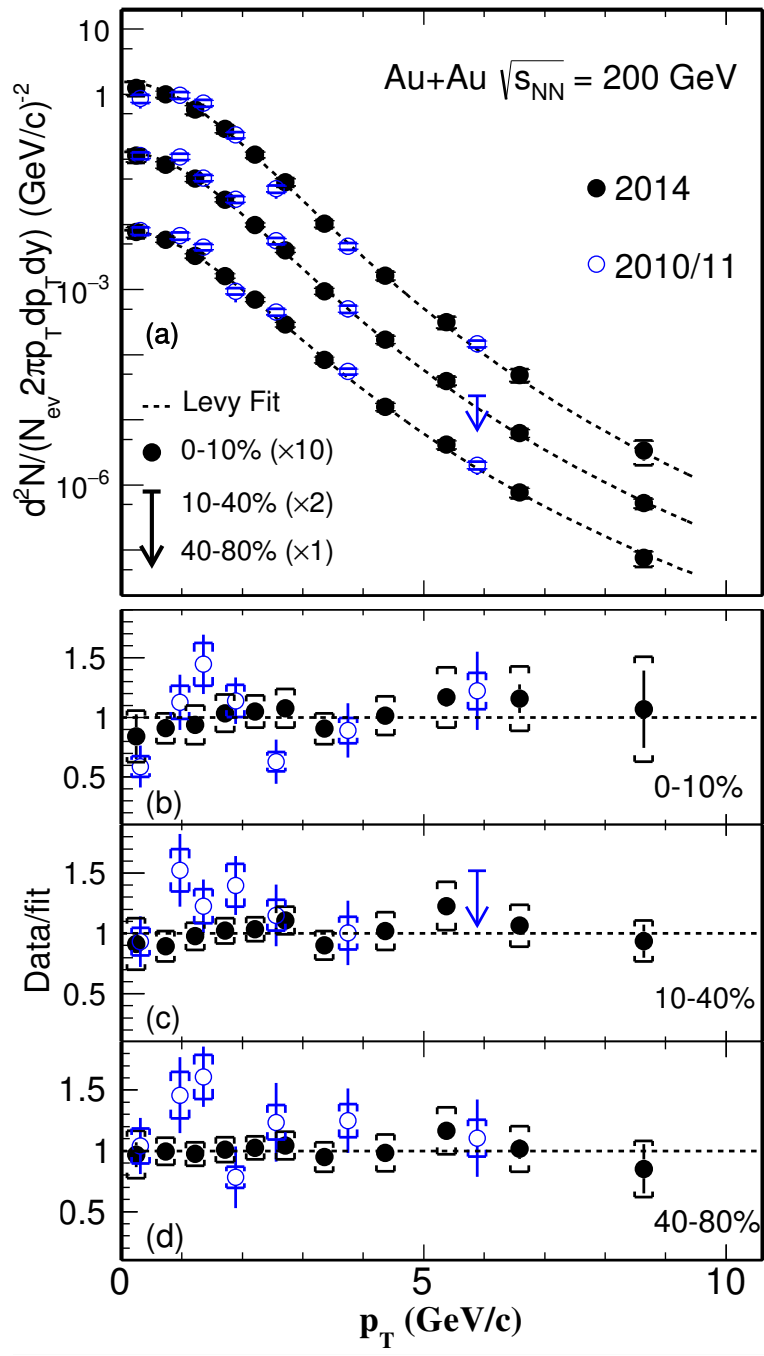


Figure 148:  $D^0$  spectra compare with the run10/11 for different centrality classes in Au + Au collisions.

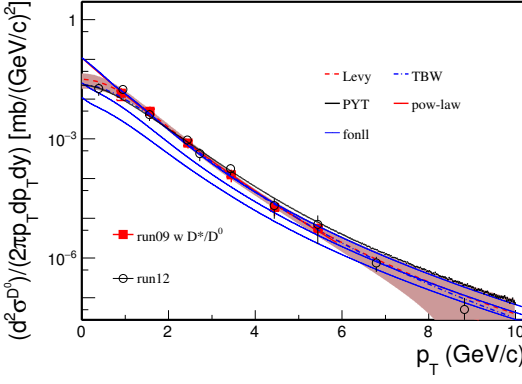


Figure 149: Run09  $D^0$  and  $D^*$  from p+p collisions fitted with the levy function, power law function, Blast Wave function (for check, exclude for the final result), PYTHIA shape and also FONLL shape used for the baseline and systematic uncertainty calculations.

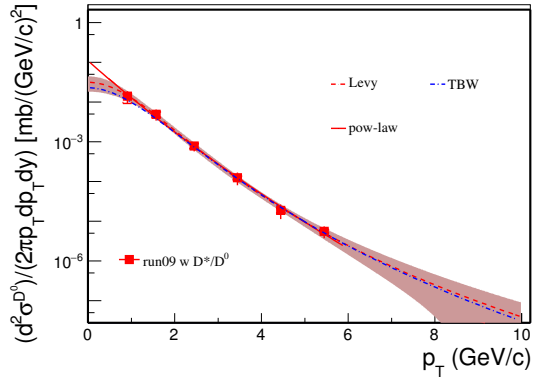


Figure 150: Run09  $D^0$  and  $D^*$  from p+p collisions fitted with the levy function, power law function, Blast Wave function (for check, exclude for the final result) which is actually used for the systematic uncertainty calculations.

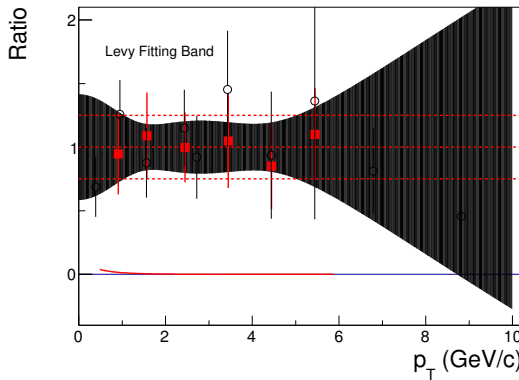


Figure 151: Run09  $D^0$  and  $D^*$  (red) run12 (black) from p+p collisions divided to the levy function. The band present the  $1\sigma$  fitting uncertainty.

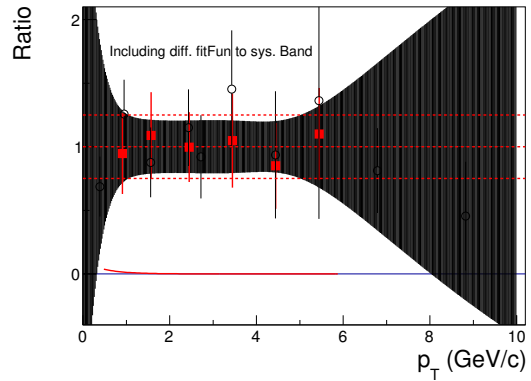


Figure 152: Run09  $D^0$  and  $D^*$  (red) run12 (black) from p+p collisions divided to the levy function. The band present the  $1\sigma$  fitting uncertainty plus the additional systematic source from other functions as described above.

1079 After the baseline was processed, another question is how to propagate the AuAu uncertainties  
 1080 and pp baseline uncertainties to the final  $R_{AA}$  uncertainties. Basically, there is an assumption here  
 1081 is that the two uncertainties from Au+Au and p+p follows the Gaussian distribution. Then what  
 1082 we did is simple, we just randomly sampling those two p+p and Au+Au distributions with a large  
 1083 samples, then calculation each  $R_{AA}$  values and extract the  $R_{AA}$  distributions. Then cumulated  
 1084 the  $1\sigma$  ( $\sim 68\%$ ) range, and quota as the as-systematic uncertainties.

1085 The slide for this study can be found here,

[https://www.star.bnl.gov/protected/heavy/xgn1992/paper/D0spectra/comments/180430\\_GPC\\_RAA\\_sys.pdf](https://www.star.bnl.gov/protected/heavy/xgn1992/paper/D0spectra/comments/180430_GPC_RAA_sys.pdf)  
[https://www.star.bnl.gov/protected/heavy/xgn1992/paper/D0spectra/comments/180505\\_GPC\\_RAA\\_sys\\_GX.pdf](https://www.star.bnl.gov/protected/heavy/xgn1992/paper/D0spectra/comments/180505_GPC_RAA_sys_GX.pdf)  
[https://www.star.bnl.gov/protected/heavy/xgn1992/paper/D0spectra/comments/180507\\_GPC\\_RAA\\_sys\\_GX.pdf](https://www.star.bnl.gov/protected/heavy/xgn1992/paper/D0spectra/comments/180507_GPC_RAA_sys_GX.pdf)

1092 We also compared with another calculates which directly calculate the RAA upper and lower  
 1093 limit and quota as the systematic uncertainties. In the above link, when the p+p uncertainties  
 1094 are under control, these two method gives a consistent results, but when the p+p uncertainties  
 1095 are larger (say  $> 50\%$ ) they show visible difference. So, note here, in our case, except for the

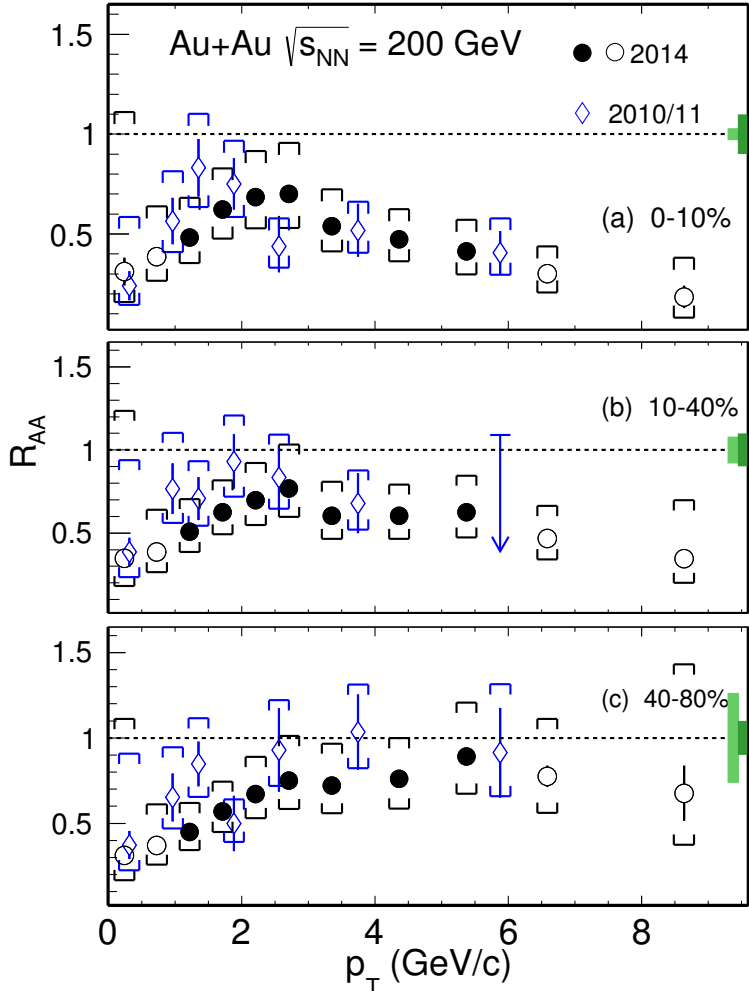


Figure 153:  $D^0 R_{AA}$  with the run9 p+p spectrum Ref.[Phys.Rev.D 86(2012)72013] as the reference for different centrality classes in Au + Au collisions.

first pt bin, we choose the method1 (which is the toyMc sampling method) to calculate the RAA uncertainties. For the first pt bin, since the second method give a more reasonable result (which relative larger uncertainties), we use method2 for that first pt bin. Also the AuAu uncertainties are calculate from the integrated cross-section.

Fig. 155 shows the calculated  $R_{CP}$  for several different centralities including 0-10%, 10-20%, 20-40% and 40-60%, here the base line is the most peripheral collisions 60-80%. In the top panel, the band around unity was the vertex contribution for the systematic uncertainties from the most peripheral collisions at 60-80%, these contribution also applied for the other  $R_{CP}$  centrality species. As a comparison, there are also three samples shown for pions,  $K_s$  and  $\phi$  in the top 10% centrality. Bottom panels show the similar  $R_{CP}$  but for the other centralities.

Fig. 156 shows the similar  $R_{CP}$  for different centralities as Fig. 155, but the base line here is change to 40-80% centralities. The band around unity in the top panel was the vertex contribution for the systematic uncertainties from 40-80% centralities, also applied to the other bottom  $R_{CP}$  centrality species. As a comparison, pions,  $K_s$  and  $\phi$  in several centralities are plotted on the correlated panel.

#### 6.4 $\bar{D}^0$ and $D^0$ spectra and double ratio

Fig. 160 shows the  $p_T$  spectra comparison between  $\bar{D}^0$  and  $D^0$  in 0-10%, 10-20%, 20-40%, 40-60% and 40-80% centrality bins. Fig. 161 shows the  $\bar{D}^0|/D^0$  double ratio in the corresponding centrality species. With the current data, there is a hint that the  $\bar{D}^0$  yield is relative larger than the  $D^0$  in

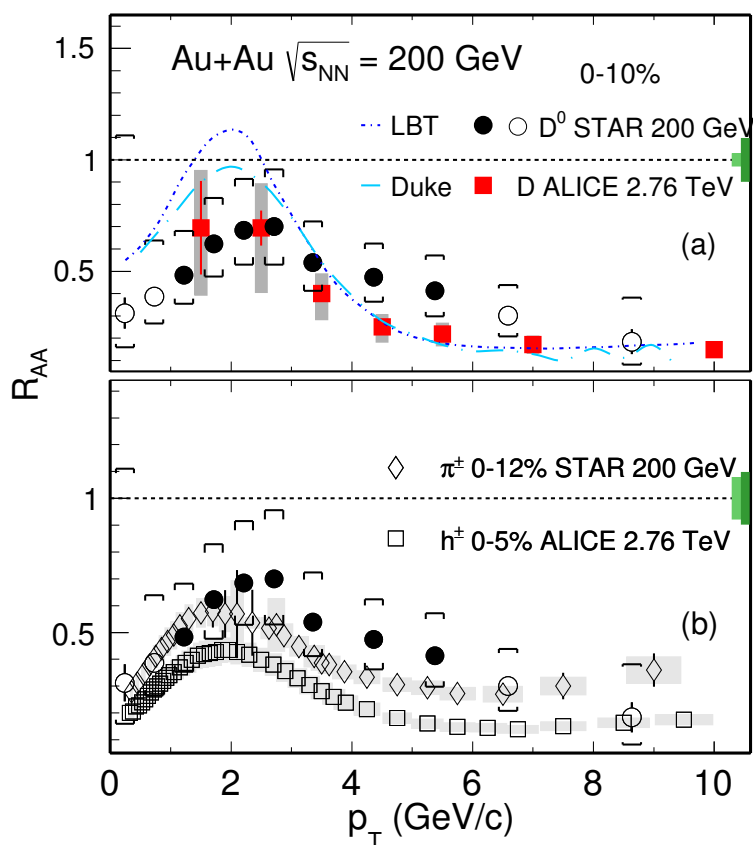


Figure 154:  $D^0 R_{AA}$  in the most central collisions at 0-10% compared to that of D meson from ALICE and charged hadron from ALICE and  $\pi^0$  from APHENIX.

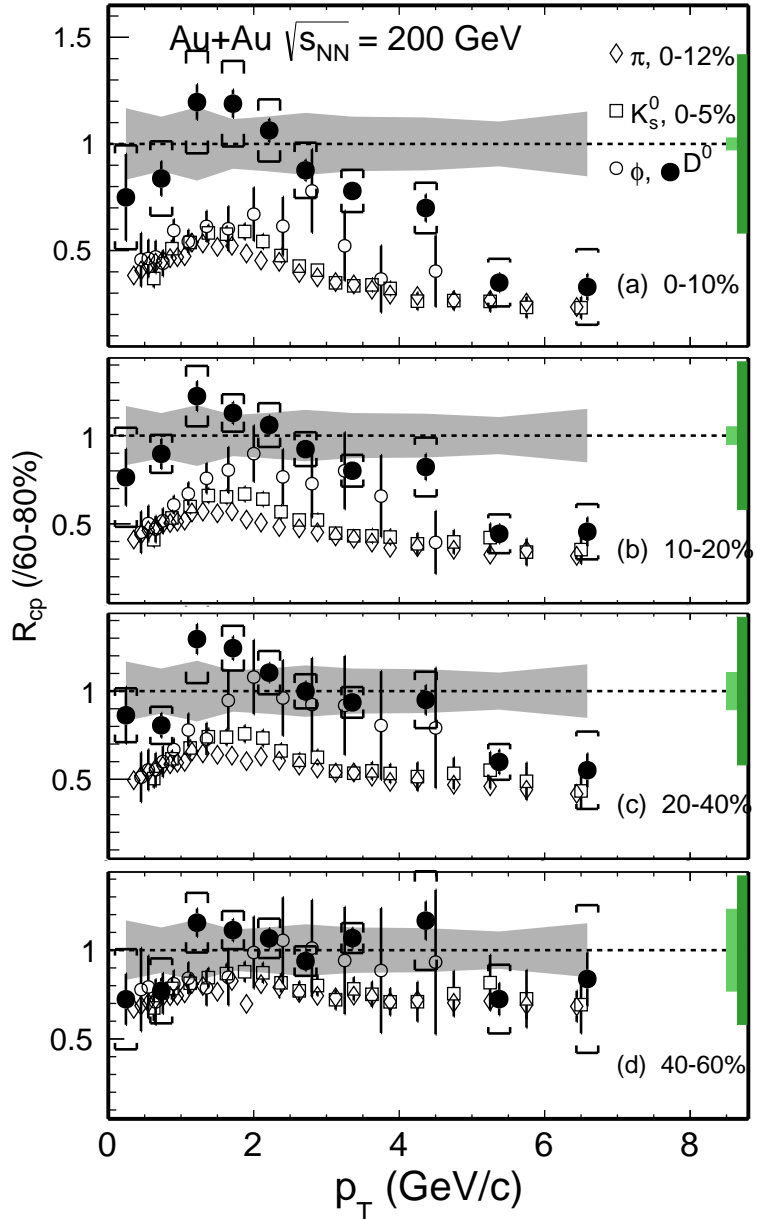


Figure 155:  $D^0 R_{CP}$  with the 60–80% spectrum as the reference for different centrality classes in Au + Au collisions at  $\sqrt{s_{NN}} = 200$  GeV compared to that of other light and strange mesons ( $\pi^\pm$ ,  $K_S^0$  and  $\phi$ ). The statistical and systematic uncertainties are shown as error bars and brackets on the data points. The grey bands around unity depict the systematic uncertainty due to vertex resolution correction, mostly from the 60–80% reference spectrum. The light and dark green boxes on the right depict the normalization uncertainty in determining the  $N_{bin}$ .

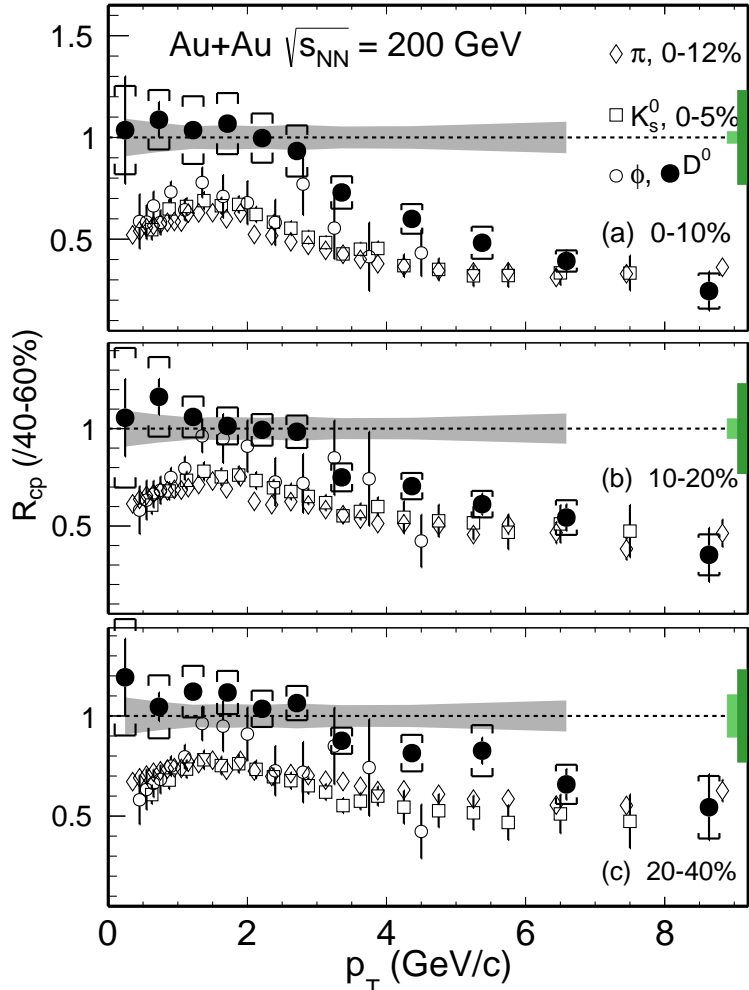


Figure 156:  $D^0 R_{CP}$  with the 40–60% spectrum as the reference for different centrality classes in Au + Au collisions at  $\sqrt{s_{NN}} = 200$  GeV compared to that of other light and strange mesons ( $\pi^\pm$ ,  $K_S^0$  and  $\phi$ ). The statistical and systematic uncertainties are shown as error bars and brackets on the data points. The grey bands around unity depict the systematic uncertainty due to vertex resolution correction, mostly from the 40–60% reference spectrum. The light and dark green boxes on the right depict the normalization uncertainty in determining the  $N_{\text{bin}}$ .

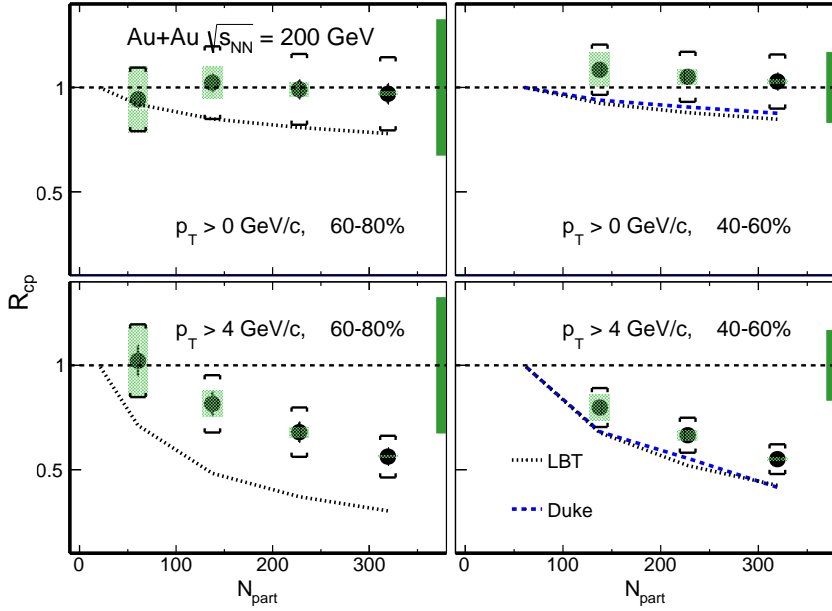


Figure 157:  $D^0$   $R_{CP}$  vs.  $N_{bin}$  in Au + Au collisions.

the most central and mid-central collisions. There could be some physics message behind, since we expect the  $\Lambda_c^-/\Lambda_c^+$  ratio should be smaller than unity due to the finite baryon density. The total charm quark and anti-charm quark should be conserved since they are created in pair, which results to the measured  $D^0$  larger than the  $\bar{D}^0$ . This could also arise the precise measurements for  $D^+/D^-$  and  $D_s^+/D_s^-$  in the future.

## 6.5 Comparison to Models

Over the past several years, there have been rapid developments in the theory model calculations

The Duke model uses a Langevin stochastic simulation to trace the charm quark propagation inside the QGP medium. Both collisional energy loss and radiative energy loss have been included in the calculation and charm quarks are hadronized via a hybrid approach combining both coalescence and fragmentation mechanisms. The bulk medium is simulated using a viscous hydrodynamic evolution for the QGP evolution and a hadronic cascade evolution using the UrQMD model. The charm quark in-medium interaction is characterized using a temperature and momentum dependent diffusion coefficient. The medium evolution parameters have been constrained via a statistical Bayesian analysis by fitting the previous experimental data of  $R_{AA}$  and  $v_2$  of light, strange and charm hadrons. The extracted charm quark spatial diffusion coefficient at zero momentum  $2\pi TD_s|_{p=0}$  is about 1–3 near  $T_c$  and exhibits a positive slope for its temperature dependence above  $T_c$ .

The Linearized Boltzmann Transport (LBT) calculation extends the LBT approach developed before to include both light and heavy flavor parton evolution in the QGP medium. The transport calculation includes all  $2 \rightarrow 2$  elastic scattering processes for collisional energy loss and the higher-twist energy loss formalism for medium induced radiative energy loss. It uses the same hybrid approach as in the Duke model for charm quark hadronization. The heavy quark transport is coupled with a 3D viscous hydrodynamic evolution which is tuned for light flavor hadron data. The charm quark spatial diffusion coefficient is estimated via the  $2\pi TD_s = 8\pi/\hat{q}$  at parton momentum  $p = 10 \text{ GeV}/c$ . The  $2\pi TD_s$  is  $\sim 3$  at  $T_c$  and increases to  $\sim 6$  at  $T = 500 \text{ MeV}$ .

We compare our measured  $R_{CP}$  to several theory model calculations, shown in Fig. 158 and Fig. 159.

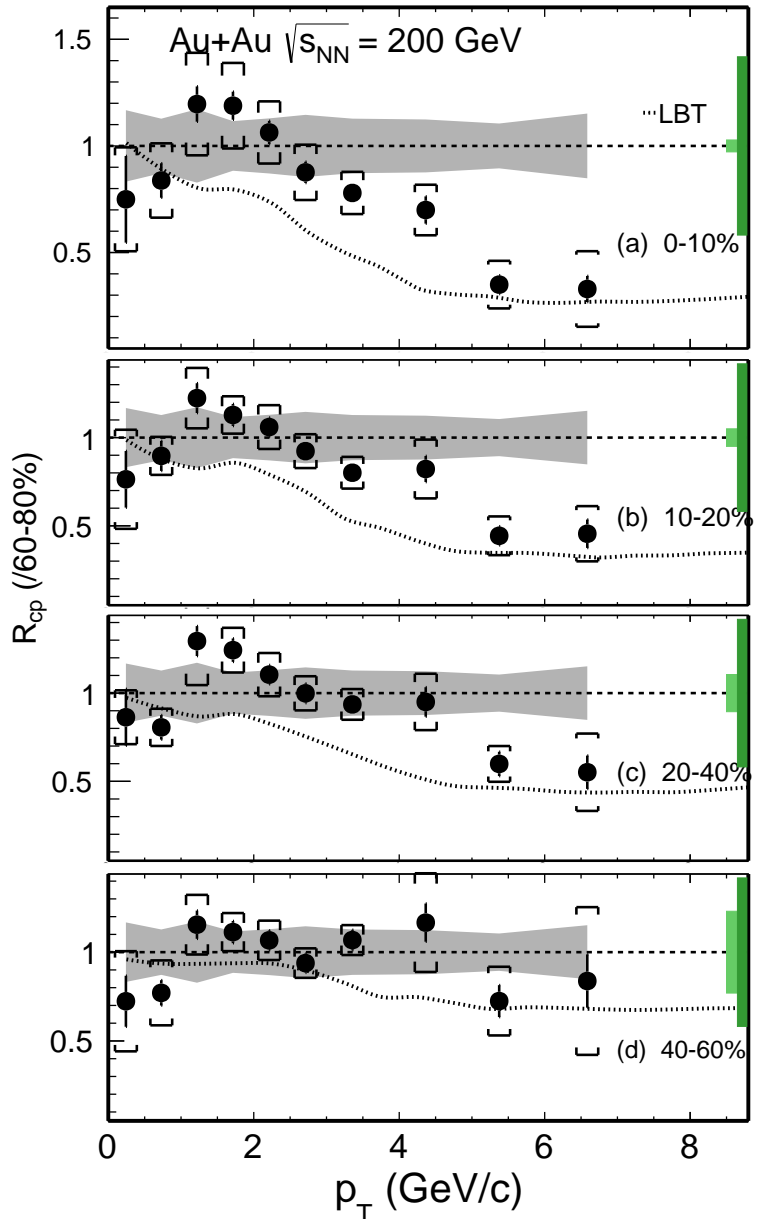


Figure 158:  $D^0 R_{CP}$  with the 60–80% spectrum as the reference for different centrality classes in Au + Au collisions compared to model calculations. The statistical and systematic uncertainties are shown as error bars and brackets on the data points. The grey bands around unity depict the systematic uncertainty due to vertex resolution correction, mostly from the 60–80% reference spectrum. The light and dark green boxes on the right depict the normalization uncertainty in determining the  $N_{\text{bin}}$ .

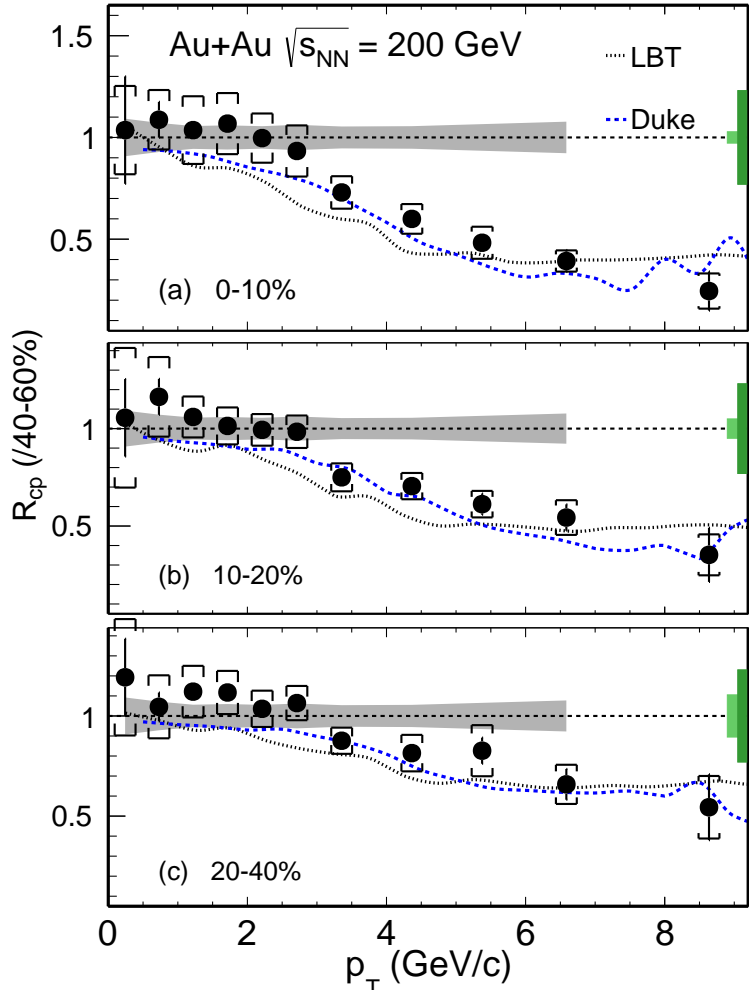


Figure 159:  $D^0 R_{CP}$  with the 40–60% spectrum as the reference for different centrality classes in Au + Au collisions compared to model calculations. The statistical and systematic uncertainties are shown as error bars and brackets on the data points. The grey bands around unity depict the systematic uncertainty due to vertex resolution correction, mostly from the 40–60% reference spectrum. The light and dark green boxes on the right depict the normalization uncertainty in determining the  $N_{\text{bin}}$ .

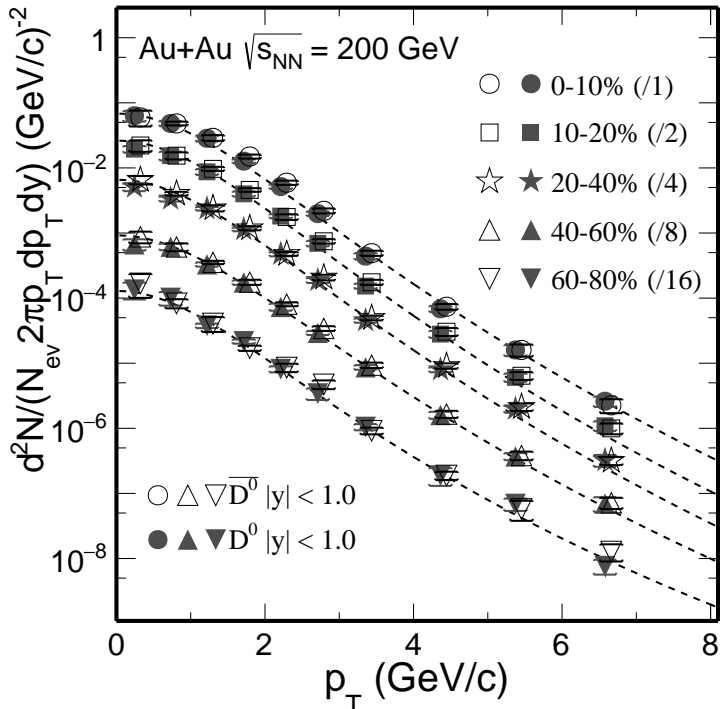


Figure 160:  $D^0$  and  $\bar{D}^0$  invariant yield at mid-rapidity ( $|y| < 1$ ) vs. transverse momentum for different centrality classes in Au + Au collisions at  $\sqrt{s_{NN}} = 200$  GeV. Error bars (not visible for many data points) indicate statistical uncertainties and brackets depict systematical uncertainties. Global systematic uncertainties in  $B.R.$  and  $N_{bin}$  are not plotted. Solid lines depict Levy function fits.

## 6.6 Total ccbar cross section

Relay on the current charm related analysis, there is a nature question regarding on the total charm cross section. So using the current D0, Dpm, Dstar and Lc results and also relay on some theory prediction for the non-measured pt range. The detail slides can be found below: and We are using 10-40% centrality for this testing.

[https://drupal.star.bnl.gov/STAR/system/files/charmCrossSection\\_v2.pdf](https://drupal.star.bnl.gov/STAR/system/files/charmCrossSection_v2.pdf)

With the current ccbar cross section in Au + Au, also shown with in p + p, within the large uncertainties they are more or less comparable with the current precision.

## 7 Re-analysis of Run10/11 data ...

### 7.1 Long and Yifei's re-analysis ...

Since at  $p_T < 2$  GeV/c a discrepancy was found between new data from Run14 with HFT and published data from Run10+Run11. A re-analysis on Run11 data was performed to check if anything was incorrect. The analysis cuts are the same as in previous analysis note:

[https://drupal.star.bnl.gov/STAR/system/files/dzeroAuAu\\_updated.pdf](https://drupal.star.bnl.gov/STAR/system/files/dzeroAuAu_updated.pdf)

also listed in Xiaolong 's analysis, see next section. The only difference is varying DCA cut with  $< 1$  cm or  $< 2$  cm.

The raw signals as a function of  $p_T$  from part of Run11 data with 85% of full statistics were extracted as Fig.167,

The raw signals were compared with Xiaolong 's independent analysis and found to be consistent, shown in Fig.168. The slight lower yield in Xiaolong 's analysis is due to the tight DCA cut  $< 1$  cm, while the DCA cut applied here is  $< 2$  cm.

In early days, there was no vertex detector, we had to use random combination of decay products to reconstruct  $D^0$  meson in hadronic channel, which suffered from huge combinatorial background.

The way to improve the significance was to enrich the kaon and pion PID probability and enhance

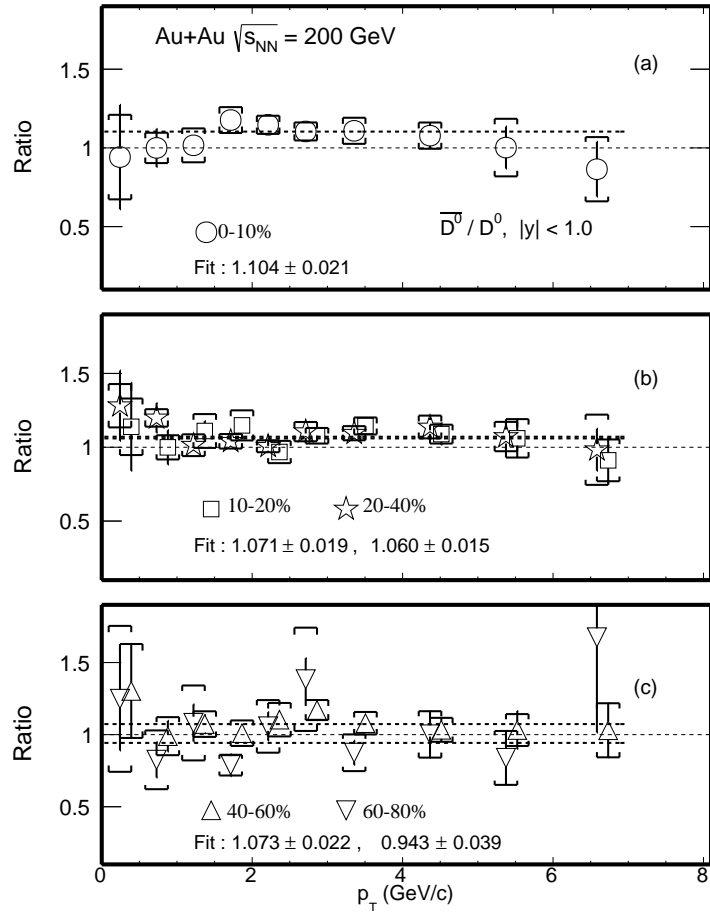


Figure 161:  $\bar{D}^0/D^0$  invariant yield ratio at mid-rapidity ( $|y| < 1$ ) vs. transverse momentum for different centrality classes in Au + Au collisions at  $\sqrt{s_{NN}} = 200$  GeV. Error bars indicate statistical uncertainties and brackets depict systematical uncertainties. Global systematic uncertainties in *B.R.* and  $N_{\text{bin}}$  are not plotted. Dashed lines depict a linear function fits.

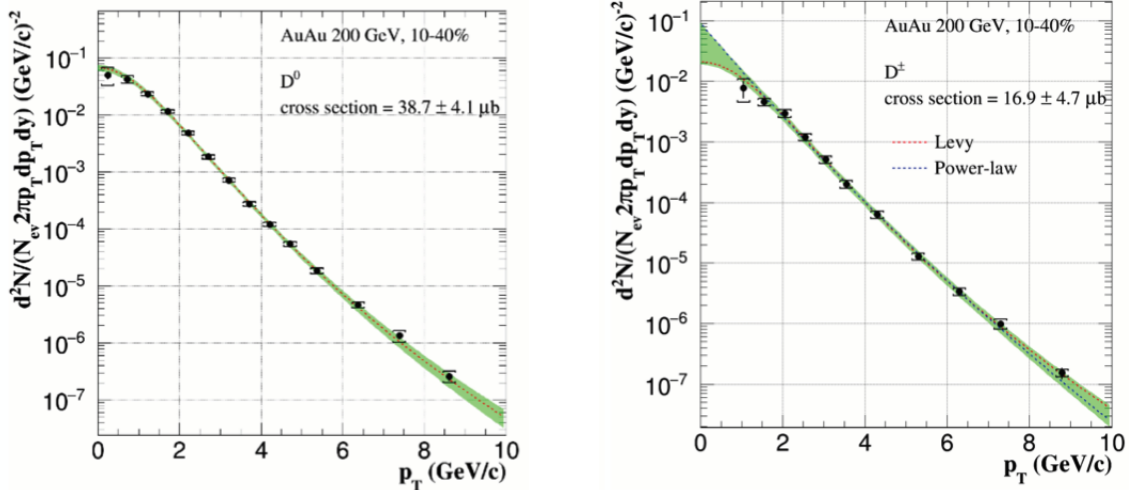


Figure 162:  $D^0$  with the 10–40% spectrum in Au + Au collisions fitted with the levy function and power low function used for the cross section calculation, then take the difference between two functions as the systematic uncertainties.

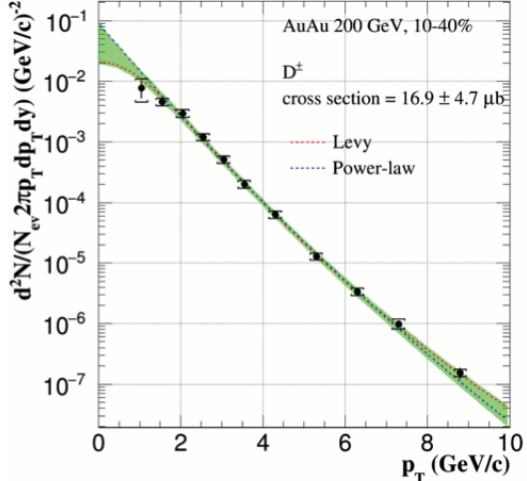


Figure 163:  $D^\pm$  with the 10–40% spectrum in Au + Au collisions fitted with the levy function and power law function used for the cross section calculation, then take the difference between two functions as the systematic uncertainties.

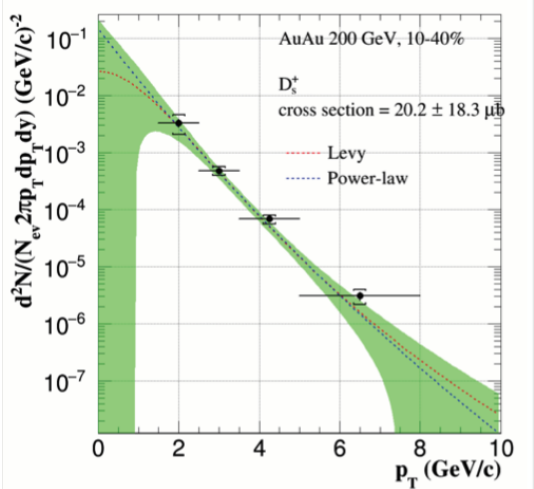


Figure 164:  $D_s^+$  with the 10–40% spectrum in  $\text{Au} + \text{Au}$  collisions fitted with the levy function and power low function used for the cross section calculation, then take the difference between two functions as the systematic uncertainties.

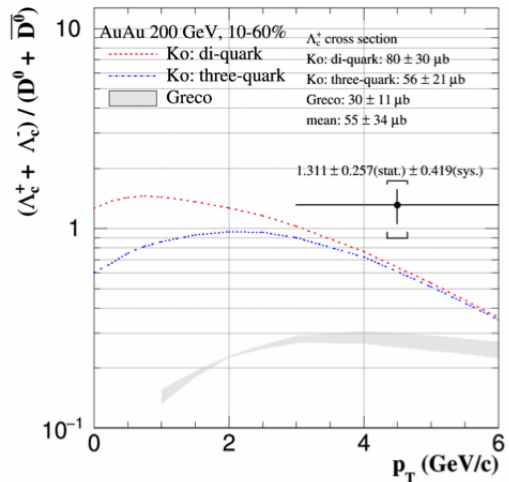


Figure 165:  $\Lambda_c$  with the 10–60% spectrum in  $\text{Au} + \text{Au}$  collisions fitted with the levy function and power law function used for the cross section calculation, then take the difference between two functions as the systematic uncertainties.

10-60% for  $\Lambda_c$ , 10-40% for others

| Charm Hadron | Cross Section ( $\mu\text{b}$ )                     |
|--------------|-----------------------------------------------------|
| $D^0$        | $39 \pm 4$                                          |
| $D^-$        | $17 \pm 5$                                          |
| $D_s^+$      | $20 \pm 18$                                         |
| $\Lambda_c$  | $55 \pm 34$                                         |
| Total        | $131 \pm 39$                                        |
| pp           | $170 \pm 45(\text{stat.})^{+38}_{-59}(\text{sys.})$ |

Figure 166: table of the current ccbar cross section, also shown with pp.

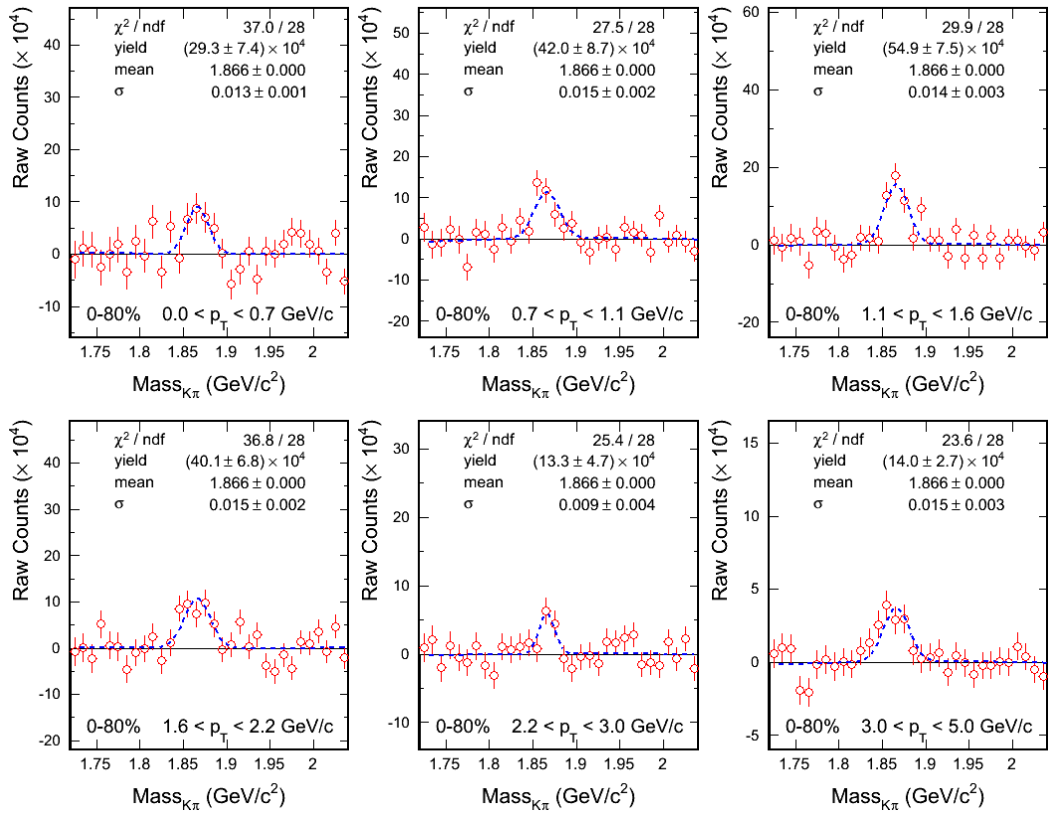


Figure 167:  $p_T$  dependence of  $D^0$  signals in 0-80% from partial Run11 data.

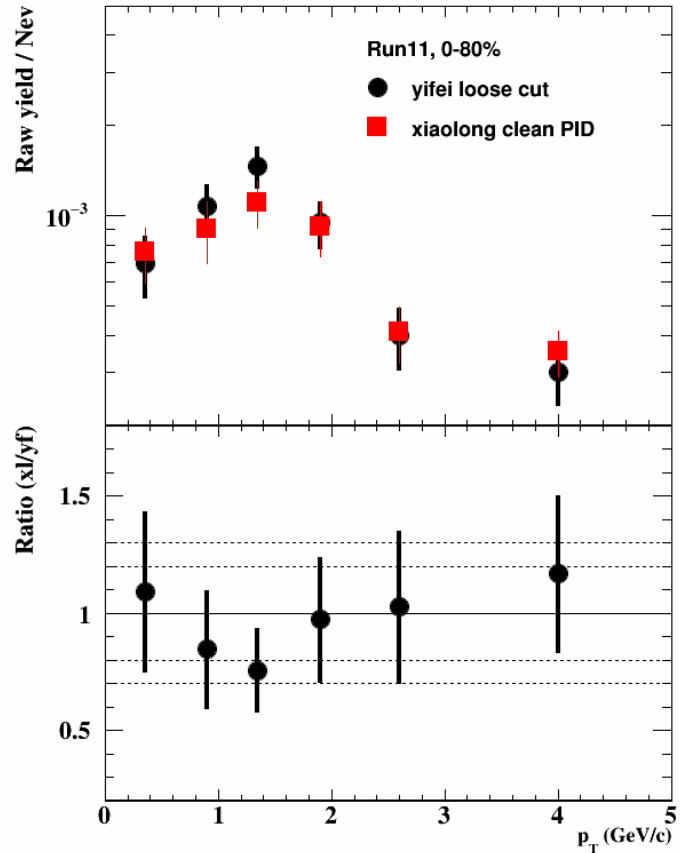


Figure 168: Raw signals comparison with Xiaolong's.

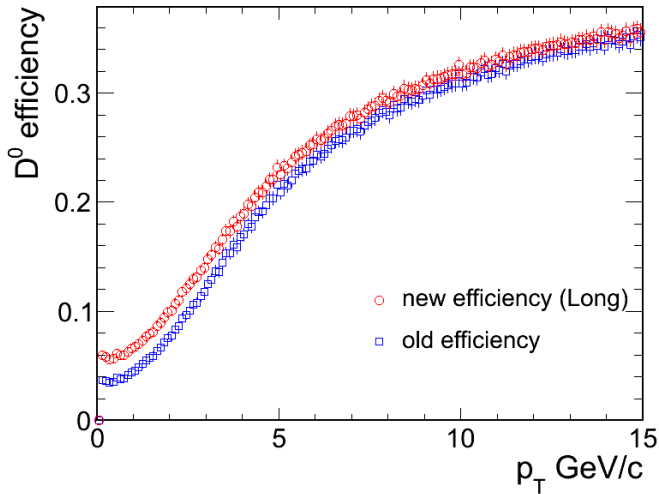


Figure 169: New efficiency checked from Long compared with old one.

the statistics as much as possible at the same time. Thus we developed a hybrid method: In low momentum region, we always required good TOF matching and TOF PID, those tracks without good TOF matching or failed to pass TOF PID were rejected. At high momentum beyond the TOF identification capability, candidates were always required to pass the TPC  $dE/dx$  cut and the TOF  $1/\beta$  cut was only required for those tracks with good TOF matching. (In order to have as much statistics as possible, we do not reject tracks passed TPC PID. But in the candidates passed TPC PID, a large overlap between kaons and pions still exists, the mis-identification probability of kaon and pion is large. What we did is to add additional constraint, TOF PID to enhance the purity of pion and kaon. We keep all of them but pion and kaon probability enhanced.) The details are list below:

A good TOF matching means tracks satisfy  $\text{TOFMatchFlag} > 0 \ \&\& \beta > 0$ .

At low momentum,  $p < 1.6 \text{ GeV}/c$ , the correct algorithm to ensure the purity of kaons and pions is:

`GoodTOFMatching && TPC PID && TOF PID (see Eq. 23 - 25)`

At high momentum,  $p > 1.6 \text{ GeV}/c$ , if there was a good TOF matching, we applied TPC PID + TOF PID, otherwise we used TPC PID only to enhance the PID efficiency:

`If (GoodTOFMatching) TPC PID + TOF PID else TPC PID`

But an issue was found in the code, that the condition to reject those tracks without matching to TOF at low momentum was different from above algorithm and also different from what we used to calculate the efficiency. We found that those tracks with  $\text{TOFMatchFlag} > 0$  but with  $\beta < 0$  were not correctly rejected, which results in higher yield obtained or lower efficiency than expected. This introduces about 15% difference at low  $p_T$  but does not affect high  $p_T$  much.

The other issue is that we applied an additional  $DCA_{XY}$  cut efficiency in previous analysis. This cut was used in TOF matching algorithm (in `TOFMatchMaker`) to require tracks with a distance of closest approach to the beam line in xy plane within 1 cm. This efficiency was studied in early days and found there was about up to 20% of tracks at low  $p_T$  rejected with this cut, see Fig.170. However, when we studied TOF matching efficiency, we used a data driven method and this efficiency should be already included. Thus we double counting this efficiency.

### 7.1.1 Added by Long Zhou

After corrected above two main issues, the corrected reconstruction efficiency can be found at Fig.171

The final  $D^0 R_{AA}$  spectra will be corrected by efficiency ratio between the published reconstruction efficiency and the corrected reconstruction efficiency. The corrected  $D^0 R_{AA}$  is shown in Fig.172

The updated  $D^0 R_{AA}$  was also compared to the previous results, shown in Fig.173. As can clearly see the difference in the middle transverse momentum range.

*Need the  $R_{AA}$  comparison plots between my  $R_{AA}$  and Run 14  $R_{AA}$  (from Xiaolong)*

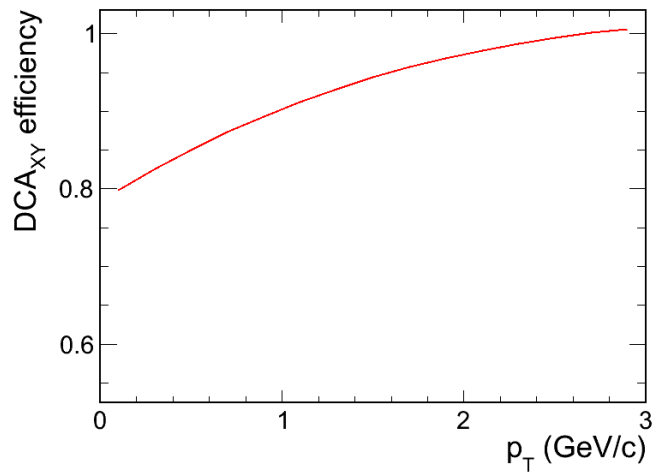


Figure 170:  $DCA_{XY}$  efficiency.

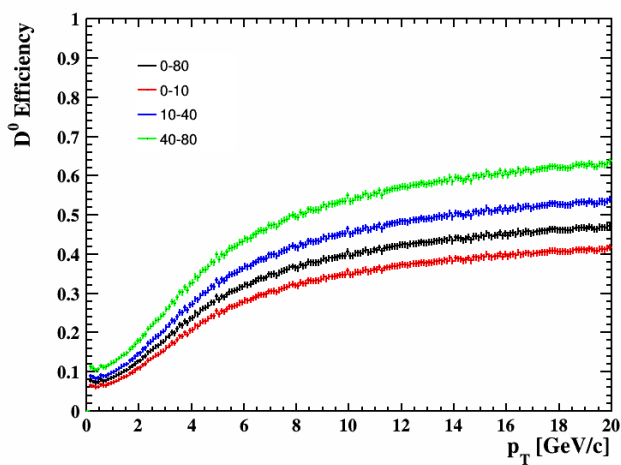


Figure 171: The reconstruction efficiency at each centrality bin

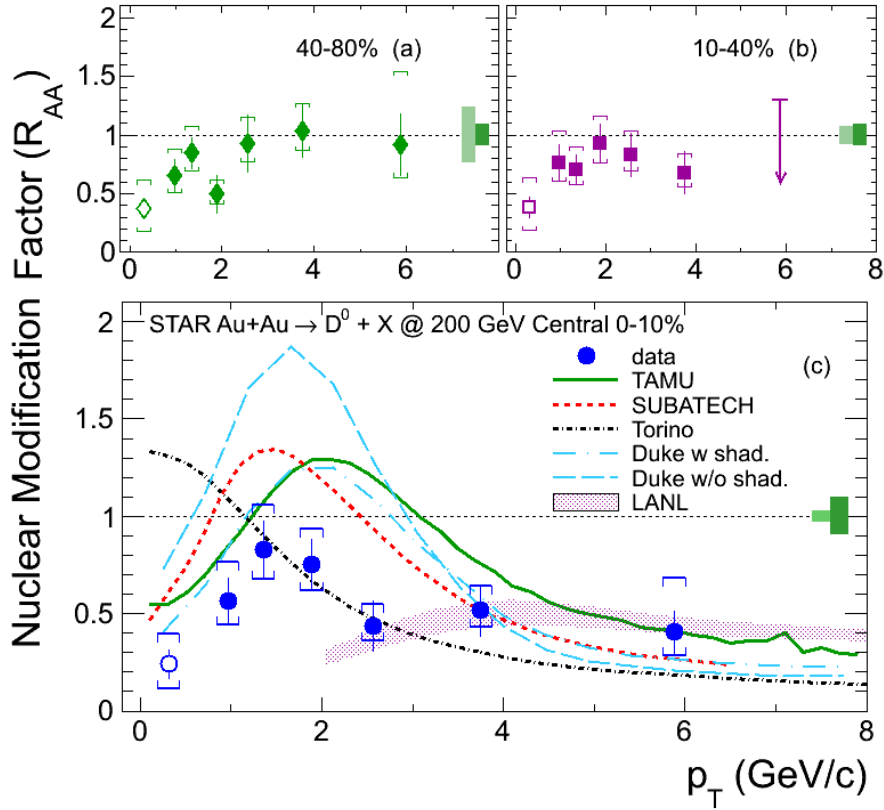


Figure 172: The Corrected  $D^0$   $R_{AA}$  in each centrality class, and compared with several model calculation

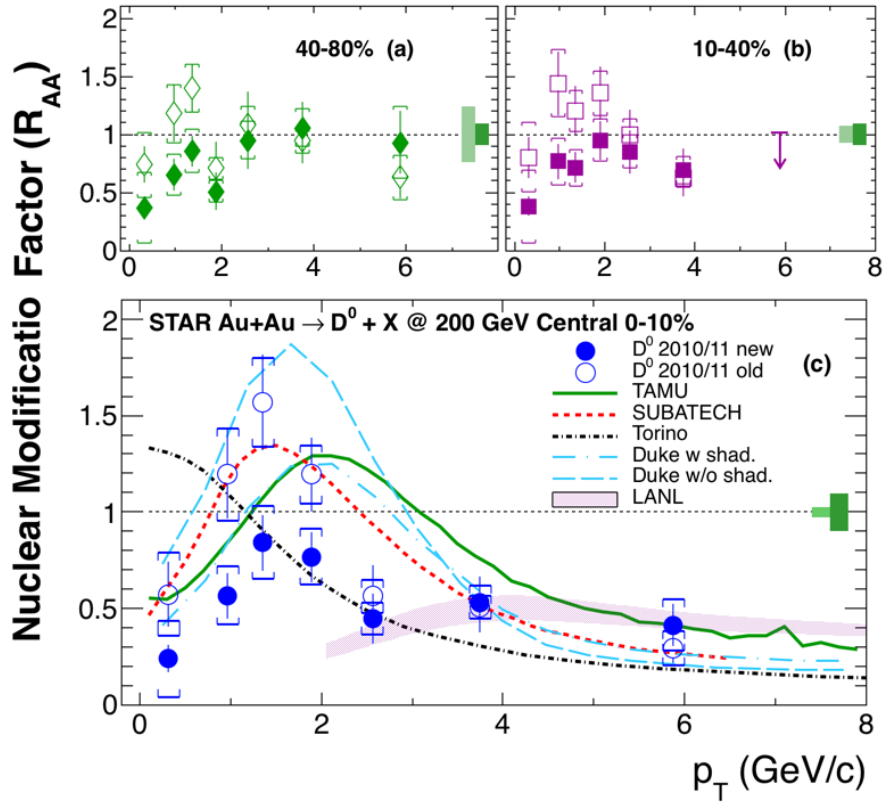


Figure 173: The Corrected  $D^0$   $R_{AA}$  in each centrality class, and compared with several model calculation, also compared to the previous publish results.

1203 More material can be found at here :  
 1204 [https://drupal.star.bnl.gov/STAR/system/files/D0\\_Eff\\_discussion\\_2016\\_11\\_7.pdf](https://drupal.star.bnl.gov/STAR/system/files/D0_Eff_discussion_2016_11_7.pdf)  
 1205 [https://drupal.star.bnl.gov/STAR/system/files/D0\\_Eff\\_discussion\\_2017\\_05\\_12.pdf](https://drupal.star.bnl.gov/STAR/system/files/D0_Eff_discussion_2017_05_12.pdf)  
 1206 [https://drupal.star.bnl.gov/STAR/system/files/D0\\_BNL170516\\_0.pdf](https://drupal.star.bnl.gov/STAR/system/files/D0_BNL170516_0.pdf)

## 1207 7.2 Xiaolong's re-analysis

### 1208 7.2.1 Datasets and Cuts

1209 In this Run11  $D^0$  re-analysis, we ran 461 million events ( $\sim 85\%$  of total). Cuts are listed in the  
 1210 following.

- 1211 • Library: P11id.
- 1212 • Trigger IDs: 350003, 350013, 350023, 350033, 350043.
- 1213 • Centrality: 0-80%.
- 1214 • Vertex selections

- 1215 –  $|v_z^{TPC}| < 30$  cm
- 1216 –  $|v_z^{TPC} - v_z^{VPD}| < 3$  cm

- 1217 • Track selections

- 1218 –  $p_T > 0.2$  GeV/c
- 1219 –  $|\eta| < 1$
- 1220 – global DCA  $< 1$  cm
- 1221 –  $20 \leq \text{nHitsFit} < 50$
- 1222 –  $\text{nHitsFit}/\text{nHitsMax} > 0.52$
- 1223 –  $\text{nHitsdEdx} > 10$

- 1224 • PID

- 1225 – TPC PID ( $dE/dx$ ):  $|n\sigma_K| < 2$  and  $|n\sigma_\pi| < 3$
- 1226 – TOF PID ( $1/\beta$ ): define  $n\sigma_X^{TOF} = (\frac{1}{\beta} - \sqrt{m_X^2/p^2 + 1})/\sigma + c$ , here  $\sigma = 0.013$ ,  $c = 0.3$ ,  
 1227  $m_X$  is particle ( $K$ ,  $\pi$ , etc.) mass. For pions, we apply  $n\sigma_\pi^{TOF} < f_\pi^{\max}(p)$ , here

$$f_\pi^{\max}(p) = \begin{cases} 5.43 - 2.14x, & p < 1.6 \\ 2, & p \geq 1.6 \end{cases} \quad (23)$$

1229 For kaons, we apply  $f_K^{\min}(p) < n\sigma_K^{TOF} < f_K^{\max}(p)$ , here

$$f_K^{\min}(p) = \begin{cases} -7.54 + 5.83p - 1.31p^2, & p < 1.3 \\ -2, & p \geq 1.3 \end{cases} \quad (24)$$

$$f_K^{\max}(p) = \begin{cases} 8.69 - 6.02p + 1.32p^2, & p < 2.0 \\ 2, & p \geq 2.0 \end{cases} \quad (25)$$

1232 There are two PID cases:

- 1233 \* hybrid PID: Apply TOF PID while TOF is available ( $\text{TOFMatchFlag} > 0 \ \&\& \ \beta > 0 \ \&\& \ \text{pathLength} > 200 \ \&\& \ |\text{ylocal}| < 1.8$ ) , otherwise use TPC PID only.
- 1234 \* clean PID: It's the same as hybrid PID, except that TOF match must be required  
 1235 at  $p < 1.6$  GeV/c ( $\text{TOFMatchFlag} > 0$ ).

- 1237 •  $D^0$  rapidity:  $|y| < 1$

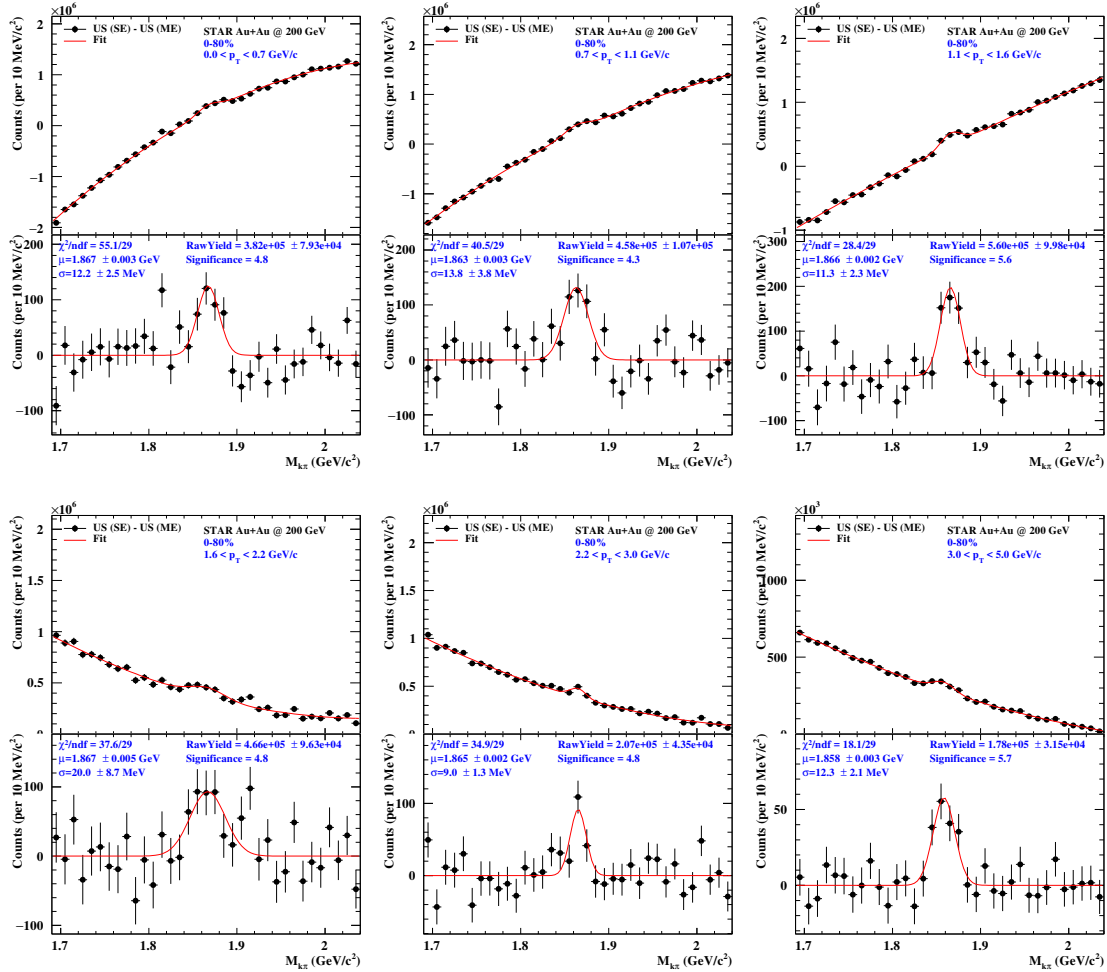


Figure 174:  $D^0$  signal at 6  $p_T$  bins (0-0.7, 0.7-1.1, 1.1-1.6, 1.6-2.2, 2.2-3.0, 3.0-5.0) in 0-80% with clean PID.

### 7.2.2 $D^0$ reconstruction

We reconstruct  $D^0$  through the channel  $D^0 \rightarrow K^- \pi^+$  (B.R. = 0.0388). Background is reconstructed with mix-event method. 9 centrality bins (0-80%) and 10 primary vertex  $v_z$  bins ( $v_z \in [-30, 30]$  cm) are used to classify mixed events with some degree of similarity. Mix-event unlike-sign background is scaled to same-event like-sign background at the mass region of  $1.69 < \text{mass}_{K\pi} < 2.04 \text{ GeV}/c^2$ . Then same event unlike-sign (signal + background) subtracted by scaled mix-event unlike-sign background are fitted with a gaussian function (signal) plus a second order polynomial function (residual background). The fit range is  $1.69$ - $2.04 \text{ GeV}/c^2$ .

Fig. 174 shows  $D^0$  signal at 6  $p_T$  bins (0-0.7, 0.7-1.1, 1.1-1.6, 1.6-2.2, 2.2-3.0, 3.0-5.0) in 0-80% with clean PID.

Fig. 175 shows  $D^0$  signal at 6  $p_T$  bins (0-0.7, 0.7-1.1, 1.1-1.6, 1.6-2.2, 2.2-3.0, 3.0-5.0) in 0-80% with hybrid PID.

Fig. 176 shows  $D^0$  signal at 2  $p_T$  bins (0-2, 2-4) and 4 centralities (0-80%, 0-10%, 10-40%, 40-80%) with clean PID.

Fig. 177 shows  $D^0$  signal at 2  $p_T$  bins (0-2, 2-4) and 4 centralities (0-80%, 0-10%, 10-40%, 40-80%) with hybrid PID.

### 7.2.3 Efficiency and acceptance correction

The efficiency and acceptance correction includes the following:

- Acceptance, including  $p_T$  and  $\eta$  cut efficiency.

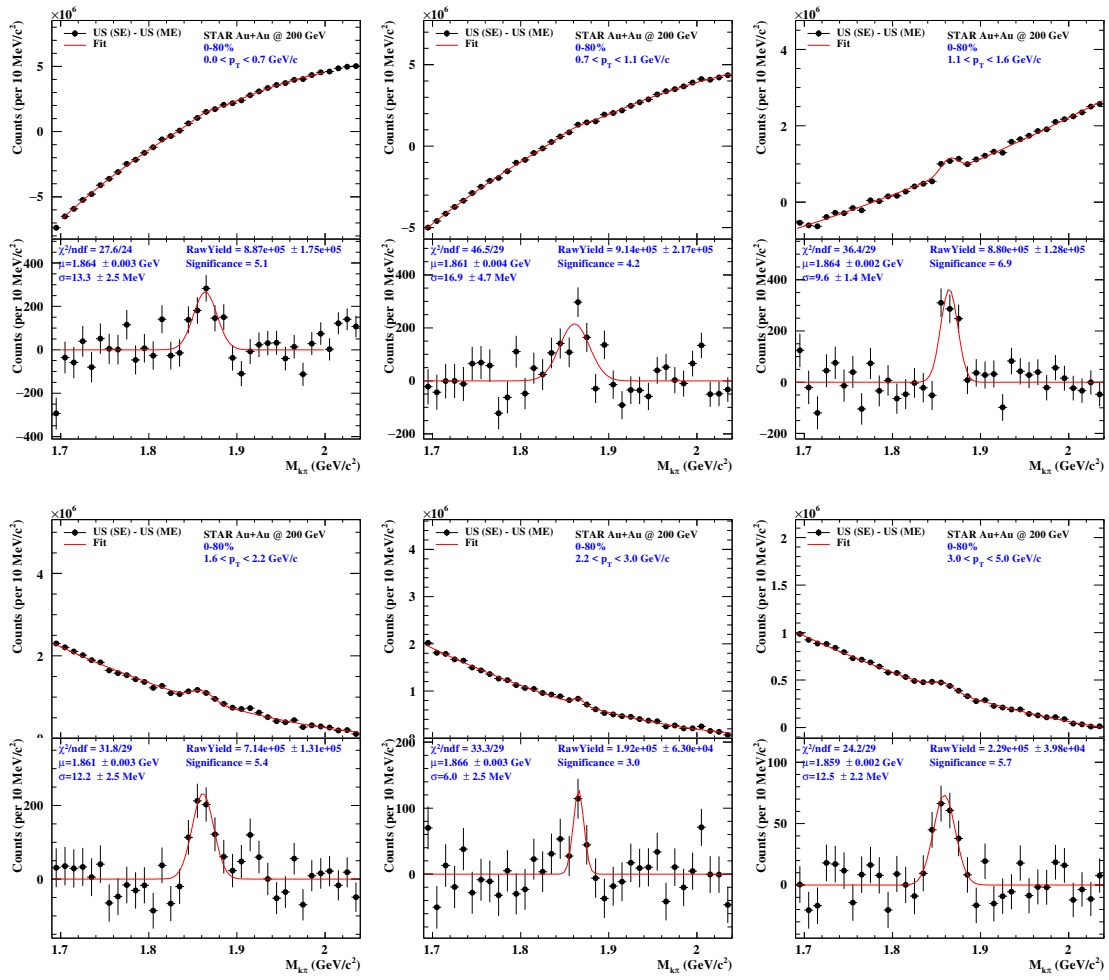


Figure 175:  $D^0$  signal at 6  $p_T$  bins (0-0.7, 0.7-1.1, 1.1-1.6, 1.6-2.2, 2.2-3.0, 3.0-5.0) in 0-80% with hybrid PID.

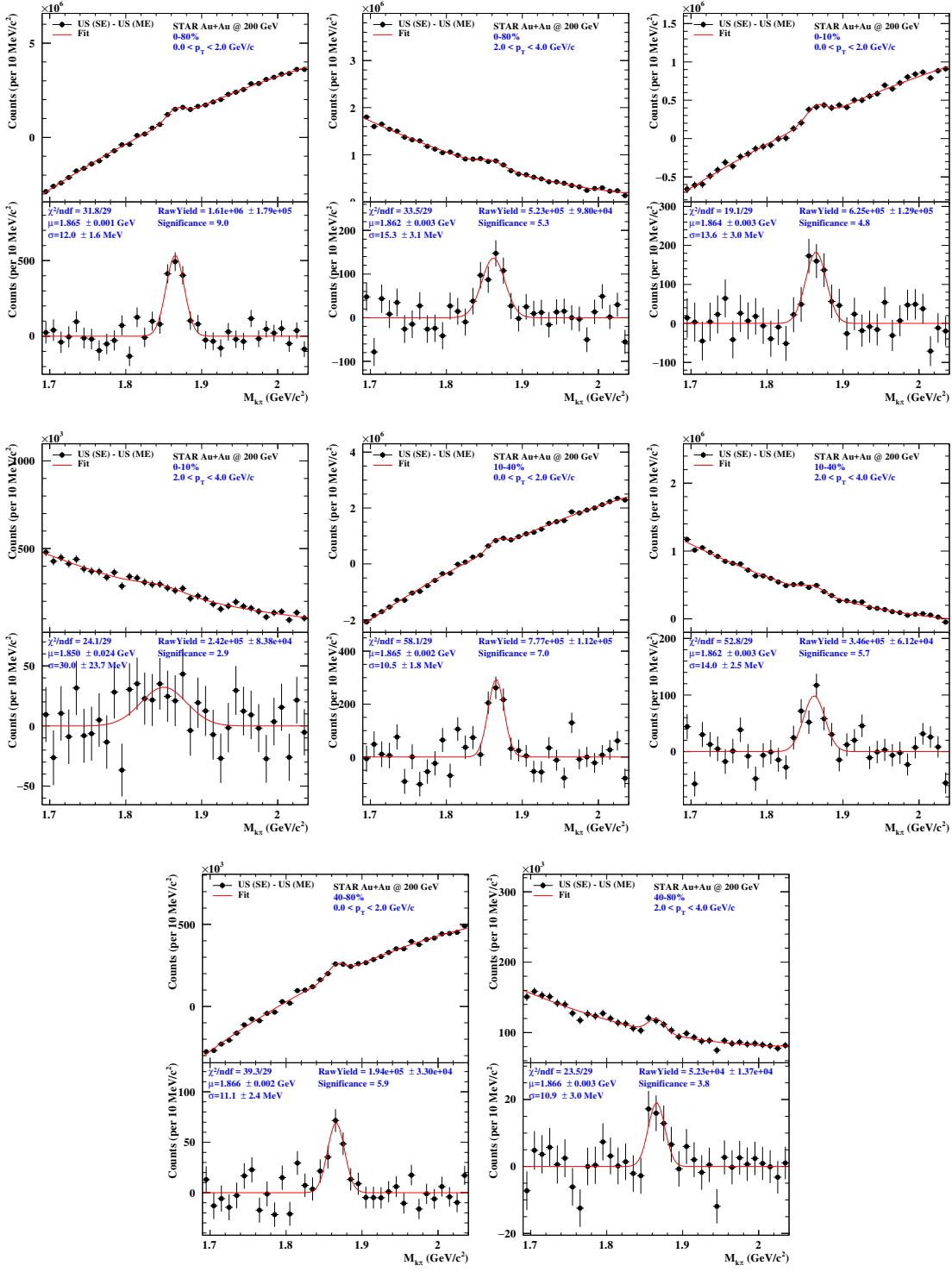


Figure 176:  $D^0$  signal at 2  $p_T$  bins (0-2, 2-4) and 4 centralalities (0-80%, 0-10%, 10-40%, 40-80%) with clean PID.

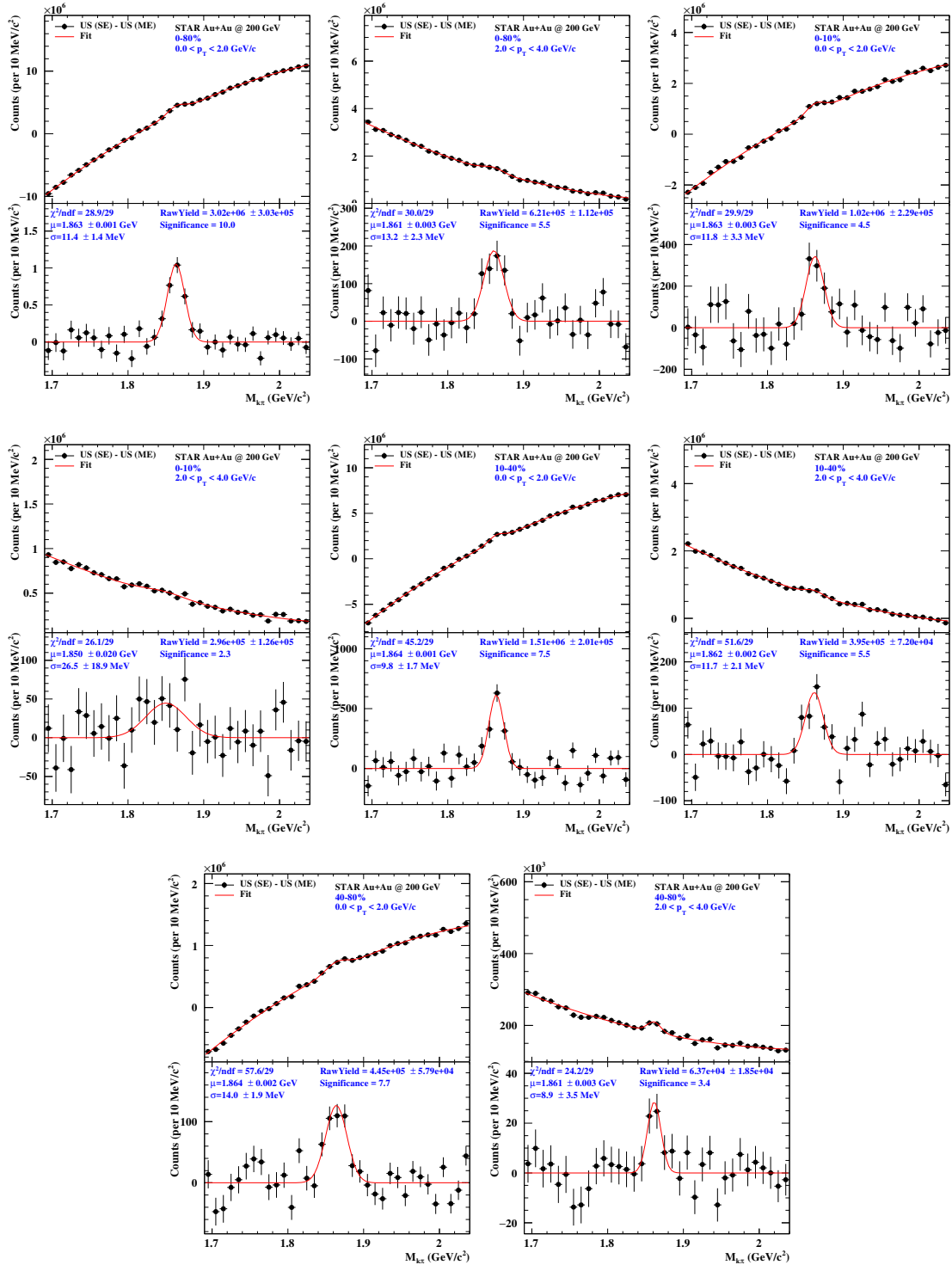


Figure 177:  $D^0$  signal at 2  $p_T$  bins (0-2, 2-4) and 4 centralalities (0-80%, 0-10%, 10-40%, 40-80%) with hybrid PID.

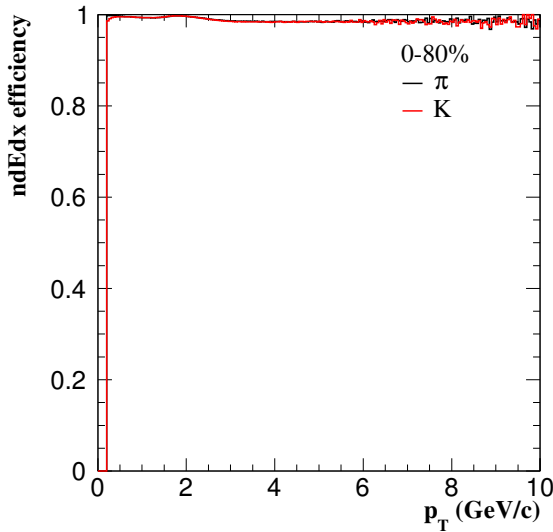


Figure 178: Run11 ndEdxHits cut efficiency.

- TPC tracking efficiency, including the basic track quality cut efficiency. ndEdxHits cut efficiency is not included.
- ndEdxHits cut efficiency. This efficiency is obtained from data ( track number with ndEdxHits cut divided by that without ndEdxHits cut ).
- TOF matching efficiency.
- PID efficiency, including TOF PID and TPC PID efficiency.

Among them, TPC tracking efficiency, PID efficiency is obtained from Yifei (published Run10+11  $D^0$ ).

Fig. 178 shows ndEdxHits cut efficiency. It's very high both for  $K$  and  $\pi$  ( $\sim 99\%$ ).

Fig. 179 shows  $K/\pi$  TOF matching efficiency at 0-80%, 0-10%, 10-40%, 40-80%. The dip at the  $p_T$  region of 0.5-0.9 GeV/c for kaons is due that we use  $n\sigma_{K/\pi}$  to identify  $K/\pi$  and  $n\sigma_K$  resolution get better at low  $p_T$  when TOF match is required. Detailed validation can be found at Section 4.3.

Fig. 180 shows single cut efficiency.

Fig. 181 shows final  $D^0$  efficiency in two PID cases, left panel for clean PID and right panel for hybrid PID.

#### 7.2.4 Results

Fig. 182 shows  $D^0$  spectra comparison between Run11 TPC and Run14 HFT in 6  $p_T$  bins. Top panel is  $D^0$  spectra and bottom panel is the ratio of Run11 TPC over Run14 HFT. Those data points are removed in which  $D^0$  significance is bad ( $< 3$ ) or  $D^0$  width is too narrow ( $< 9 \text{ MeV}/c^2$ ) or too wide ( $> 25 \text{ MeV}/c^2$ ). Run11 TPC results are consistent with Run14 HFT results ( $< 1\sigma$ ).

In order to get good  $D^0$  significance in different centralities, we also use two wide  $p_T$  bins (0-2 and 2-4  $\text{GeV}/c$ ). Fig. 183 shows  $D^0$  spectra comparison between Run11 TPC and Run14 HFT in two  $p_T$  bins. In different centralities, Run11 TPC results are also consistent with Run14 HFT results ( $< 1\sigma$ ).

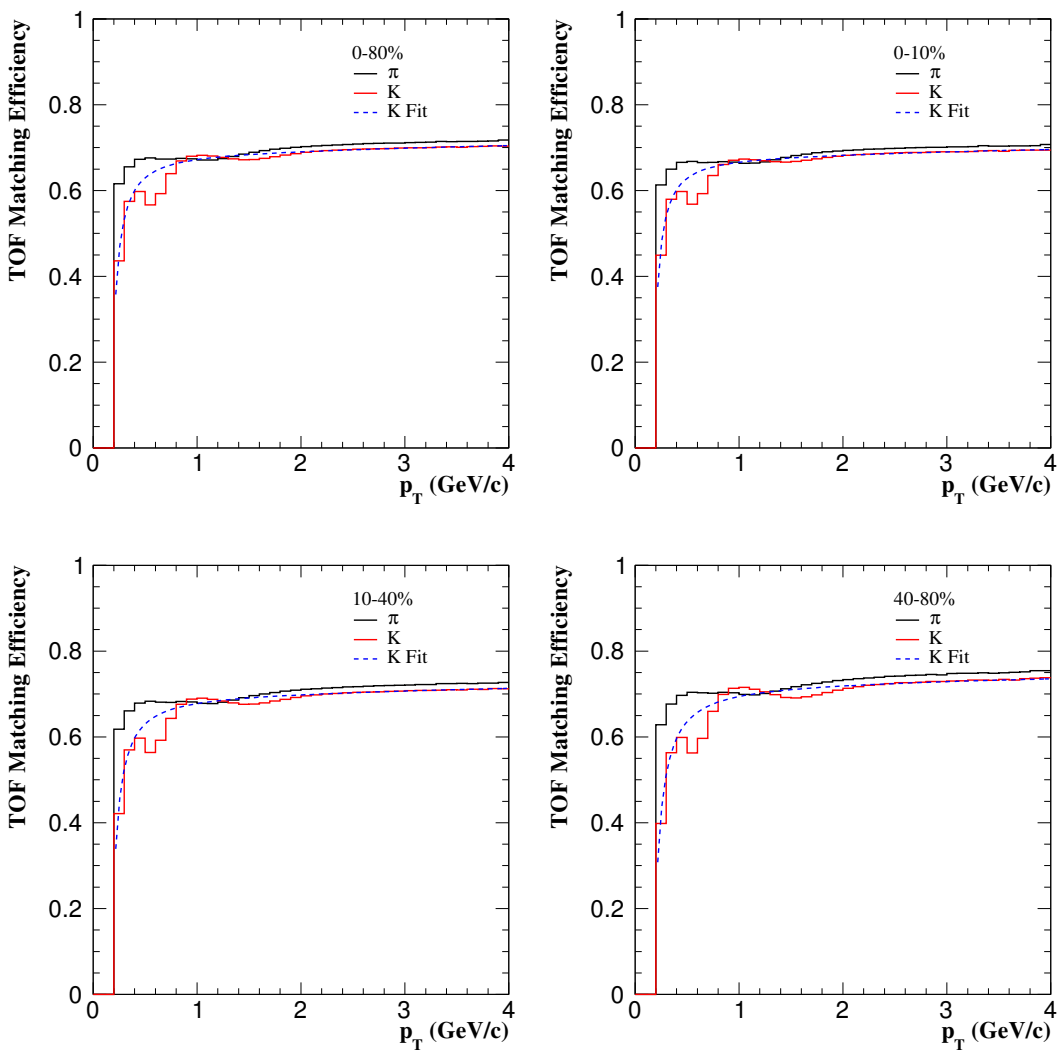


Figure 179: Run11  $K/\pi$  TOF matching efficiency at 0-80%, 0-10%, 10-40%, 40-80%.

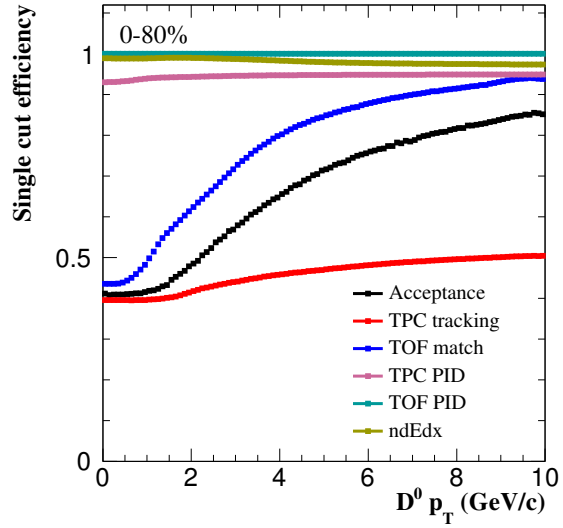


Figure 180: Run11 single cut efficiency.

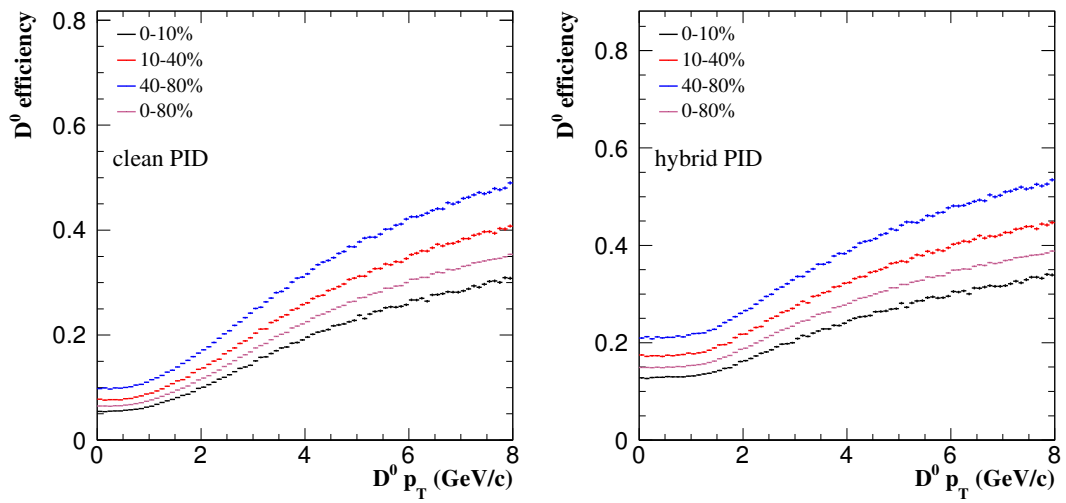


Figure 181: Run11  $D^0$  efficiency.

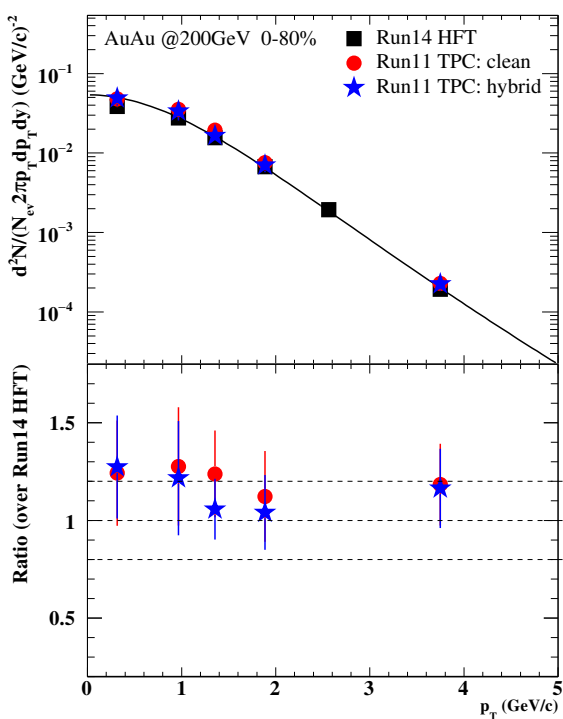


Figure 182:  $D^0$  spectra comparison between Run11 TPC and Run14 HFT.

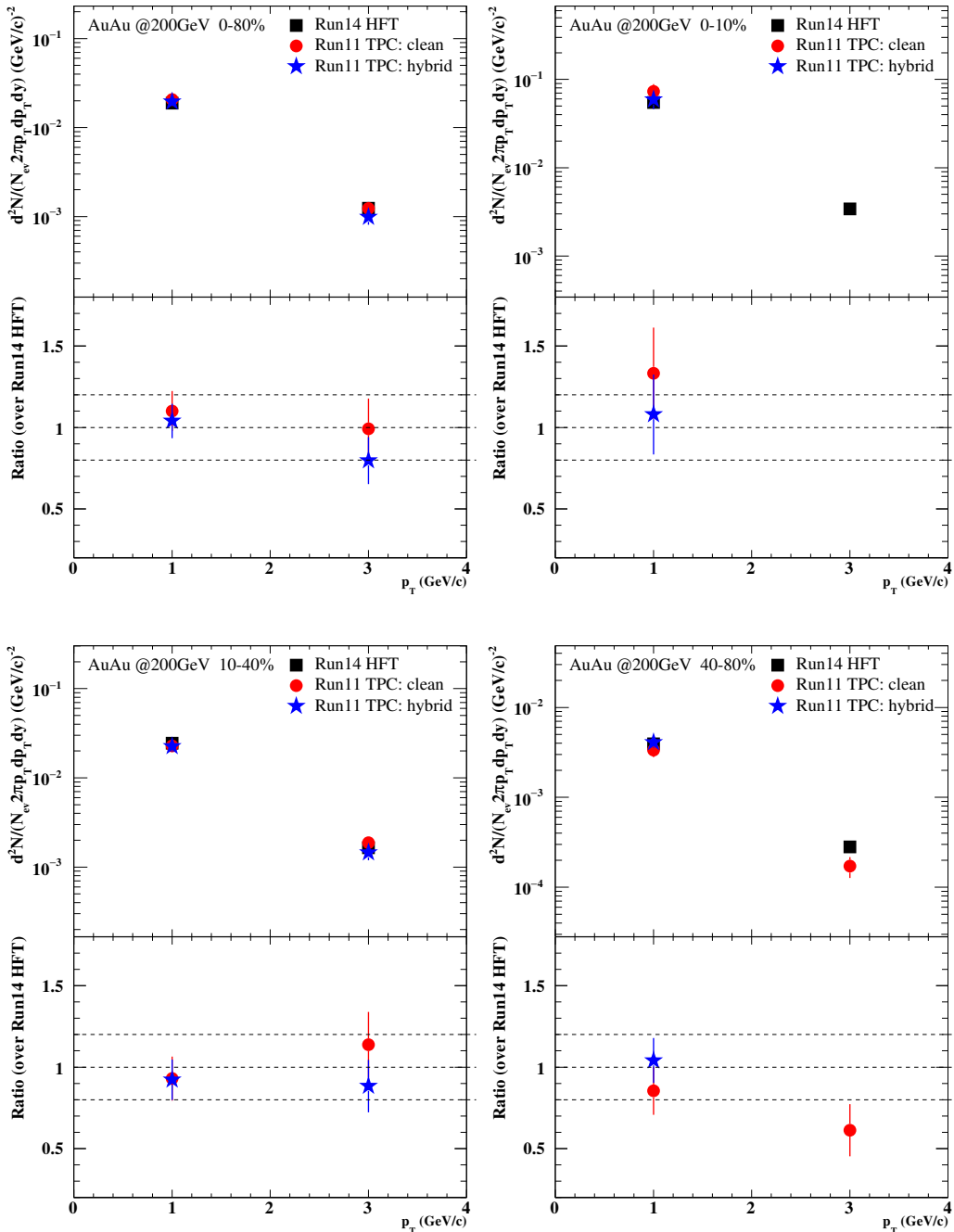


Figure 183:  $D^0$  spectra comparison between Run11 TPC and Run14 HFT in different centralities.

## 8 Run14 TPC analysis

### 8.1 Datasets and Cuts

In this Run14  $D^0$  TPC analysis, we ran 667 million events ( $\sim 62\%$  of total). Cuts are listed in the following.

- **Library:** P16id.
- **Trigger IDs:** 450050, 450060, 450005, 450015, 450025.

- **Centrality:** 0-80%.

- **Vertex selections**

$$\begin{aligned} & - |v_z^{TPC}| < 6 \text{ cm} \\ & - |v_z^{TPC} - v_z^{VPD}| < 3 \text{ cm} \end{aligned}$$

- **Track selections**

$$\begin{aligned} & - p_T > 0.2 \text{ GeV/c} \\ & - |\eta| < 1 \\ & - \text{global DCA} < 1 \text{ cm} \\ & - 20 \leq \text{nHitsFit} < 50 \\ & - \text{nHitsFit/nHitsMax} > 0.52 \\ & - \text{nHitsdEdx} > 15 \end{aligned}$$

- **PID**

$$\begin{aligned} & - \text{TPC PID (dE/dx): } |n\sigma_K| < 2 \text{ and } |n\sigma_\pi| < 2 \\ & - \text{TOF PID (1/\beta): define } n\sigma_X^{TOF} = (\frac{1}{\beta} - \sqrt{m_X^2/p^2 + 1})/\sigma + c, \text{ here } \sigma = 0.013, c = 0, m_X \\ & \text{is particle (} K, \pi, \text{ etc.) mass. For pions, we apply } -2.0 < n\sigma_\pi^{TOF} < f_\pi^{\max}(p), \text{ here} \end{aligned}$$

$$f_\pi^{\max}(p) = \begin{cases} 5.43 - 2.14x, & p < 1.6 \\ 2, & p \geq 1.6 \end{cases} \quad (26)$$

For kaons, we apply  $f_K^{\min}(p) < n\sigma_K^{TOF} < f_K^{\max}(p)$ , here

$$f_K^{\min}(p) = \begin{cases} -7.54 + 5.83p - 1.31p^2, & p < 1.37 \\ -2, & p \geq 1.37 \end{cases} \quad (27)$$

$$f_K^{\max}(p) = \begin{cases} 8.69 - 6.02p + 1.32p^2, & p < 1.9 \\ 2, & p \geq 1.9 \end{cases} \quad (28)$$

There are two PID cases:

- \* hybrid PID: Apply TOF PID while TOF is available ( $\text{TOFMatchFlag} > 0 \&\& \beta > 0 \&\& |\text{ylocal}| < 1.8$ ), otherwise use TPC PID only.
- \* clean PID: It's the same as hybrid PID, except that TOF must be used at  $p < 1.6$  GeV/c ( $\text{TOFMatchFlag} > 0 \&\& \beta > 0 \&\& |\text{ylocal}| < 1.8$ ).

- $D^0$  rapidity:  $|y| < 1$ .

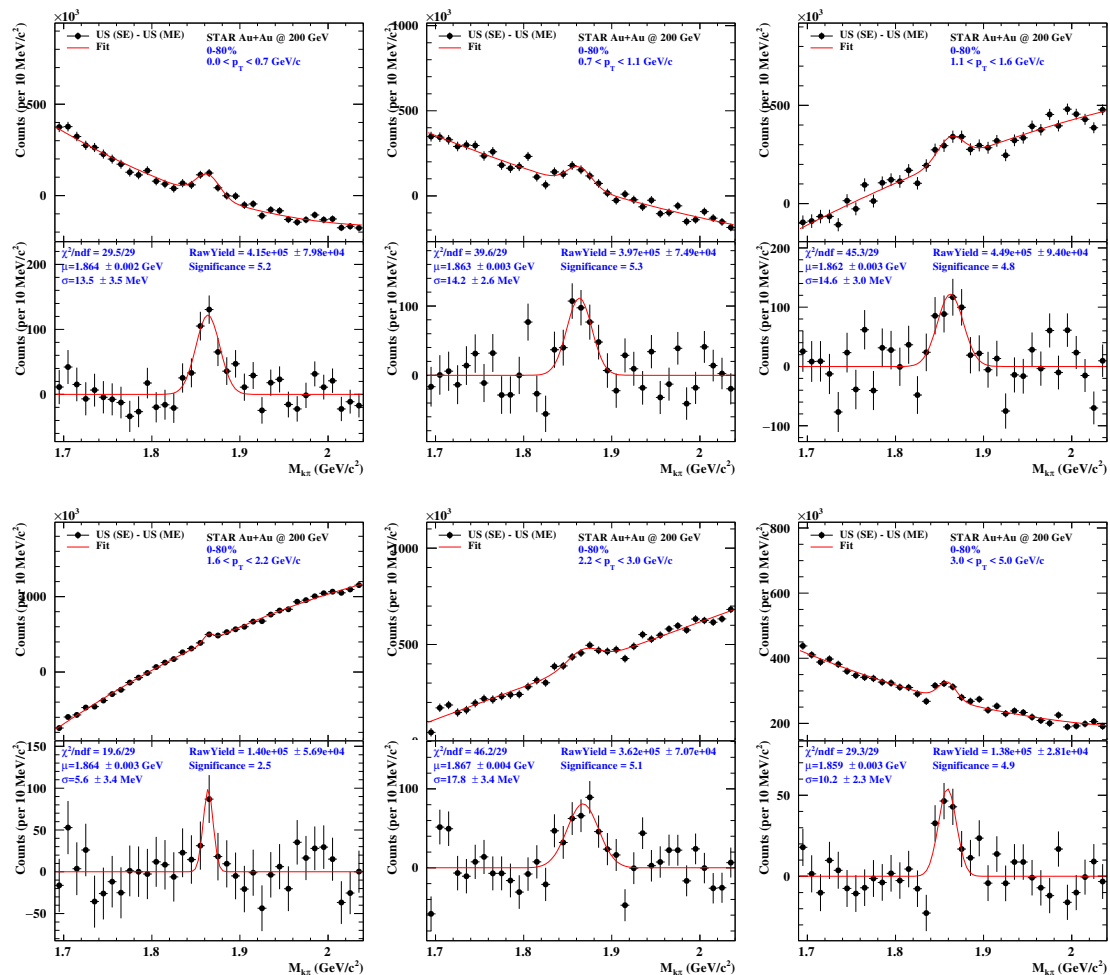


Figure 184:  $D^0$  signal at 6  $p_T$  bins ( $0-0.7$ ,  $0.7-1.1$ ,  $1.1-1.6$ ,  $1.6-2.2$ ,  $2.2-3.0$ ,  $3.0-5.0$ ) in 0-80% with clean PID.

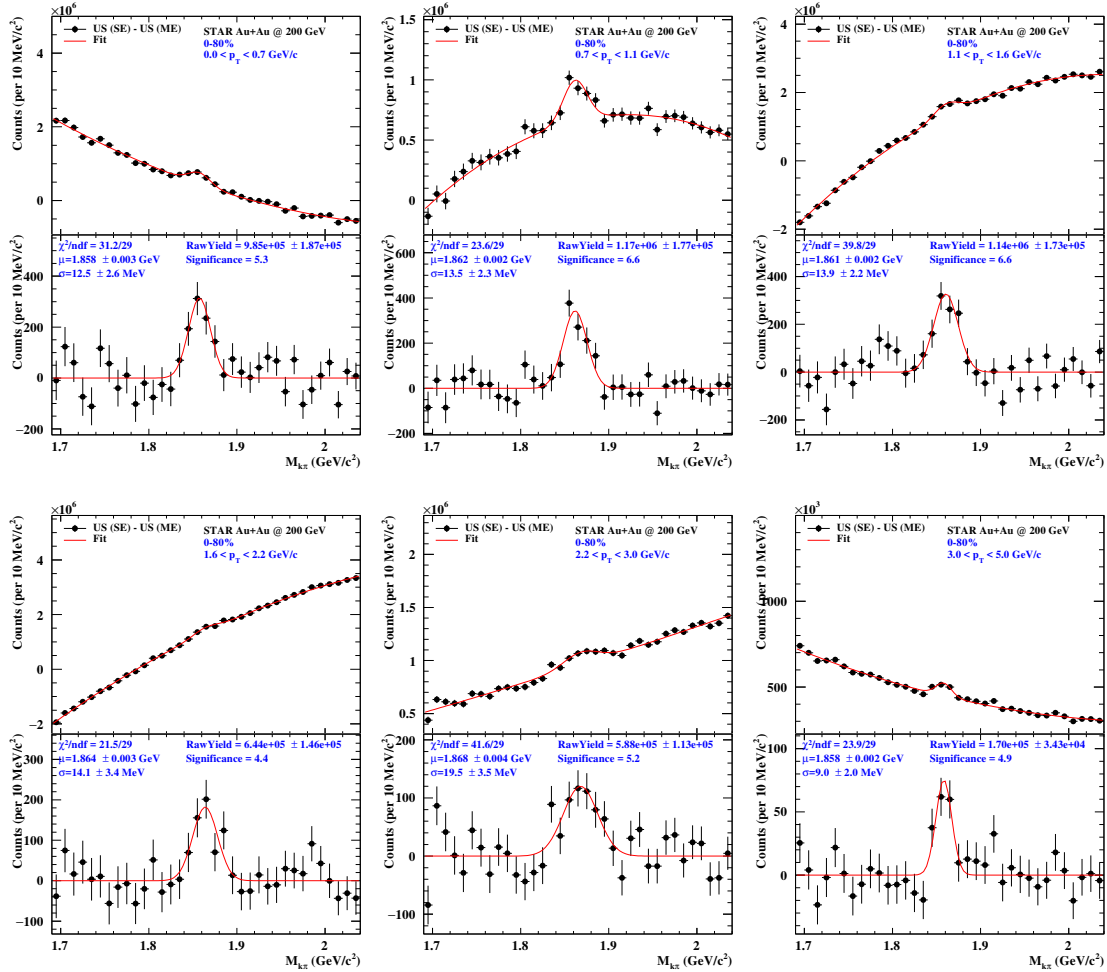


Figure 185:  $D^0$  signal at 6  $p_T$  bins (0-0.7, 0.7-1.1, 1.1-1.6, 1.6-2.2, 2.2-3.0, 3.0-5.0) in 0-80% with hybrid PID.

## 8.2 $D^0$ reconstruction

We reconstruct  $D^0$  through the channel  $D^0 \rightarrow K^- \pi^+$  (B.R. = 0.0388). Background is reconstructed with mix-event method. 9 centrality bins (0-80%), 4 primary vertex  $v_z$  bins ( $v_z \in [-6, 6] \text{ cm}$ ) and 12 event plane bins ( $\Psi_2 \in [0, \pi]$ ) are used to classify mixed events with some degree of similarity. Mix-event unlike-sign background is scaled to same-event like-sign background at the mass region of  $1.69 < \text{mass}_{K\pi} < 2.04 \text{ GeV}/c^2$ . Then same event unlike-sign (signal + background) subtracted by scaled mix-event unlike-sign background are fitted with a gaussian function (signal) plus a second order polynomial function (residual background). The fit range is  $1.69$ - $2.04 \text{ GeV}/c^2$ .

Fig. 184 shows  $D^0$  signal at 6  $p_T$  bins (0-0.7, 0.7-1.1, 1.1-1.6, 1.6-2.2, 2.2-3.0, 3.0-5.0) in 0-80% with clean PID.

Fig. 185 shows  $D^0$  signal at 6  $p_T$  bins (0-0.7, 0.7-1.1, 1.1-1.6, 1.6-2.2, 2.2-3.0, 3.0-5.0) in 0-80% with hybrid PID.

Fig. 186 shows  $D^0$  signal at 2  $p_T$  bins (0-2, 2-4) and 4 centralities (0-80%, 0-10%, 10-40%, 40-80%) with clean PID.

Fig. 187 shows  $D^0$  signal at 2  $p_T$  bins (0-2, 2-4) and 4 centralities (0-80%, 0-10%, 10-40%, 40-80%) with hybrid PID.

## 8.3 Efficiency and acceptance correction

The efficiency and acceptance correction includes the following:

- Acceptance, including  $p_T$  and  $\eta$  cut efficiency.

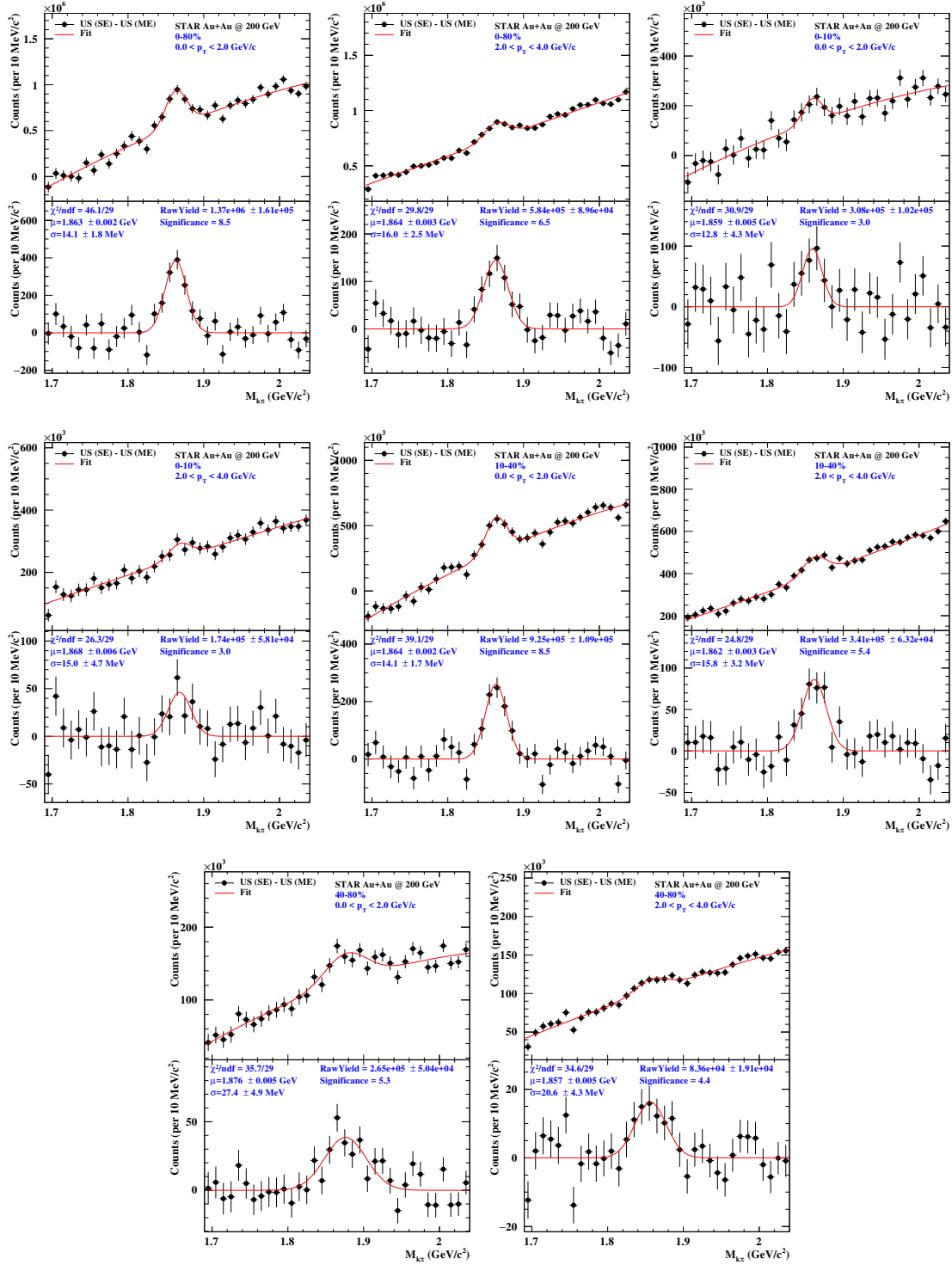


Figure 186:  $D^0$  signal at 2  $p_T$  bins (0-2, 2-4) and 4 centralalities (0-80%, 0-10%, 10-40%, 40-80%) with clean PID.

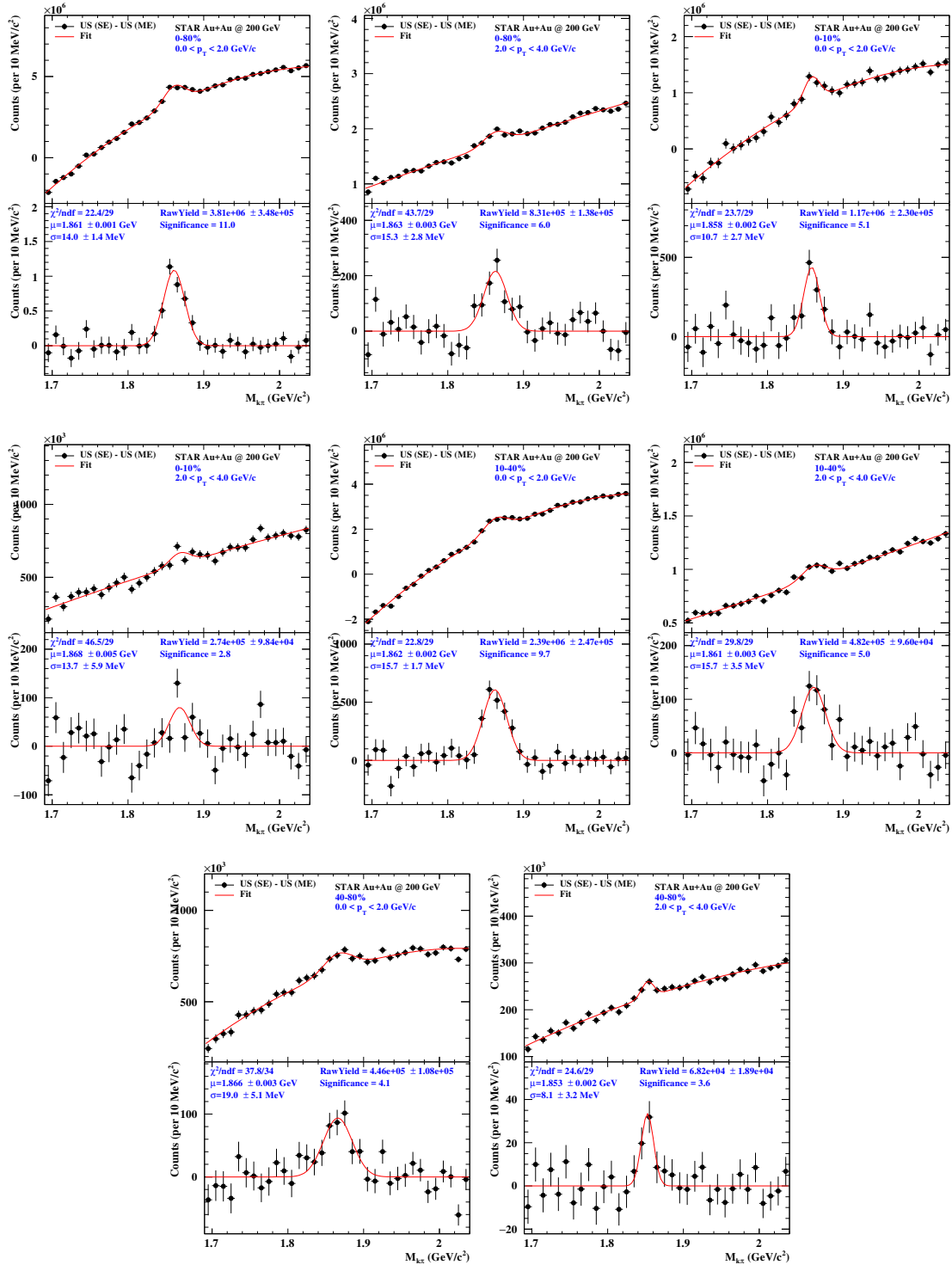


Figure 187:  $D^0$  signal at 2  $p_T$  bins (0-2, 2-4) and 4 centralalities (0-80%, 0-10%, 10-40%, 40-80%) with hybrid PID.

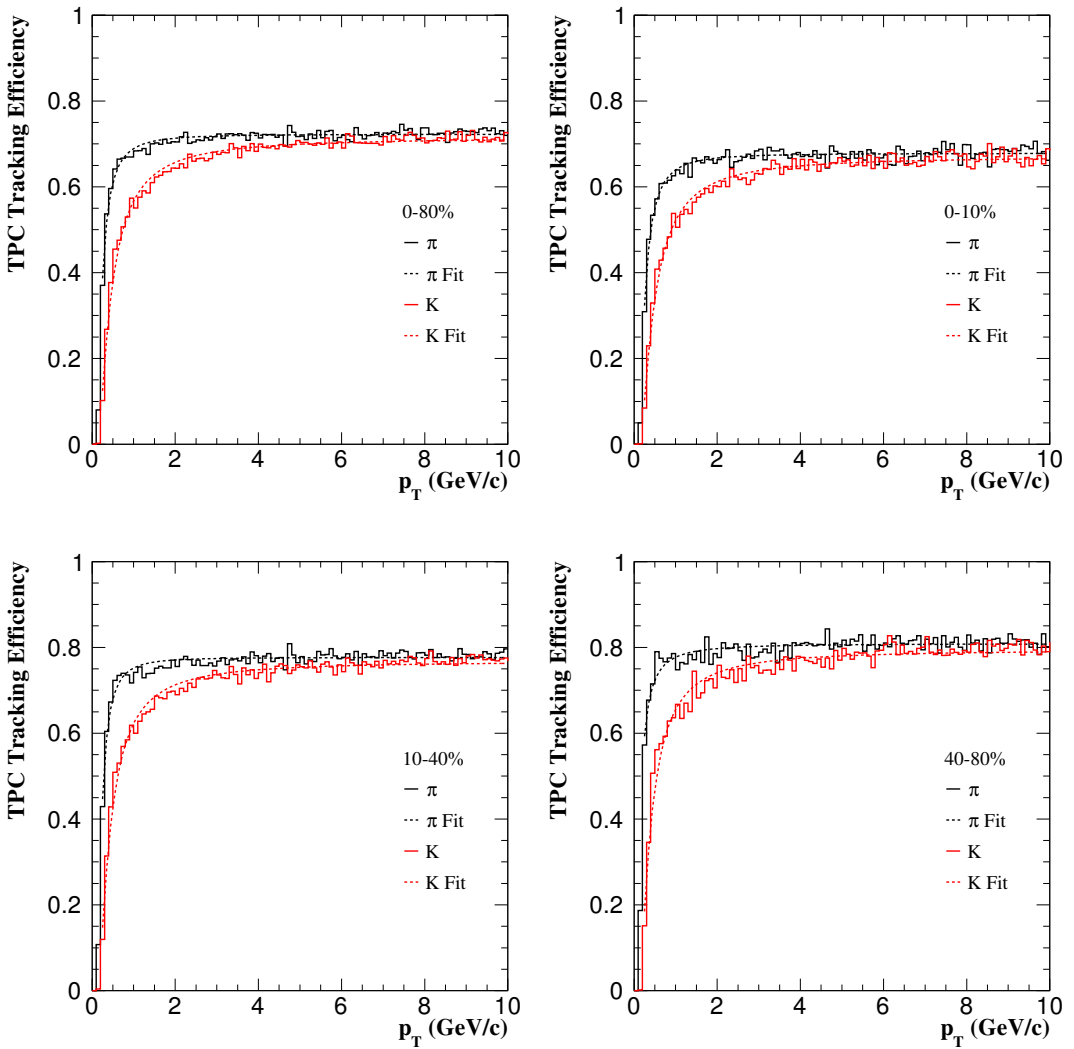


Figure 188: Run14 TPC tracking efficiency.

- TPC tracking efficiency, including the basic track quality cut efficiency (`nHitsFit`, `ndEdxHits`, `nHitsRatio`, `gDca`).
- TOF matching efficiency.
- PID efficiency, including TOF PID and TPC PID efficiency.

TPC tracking efficiency is obtained from  $K/\pi$  embedding, showed in Fig. 188.

Fig. 189 shows  $K/\pi$  TOF matching efficiency at 0-80%, 0-10%, 10-40%, 40-80%. The dip at the  $p_T$  region of 0.5-0.9 GeV/c for kaons is due that we use  $n\sigma_{K/\pi}$  to identify  $K/\pi$  and  $n\sigma_K$  resolution get better at low  $p_T$  when TOF match is required. Detailed validation can be found at Section 4.3.

Fig. 190 shows  $K/\pi$  PID efficiency. Top panels are  $K/\pi$  TPC PID efficiency and bottom panels are  $K/\pi$  TOF PID efficiency. Pure pions are obtained by reconstructing  $K_S^0$  ( $K_S^0 \rightarrow \pi^+\pi^-$ ) and pure kaons are obtained by reconstructing  $\phi$  ( $\phi \rightarrow K^+K^-$ ). Detailed information can be found at [https://drupal.star.bnl.gov/STAR/system/files/Pid\\_eff\\_new.pdf](https://drupal.star.bnl.gov/STAR/system/files/Pid_eff_new.pdf).

Fig. 191 shows single cut efficiency.

Fig. 192 shows final  $D^0$  efficiency in two PID cases, left panel for clean PID and right panel for hybrid PID. TPC PID efficiency are fixed to be 0.95 both for kaons and pions.

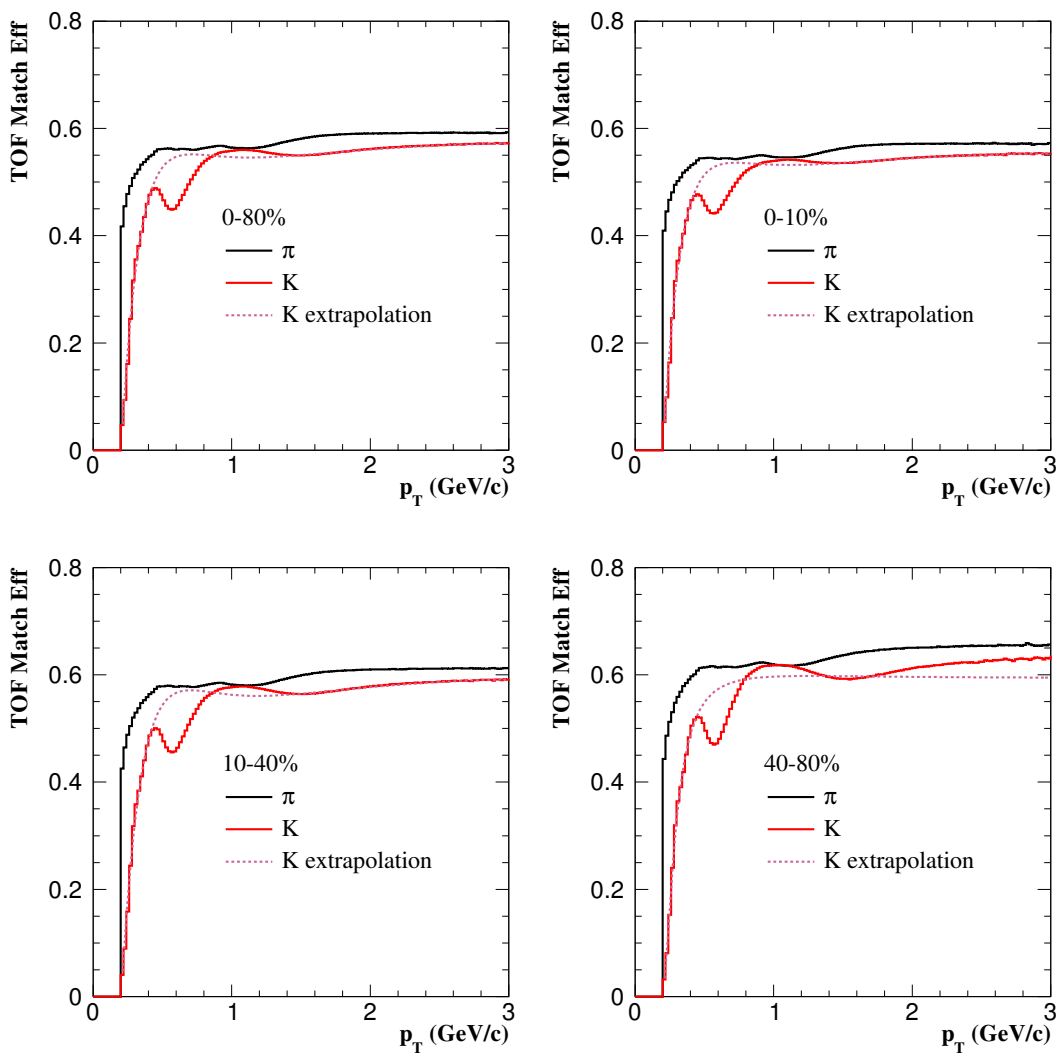


Figure 189: Run14  $K/\pi$  TOF matching efficiency at 0-80%, 0-10%, 10-40%, 40-80%.

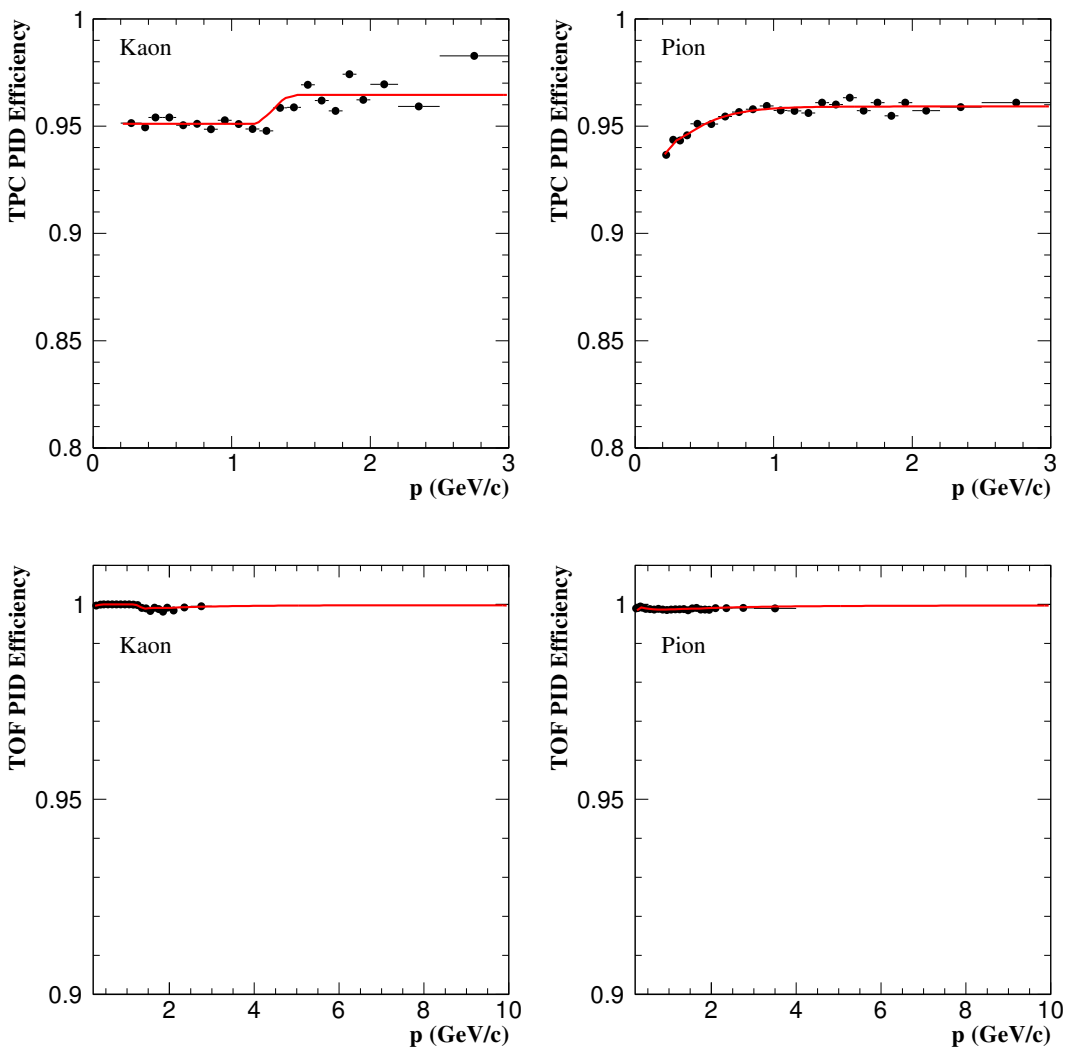


Figure 190:  $K/\pi$  PID efficiency.

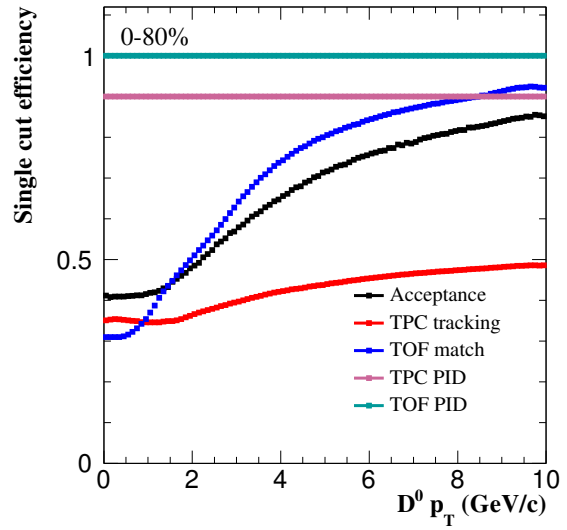


Figure 191: Run14 single cut efficiency.

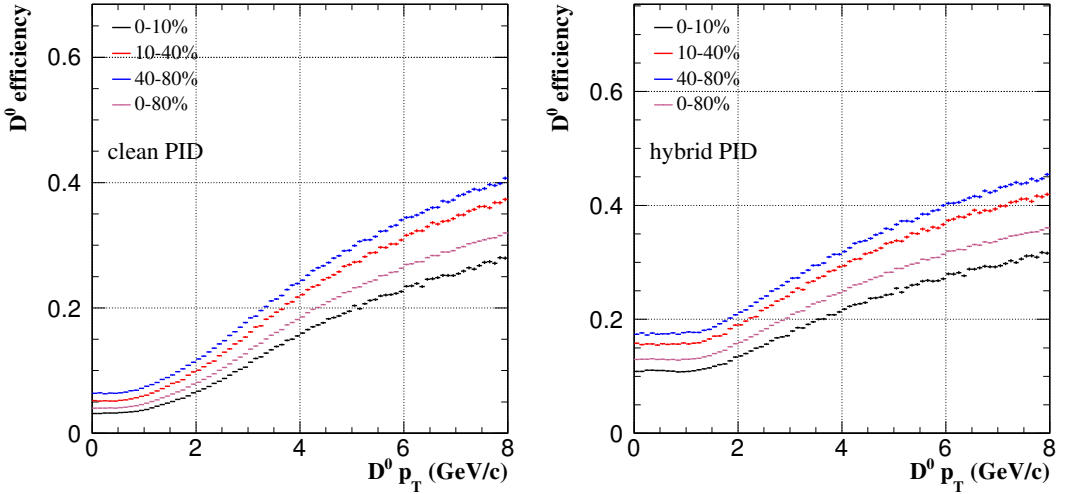


Figure 192: Run14  $D^0$  efficiency.

## 8.4 Results

Fig. 193 shows  $D^0$  spectra comparison between Run14 TPC and Run14 HFT in 6  $p_T$  bins. Top panel is  $D^0$  spectra and bottom panel is the ratio of Run14 TPC over Run14 HFT. Those data points are removed in which  $D^0$  significance is bad ( $< 3$ ) or  $D^0$  width is too narrow ( $< 9 \text{ MeV}/c^2$ ) or too wide ( $> 25 \text{ MeV}/c^2$ ). Run14 TPC results are consistent with Run14 HFT results within their statistical errors.

In order to get good  $D^0$  significance in different centralities, we also use two wide  $p_T$  bins (0-2 and 2-4  $\text{GeV}/c$ ). Fig. 194 shows  $D^0$  spectra comparison between Run14 TPC and Run14 HFT in two  $p_T$  bins. In different centralities, Run14 TPC results are also consistent with Run14 HFT results within their statistical errors.

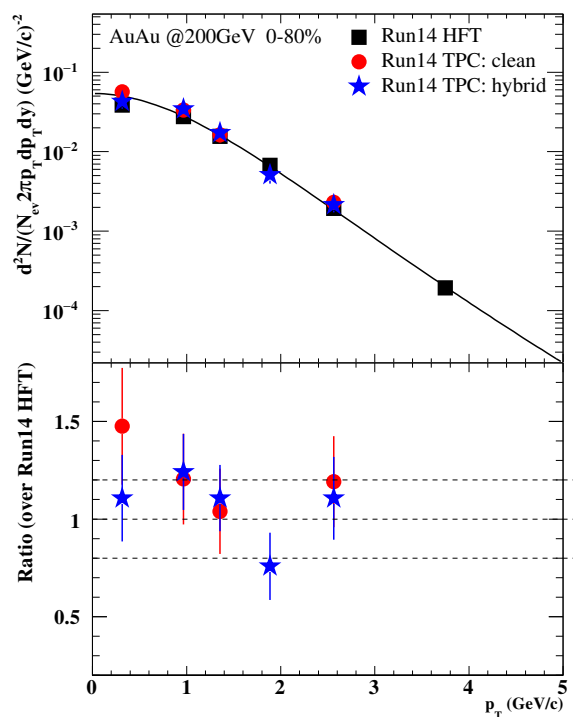


Figure 193:  $D^0$  spectra comparison between Run14 TPC and Run14 HFT.

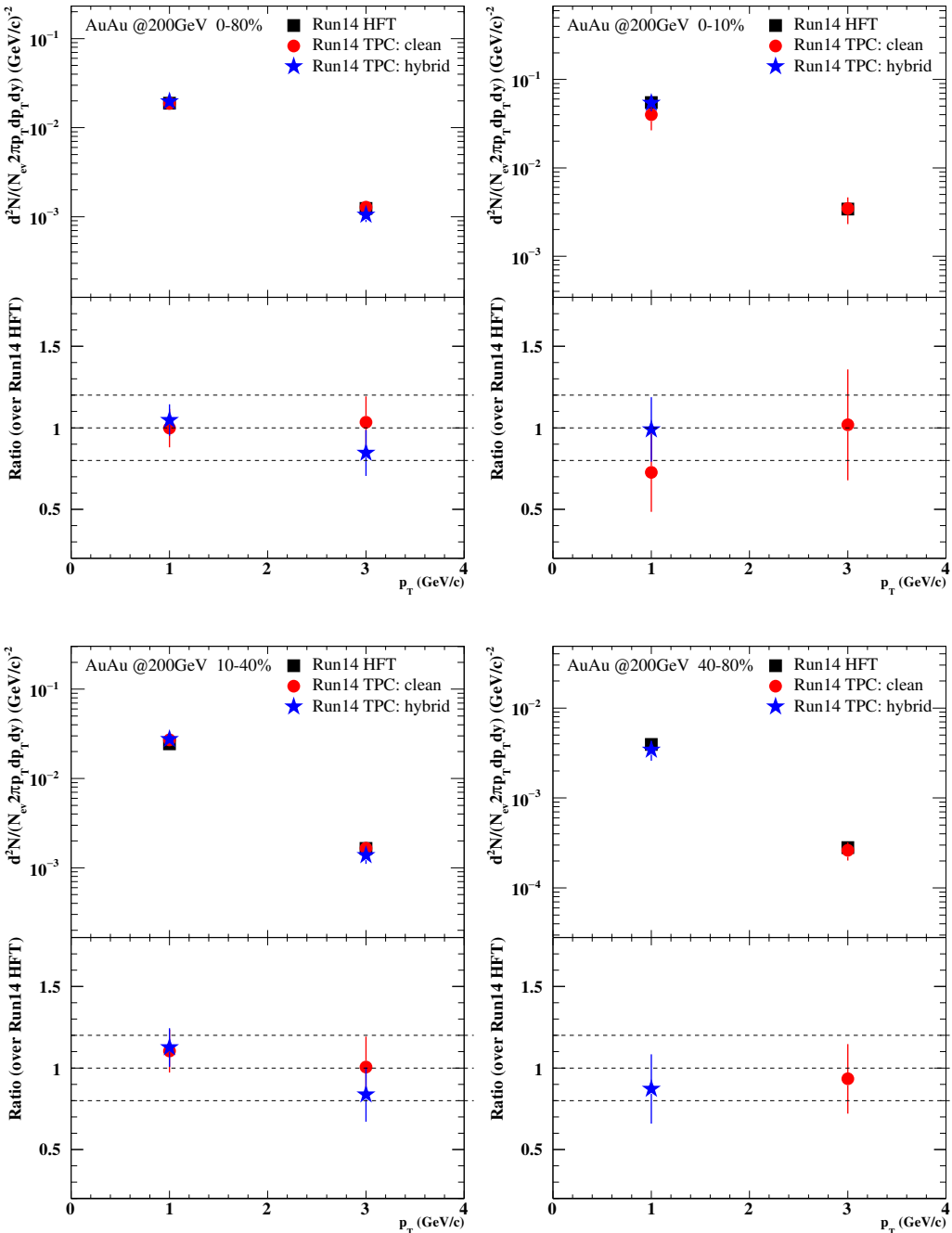


Figure 194:  $D^0$  spectra comparison between Run14 TPC and Run14 HFT in different centralities.